

Mantle and crust interaction in post-collisional setting, a case study of
lamprophyric-granitic composite dykes of northern Aigoual pluton, French
Massif Central

by
Mariana Werle

*Thesis presented in partial fulfilment of the requirements for the degree of Masters of
Earth Sciences in the Faculty of Sciences at Stellenbosch University*

Supervisor: Prof. Gary Stevens
Co-supervisors: Prof. Jean-François Moyen
Dr. Oscar Laurent

March 2022

Declaration

By submitting this assignment electronically, I declare that the entirety of the work contained therein is my own, original work, that I am the sole author thereof (save to the extent explicitly otherwise stated), that reproduction and publication thereof by Stellenbosch University will not infringe any third party rights and that I have not previously in its entirety or in part submitted it for obtaining any qualification.

March 2022

Acknowledgements

It is time to write the acknowledgements and to properly thank everyone this section will be in English and Portuguese. First, I would like to thank my supervisor Prof. Gary Stevens for your excellent guidance in my studies, for the patience and for sharing your knowledge in igneous petrology. I could certainly learn a lot during the development of this work. I also would like to thank my co-supervisors, Jeff and Oscar. Thank you Jeff for your patience in teaching me modelling and for your time in Badplaas helping me with the manuscript. Thank you Oscar for the help in geochronology and for always replying to all my questions about it.

I would like to thank IRP BuCoMo, a collaborative research project funded by the NRF and CRNS for funding this work.

Moving to South Africa in the middle of a pandemic situation with all the uncertainties imposed by this scenario has been a challenging process. I would like to thank my supervisor Gary Stevens who offered me all necessary support to start my MSc studies from Brazil and for offering me all support to have a safe trip to South Africa. I also would like to thank Llelani for the sample preparation in 2020, Madelaine, and Alicia from CAF Unity for the remote SEM analysis while I was in Brazil.

Now switching to Portuguese...

Gostaria de agradecer ao Prof. Léo Hartmann pela ajuda na redação do artigo científico e correções de inglês e a Dra. Karine Arena e Dra. Tiara Cerva-Alves pela ajuda com o Isoplot e isótopos de Hf. Gostaria de agradecer também aos brasileiros da Stellenbosch University, Alan e Marcel. Obrigada por todas as conversas, ensinamentos geológicos e cervejas.

Gostaria de agradecer imensamente aos meus pais e minha irmã por todo amor e suporte fornecidos mesmo a um oceano de distância. Vocês são e sempre serão meu porto seguro.

Last but not least, thanks Geology! Being able to study and understand (at least a little bit) the Earth and its process has been a privilege.

Table of Contents

List of Figures	v
List of Tables	viii
Abstract	ix
Resumo	x
Chapter I.....	11
1. Introduction.....	11
2. Objectives and Methodology.....	12
3. Geological Background	13
3.1. The French Massif Central (FMC).....	13
3.2. Magmatism in the E-FMC	17
3.2.1. Aigoual pluton.....	19
4. References	21
Chapter II.....	25
Abstract	26
1. Introduction.....	27
2. Geological setting	28
2.1 The French Massif Central	28
2.2 Magmatic relations in the E-FMC and Aigoual pluton	29
3 Analytical methods.....	32
3.1 Petrography and mineral chemistry	32
3.2 Whole-rock major and trace elements	32
3.3 Sr-Nd-Hf isotopes	33
3.4 Zircon U-Pb dating	34
3.5 Zircon Lu-Hf isotopes	34

3.6 Oxygen isotopes	35
4 Results	36
4.1 Field relations.....	36
4.2 Whole-rock major and trace element chemistry	37
4.3 Petrography and Mineral chemistry	41
4.4 Whole-rock Sr-Nd-Hf isotopes	45
4.5 Zircon U-Pb ages and Lu-Hf isotopes	46
4.6 Quartz, and feldspar O isotopes.....	49
5 Discussion	51
5.1 Timing of magma emplacement	51
5.2 Origin of lamprophyres and granites	53
5.3 Implications for crustal growth.....	65
6 Conclusions	67
7 References	68
Chapter III.....	83
1. Summary of findings and general discussion	83
2. Conclusions	87
3. References	89
Supplementary Material.....	92
1. Introduction.....	92
2. Textural evidence of magmatic carbonate	92
3. C-O isotopes from carbonates	97
4. References	100
Appendices	103

List of Figures

Chapter I

Figure I 1 (a) General location of Variscan Belt in Western Europe (b) Geological map from eastern French Massif Central modified from Moyen et al. (2017). Post-collisional mafic magmatic rock (vaugnerites) occurrences from Couzinié et al. (2016).	16
Figure I 2 Summary of the magmatic events in eastern French Massif Central. Modified from Laurent et al. (2017).	19
Figure I 3 Geological map of Aigoual pluton and composite dykes modified from Talbot et al. (2005).	20

Chapter II

Figure II 1 (a) General location of Variscan belt in Western Europe. (b) Geological map from eastern French Massif Central modified from Moyen et al. (2017). Post-collisional mafic magmatic rock (vaugnerites) occurrences from Couzinié et al. (2016). (c) Geological map of Aigoual pluton and composite dykes modified from Talbot et al. (2005).	31
Figure II 2 Selected field photos (a) Composite dyke with lamprophyre to granite gradational contact with increasing of volume and size of megacrysts of K-feldspars; (b) Field relationships between lamprophyre and granite; (c) Aigoual granitic pluton with enclave of lamprophyre.....	37
Figure II 3 (a) SiO ₂ vs. K ₂ O classification diagram; (b) A/CNK vs. A/NK diagram.	39
Figure II 4 Whole-rock major and trace element compositions of lamprophyre and granite from composite dykes and Aigoual pluton. Symbols as in Figure II 3.	40
Figure II 5 (a) Primitive mantle-normalized rare earth element (REE) patterns from Sun and McDonough (1989); (b) Multi-element normalized to Primitive mantle from Sun and McDonough (1989). GLOSS composition from Plank and Langmuir (1998); PCMM – post-collisional mafic magmatism from FMC from Couzinié et al. (2016); CAL – China – Calc-alkaline lamprophyre derived from partial melting of sediments from Su et al. (2017).....	41
Figure II 6 Photomicrographs and BSE images from lamprophyres and granites from composite dykes. (a) (b) Euhedral biotite in lamprophyre; (c) Interstitial dolomite in lamprophyre associated with euhedral quartz, plagioclase and biotite; (d) Calcite associated with biotite in granite; (e) Ocellar carbonate and microcrysts of K-feldspar in lamprophyre; (f) Plagioclase and biotite phenocryst in lamprophyre; (g) (h) BSE images with compositional variation from biotite/phlogopite from lamprophyre; (i) Fine grained texture in granite from composite dykes; (j) (k) (l) Textural variation in granite from composite dykes with phenocrysts of zoned plagioclase, quartz and corroded megacryst of K-feldspar. Mineral abbreviation from Warr (2021).....	44
Figure II 7 (a) Al – Mf – Fe ²⁺ ternary diagram showing compositional variations between biotite and phlogopite. Minette and lamproite fields after Rock (1991). (b) Al ₂ O ₃ vs. FeO ^T and (c) Al ₂ O ₃ vs. TiO ₂ discrimination diagram for micas after Mitchell and Bergman (1991). Abbreviations: Eas = Eastonite, Phl = Phlogopite, Sid = Siderophyllite, and Ann = Annite.....	45
Figure II 8 Zircon U-Pb Terra-Wasserburg concordia diagrams ²³⁸ U/ ²⁰⁶ Pb age (Ma) from composite dykes and Aigoual pluton. Data-point error ellipses are 2σ.	48

Figure II 9 $^{206}\text{Pb}/^{238}\text{U}$ age (Ma) versus $\varepsilon\text{Hf(t)}$ from zircons from composite dykes and Aigoual pluton. $\varepsilon\text{Hf(t)}$ lower and upper limit for Depleted Mantle (DM) are from Naeraa et al. (2012) and Griffin et al. (2004). The KDE curve is included in the diagram (light pink) for the $^{206}\text{Pb}/^{238}\text{U}$ age distribution used to calculate the Concordia age.	49
Figure II 10 (a) SiO_2 versus $\delta^{18}\text{O}$ quartz; (b) $\text{Ni} + \text{Cr}$ (log scale) versus $\delta^{18}\text{O}$ quartz; (c) $\delta^{18}\text{O}$ quartz versus $\delta^{18}\text{O}$ feldspar. Quartz-feldspar isotherms for 550°C and 950°C calculated using the calibrations of Chiba et al. (1989). Symbols as in Figure II 3.	51
Figure II 11 (a) Ba/Rb vs. Rb/Sr diagram (after Furman and Graham, 1999) suggesting presence of phlogopite in the mantle source region; (b) La/Yb vs. Nb/La after Smith et al. (1999); (c) Nb/Yb vs. Th/Yb after Pearce (2008) suggesting subduction enrichment. Granite plotting together in pale colors, as they are co-magmatic. Symbols as in Figure II 3.	61
Figure II 12 Histogram of $\delta^{18}\text{O}$ quartz analysis. Mantle O isotopic value ($\sim 5.7\text{\textperthousand}$) from Eiler (2001); I- and S-type granites from Harris et al. (1997) and peraluminous granite from Oman-United Arab Emirates (UAE) ophiolite from Spencer et al. (2017).	62
Figure II 13 (a) Results of mixing models between mantle ($\delta^{18}\text{O} = 5.7\text{\textperthousand}$ and $^{87}\text{Sr}/^{86}\text{Sr}_{\text{initial}} = 0.703$) and three different contaminants all characterized by $^{87}\text{Sr}/^{86}\text{Sr}_{\text{initial}} = 0.715$ (GLOSS, Plank and Langmuir 1998) but different $\delta^{18}\text{O}$ values characterizing different contaminants. Carbonate bearing sediments $\delta^{18}\text{O} = 28\text{\textperthousand}$; Pelagic clays $\delta^{18}\text{O} = 20\text{\textperthousand}$ and average continental crust $\delta^{18}\text{O} = 15\text{\textperthousand}$. $\delta^{18}\text{O}$ from Eiler (2001). Symbols as in Figure II 3.	62
Figure II 14 (a) $\varepsilon\text{Nd}_{\text{initial}}$ vs. $^{87}\text{Sr}/^{86}\text{Sr}_{\text{initial}}$ for composite dykes and Aigoual pluton. Initial ratios calculated for 311 Ma. Lithospheric mantle melting field from Davis and Blanckenburg (1995); Vaugnerites French Massif Central (FMC) from Moyen et al. (2017); Variscan lamprophyres from Soder and Romer (2018). For mixing calculation we used Variscan mantle composition from Pin and Paquette (1997), GLOSS from Plank and Langmuir (1998) and paragneiss composition from FMC from Moyen et al. (2017); (b) $\varepsilon\text{Nd}_{\text{initial}}$ vs. $\varepsilon\text{Hf}_{\text{initial}}$ values for composite dykes and Aigoual pluton. Data from MORB and OIB is taken from Stracke (2012) and mantle array regression line from Chauvel et al. (2008). Global kimberlites field from Tappe et al. (2018).	63
Figure II 15 (a) Yb vs. La/Yb plot with batch models of spinel and garnet phlogopite peridotite. The calculated sources correspond to Depleted Mantle (Workam and Hart 2005) mixed with 20% to 30% GLOSS (Plank and Langmuir 1998). Modal proportions in the residue are recalculated from Condamine and Médard (2014) for spinel peridotite (olivine 0.69, orthopyroxene 0.15, clinopyroxene 0.08, phlogopite 0.07, spinel 0.01) and Thibault et al. (1992) for garnet peridotite (olivine 0.25, orthopyroxene 0.5, clinopyroxene 0.15, phlogopite 0.03, garnet 0.07). Partition coefficients from mafic and intermediate rocks from Laurent (2012). (b) Multi-element pattern of lamprophyres and granites and calculated compositions generated by 5, 10 and 20% of partial melting of a spinel phlogopite-peridotite source. Black and gray continuous line represent partial melting of a calculated source with DM + 20% GLOSS and blue dashed lines represent partial melting of a calculated source with DM + 35% GLOSS. Partition coefficients from mafic and intermediate rocks from	

Laurent (2012). The melt composition from calculated source replicates the multi-element pattern exhibit by lamprophyres and granites as well, except for the LREEs. Symbols as in Figure II 3.....64

Chapter III

Figure III 1 Simple sketch showing the mantle and crust influence in the composition of post-collisional magmatism. Modified from Couzinié (2018)

85

Supplementary Material

Figure S 1 Photomicrographs of different textures (cross-polarized light) (a) Ocellar – globules of dolomite and K-feldspar in a matrix with plagioclase, quartz and biotite. (b) Xenocrysts of quartz mantled by dolomite. (c) (d) Interstitial dolomite associated with euhedral quartz, biotite and plagioclase. (e) (f) Carbonate associated with biotite.94

Figure S 2 BSE image and X-ray maps of ocellar dolomite.....94

Figure S 3 BSE image and X-ray maps of interstitial carbonate.....95

Figure S 4 BSE image and X-ray maps of the carbonate associated with biotite/phlogopite.95

Figure S 5 Oxygen and carbon isotopic compositions of different carbonates from lamprophyric-granite composite dykes, northern Aigoual pluton, FMC. C-O isotope ratios from ocelli dolomite were measured in pure carbonate whereas carbonate associated with biotite/phlogopite and interstitial were analyzed in powdered samples and include different textural forms.....98

Appendices

Appendice Figure 1 (a) Ternary diagram of classification of feldspars; (b) Ternary diagram of classification of pyroxene; (c) (d) Amphibole classification.103

Appendice Figure 2 BSE images and X-ray maps of three different magmatic textures of carbonate.....104

Appendice Figure 3 Selected CL images of zircon from composite dykes and Aigoual pluton with U-Pb age and ϵ Hf values.105

List of Tables

Chapter II

Table II 1 $\delta^{18}\text{O}$ values from quartz and feldspar from lamprophyre and granite of composite dykes and Aigoual pluton (AG14A).....	50
--------------------------------------------------------------------------------------------------------------------------------------------------	----

Supplementary Material

Table S1 1 C-O isotope data from carbonates.....	99
--------------------------------------------------	----

Appendices

Table 1 Sample name, coordinates and lithology	106
Table 2 Whole-rock major (wt.%) and trace (ppm) element compositions of composite dykes from Aigoual pluton, French Massif Central.	107
Table 3 Mineral chemistry of biotite/phlogopite.....	110
Table 4 Mineral chemistry of feldspars	119
Table 5 Mineral chemistry of pyroxene	127
Table 6 Mineral chemistry of amphibole	131
Table 7 Whole-rock Sr, Nd, Hf isotopes	134
Table 8 Zircon LA-SF-ICP-MS U-Pb geochronology data	136
Table 9 Analytical results zircon Lu-Hf isotopes	141

Abstract

Lamprophyre to granite composite dykes in the northern extremity of the post-Variscan Aigoual pluton, French Massif Central (FMC), offer an opportunity to study the complexity of the processes that control crustal growth in post-collisional tectonic settings through mantle and crust interactions. The aim of this thesis is to contribute to an improved understanding of the petrogenesis of the composite dykes and to constrain the mantle contribution to post-collisional magmatism in the FMC. In the field, most dykes are composite and vary gradationally from lamprophyres to granites. The lamprophyres are metaluminous to slightly peraluminous, display moderate to high compatible element contents such as Cr (54 – 572 ppm) and Ni (23 – 148 ppm) and coupled with the relative high Mg# (up to 60) indicate a mantle-derived source for at least this component of the composite system. However, the lamprophyres display crustal-like signatures with enrichment in LILE (K_2O , Sr, Rb, Ba, Pb, V) and LREE and in both radiogenic (Sr, Nd and Hf whole-rock and zircon) and stable (O) isotopic systems. The data indicate the dual geochemical signature is source-related and lamprophyres were generated by partial melting within the spinel-lherzolite stability field of an enriched mantle highly metasomatized by sediment-derived melts or fluids introduced to the mantle during subduction preceding Variscan continental collision. The granites from composite dykes are peraluminous, have high K_2O with shoshonitic affinity and trace elements and isotopic signatures alike lamprophyres. These similarities and relative high contents of Cr, Ni, Mg and Fe related to crustal-derived granites in FMC display a mantle-derived component involved in the petrogenesis of granites from composite dykes. Although completely hidden from both radiogenic and stable isotopes and incompatible element contents, addition of new mantle-material is identified in lamprophyres and granites by the high compatible element contents such Cr, Ni, Fe and Mg. Combining geochemical modelling with outcrop patterns, addition of new-mantle material represents ca. 22 – 28% of the post-collisional magmatic material in FMC and crustal growth may be significant in post-collisional sites. This work demonstrate the intimate relation (physically, petrologically and geochemically) between lamprophyres and granites in the composite dykes of northern border of Aigoual pluton and provide constraints about the mantle and crust interaction and contribution of mantle material in post-collisional granitoids from the FMC.

Resumo

Diques compostos por lamprófiros e granitos na extremidade norte do plúton Aigoual pós-Variscano, Maciço Central Francês (MCF), permitem estudar a complexidade dos processos que controlam a formação de crosta em ambiente pós-colisional através de interações entre manto e crosta. O objetivo dessa tese é a petrogênese dos lamprófiros e granitos em um sistema de diques compostos e estabelecer a contribuição mantélica no magmatismo pós-colisional do MCF. Em campo, os diques compostos variam gradacionalmente de lamprófiros a granitos. Os lamprófiros variam de metaluminosos a fracamente peraluminosos, possuem teores moderados a altos de elementos compatíveis como Cr (54 – 572 ppm) e Ni (23 – 148 ppm) e, juntamente com o relativo alto Mg# (maior que 60), indicam uma fonte manto derivada para esse componente do sistema composto. Entretanto, os lamprófiros possuem assinatura crustal com enriquecimento em LILE (K_2O , Sr, Rb, Ba, Pb, V) e ETRL e nos sistemas isotópicos radiogênicos (Sr, Nd e Hf rocha total e zircão) e estável (O). Os estudos indicam essa dualidade geoquímica é relacionada à fonte. Os dados indicam fusão parcial no campo de estabilidade do espinélio-herzolito de um manto fortemente metassomatizado por fluidos ou magmas derivados de sedimentos introduzidos no manto durante a subducção que precede a colisão continental na orogênese Variscana. Os granitos dessa área são peraluminosos, possuem alto K_2O com afinidade shoshonítica e possuem conteúdos de elementos traço e assinaturas isotópicas similares aos lamprófiros. Essas similaridades e relativo alto conteúdo de Cr, Ni, Mg e Fe comparados aos granitos derivados da crosta no MCF demonstram que há componente mantélico envolvido na petrogênese da porção granítica dos diques compostos. Apesar de completamente oculto do ponto de vista de isótopos estáveis e radiogênicos, a adição de novo material proveniente do manto é identificada pelo alto teor em elementos compatíveis como Cr, Ni, Mg e Fe. Combinando modelagem geoquímica com o padrão dos afloramentos, a adição de novo material manto derivado representa cerca de 22 – 28% do material magmático no MCF indicando que o crescimento crustal no ambiente pós-colisional é significante. Esse estudo demonstra a relação intrínseca (física, petrológica e química) entre lamprófiros e granitos em um sistema de diques compostos da porção norte do plúton Aigoual e fornece indícios sobre a relação manto e crosta nos granitoides pós-colisionais do MCF.

Chapter I

1. Introduction

The growth of continental crust is controlled by addition of new mantle-derived material to the crust relative to recycling of continental materials in the subduction zones. It is well known that mantle and crust represent two distinct and complementary geochemical reservoirs on Earth, with pronounced compositions and isotopic signatures (Dhuime et al. 2011; Rudnick and Gao 2003; Stein and Ben-Avraham 2007). During the subduction process, crustal materials are introduced to the mantle and react with peridotite in a geochemical exchange between mantle and crust through geological time. This process results in contrasting types of metasomatism, and thus, contrasting chemical and isotopic signatures of magmas product of melt of metasomatized mantle (e.g. Clemens et al. 2017; Pandey et al. 2017, 2018; Wang et al. 2020).

The post-collisional tectonic setting established after the main collision in the orogenic cycle is characterised by changing in the geodynamics of the orogeny causing thermal disturbance and consequently intense magmatism melting rocks from both mantle and crustal sources (e.g. Bonin 2004; Clemens et al. 2009). In this context, post-collisional high K-Mg mafic mantle-derived rocks (i.e. lamprophyres, lamproites, vaugnerites, durbanchites etc.) are extensively described at the end of collisional orogenies and, besides less voluminous, contribute to crustal growth by addition of new mantle-derived material to the crust.

The Variscan belt, situated in central and Western Europe, resulted from the collision between Gondwana and Laurussia to assemble Pangea, the latest supercontinent on Earth. The French Massif Central (FMC) corresponds to one of the largest exposures of the Variscan belt and represents the inner part of the orogeny (e.g. Lardeaux et al. 2014) exposing allochthonous and paraautochthonous units at different crustal levels (Faure et al. 2009; Vanderhaeghe et al. 2020). Furthermore, the Carboniferous evolution of the Variscan belt is marked by massive post-collisional magmatism with extensive and ~40 Ma long-lived generation of coeval granites and mantle-derived mafic rocks (Couzinié et al. 2014; Laurent et al. 2017). Thus, the FMC is a remarkable place to study processes of

crustal formation by addition of new mantle-derived magma, recycling and reworking of ancient continental crust (e.g. Chelle-Michou et al. 2017; Couzinié 2018; Melletton et al. 2010; Moyen et al. 2017).

The mantle-derived mafic rocks of FMC are described as enclaves in felsic rocks, decametric small bodies associated with granites and migmatites and also as lamprophyre dykes. They are characterised by mafic to intermediate compositions, metaluminous to slightly peraluminous, high-K to shoshonitic affinity ($K_2O = 1.5 - 6$ wt. %), volatile-rich and enriched in both compatible (Fe, Mg, Ni, Cr) and incompatible elements (K, Rb, Ba, Sr) (Couzinié et al. 2016; Sabatier 1991; von Raumer et al. 2014). Although well defined in space and time, the role of the post-Variscan mafic magmatism in the FMC is still debated (Couzinié et al. 2016; Jacob et al. 2021). Precisely, the association with crustal-derived magmas and the balance between crustal growth by addition of new mantle-derived magma and crustal recycling remains poorly understood.

Located in the southeast part of FMC, the post-Variscan Aigoual granitic pluton is part of a major L-shape pluton called Aigoual – Saint Guiral – Liron pluton. The northern extremity of Aigoual pluton consists of NE-SW dyke swarms that record co-magmatic lamprophyres and granites. The composite dykes display a great area to unravel the relation of mantle and crust contributions in the post-collisional magmatism from FMC and are the subject of this thesis.

2. Objectives and Methodology

The objective of this thesis consists in the petrogenesis of the lamprophyres and granites from composite dykes in the northern of Aigoual pluton and constrain the mantle contribution in the post-collisional magmatism in FMC and consequently implications for crustal growth. To achieve the proposed objective the following methodology was applied:

- 1) Field work and sample collection (made by my supervisors in 2019);
- 2) Petrography and mineral chemistry;
- 3) Whole-rock major and trace elements;
- 4) Sr-Nd-Hf isotopes in whole-rock;
- 5) U-Pb and Lu-Hf isotopes in zircon;
- 6) Oxygen isotopes in quartz and feldspar.

Details about each methodology as well the results and discussions acquired in this research are shown in a manuscript presented in Chapter II. The manuscript is in preparation for submission to the journal *Contributions to Mineralogy and Petrology*.

Additionally, three different carbonate textures in lamprophyres and granites were studied. The carbonate textures and textural relationships with co-genetic silicate phases are consistent with magmatic origin. Details about textures and C-O isotopes in carbonate are presented as a Supplementary Material in this thesis.

3. Geological Background

3.1. The French Massif Central (FMC)

The Variscan belt is an extensive orogenic belt (~3000 km) in central and Western Europe. It was formed during Upper Paleozoic between 480 and 250 Ma in a complex collisional history involving two main continents Gondwana and Laurussia, micro-continental plates and oceanic basins resulting in the Pangea supercontinent at the end of Paleozoic (Kröner and Romer 2013; Matte 1991, 2001).

One of the largest exposures of the Variscan Belt in Western Europe is preserved in the French Massif Central (FMC) (Vanderhaeghe et al. 2020). The FMC represents the north portion of the Gondwana margin and exposes a south-verging stack of nappes with metamorphic and plutonic rocks generated during several tectonic-metamorphic-magmatic events from collision to collapse of Variscan Orogeny at Devonian to early-Carboniferous (Faure et al. 2009; Lardeaux et al. 2014; Villaros et al. 2018). In the eastern portion, the stack of nappes are composed by four main units, from top to bottom and from north to south:

1. The Brévenne Unit: the Brévenne Unit consists of mafic-ultramafic, siliceous sedimentary rocks metamorphosed under greenschist facies conditions. These rocks were dated of late Devonian and were interpreted as fragments of mantle and oceanic crust in an ophiolitic association in a back-arc environment, as a result of subduction and closure of the ancient Rheic Ocean (Lardeaux et al. 2014).
2. Upper Gneiss Unit (UGU): the UGU forms the overlying nappe and is composed by ortho and paragneisses containing relicts of (ultra) high-pressure eclogites (Faure et al. 2005; Lardeaux et al. 2001). Furthermore, the lower section of UGU is

characterised by mafic-felsic rocks called leptynite-amphibolite complex interpreted as forming during the rifting in a continental-oceanic crust transition zone (Faure et al. 2005; Lardeaux et al. 2014). The upper section is composed by Devonian (ca. 360 Ma) migmatites formed by partial melting of pelitic and quartz-feldspathic rocks. The mafic restites under amphibolite facies are interpreted as retrogressed eclogites.

3. Lower Gneiss Unit (LGU): the underlying nappe LGU is composed by amphibolite facies-micaschists, ortho and paragneisses with Ediacaran-early Cambrian protoliths (Chelle-Michou et al. 2017) and minor amphibolites. These rocks experienced a LP/HT metamorphism during the late-Carboniferous and orogenic collapse (ca. 300 Ma) melted and formed several granitic plutons including the Velay granite-migmatite in the eastern part of FMC (Ledru et al. 2001; Villaros et al. 2018).
4. The Parautochthonous Unit: the low-grade called parautochthonous unit is widely exposed in southern FMC (Cévennes area). This unit thrusts over the Paleozoic fold-thrust belt and is essentially composed of metasediment deposited between the Neoproterozoic and early-Cambrian followed by greenschist to amphibolite facies metamorphism (Melleton et al. 2010).

The first tectono-metamorphic event (D0) is characterised by collision between Gondwana and America micro-plate and is recorded by eclogite relicts in the UGU (Faure et al., 2009). The U(HP) event is dated between 430 and 410 Ma (U-Pb in zircon) (Do Couto et al. 2015; Paquette et al. 1995) and experienced 1.8 – 2 GPa and 650 - 750°C conditions of pressure and temperature, respectively (Lardeaux et al. 2001). A second event D1 is marked by a widespread flat-lying foliation with NE-SW trending associated with top to the SW ductile shearing. This event is coeval with exhumation of HP rocks. D1 is the first significant event in the generation of stack of nappes thrusting the UGU over the LGU (Faure et al. 2009) and triggered melting of para and orthogneisses from UGU and LGU. The migmatisation is dated from middle-Devonian (~380 Ma) (Duthou et al., 1994). At late-Devonian, early-Carboniferous, the D2 event corresponds to the main event of nappe stacking (Faure et al. 2009). The top-to-the-NW thrusting juxtaposed the UGU to the north to the Brévenne Unit (Leloix et al. 1999). The geodynamic scenario of D2

event is related with the closure of Rheic Ocean and coeval with MP/MT metamorphism (Faure et al. 2005, 2009). The Middle Carboniferous D3 event took different geotecnical scenarios in the FMC. Whereas in the southern area (e.g. Cévennes) D3 is responsible for crustal thickening with top-to-the-S thrusting and LP/LT metamorphism, in the northern syn-orogenic extension took place to Visean volcano-sedimentary rocks (Bruguier et al. 1998; Faure et al. 2009). D4 and D5 N(W)-S(E) extensional events correspond to the syn- and post-orogenic collapse of the orogeny in the late Carboniferous – early Permian (Faure et al. 2005, 2009). The development of normal faults and grabens and half-grabens took place in the formation of the Stephanian intramontane coal basins (Malavieille et al. 1990).

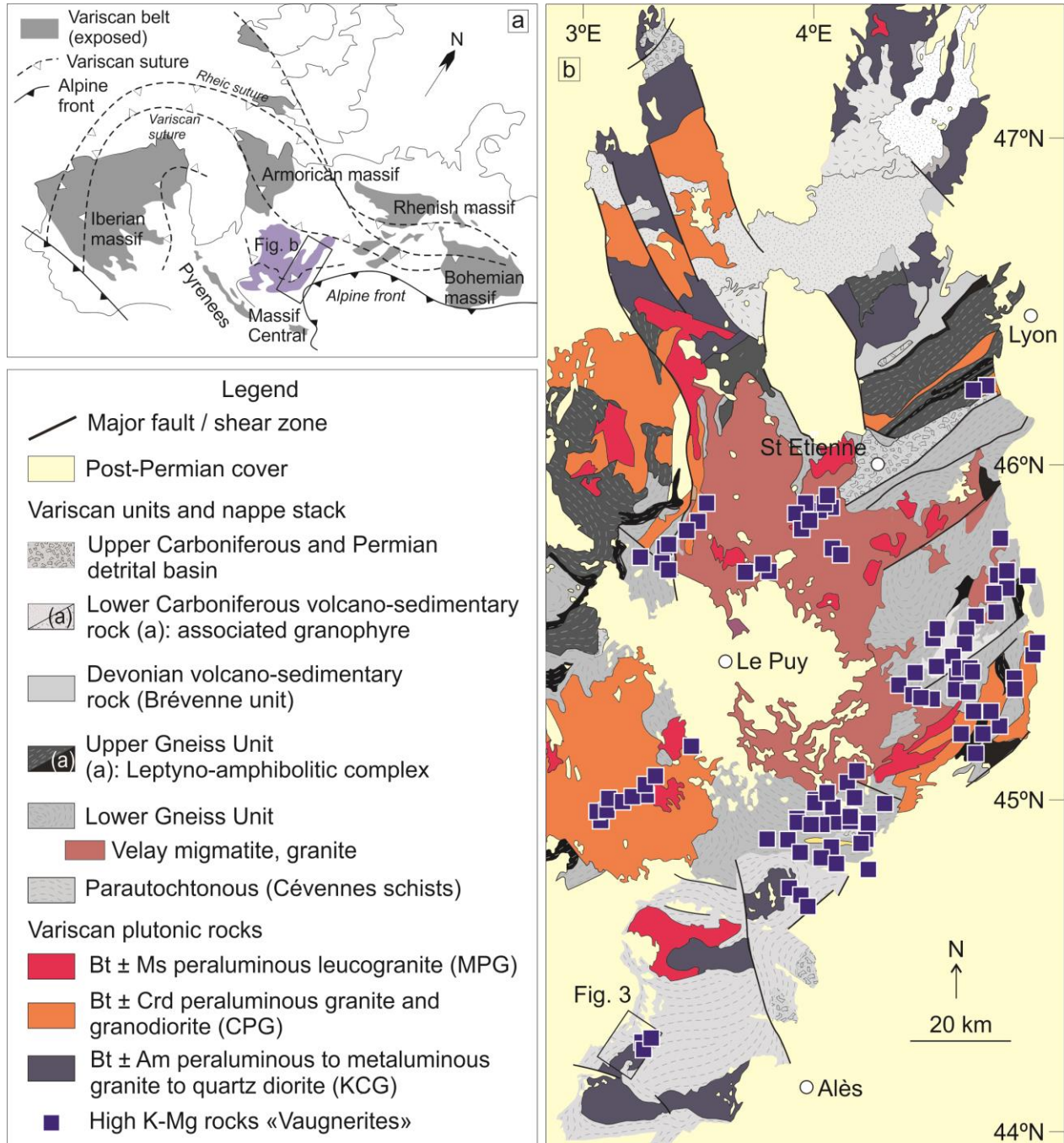


Figure I 1 (a) General location of Variscan belt in Western Europe (b) Geological map from eastern French Massif Central modified from Moyen et al. (2017). Post-collisional mafic magmatic rock (vaunderites) occurrences from Couzinié et al. (2016).

3.2. Magmatism in the E-FMC

The Variscan belt is characterised as a hot orogeny due to the large amount of granitoid magmas emplaced in the metamorphic units during the orogenic collapse. In this work, for further details, we focused on the post-collisional magmatic rocks of Eastern part of the FMC.

Based on nomenclature defined by Barbarin (1999), the plutonic rocks of E-FMC can be subdivided into four main groups (Chantraine et al. 1996).

- 1) Two-mica or muscovite-bearing peraluminous granitoids (“MPG”) outcrop as small plutons, laccoliths intruding the Velay complex (Ledru et al. 2001) and dykes. These rocks are granite *sensu stricto* with SiO_2 (>70 wt.%) and its peraluminous character indicate crustal source (Barbarin 1999; Pin and Duthou 1990);
- 2) Cordierite-bearing peraluminous granitoids (“CPG”) are peraluminous to slightly metaluminous granites and granodiorites with biotite and cordierite ranging from abundant to rare. These rocks have elevated SiO_2 content (> 65 wt.%), K_2O (3-7 wt.%) and together with Sr-Nd isotopic data indicate melting of local crust (Duthou et al. 1984; Pin and Duthou 1990; Williamson et al. 1997).
- 3) K-feldspar porphyritic, biotite \pm amphibole-bearing granites, granodiorites and quartz diorites (“KCG”). These rocks are high-K, weakly peraluminous to metaluminous and forms large plutons (e.g. Aigoual) or enclaves in the Velay complex and are, in general, more mafic than CPG with SiO_2 content average ~69 wt.% and $\text{FeO}_{\text{t}} + \text{MgO} \sim 4$ wt.%. The KCG group is often associated with intermediate to mafic rocks.
- 4) A suite of biotite-, amphibole-, \pm clinopyroxene- bearing intermediate to mafic rocks is described throughout the Variscan Belt (von Raumer et al. 2013) and in the E-FMC is locally called vaugnerites (Couzinié et al. 2014; Sabatier 1991). These rocks are metaluminous with low-silica content ($44 < \text{SiO}_2 < 63$ wt.%), high $\text{FeO}_{\text{t}} + \text{MgO}$ (10–24 wt.%), Cr (200–600 ppm) and Ni (100–220 ppm) contents, Mg# (molecular Mg/Mg + Fe) higher than 0.65; they also have high K_2O contents (1.6–6.7 wt.% corresponding to high-K to shoshonitic affinity), Ba and Sr (1000–2000 ppm; Couzinié et al. 2016). They outcrop as small bodies

as enclaves in granites and migmatites and form sills and dykes with lamprophyric affinity.

The magmatic rocks were generated during a long lived magmatic activity (~40 Ma; Couzinié et al. 2014; Laurent et al. 2017) during D3 and D4 tectono-metamorphic events culminating with the late-Variscan collapse under LP-HT conditions with the formation of granite-migmatite Velay dome (Figure I 2).

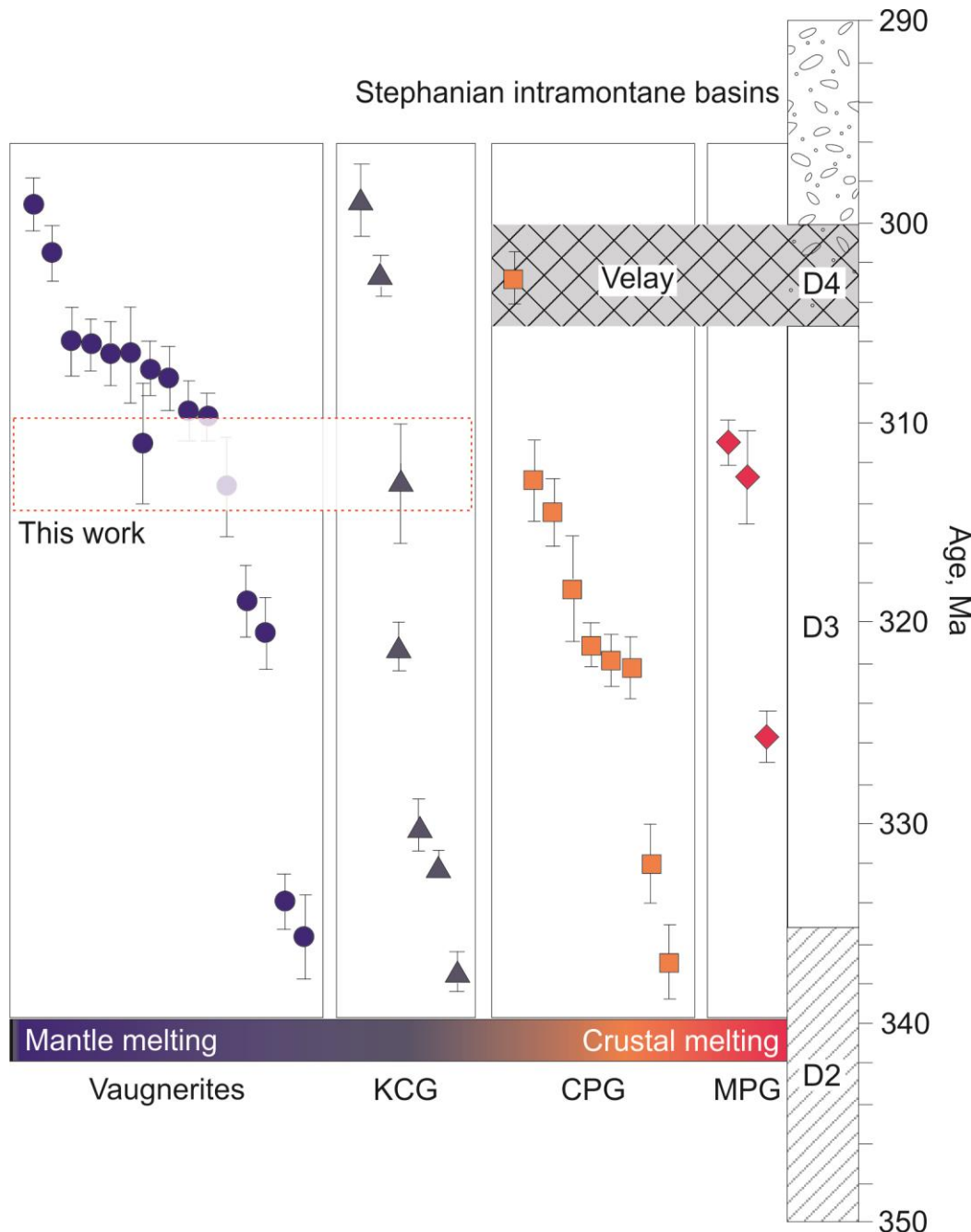


Figure I 2 Summary of the magmatic events in eastern French Massif Central. Modified from Laurent et al. (2017).

3.2.1. Aigoual pluton

The Aigoual pluton is the northern termination part of an L-shape major pluton called Aigoual-Saint Guiral-Liron Pluton (ASGL) that outcrops in the southeast of FMC. The ASGL intrudes the “micaschistes des Cévennes” at shallow depth (1–2 kb; 690–700°C) (Najoui et al. 2000) developing a contact metamorphic aureole. Based on $^{40}\text{Ar}/^{39}\text{Ar}$ dating

in biotite and U-Pb in zircon and monazite, the main intrusion occurred between 305-310 Ma and is synchronous with the late stage of migmatization in the Velay dome and the late Variscan extensional event in this area (Brichau et al. 2008). The ASGL is classified as K-feldspar porphyritic calc-alkaline granitoids (KCG) and is composed by two cogenetic porphyritic monzogranite and microgranite (Chantraine et al. 1996; Sabourdy 1975).

The northern termination of Aigoual pluton consists of a series of 5 – 20 m NE-SW to NNE-SSW dykes swarms (Figure I 3). Some individual dykes vary from lamprophyric dark borders with aphanitic texture progressively grading to microgranite (Sabourdy 1975). The composite dykes are subject of this study.

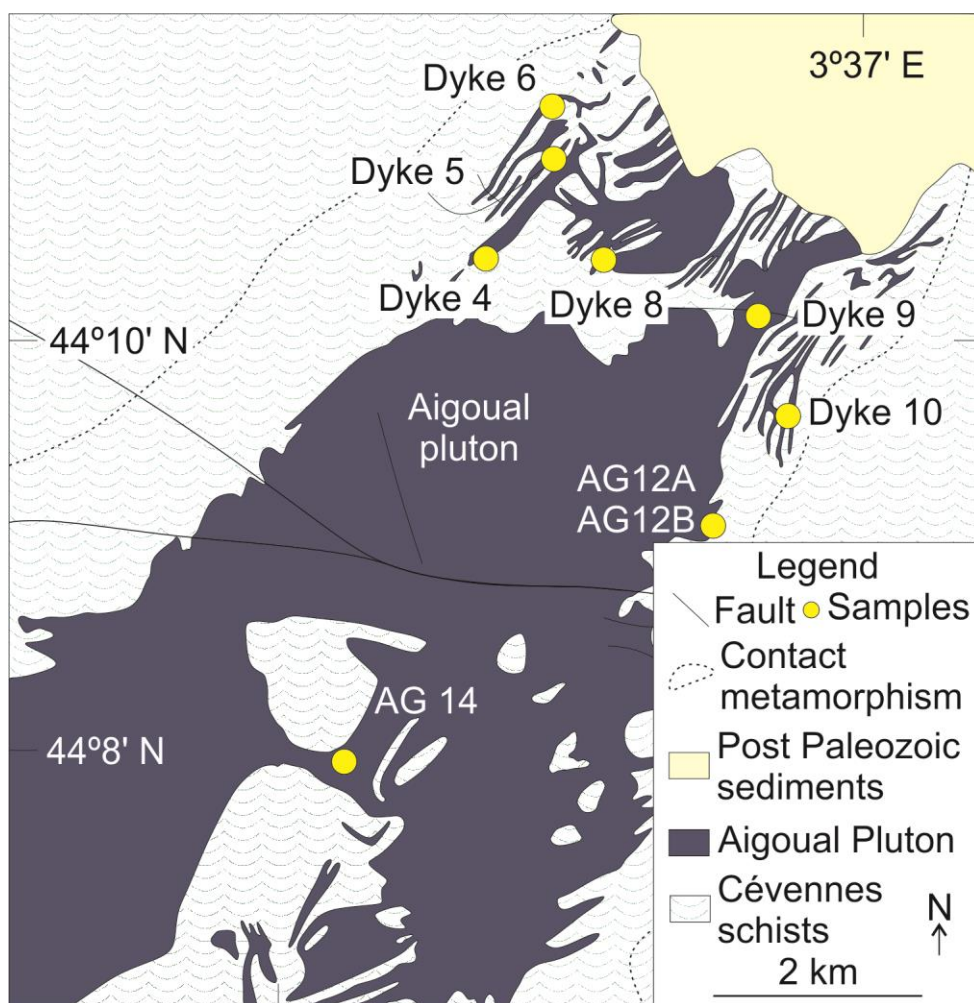


Figure I 3 Geological map of Aigoual pluton and composite dykes modified from Talbot et al. (2005).

4. References

- Barbarin B (1999). A review of the relationships between granitoid types, their origins and their geodynamic environments. *Lithos* 46(3):605-626.
- Bonin B (2004). Do coeval mafic and felsic magmas in post-collisional to within-plate regimes necessarily imply two contrasting, mantle and crustal, sources? A review. *Lithos* 78:1-24.
- Brichau S, Respaut JP, Monié P (2008). New age constraints on emplacement of the Cévenol granitoids, South French Massif Central. *International Journal of Earth Sciences* 97:725–738.
- Bruguier O, Becq-Giraudon JF, Bosch D, Lancelot J (1998). Late Visean hidden basins in the internal zones of the Variscan belt: U-Pb zircon evidence from the French Massif Central. *Geology* 26(7):627–630.
- Chantraine J, Autran A and Cavelier C (1996). *Carte géologique de la France à l'échelle du millionième (6e édition)*, BRGM, Orléans.
- Chelle-Michou C, Laurent O, Moyen JF, Block S, Paquette JL, Couzinié S, Gardien V, Vanderhaeghe O, Villaros A, Zeh A (2017). Pre-Cadomian to late-Variscan odyssey of the eastern Massif Central, France: formation of the West European crust in a nutshell. *Gondwana Research* 46:170-190.
- Clemens JD, Buick IS, Frei D, Lana C, Villaros A (2017). Post-orogenic shoshonitic magmas of the Yzerfontein pluton, South Africa: the ‘smoking gun’ of mantle melting and crustal growth during Cape granite genesis? *Contributions to Mineralogy and Petrology* 172:72 DOI 10.1007/s00410-017-1390-9.
- Clemens JD, Darbyshire DPF, Flinders J (2009). Sources of post-orogenic calc-alkaline magmas: the Arrochar and Garabal Hill–Glen Fyne complexes, Scotland. *Lithos* 112:524–542.
- Couzinié S, Bouilhol P, Laurent O, Marko L, Moyen JF (2021). When zircon drowns: Elusive geochronological record of water-fluxed orthogneiss melting in the Velay dome (Massif Central, France). *Lithos* 384-385:105938.
- Couzinié S, Laurent O, Moyen JF, Zeh A, Bouilhol P, Villaros A (2016). Post-collisional magmatism: Crustal growth not identified by zircon Hf-O isotopes. *Earth and Planetary Science Letters* 456:182-195.
- Couzinié S. et al. (2014). Temporal relationships between Mg-K mafic magmatism and catastrophic melting of the Variscan crust in the southern part of the Velay Complex (Massif Central, France). *Journal of Geosciences* 59(1-4):1-18.

Couzinié S. (2018). Evolution of the continental crust and significance of the zircon record, a case study from the French Massif Central. PhD thesis, Stellenbosch University and Saint-Etienne University. 436 pp.

Dhuime B, Hawkesworth C, Cawood P (2011). When continents formed. *Science* 331:154-155 DOI: 10.1126/science.1201245.

Duthou JL, Cantagrel JM, Didier J, Vialette Y (1984). Paleozoic Granitoids from the French Massif Central - Age and Origin Studied by Rb-87-Sr-87 System. *Physics of the Earth and Planetary Interiors* 35(1-3):131-144.

Faure M, Bé Mézème E, Duguet M, Cartier C, Talbot JY (2005) Paleozoic tectonic evolution of medio-Europa from the example of the French Massif Central and Massif Armorican. In: Carosi R, Dias R, Iacopini D, Rosenbaum G (eds) The southern Variscan belt. *J Virtual Explorer* 19, paper 5.

Faure M, Lardeaux JM, Ledru P (2009). A review of the pre-Permian geology of the Variscan French Massif Central. *Comptes Rendus Geoscience* 341:202-213.

Jacob JB, Moyen JF, Fiannacca P, Laurent O, Bachmann O, Janoušek V, Farina F, Villaros A (2021). Crustal melting vs. fractionation of basaltic magmas: Part 2, attempting to quantify mantle and crustal contributions in granitoids. *Lithos* 402-403:106292.

Kröner U and Romer RL (2013). Two plates – many subduction zones: The Variscan orogeny reconsidered. *Gondwana Research* 24:298-329.

Lardeaux JM, Ledru P, Daniel I, Duchene S (2001). The Variscan French Massif Central – a new addition to the ultra-high pressure metamorphic ‘club’: exhumation processes and geodynamic consequences. *Tectonophysics* 332:143-167.

Lardeaux JM et al. (2014). The Moldanubian Zone in the French Massif Central, Vosges/Schwarzwald and Bohemian Massif revisited: differences and similarities. In: K. Schulmann JR, Martinez Catalan JM, Lardeaux V, Janousek G. and Oggiano (eds) The Variscan Orogeny: Extent, Timescale and the Formation of the European Crust. Special publications. Geological Society, London.

Laurent O, Couzinié S, Zeh A, Vanderhaeghe O, Moyen JF, Villaros A, Gardien V, Chelle-Michou C (2017). Protracted, coeval crust and mantle melting during Variscan late-orogenic evolution: U-Pb dating in the eastern French Massif Central. *International Journal of Earth Sciences (Geol Rundsch)* 106:421–451.

Ledru P, Courrioux G, Dallain C, Lardeaux JM, Montel JM, Vanderhaeghe O, Vitel G (2001). The Velay dome (French Massif Central): melt generation and granite emplacement during orogenic evolution. *Tectonophysics* 342(3-4): 207-237.

Leloix C, Faure M, Feybesse JL (1999) Hercynian polyphase tectonics in the northeast French Massif Central: the closure of the Brévenne Devonian-Dinantian rift. *International Journal of Earth Sciences* 88:409–421.

- Malavieille J, Guilhot P, Costa S, Lardeaux JM, Gardien V (1990). Collapse of the thickened Variscan crust in the French Massif Central: Mont Pilat extensional shear zone and St. Etienne Late Carboniferous basin. *Tectonophysics* 177(1–3):139–149
- Matte P (1991). Accretionary history and crustal evolution of the Variscan belt in Western Europe. *Tectonophysics* 196:309–337.
- Matte P (2001). The Variscan collage and orogeny (480 - 290 Ma) and the tectonic definition of the Armorica microplate: a review. *Terra Nova* 13(2) :122-128.
- Melleton J, Cocherie A, Faure M, Rossi P (2010). Precambrian protoliths and Early Paleozoic magmatism in the French Massif Central: U-Pb data and the North Gondwana connection in the west European Variscan belt. *Gondwana Research* 17:13-25.
- Moyen JF, Laurent O, Chelle-Michou C, Couzinie S, Vanderhaeghe O, Zeh A, Villaros S, Gardien V (2017). Collision vs. subduction-related magmatism: Two contrasting ways of granite formation and implications for crustal growth. *Lithos* 277:154-177.
- Najoui K, Leyreloup AF, Monié P (2000). Conditions et âges $^{40}\text{Ar}/^{39}\text{Ar}$ de mise en place des granitoïdes de la zone externe sud du Massif central français: Exemple des granodiorites de St-Guiral et du Liron (Cévennes, France). *Bulletin de la Société Géologique de France* 171:495– 510.
- Pandey A, Chalapathi Rao NV, Chakrabarti R, Pandit D, Pankaj P, Kumar A, Sahoo S (2017). Petrogenesis of a Mesoproterozoic shoshonitic lamprophyre dyke from the Wajrakarur kimberlite field, southern India: Geochemical and Sr-Nd isotopic evidence for a modified sub-continental lithospheric mantle source. *Lithos* 292–293:218–233.
- Pandey A, Chalapathi Rao NV, Chakrabarti R, Pankaj P, Pandit D, Pandey R, Sahoo S (2018). Post-collisional calc-alkaline lamprophyres from de Kadiri greenstone belt: Evidence for the Neoarchean convergence-related evolution of the Eastern Dharwar Craton and its schist belts. *Lithos* 320-321:105-117.
- Paquette LD, Monchoux P, Couturier M (1995) Geochemical and isotopic study of a norite-eclogite transition in the European Variscan belt: implications for U–Pb zircon systematics in metabasic rocks. *Geochimica et Cosmochimica Acta* 59(8):1611–1622.
- Pin C, Duthou J (1990). Sources of Hercynian granitoids from the French Massif Central: inferences from Nd isotopes and consequences for crustal evolution. *Chemical Geology* 83:281–296.
- Rudnick RL and Gao S (2003). Composition of the continental crust. In: Rudnick RL (Eds) *The Crust*. Elsevier–Pergamon, Oxford, pp.1–64.
- Sabourdy G (1975). Apport de la géochimie à la connaissance de la pétrogenèse des granitoïdes des Cévennes méridionales, Massif central Français, PhD thesis, Univ. de Clermont-Ferrand, Clermont- Ferrand, France, 278 pp.

Sabatier H (1991). Vaugnerites: special lamprophyre-derived mafic enclaves in some Hercynian granites from Western and Central Europe. In: Didier JP, Barbarin B (eds) Enclaves and Granite Petrology. Amsterdam, Elsevier 13:63-81.

Stein M and Ben-Avraham B (2007). Mechanism of Continental Crust Growth. Treatise on Geophysics 9:171-195.

Talbot JY, Chen Y, Faure M (2005). A magnetic fabric study of the Aigoual–Saint Guiral–Liron granite pluton (French Massif Central) and relationships with its associated dikes. *Journal of Geophysical Research* 110:B121106.

Vanderhaeghe O, Laurent O, Gardien V, Moyen JF, Gébelin A, Chelle-Michou C, Couzinié S, Villaros A., Bellanger M (2020). Flow of partially molten crust controlling construction, growth and collapse of the Variscan orogenic belt: the geologic record of the French Massif Central. *BSGF Earth Sciences Bulletin, Société géologique de France* 191:25.

Villaros A, Laurent O, Couzinié S, Moyen JF, Mintrone M (2018). Plutons and domes: the consequences of anatetic magma extraction – example from the south-eastern French Massif Central. *Int. J. Earth Sci.* 107:2819–2842.

von Raumer JF, Finger F, Vesela P, Stampfli GM (2014). Durbanchites-Vaugnerites – a geodynamic marker in the central European Variscan orogen. *Terra Nova* 26:85-95

Wang X, Wang Z, Cheng H, Foley S, Xiong L, Hu Z (2020). Early cretaceous lamprophyre dykes swarms in Jiaodong Peninsula, eastern North China Craton, and implications for mantle metasomatism related to subduction. *Lithos* 368-368:105593.

Williamson B, Downes H, Thirlwall M, Beard A (1997). Geochemical constraints on restite composition and unmixing in the Velay anatetic granite, French Massif Central. *Lithos* 40(2–4):295–319.

Chapter II

The Chapter II presents the results obtained in this research in a manuscript in preparation for submission to the journal Contributions to Mineralogy and Petrology. The research was done independently by Mariana Werle supervised by Gary Stevens, Jean-François Moyen and Oscar Laurent.

Title: Cryptic crustal growth identified by Variscan post-collisional lamprophyre-granite composite dykes, French Massif Central.

Mariana Werle^a, Gary Stevens^a, Jean-François Moyen^b, Oscar Laurent^c, Chris Harris^d, Cristiano C. Lana^e, Philip E. Janney^d

^a Stellenbosch University, Department of Earth Sciences, Private Bag X1, 7602 Matieland, South Africa

^b Université de Lyon, Laboratoire Magmas et Volcans, UJM-UCA-CNRS-IRD, 23, rue Dr. Paul Michelon, 42023 Saint-Étienne, France

^c GET, UPS, CNRS, IRD, 14, avenue E. Belin, F-31400 Toulouse, France

^d University of Cape Town, Department of Geological Sciences, Rondebosch, 7700, South Africa

^e Universidade Federal de Ouro Preto, Departamento de Geologia, Escola de Minas, Morro do Cruzeiro, 35400-000, Ouro Preto, Minas Gerais, Brazil

Abstract

The processes that control crustal growth by addition of new mantle-derived material to the crust and the recycling of crustal components that were introduced into the mantle during subduction remain poorly understood in collisional orogeny. Here, we present a study of lamprophyric-granitic composite dykes from the northern border of the post-collisional Variscan Aigoual pluton, French Massif Central (FMC). At Aigoual, lamprophyres and granites display gradational contacts and are co-magmatic. U-Pb dating of zircon yield crystallization ages between 311 ± 2.9 Ma and 313 ± 3.0 Ma for dykes, which are synchronous within uncertainty with the ages of 312 ± 3.1 Ma and 313 ± 3.2 Ma obtained for the emplacement of the Aigoual pluton. The lamprophyres are metaluminous to slightly peraluminous and display enrichment in both compatible (Fe, Mg, Ni, Cr) and incompatible elements (K_2O , LILE, LREE) and have crustal isotopic signatures in both radiogenic (Sr, Nd and Hf) and stable (O) isotope systems. This dual crust/mantle signature of lamprophyres indicates partial melting within the spinel-herzolite field of an enriched mantle that was metasomatized by sediment-derived melts or fluids, related to subduction preceding continental collision. Granites are peraluminous, display high K_2O with shoshonitic affinity and have similar trace elements patterns as lamprophyres. The isotope composition of the granites overlap those of the lamprophyres. The high Cr, Ni, FeO, and MgO contents of the granites FMC are consistent with a mantle component into the granite magmas. Based on our results, we suggest that between 65 – 80% of material in lamprophyres and granites derived from the mantle. Although blurred in an isotopic point of view, this configures significant crustal growth in the post-collisional magmatism from FMC. Coupled with the high preservation potential, post-collisional sites might represent significant sites of crust growth.

Key words: Composite Dykes; Crustal Growth; Variscan Belt; Lamprophyre; Metasomatized mantle

1. Introduction

The process of crust generation and evolution involves addition of new, mantle-derived magma, recycling and melting of oceanic crust and sediments in subduction sites and reworking of crustal components in collisional environment (Cawood et al. 2013; Condie et al. 2011; Dhuime et al. 2011; Jacob et al. 2021; Moyen et al. 2021). The crust grows when new mantle-derived igneous material is added to the continent. This process occurred extensively in arc settings throughout geological time, where large amounts of mantle-derived mafic and intermediate magmas (and their differentiates) are added to the crust (e.g. Andes – Serra-Varela et al. 2021; Himalayas – Jagoutz et al. 2009; Japan – Gao et al. 2021). Nevertheless, this does not necessarily imply significant long-term crustal-growth, because arc settings display poor preservation potential. A high proportion of the generated crust may be recycled back to the mantle shortly after formation (Condie 2014; Korenaga 2018; Scholl and von Huene 2009; Stern 2011). Although less efficient than arc settings in producing new continental crust, the post-collisional sites display the highest potential for preservation in the geological record (Hawkesworth et al. 2009, 2010; Spencer et al. 2015). Post-collisional sites involve changes in the geodynamics with orogenic collapse, delamination of the lithosphere and hence asthenosphere upwelling associated with extension and is marked by magmatism with emplacement of granitoids from both mantle and crustal sources (Bonin 2004; Clemens et al. 2009; Laurent et al. 2014). Thus, post-collisional processes may represent significant contributions for the long-term crustal growth (Couzinié et al. 2016; Moyen et al. 2017).

In this context, high K-Mg mantle-derived magmatic suites occurs systematically in post-collisional settings. Although relatively scarce, the suites are considered a significant contributor to crustal growth throughout geological time (Choi et al. 2020; Dijkstra and Hatch 2018; Fowler et al. 1996; Pandey et al. 2017; Prelević et al. 2012; Scarroo et al. 2008). Post-collisional high K-Mg mafic rocks were described in the Variscan belt of Western Europe (Couzinié et al. 2016; Errandonea-Martin et al. 2018; Janoušek and Holub 2007; Scarroo et al. 2011; Soder and Romer, 2018; Tabaud et al. 2014; von Raumer et al. 2014). These rocks are characterized by SiO₂ contents ranging from 45 to 65 wt.%, high-K to shoshonitic affinity (K₂O = 1.5-6.0 wt.%), high FeOt + MgO (up to 25 wt.%). They are enriched in volatiles, compatible (Fe, Mg, Ni, Cr) and incompatible

elements (K, Rb, Ba, Sr). The French Massif Central is a segment of the Variscan Belt, where high K-Mg mafic rocks are spatially and temporally associated with the peak of granite magmatism (335 to 300 Ma; Couzinié et al. 2014; Laurent et al. 2017). The mafic rocks are described as either enclaves in felsic rocks; decametric small bodies associated with granites and migmatites; or lamprophyric dykes (Couzinié et al. 2014, 2016; Ledru et al. 2001; Sabatier 1991). Despite being well defined in space and time, the role of this mafic magmatism in post-Variscan setting is still debated (Couzinié et al. 2016). More specifically, it is unclear whether the volumetrically more significant granites represent differentiated magmas from the mafic rocks (Moyen et al. 2017) or the products of hybridization between the latter and crustal melts (Laurent et al. 2017, Solgadi et al. 2007). In turn, the balance between crustal growth by addition of new mantle-derived material and recycling of crust in the mantle in post-collisional sites is poorly understood (Jacob et al. 2021; Storck et al. 2021, and references therein).

We selected co-magmatic lamprophyre and granite in a system of parallel dykes associated with the northern boundary of the late-Variscan Aigoual granitic pluton, French Massif Central, to investigate the petrogenesis of both rock types, the existence of potential genetic links between them and to constrain the contribution of mantle-derived material in post-collisional magmas. Methods used included field work; petrography and mineral chemistry; whole-rock major, trace elements and Sr-Nd-Hf isotopes; zircon U-Pb geochronology and Hf isotopes; and O isotopes in quartz and feldspar. We interpret our results as demonstrating the involvement in the lamprophyres and granites of both recycled crustal components and newly extracted material from the mantle. As a consequence, this illustrates that both lamprophyres and granites represent addition of new mantle-derived material, contributing to long-term crustal growth in a post-collisional setting.

2. Geological setting

2.1 The French Massif Central

The orogenic Variscan Belt in central and Western Europe formed between c. 400 and 280 Ma in a complex collisional history of two main continents, Gondwana and Laurussia, micro-continents and oceanic basins, resulting in the formation of the Pangea

supercontinent at the end of the Paleozoic (Kröner and Romer 2013; Matte 1991, 2001). One of the largest exposures of the Variscan Belt in Western Europe (Vanderhaeghe et al. 2020) is preserved in the French Massif Central (FMC). Igneous and metamorphic rocks are exposed that represent the exhumed inner zone of the orogen (Lardeaux et al. 2014), constructed over the northern margin of Gondwana (Figure II 1b).

From Ordovician to late-Carboniferous, the FMC experienced several tectonic-metamorphic-magmatic events with opening of ocean basins (ca. 500–450 Ma) and subsequently closure and subduction between 420 and 360 Ma, to proper collision between ca. 350–320 Ma. Orogenic collapse occurred in the late-Carboniferous (ca. 320–300 Ma) (Chelle-Michou et al. 2017; Faure et al. 2009; Lardeaux et al. 2014; Matte 2001; Vanderhaeghe et al. 2020; Whitney et al. 2020). In the eastern portion, the FMC is made of a south-verging stack of nappes composed by four main metamorphic units (Faure et al. 2009; Vanderhaeghe et al. 2020).

In the southeastern area of the FMC, the low-grade metamorphic unit called Parautochthonous Unit represents the lowermost unit of the nappe pile and expos essentially metasediment (micaschist, quartzite, graphite metapelite; Faure et al. 1999) deposited between the Neoproterozoic and early Cambrian (Melleton et al. 2010); and orthogneisses formed after late-Cambrian to early-Ordovician (490–485 Ma) rhyolites (Couzinié et al. accepted). These rocks underwent polyphase deformation and metamorphism between ca. 340 to 310 Ma under greenschist to amphibolite facies (Caron 1994; Faure et al. 1999, 2001) (Figure II 1b). This unit was intruded by the Aigoual-Saint Guiral-Liron Pluton (ASGL) at shallow depth (1–2 kb; Najoui et al. 2000) developing a contact metamorphic aureole. Based on $^{40}\text{Ar}/^{39}\text{Ar}$ dating in biotite and U-Pb in zircon and monazite, the main intrusion occurred between 305–310 Ma and was synchronous with the late stage of migmatization in lower structural levels and the late Variscan extensional event in this area (Brichau et al. 2008).

2.2 Magmatic relations in the E-FMC and Aigoual pluton

The French Massif Central is characterised by intense and long-lived magmatic activity during collisional to extensional tectonics. The activity occurred during the transition from collision (in mid-Carboniferous) to the syn- and post-orogenic collapse of

the orogeny in the late Carboniferous – early Permian (Faure et al. 2005, 2009; Laurent et al. 2017)

Based on nomenclature defined by Barbarin (1999), the plutonic rocks of E-FMC can be subdivided in four main groups (Chantraine et al. 1996). (1) Two-mica or muscovite-bearing peraluminous granitoids (“MPG” of Barbarin 1999) outcropping as small plutons and dykes. These rocks are granite *sensu stricto* with SiO_2 (>70 wt.%); the peraluminous character indicates crustal source (Barbarin 1999; Pin and Duthou 1990); (2) Cordierite-bearing peraluminous granitoids (“CPG”), which are peraluminous to slightly metaluminous granites and granodiorites with biotite and cordierite from abundant to rare. These rocks have SiO_2 content (>65 wt. %), K_2O (3-7 wt. %), integrated with isotopic data melting of local crust is indicated (Duthou et al. 1984; Pin and Duthou 1990; Williamson et al. 1997). CPG display melting conditions at higher temperature than for MPG (Laurent et al. 2017; Villaros et al. 2018) and/or with greater proportions of orthogneisses in the source (Downes et al. 1997; Moyen et al. 2017). (3) K-feldspar porphyritic, biotite ± amphibole-bearing granites, granodiorites and quartz diorites (“KCG”). These rocks are high-K, weakly peraluminous to metaluminous and form large plutons (e.g. Aigoual-Saint Guiral-Liron) or enclaves in the Velay complex and are, in general, more mafic than CPG with SiO_2 content average around ~69 wt.% and $\text{FeO}^\text{t} + \text{MgO}$ ~4 wt.%. (4) A suite of biotite-amphibole ± clinopyroxene- bearing intermediate to mafic rocks was described throughout the Variscan Belt (von Raumer et al. 2013) and is locally called in the vaugnerites in the E-FMC (Couzinié et al. 2016; Michon 1987; Sabatier 1991). These rocks are metaluminous with low-silica content ($44 < \text{SiO}_2 < 63$ wt.%), high $\text{FeO}^\text{t} + \text{MgO}$ (10–24 wt.%), Cr (200–600 ppm) and Ni (100–220 ppm) contents, Mg# (molecular $\text{Mg/Mg} + \text{Fe}$) higher than 0.65; they also have high K_2O contents (1.6–6.7 wt.%), corresponding to high-K to shoshonitic affinity, Ba and Sr (1000–2000 ppm; Couzinié et al. 2016). Vaugnerites outcrop as small bodies in enclaves in granites and migmatites and from sills and dykes with lamprophyric affinity.

The Aigoual pluton occurs in the northern termination part of the L-shape ASGL pluton in the southeastern FMC. The ASGL rocks are classified as K-feldspar porphyritic calc-alkaline granitoids (KCG) (Chantraine et al. 1996), the northern termination consists of a

swarm of NE-SW to NNE-SSW lamprophyre-granite composite dykes, which are the subject of this study (Figure II 1c).

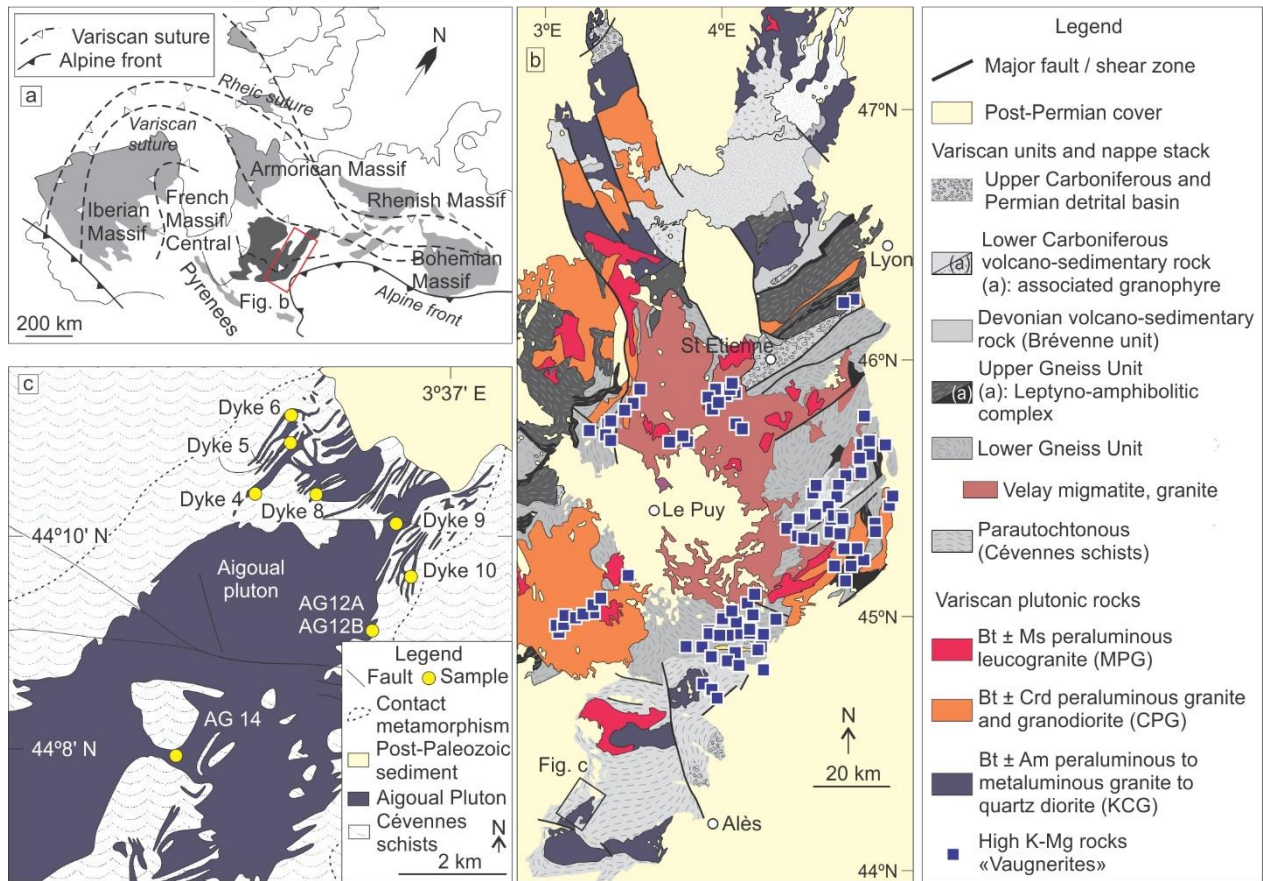


Figure II 1 (a) General location of Variscan belt in Western Europe. (b) Geological map from eastern French Massif Central modified from Moyen et al. (2017). Post-collisional mafic magmatic rock (vaugnerites) occurrences from Couzinié et al. (2016). (c) Geological map of Aigoual pluton and composite dykes modified from Talbot et al. (2005).

3 Analytical methods

3.1 Petrography and mineral chemistry

Mineral compositional analysis was undertaken at Department of Earth Sciences, Stellenbosch University, South Africa using a Zeiss EVO MA 15 Scanning Electron Microscope (SEM). Prior to imaging and analysis, the thin sections were coated with carbon. Textures were studied in backscattered electron (BSE) mode and mineral compositions quantified by EDX (Energy Dispersive X-ray) analysis using an Oxford Instruments ® 133 kV ED X-ray detector and Oxford INCA software. Beam conditions during the quantitative analyses were 20 kV accelerating voltage and 1.0 A probe current, with a working distance of 8.5 mm and a specimen beam current of -19.0 nA. X-ray counts were typically ~7000 cps, and the counting time was 50 s live-time. Analyses were quantified using natural mineral standards and mineral chemical compositions were recalculated to mineral stoichiometry to obtain mineral structural formula.

3.2 Whole-rock major and trace elements

Whole-rock major- and trace-element analyses were determined at the Central Analytical Facilities, Stellenbosch University, South Africa. The analyses followed the protocols described by Mühlberg et al. (2021). Fused disks were prepared using 0.7 g of sample powder mixed with 7 g of high purity flux (32.83% LiBO₂, 66.67% Li₂B₄O₇, 0.50% LiI). Major-element compositions were determined on a PAN analytical wavelength dispersive x-ray fluorescence (XRF) spectrometer. The accuracy and reproducibility of the analyses were determined using the reference materials BE-N, JB-1, BHVO-1, JG-1, HUSG-1, WITS-G. Trace-element compositions were analyzed on fragments of the glass disks used for major element analysis. Ablation was done with a 193 nm Resolution M50 LR Excimer laser connected to an Agilent 8800 Photo Multiplier ICP-MS system. The standard NIST SRM 612 glass (Jochum et al. 2005a) was used to calibration. The USGS BCR and BHVO glass reference materials were used for quality control. The major-element data were recalculated to anhydrous compositions for data comparison. Major and trace element compositions are listed in Table 1 from Appendices.

3.3 Sr-Nd-Hf isotopes

Whole-rock Nd, Sr and Hf isotopes were determined at University of Cape Town (UCT) on a Nu Instruments NuPlasma HR multi-collector inductively coupled plasma mass spectrometer (MC-ICP-MS) equipped with a DSN-100 desolvating nebulizer in the MC-ICP-MS facility, housed in the Department of Geological Sciences. Isotopes are listed in *Table 7* from Appendices. The methodology for Nd and Sr follows that described by Ódri et al. (2020) and Howarth et al. (2019). Strontium isotope ratios were analyzed as a 200 ppb 0.2% HNO₃ solution and data were referenced to an ⁸⁷Sr/⁸⁶Sr normalizing value of 0.710255 for the bracketing analyses of NIST987. Sr isotopic data were corrected for Rb interference using the measured signal for ⁸⁵Rb and the natural ⁸⁵Rb/⁸⁷Rb ratio. Instrumental mass fractionation was corrected using the exponential law and an ⁸⁶Sr/⁸⁸Sr value of 0.1194. Internal 2 σ analytical uncertainty for ⁸⁷Sr/⁸⁶Sr was <0.000013, similar to the long-term 2 σ external reproducibility for ⁸⁷Sr/⁸⁶Sr analysis in this facility of 0.000020, and all error bars fall within the symbol size plotted. Neodymium isotope ratios were analyzed as 50 ppb 2% HNO₃ solutions and data were referenced to a ¹⁴³Nd/¹⁴⁴Nd normalizing value of 0.512115 for the bracketing analyses of JNd-1 (Tanaka et al. 2000). All Nd isotope data were corrected for Sm and Ce interference using the measured signal for ¹⁴⁷Sm and ¹⁴⁰Ce, and natural Sm and Ce isotope abundances. Instrumental mass fractionation was corrected using the exponential law and a ¹⁴⁶Nd/¹⁴⁴Nd value of 0.7219. Internal 2 σ analytical uncertainty for ¹⁴³Nd/¹⁴⁴Nd ranged from 0.000009 to 0.000016 and are similar to the long-term 2 σ external reproducibility for ¹⁴³Nd/¹⁴⁴Nd analysis in this facility at 0.000020. Error bars are plotted throughout. Lu-Hf isotopic measurement follow the patterns described by Janney et al. (2005) and Hf separation were conducted using three columns, cation-anion-cation separation in a HCl-HF solution followed Blichert-Toft et al. (1997). Analyses were performed in a static mode, with ¹⁷³Yb and ¹⁷⁵Lu monitored to allow correction of ¹⁷⁶Hf for isobaric interferences by ¹⁷⁶Yb and ¹⁷⁶Lu. Hf isotopic ratios measurements of samples were normalized to a ¹⁷⁶Hf/¹⁷⁷Hf value for JMC 475 of 0.282166 (Jochum et al. 2005b). The average measured ¹⁷⁶Hf/¹⁷⁷Hf ratio for JMC 475 during the period of data collection was 0.283057, with a 2SD external reproducibility of \pm 0.000064.

3.4 Zircon U-Pb dating

Zircon crystals from two different composite dykes (lamprophyres and granites) and two samples from Aigoual pluton were separated by conventional methods. The grains were hand-picked, mounted in epoxy resin and polished to expose their interiors. To characterize textural features and internal zoning of zircons, back-scattered electron (BSE) and cathodoluminescence (CL) images were obtained using a Zeiss Merlin Gemini 2-FI7 scanning electron microscope (SEM) at CAF, Stellenbosch University.

Zircon U–Pb isotope analyses were obtained at the CAF, Stellenbosch University, South Africa and are listed in Table 8 from Appendices. The analytical technique used a laser ablation-single collector-magnetic sector field-inductively coupled plasma-mass spectrometry (LA-SF-ICP-MS) employing a Thermo Finnigan Element 2 mass spectrometer coupled to a Resonetics Resolution S155 excimer laser ablation system. The procedures followed the pattern described in Frei and Gerdes (2009) and Lana et al. (2011). The GJ-1 zircon reference material (Jackson et al. 2004) was used as primary standard and the 91500 for quality control (Wiedenbeck et al. 1995), Plešovice (Sláma et al. 2008) and M127 (Nasdala et al. 2008; Mattinson 2010) zircon reference materials were analyzed for quality control. The data were reduced using the software Iolite v.3.5 (Paton et al. 2011) and the calculation of weighted mean, Concordia ages and plotting were performed using the IsoplotR package (Vermeesch et al. 2018). No common Pb correction was applied. All uncertainties are reported at the 2σ level and systematic uncertainties were propagated for the weighted mean and Concordia ages following the recommendations of Horstwood et al. (2016).

3.5 Zircon Lu-Hf isotopes

Zircon Lu-Hf isotopes and trace elements compositions were obtained in same grains with previous U-Pb dating and followed the patterns described by Schannor et al. (2019) and Cerva-Alves et al. (2021) and are listed in Table 9 from Appendices.

Zircon Lu-Hf isotopic analyses were undertaken at UFOP, Brazil. The analytical technique used a Thermo-Finnigan Neptune with a multicollector ICP-MS coupled to a Photon-Machines 193 nm laser ablation system. The 40 μm spot size laser was fired at 8 Hz repetition rate in static mode using 3 J cm^{-2} of energy density. Nitrogen ($\sim 0.02 \text{ l/min}$)

was introduced into the Ar (1.01 l/min) sample-carrier gas. The signal intensity was ca. 10 V for ^{180}Hf . During the analysis step, the isotopes ^{172}Yb , ^{173}Yb and ^{175}Lu were simultaneously monitored to permit corrections of isobaric interferences of Lu and Yb isotopes on mass 176. The ^{176}Yb and ^{176}Lu were calculated using a $^{176}\text{Yb}/^{173}\text{Yb}$ of 0.796218 (Chu et al., 2002) and $^{176}\text{Lu}/^{175}\text{Lu}$ of 0.02658 (in-house value). Corrections for instrumental mass bias used an exponential law and $^{179}\text{Hf}/^{177}\text{Hf}$ value of 0.7325 (Patchett and Tatsumoto 1981) for correction of Hf isotopic ratios. Yb and Lu isotopic ratios were corrected using βHf of individual integration steps of each analysis divided by the average offset factor of the analytical session. For calibration, were used the standards BB (560 Ma) with $^{176}\text{Hf}/^{177}\text{Hf} = 0.281674 \pm 0.0000028$ (Santos et al., 2017); GJ-1 (602 Ma) with $^{176}\text{Hf}/^{177}\text{Hf} = 0.282000 \pm 0.000005$ (Morel et al., 2008); Temora (417 Ma) with $^{176}\text{Hf}/^{177}\text{Hf} = 0.282686 \pm 0.000007$ (Woodhead et al., 2005); Plesovice (337 Ma) with $^{176}\text{Hf}/^{177}\text{Hf} = 0.282482 \pm 0.000013$ (Slama et al., 2008) and Mudtank (732 Ma) with $^{176}\text{Hf}/^{177}\text{Hf} = 0.282507 \pm 0.000006$ (Woodhead and Herdt, 2005). The ^{176}Lu decay constant of $1.867 \times 10^{-11} \text{ yr}^{-1}$ was used for initial epsilon hafnium $\epsilon\text{Hf}(t)$ calculations (Söderlund et al., 2004). The values of average MORB (DM) is 0.03933 for $^{176}\text{Lu}/^{177}\text{Hf}$, 0.283294 for $^{176}\text{Hf}/^{177}\text{Hf}$ (Blichert-Toft and Puchtel 2010); $^{176}\text{Lu}/^{177}\text{Hf} = 0.0113$ for the average continental crust (Rudnick and Gao 2003); the average Chondritic Uniform Reservoir (CHUR) of 0.0336 for $^{176}\text{Lu}/^{177}\text{Hf}$, and 0.282785 for $^{176}\text{Hf}/^{177}\text{Hf}$ (Bouvier et al. 2008).

3.6 Oxygen isotopes

Oxygen-isotope ratios were determined at the University of Cape Town (UCT) and following the methods described by Harris and Ashwal (2002) and Harris and Vogeli (2010). Crystals of quartz and feldspar were separated by hand picking. The laser fluorination method was used for quartz whereas conventional fluorination was used for feldspars, which are unstable during pre-fluorination. The reagent used for both laser and conventional extraction was ClF_3 ; the laser analyses were measured on O_2 gas whereas in the conventional method O_2 was converted to CO_2 using a hot platinized carbon rod. The O-isotopes ratios were measured offline using a Thermo Finnegan DeltaXP mass spectrometer, in dual inlet mode, and are reported in δ notation where $\delta = (\text{Rsample}/\text{Rstandard} - 1) \times 1000$ where $\text{R} = ^{18}\text{O}/^{16}\text{O}$ and SMOW is the standard. For feldspar, the in-house standard MQ was analyzed in duplicate with each batch of eight

samples and used to convert the raw data to the SMOW scale. For quartz, the in-house Monastery garnet (MON GT) standard was analysed in duplicate with each batch of 10 samples. All raw data were normalized to a MON GT value of 5.38‰. The long-term variability of MQ suggests a 2σ error of 0.16 ‰. The long-term average difference in $\delta^{18}\text{O}$ values of the two MONT GT standards run with each batch of 10 samples was 0.11‰ ($n = 216$), which corresponds to a 2σ value of 0.15‰. The results are listed in Table II 1.

4 Results

4.1 Field relations

In the northern end of the ASGL complex, several 5-20 m-long, NE-trending dykes intrude the Cévennes micaschists. Most dykes are composite and display complex relations between granitic and lamprophyric components. The wider dykes (described by Sabourdy, 1975) display lamprophyric dark borders with aphanitic textures, progressively grading to porphyritic microgranite with some mafic enclaves in the core. The dyke illustrated in Figure II 2 has SiO_2 from 57.20 to 67.81 wt.% from left to right in the image. The increase in volume and size of megacryst K-feldspar from lamprophyric to granitic end-members (Figure II 2a) was observed in the field. In other outcrops, lamprophyric and granitic components form independent dykes mutually intrusive (Figure II 2b). The main pluton is a strongly porphyritic, coarse-grained granite with megacrysts of K-feldspar reaching 5-8 cm. The granite contains many lamprophyric enclaves with resorbed megacrysts of K-feldspar. These integrated features demonstrate the synchronous nature of the granitic and lamprophyric magmas; they interacted in different ways locally depending on relative abundance (Figure II 2c).

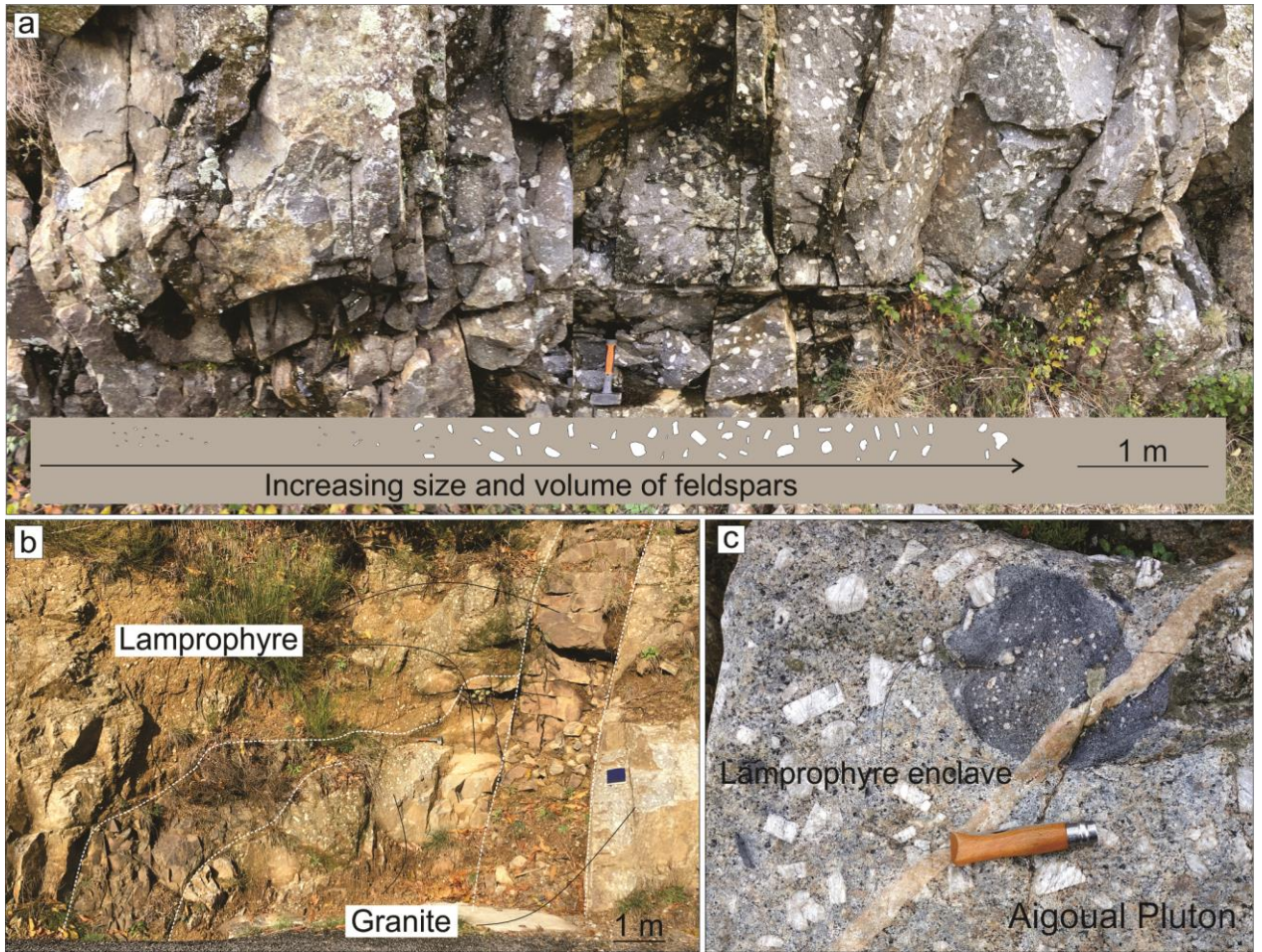


Figure II 2 Selected field photos (a) Composite dyke with lamprophyre to granite gradational contact with increasing of volume and size of megacrysts of K-feldspars; (b) Field relationships between lamprophyre and granite; (c) Aigoual granitic pluton with enclave of lamprophyre.

4.2 Whole-rock major and trace element chemistry

The composite dykes show a wide range in the SiO_2 varying from 53.16 to 72.57 wt.%. Lamprophyric and granitic samples are high-K (4.08 – 6.55 wt.%) with shoshonitic affinity (Figure II 3a) and high Al_2O_3 (13.63 – 17.18 wt.%). In the A/NK vs. A/CNK (molar $\text{Al}_2\text{O}_3/(\text{Na}_2\text{O} + \text{K}_2\text{O})$ vs. $\text{Al}_2\text{O}_3/(\text{CaO} + \text{Na}_2\text{O} + \text{K}_2\text{O})$) diagram of Shand (1943), lamprophyric samples are metaluminous to slightly peraluminous with higher A/NK values, whereas granitic samples are weakly to (a few) strongly peraluminous (Figure II 3b).

A number of elements vary according to the silica content. From the granitic to the lamprophyric rocks, Cr, Ni and Ba are high and vary from 30.35 – 572.85 ppm, 14.7 – 148.85 ppm and 403.85 – 2416 ppm, respectively. Mg# varies from 40.79 – 70.84; TiO_2 ,

P_2O_5 and CaO increase from granites to lamprophyres whereas Na_2O content decreases (Figure II 4). For several elements (e.g. Sr , CaO , but also Ni and Cr to a lesser degree), the two rock types do not define a single trend against SiO_2 .

In the REE variation diagram, lamprophyres and granites from composite dykes as well as the Aigoual pluton samples show similar patterns. The samples are enriched in LREE ($La_N = 23.53 - 147.37$; normalized to the primitive mantle from McDonough and Sun 1995), with negative Eu anomalies ($Eu/Eu^* = 0.38 - 0.86$) and depleted in HREE with La/Yb_N ratios of $3.34 - 22.81$. In general, lamprophyres show smaller negative Eu anomalies ($Eu/Eu^* = 0.60 - 0.85$) than granites ($Eu/Eu^* = 0.38 - 0.86$) (Figure II 5a). The lamprophyric-granitic rocks from composite dykes and Aigoual pluton are enriched in large ion lithophile elements (LILE, e.g. Cs , Rb , Ba , Th , U ; normalized to Primitive mantle from McDonough and Sun (1995)) and Pb relative to high field strength elements (HFSE, e.g. Nb , Ta , P , Zr and Ti). The lamprophyres show sharp Nb , Ta and Ti anomalies, Ta anomaly not observed in granites (Figure II 5b). In general, the lamprophyres are richer in REE and incompatible elements than the granites, as commonly observed in this type of rocks (e.g. Couzinié et al. 2016; Fowler et al. 1996).

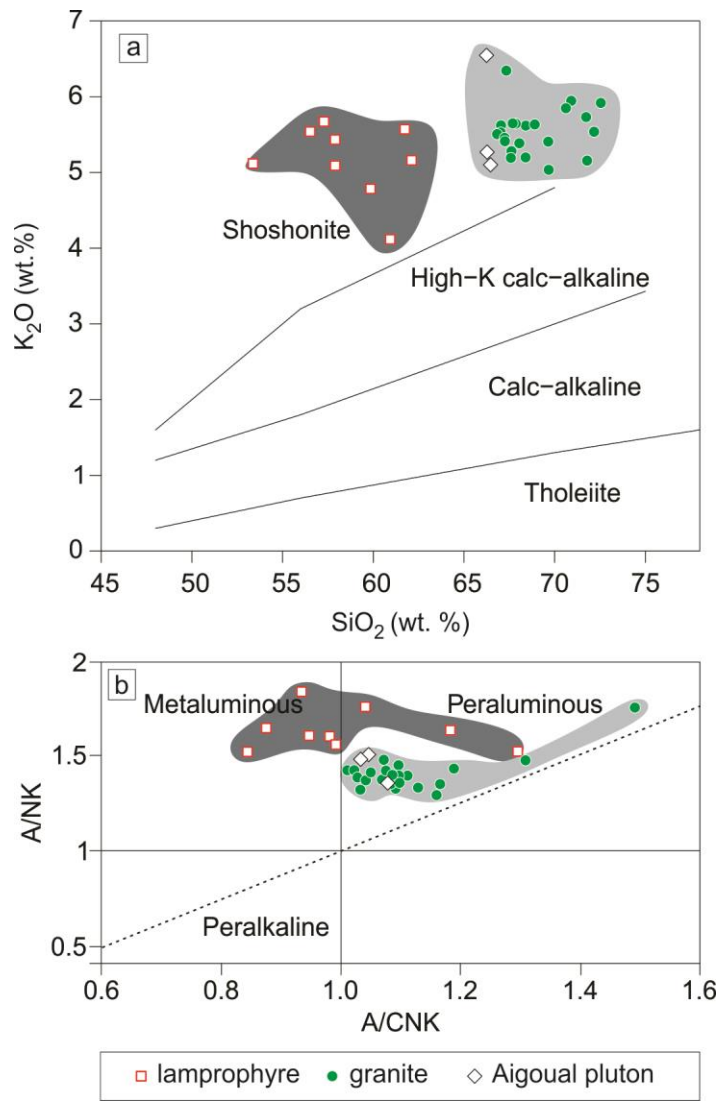


Figure II 3 (a) SiO₂ vs. K₂O classification diagram; (b) A/CNK vs. A/NK diagram.

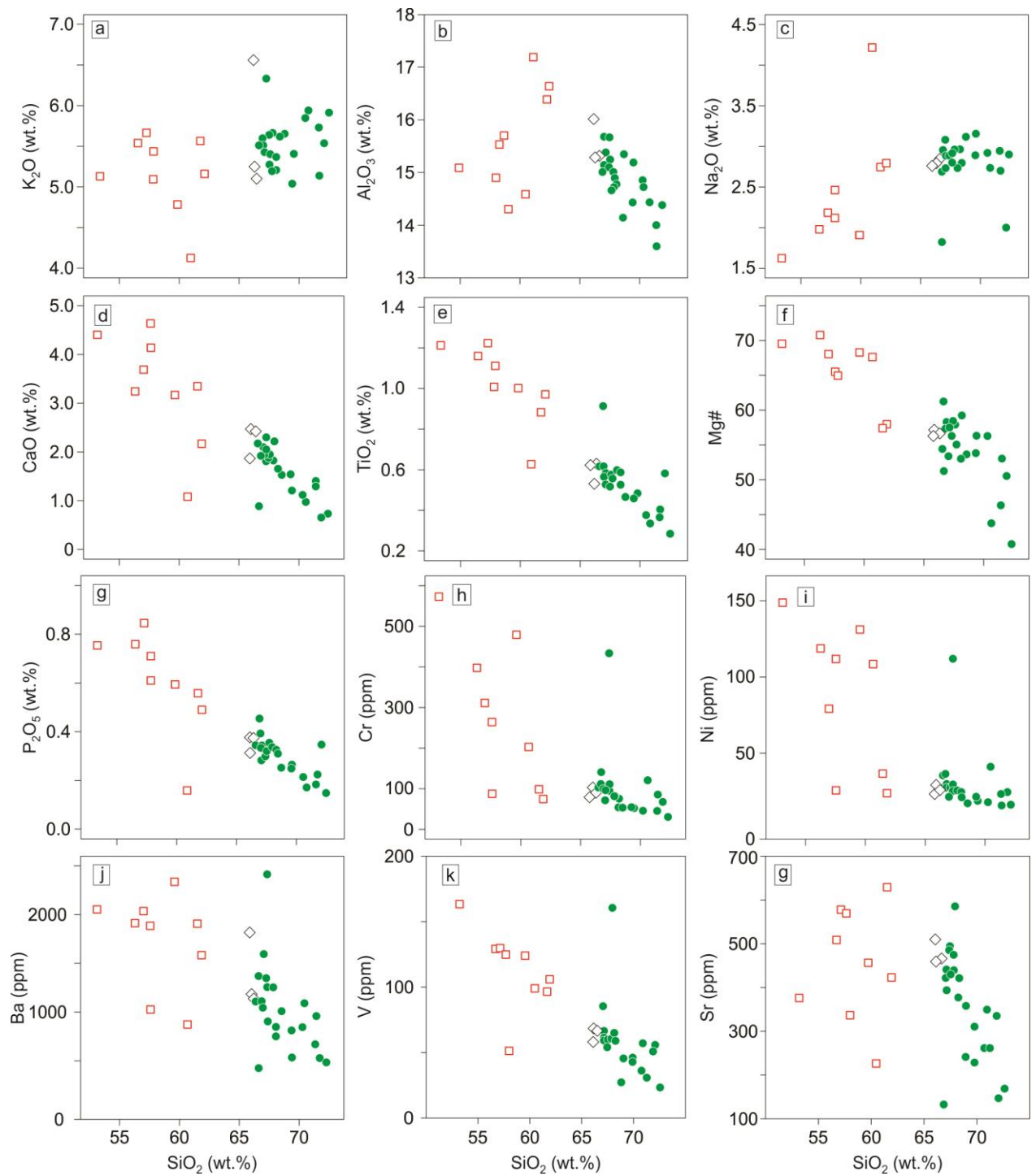


Figure II 4 Whole-rock major and trace element compositions of lamprophyre and granite from composite dykes and Aigoual pluton. Symbols as in Figure II 3.

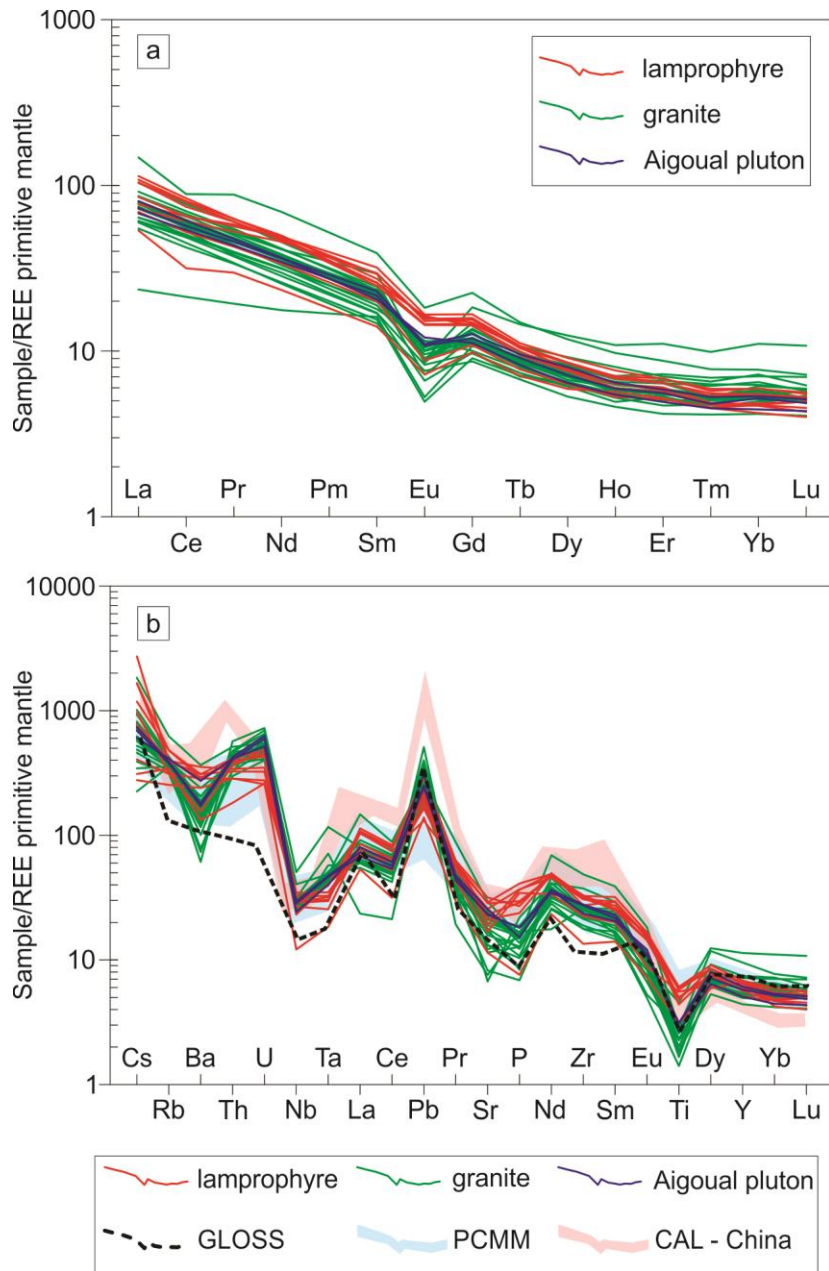


Figure II 5 (a) Primitive mantle-normalized rare earth element (REE) patterns from Sun and McDonough (1989); (b) Multi-element normalized to Primitive mantle from Sun and McDonough (1989). GLOSS composition from Plank and Langmuir (1998); PCMM – post-collisional mafic magmatism from FMC from Couzinié et al. (2016); CAL – China – Calc-alkaline lamprophyre derived from partial melting of sediments from Su et al. (2017).

4.3 Petrography and Mineral chemistry

4.3.1. Lamprophyres

Lamprophyres from composite dykes have panidiomorphic-porphyritic texture with phenocrysts of euhedral mica (~25 - 30 %), plagioclase (~20%), quartz (~5%), K-feldspar

(~5%), in a fine matrix composed by quartz, K-feldspar, plagioclase, mica, ± amphibole, ±carbonate (Figure II 6a, b, c, f). Olivine and pyroxene were not observed within lamprophyres, however, some pseudomorphs indicate the presence of these mafic phases in some lamprophyric samples and are reported by Sabourdy (1975) from the same outcrops. Accessories are apatite, zircon, ±allanite, ±rutile. A characteristic of the lamprophyres is the presence of carbonate in three main different textural forms: 1) Globular, ocellar (Figure II 6e); 2) Interstitial in lamprophyre (Figure II 6c) and 3) Associated with biotite/phlogopite in lamprophyre and granite (Figure II 6d). The different textures appear to indicate primary magmatic origin for carbonates.

Ocellar carbonates vary from 1.6 mm to 200 µm in diameter; the ocelli also contain very fine-grained K-feldspar (Figure II 6e). The matrix of the ocelli is aphanitic, composed of quartz, plagioclase, biotite and chlorite. Plagioclase from the matrix displays an orientation tangential to the margins of the carbonate globules (Appendice Figure 2). Moreover, carbonate was observed mantling corroded quartz that varies from 400 to 600 µm in size (Appendice Figure 2a). Ocellar carbonates are commonly described as the product of immiscibility between silicate and carbonate liquids in the mantle (Huang et al. 2002; Nosova et al. 2021; Scarroo et al. 2011; Vichi et al. 2005; Yang et al. 2014). Interstitial carbonate is present among euhedral quartz, plagioclase and biotite (Appendice Figure 2d). The interstitial character of the carbonate relative to euhedral quartz, biotite and plagioclase crystals is shown in Si X-ray map (Appendice Figure 2e). In the Na X-ray map, plagioclase displays normal magmatic zoning with increasing Na content towards the rim (Ab₅₆ to Ab₇₅) (Appendice Figure 2f). The carbonate associated with biotite/phlogopite interpreted as pseudomorphosed after a high-temperature ferromagnesian phase was observed in both granitic and lamprophyric samples (Appendice Figure 2g, h). Calcite-dolomite cores are rimmed by blocky phlogopite and both replace a former phenocryst with rectangular habit, possibly pyroxene. Collectively, the textures indicate that carbonate is primarily magmatic in the system.

In terms of mineral chemistry, euhedral crystals of mica from lamprophyres have Mg# varying from 0.47 to 0.80, corresponding to gradation between biotite (Mg# < 0.65) and phlogopite compositions (Mg# > 0.65). Biotite/phlogopite has low to moderate Cr₂O₃ content (0 – 0.75 wt.%), high Ti (0.37 – 0.97 a.p.f.u.) and in some samples displays zoning

in BSE images with dark grey cores and light gray discordant rims (Figure II 6g). The core has lower Ti (0.42 – 0.59 apfu) than the rim (0.78 – 0.97 apfu) and biotite in matrix shows similar compositions to rims with high Ti (0.69 – 0.94 apfu). In the FeO^t vs. Al₂O₃ and TiO₂ vs. Al₂O₃ mica discrimination diagram, the biotite/phlogopite follows a minette trend, typical of calc-alkaline lamprophyres (Figure II 7; Rock, 1991) (Table 3 from Appendices).

Feldspars from lamprophyres are plagioclase and K-feldspar with higher modal abundance of plagioclase relative to K-feldspar and compositions display albite, oligoclase and andesine relative to orthoclase, typical from calc-alkaline lamprophyres (Table 4 from Appendices; Rock 1991). Amphiboles from lamprophyres are calcic ($\text{Ca}_B \geq 1.50$; $(\text{Na}+\text{K})_A < 0.50$; $\text{Ca}_A < 0.50$), have high Si content (7.53 – 7.90 apfu) and Mg# (0.62 – 0.88) and are classified as actinolite, typical for secondary amphiboles in lamprophyres (Appendice Figure 1c,d; Table 6 from Appendices).

4.3.2 Granites

Granitic samples from composite dykes display variable porphyritic textures with extreme average crystal size variations in most examples between the phenocrysts and the matrix. In general, granites display porphyritic texture with phenocrysts and megacrysts (up to 5 cm) of plagioclase (~30%), K-feldspar (~30%), quartz (~20%) biotite (~5-10%) and ±clinopyroxene (~3%) in a fine to medium grained matrix composed by quartz, K-feldspar and ±plagioclase. Accessories are apatite, zircon, ±allanite and ±titanite. Phenocrysts of plagioclase display oscillatory zoning in some samples and megacrysts of K-feldspar display corroded margins (Figure II 6j, l).

Feldspars from granites are K-feldspar and plagioclase in similar proportions. Mineral chemistry of plagioclase displays andesine and labradorite compositions (Appendice Figure 1a; Table 4 from Appendices). Micas from granite have Mg# ~0.52 and are classified as biotite with a few analyses with Mg# > 0.65 plotting in the phlogopite field (Figure II 7a; Table 3 from Appendices). Clinopyroxene in the granites is augite with $\text{Wo}_{26}\text{En}_{46}\text{Fs}_{27}$ and have low Ti (0 – 0.02 apfu), Ca (0.44 – 0.50 apfu) and low to moderate Cr₂O₃ (0 – 1.02 wt.%) (Appendice Figure 1b; Table 5).

The Aigoual pluton itself is coarse-grained and porphyritic with phenocrysts of K-feldspar (~30%), plagioclase (~20%) and quartz (15%) in a coarse matrix with quartz,

plagioclase and K-feldspar (~20%) and euhedral mica (~7%) and clinopyroxene (~5%). Micas have Mg# ~0.52 and are classified as biotite. The clinopyroxene is augite and similar in composition to the granite from composite dykes ($\text{Wo}_{26}\text{En}_{44}\text{Fs}_{29}$).

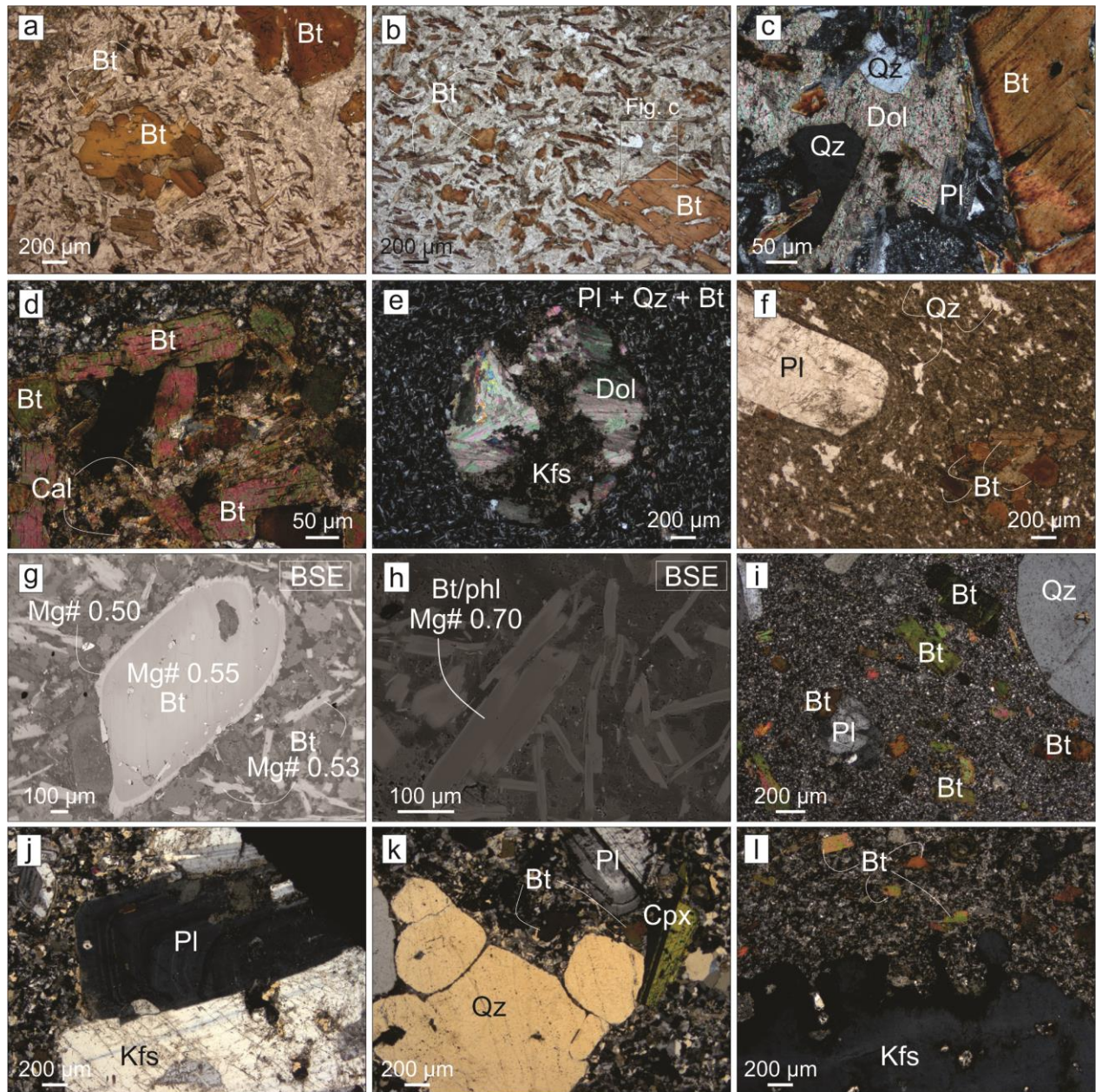


Figure II 6 Photomicrographs and BSE images from lamprophyres and granites from composite dykes. (a) (b) Euhedral biotite in lamprophyre; (c) Interstitial dolomite in lamprophyre associated with euhedral quartz, plagioclase and biotite; (d) Calcite associated with biotite in granite; (e) Ocellar carbonate and microcrystals of K-feldspar in lamprophyre; (f) Plagioclase and biotite phenocryst in lamprophyre; (g) (h) BSE images with compositional variation from biotite/phlogopite from lamprophyre; (i) Fine grained texture in granite from composite dykes; (j) (k) (l) Textural variation in granite from composite dykes with phenocrysts of zoned plagioclase, quartz and corroded megacryst of K-feldspar. Mineral abbreviation from Warr (2021).

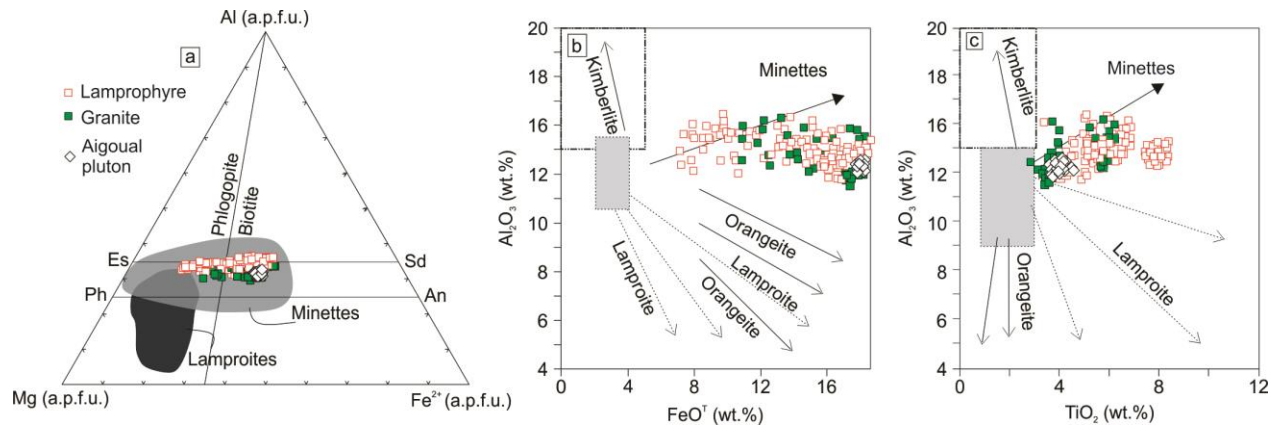


Figure II 7 (a) Al – Mf – Fe²⁺ ternary diagram showing compositional variations between biotite and phlogopite. Minette and lamproite fields after Rock (1991). (b) Al₂O₃ vs. FeO^T and (c) Al₂O₃ vs. TiO₂ discrimination diagram for micas after Mitchell and Bergman (1991). Abbreviations: Eas = Eastonite, Phil = Phlogopite, Sid = Siderophyllite, and Ann = Annite

4.4 Whole-rock Sr-Nd-Hf isotopes

Lamprophyre and granite from the composite dykes show little variation in Sr, Nd and Hf isotope ratios. Initial ⁸⁷Sr/⁸⁶Sr ratios of lamprophyres and granites overlap and vary from 0.70803 to 0.71063, with granites being slightly more radiogenic than lamprophyres (0.70884 to 0.71063 and 0.70803 to 0.71058, respectively). The ¹⁴³Nd/¹⁴⁴Nd (311 Ma) ratio from lamprophyres varies from 0.51196 to 0.51205 (ε Nd (311 Ma) -5.39 to -3.60) and overlaps with ¹⁴³Nd/¹⁴⁴Nd (311 Ma) from granites that vary from 0.51198 to 0.512001. (ε Nd (311 Ma) -5.39 to -4.62). ¹⁷⁶Hf/¹⁷⁷Hf (311 Ma) ratios from lamprophyres vary from 0.282452 to 0.282584 (ε Hf (311 Ma) -4.92 to -0.26) and ¹⁷⁶Hf/¹⁷⁷Hf (311 Ma) from granites vary from 0.282493 to 0.282526 (ε Hf (311 Ma) vary from -3.47 to -2.31) (Table 7 from Appendices). Lamprophyres have slightly more radiogenic values on average of ε Nd and ε Hf than granites (ε Nd = -4.40 and -5.13, respectively and ε Hf = -2.81 and -3.20, respectively). The Aigoual pluton has initial ⁸⁷Sr/⁸⁶Sr value of 0.70941, ε Nd = -5.43 and ε Hf = -3.71. The Lu-Hf and Sm-Nd isotopic systems display decoupling for both lamprophyres and granites with $\Delta\varepsilon\text{Hf}(t)$ ($\Delta\varepsilon\text{Hf}(t)$ = $\varepsilon\text{Hf}(t)$ - 1.36 \times $\varepsilon\text{Nd}(t)$ - 2.89; Vervoort et al. 1999) varying between -0.48 and 2.82.

4.5 Zircon U-Pb ages and Lu-Hf isotopes

In this work, the geochronological data are from individual composite dykes, with lamprophyre and granite being co-magmatic and part of the same outcrop. The morphology and CL patterns from zircon crystals are very similar from dykes 5 and 10 as well from samples 12A and 12B representing a margin of Aigoual pluton (Figure II 1c) and Aigoual pluton (samples 14(1) and 14(3)). The zircons are euhedral to subhedral with size ranging from 450 µm to 50 µm. The crystals have prismatic, surrounded prismatic, pyramidal to bipyramidal tips, aspect ratios from 4:1 to 1:1 and have igneous oscillatory to weakly oscillatory zoning, diffuse zoning or dark grains in CL images (Appendice Figure 3). Many grains show a core/rim texture with diffuse or oscillatory core surrounded by a dark rim. Inherited cores display bright diffuse, oscillatory truncated zoning with dark rims.

The $^{206}\text{Pb}/^{238}\text{U}$ dates show a large variation of concordant ages, scattering from 300 to 340 Ma. However, this large dispersion displays no correlation with morphology and texture of zircon. Older ages between 320 and 340 Ma were obtained in dark rims and dark grains in CL images with unusually high U content (> 1000 ppm). Due to the high U content, these zircons might not be crystalline anymore (Ewing 2003). The absence of correlation between age and Hf isotopic composition shows that age dispersion has no geological significance. Rather, it displays that the older ages between 320 and 340 Ma are likely an artefact caused by inaccurate laser downhole fractionation due the reference material and strongly radiation damaged zircon. Accordingly, the Concordia ages were calculated based on crystalline zircons ($\text{U} < 1000$ ppm) and KDE variation, which display a peak at 310 – 315 Ma for most of the samples.

Isotopic data from 11 concordant analyses from dyke 5 yielded a Concordia date of $^{206}\text{Pb}/^{238}\text{U} = 313 \pm 3.02$ Ma (MSWD conc. + equiv. = 1.7; n = 11) (Figure II 8a). Inherited grains yielded $^{206}\text{Pb}/^{238}\text{U}$ ages of = 537 ± 9.6 , 541 ± 14 , 545 ± 8.5 , 649 ± 10 and 673 ± 7.4 Ma with $\varepsilon\text{Hf}(t) = +0.9$ to $+6.8$. Younger ages of 296 ± 3.8 and 291 ± 4.9 Ma are interpreted as reflecting Pb loss. Magmatic zircons from dyke 5 have initial $^{176}\text{Hf}/^{177}\text{Hf}$ ratios between 0.28235 and 0.28253 and have $\varepsilon\text{Hf}(t) = -8.1$ to -1.6 (± 1.2 εHf -units) with $T_{\text{DM}} = 1.3$ to 1.7 Ga (Figure II 9).

Isotopic data from 33 concordant analyses from dyke 10 yielded a Concordia date of $^{206}\text{Pb}/^{238}\text{U} = 311 \pm 2.9$ Ma (MSWD conc. + equiv. = 1.5; n = 33) (Figure II 8b). A large

population of inherited grains yielded several date groups from Paleoproterozoic (2040 – 2480 Ma), early Neoproterozoic (920 – 1000 Ma) and late Neoproterozoic – early Paleozoic (450 – 730 Ma). Zircons from dyke 10 have initial $^{176}\text{Hf}/^{177}\text{Hf}$ ratios between 0.28236 and 0.28269 and yielded $\varepsilon\text{Hf}(t) = -7.7$ to 3.6 ($\pm 1.5 \varepsilon\text{Hf-units}$) (Figure II 9), with $T_{\text{DM}} = 1.1$ to 1.7 Ga. Inherited grains with $^{206}\text{Pb}/^{238}\text{U}$ ages between 450 and 600 Ma have $\varepsilon\text{Hf}(t) = 0$ to +2.5 whereas inherited grains > 600 Ma have $\varepsilon\text{Hf}(t) = -13.5$ to +2.9.

Samples 12A and 12B represent the eastern margin of Aigoual pluton (Figure II 1c) with microgranite and monzonite associated in a large mass instead composite dykes. Isotopic data from 10 concordant analyses display a Concordia date of 312 ± 3 Ma (MSWD conc. + equiv. = 1.7; n = 10) (Figure II 8c). No inherited grains were observed. Zircon grains from localization 12 have initial $^{176}\text{Hf}/^{177}\text{Hf}$ between 0.28241 and 0.28260 and yielded $\varepsilon\text{Hf}(t) = -6.8$ to 0.4 ($\pm 1.4 \varepsilon\text{Hf-units}$) with $T_{\text{DM}} = 1.2$ to 1.6 Ga (Figure II 9).

Zircons from the Aigoual pluton display a Concordia date of 313 ± 3.2 Ma (MSWD conc. + equiv. = 1.3; n = 7) (Figure II 8c) with initial $^{176}\text{Hf}/^{177}\text{Hf}$ ratios between 0.28243 and 0.28248 corresponding to $\varepsilon\text{Hf}(t)$ values from -5.6 to -3.3 ($\pm 1.1 \varepsilon\text{Hf-units}$) and $T_{\text{DM}} = 1.4$ to 1.5 Ga (Figure II 9).

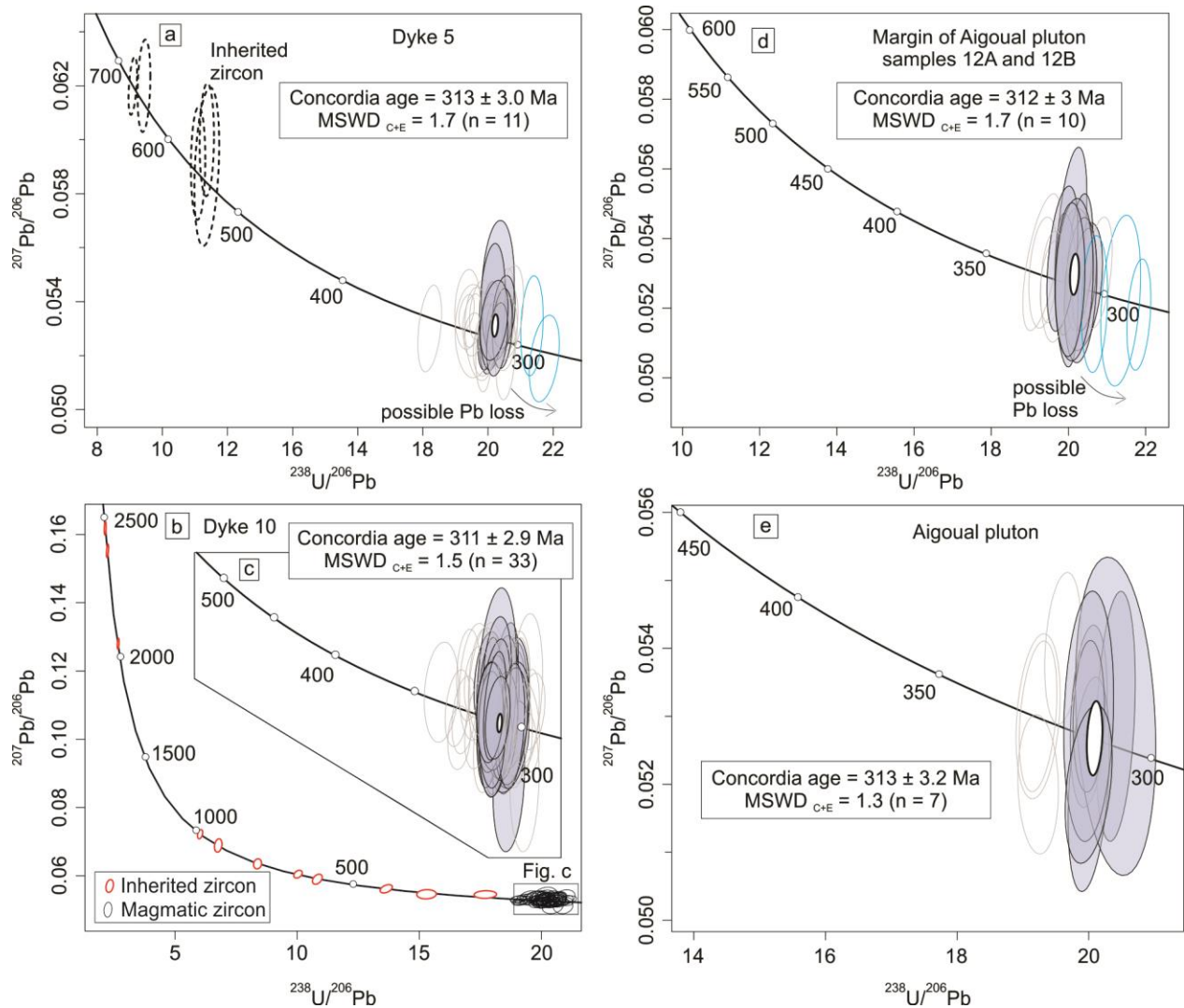


Figure II 8 Zircon U-Pb Terra-Wasserburg concordia diagrams $^{238}\text{U}/^{206}\text{Pb}$ age (Ma) from composite dykes and Aigoual pluton. Data-point error ellipses are 2σ .

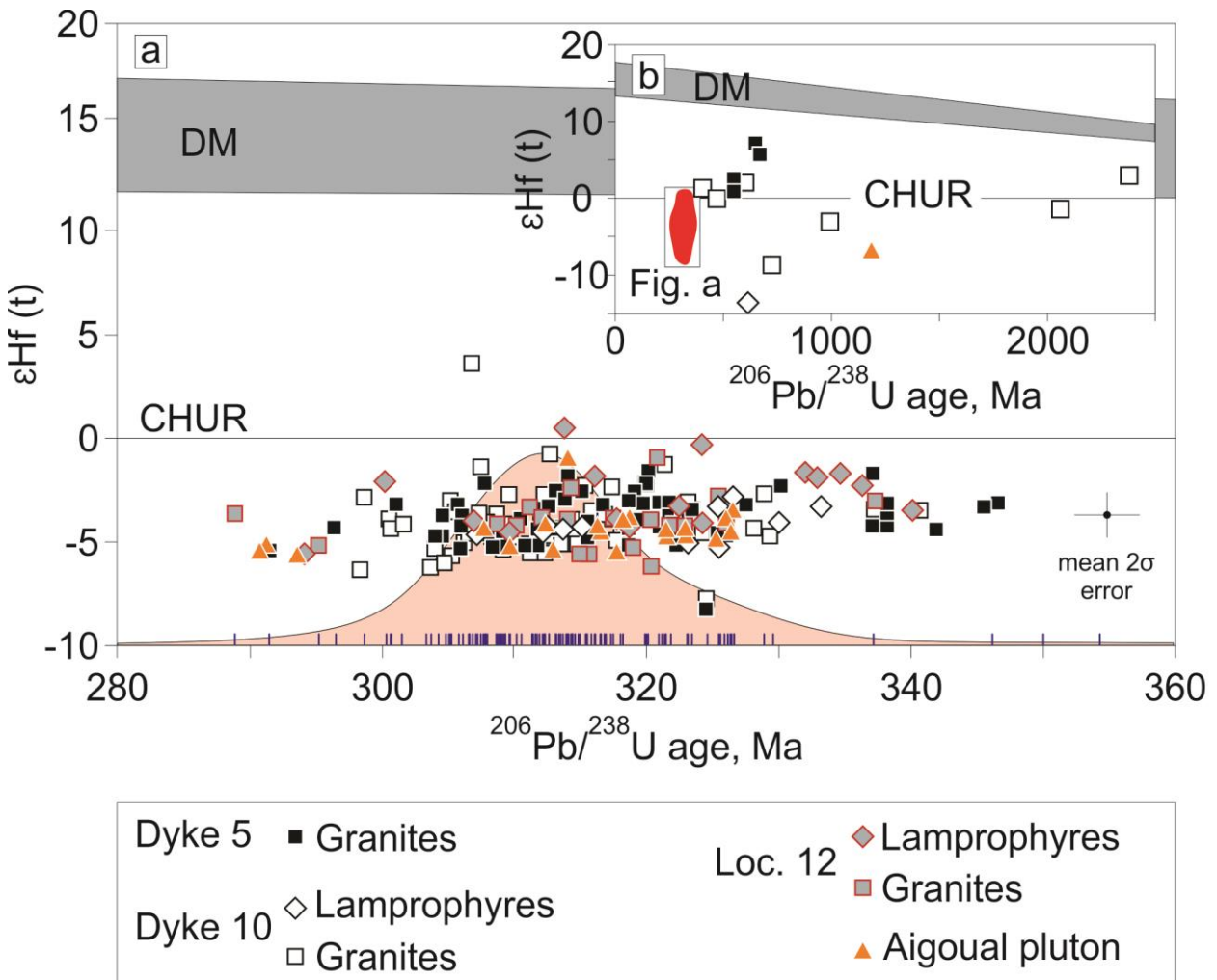


Figure II 9 $^{206}\text{Pb}/^{238}\text{U}$ age (Ma) versus $\epsilon\text{Hf(t)}$ from zircons from composite dykes and Aigoual pluton. $\epsilon\text{Hf(t)}$ lower and upper limit for Depleted Mantle (DM) are from Naeraa et al. (2012) and Griffin et al. (2004). The KDE curve is included in the diagram (light pink) for the $^{206}\text{Pb}/^{238}\text{U}$ age distribution used to calculate the Concordia age.

4.6 Quartz, and feldspar O isotopes

The $\delta^{18}\text{O}$ values of quartz and feldspar from composite dykes are listed in Table II 1. The $\delta^{18}\text{O}$ values of quartz vary from 10.76 to 11.21‰ ($n = 9$; average = 10.97‰) and, despite the narrow range in $\delta^{18}\text{O}$ value show a positive correlation with SiO_2 ($r^2 = 0.73$) (Figure II 10a) and Cr and Ni content ($r^2 = -0.66$) (Figure II 10b), the $\delta^{18}\text{O}$ values display no correlation with initial $^{87}\text{Sr}/^{86}\text{Sr}$ ($r^2 = 0.13$) (Figure II 10d), ϵNd ($r^2 = 0.17$) and ϵHf ($r^2 = 0.23$). The $\delta^{18}\text{O}$ values of feldspar vary from 6.4 to 13‰ ($n = 9$; average = 9.4‰), and are much more variable than quartz. There is no correlation between $\delta^{18}\text{O}$ values of quartz and feldspar (Figure II 10c). The three samples with $\text{SiO}_2 < 63$ wt.% plot between the

closure and crystallization isotherms on a δ – δ plot (Figure II 10c). The samples with $\text{SiO}_2 > 65$ wt.% show a wide range in feldspar $\delta^{18}\text{O}$ values, with the feldspar $\delta^{18}\text{O}$ value being both higher and lower than quartz. The wide range in feldspar $\delta^{18}\text{O}$ values is consistent with interaction with fluids at a range of temperatures.

Table II 1 $\delta^{18}\text{O}$ values from quartz and feldspar from lamprophyre and granite of composite dykes and Aigoual pluton (AG14A)

Sample	SiO_2 (wt.%)	$\delta^{18}\text{O}$ quartz (‰)	$\delta^{18}\text{O}$ feldspar (‰)
AG05C	67.77	10.89	6.6
AG06E	67.91	11.09	13
AG06F	67.92	11	10.7
AG09	59.85	10.76	8.52
AG10A	61.76	10.8	9.64
AG10D	69.89	11.21	6.37
AG12A	69.06	11.19	10.12
AG12B	57.82	10.8	8.12
AG14A	66.46	10.95	11.13

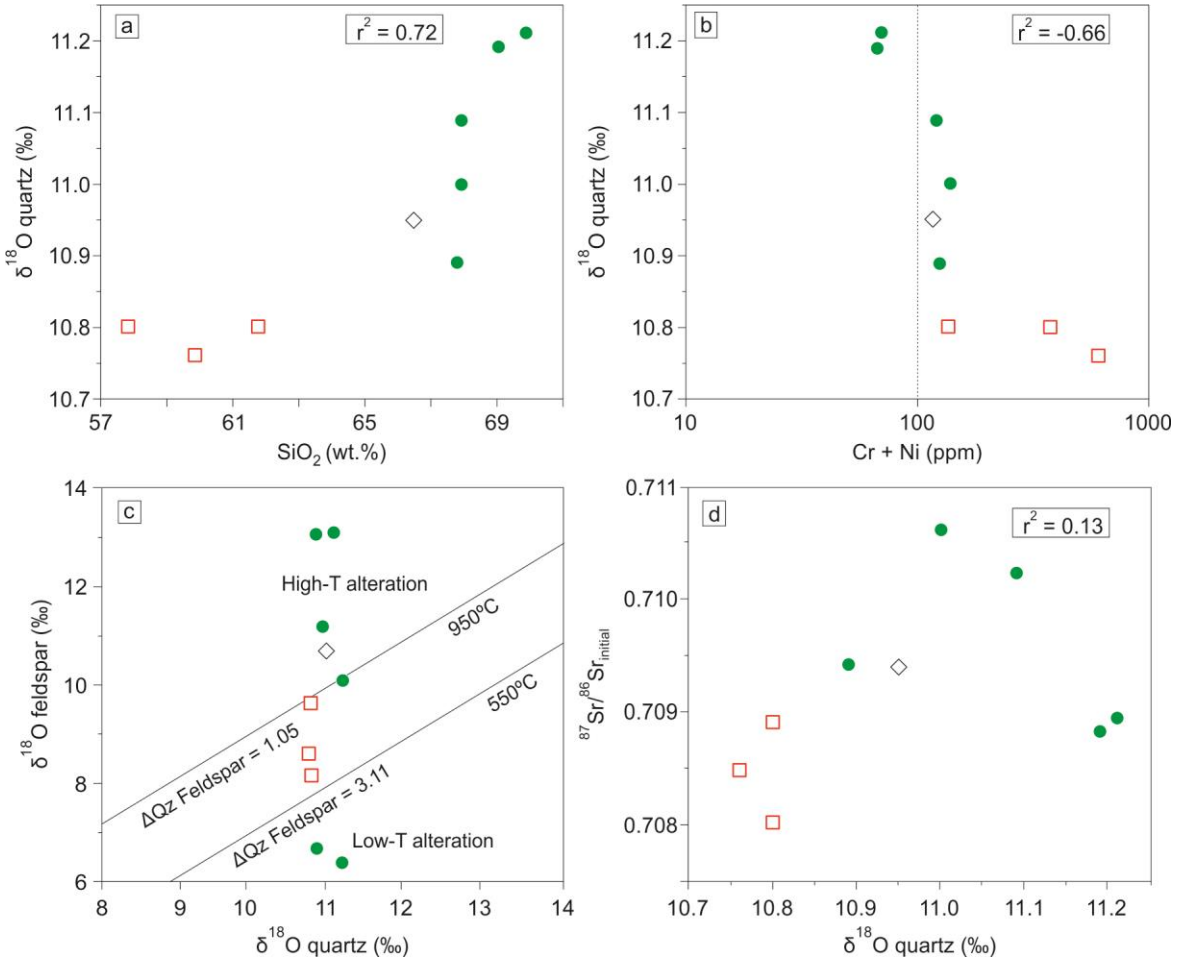


Figure II 10 (a) SiO_2 versus $\delta^{18}\text{O}$ quartz; (b) $\text{Ni} + \text{Cr}$ (log scale) versus $\delta^{18}\text{O}$ quartz; (c) $\delta^{18}\text{O}$ quartz versus $\delta^{18}\text{O}$ feldspar. Quartz-feldspar isotherms for 550°C and 950°C calculated using the calibrations of Chiba et al. (1989). Symbols as in Figure II 3.

5 Discussion

5.1 Timing of magma emplacement

The large variation in $^{206}\text{U}/^{238}\text{Pb}$ ages (~40 Ma) has no geological significance. Rather, it is likely to be an analytical artefact caused by the high U (over 1000 ppm) contents in dark grains and dark rims at CL images. Considering $^{206}\text{U}/^{238}\text{Pb}$ ages in crystalline grains, the KDE distribution shows ages between 305 and 320 Ma with a peak in 310 – 315 Ma (Figure II 9a). U-Pb analysis in zircon from lamprophyres and granites from dyke 5 and 10 display a $^{206}\text{Pb}/^{238}\text{U}$ age of 313 ± 3.0 Ma and 311 ± 2.9 Ma, respectively. Localization 12 in the eastern border of Aigoual pluton displays a $^{206}\text{Pb}/^{238}\text{U}$ age of 312 ± 3.1 Ma and central Aigoual pluton display a $^{206}\text{Pb}/^{238}\text{U}$ age of 313 ± 3.2 Ma. All samples of dykes and the Aigoual pluton show the same crystallization age within uncertainties. These ages are

statistically undistinguishable from the U-Pb age of 304 ± 12 Ma reported by Brichau et al. (2008) from the Southern portion of the ASGL complex – the “Liron” and “Saint-Guiral” portions.

The spatial distribution of the high K-Mg rocks in FMC in a preferential NE-SW trend (Fig. 1b) suggest that the emplacement occurs following weakened zones in the crust, possibly controlled by NW-SE extensional fields accompanied with crustal thinning of Variscan Belt during syn- to post-collisional period (Faure et al. 2009; Talbot et al. 2005). Data from anisotropy of magnetic susceptibility in the dykes from northern Aigoual pluton display magnetic fabric with NE-SW stretching. This fabric is controlled by magmatic flow instead of regional extension, suggesting a southwestward source feeding the magmatic system (Talbot et al. 2005).

A wide distribution in the ages of the inherited zircons were found within granitic samples compared with lamprophyres (Figure II 8b). The lack of inherited or xenocrystic grains in lamprophyres can be explained by Zr undersaturation due to the high-temperature and mafic composition of these magmas (Laurent et al. 2017). The inherited grains in granitic samples display Paleoproterozoic to late-Ordovician ages and ε_{Hf} signatures from -13 to +6.8, which is consistent with age distribution and isotopic signatures from ortho and paragneiss from Variscan crust in FMC (Chelle-Michou et al. 2017; Couzinié et al. 2019), suggesting melting and/or assimilation of local crust as mechanisms to incorporate these grains in the magma.

Geochronology in crustal-derived granites and mantle-derived magmas has been carried out in the EFMC (Couzinié et al. 2014; Laurent et al. 2017). These studies revealed that crust and mantle magmatism are related in space and time marking a coeval and protracted 40 Ma magmatic period with granites emplaced between 337.4 ± 1.0 and 298.9 ± 1.8 Ma and vaugnerites between 335.7 ± 2.1 and 299.1 ± 1.3 Ma (Laurent et al. 2017). The age distribution displays migration of magmatism towards the south, where younger ages of 307 and 298 in the Cévennes area were reported in KCG plutons (Couzinié et al. 2014; Laurent et al. 2017). These ages are substantially younger than reported in this work and this difference may indicate different magmatic pulses. A southward delamination of the lithospheric mantle and asthenosphere upwelling during late

Carboniferous may be the explanation for long-lived lithospheric-scale thermal anomaly producing melts from both crustal and mantle-derived melts (Laurent et al. 2017).

5.2 Origin of lamprophyres and granites

5.2.1 Origin of lamprophyres

The lamprophyre has moderate to high compatible elements contents such as Cr (74 – 572 ppm) and Ni (23 – 148 ppm) and coupled with the relative high Mg# (up to ~ 60) is consistent with mantle-derived source for this component of the composite system (e.g. Pandey et al. 2018; Sabatier 1991). However, the lamprophyres display elevated concentrations in LILE (K_2O , Sr, Rb, Ba, Pb, V), LREE and depletion in HFSE such Nb, Ta and Ti in relation to the primitive mantle. Radiogenic whole-rock Sr-Nd-Hf isotopes and Hf isotopes in zircon display crustal-like signatures with subchondritic ε_{Nd} and ε_{Hf} values and $\delta^{18}O$ values that are 5‰ higher than depleted mantle (Eiler 2001). The crustal-like signatures of lamprophyres can result from two process involving assimilation of crust and/or fractional crystallization from a primitive basaltic liquid (AFC process) or partial melting of a mantle-source already enriched and metasomatized, for instance by fluids or magma derived from crustal material during the subduction stage preceding continental collision (e.g. Couzinié et al. 2016).

Several lines indicate that the AFC process is unlikely. The absence of correlation between Mg#, Cr, Ba, Ni and $^{87}Sr/^{86}Sr$, ε_{Nd} , ε_{Hf} suggests that the isotopic enrichment did not result from crustal contamination. Moreover, the most mafic terms display similar crustal signatures to the intermediate terms and even to the granites from composite dykes. Even considering a possible contaminant in the area (e.g. graphite metapelites described in the Parautochthonous Unit (Faure et al. 2001)) with the adequate trace element composition (i.e. Cr, Ni rich), the AFC process cannot account for the high incompatible trace element contents (e.g. Rb, Sr, Ba) of lamprophyres. Furthermore, lamprophyres and others high K-Mg referred to as vaugnerites are ubiquitous in FMC (Figure II 1b) and intrude several lithologies from the nappe pile. All these rocks display similar signatures to lamprophyres reported in this work and point to enriched mantle as the most likely source. Therefore, the AFC process is unlikely.

Magmas derived from mantle sources modified by subducted components usually differ from MORBs and OIB by enrichment in Th and Nb compared to Yb (Pearce et al. 2008) (Figure II 11a). Similar to modern sediments (Global subducted sediments – GLOSS; Plank and Langmuir 1998), the studied calc-alkaline lamprophyres show jagged spidergrams marked by low Nb-Ta-Ti concentrations and elevated Th-U and Pb concentrations. All these geochemical features coupled with low Nb/La ratios, enrichment in LILE, LREE and depletion in HFSE in primitive mantle-normalized trace element diagrams suggest that the enriched lithospheric mantle is the most likely source for the lamprophyres. Likewise, the low $^{87}\text{Sr}/^{86}\text{Sr}$ ratios are consistent with mantle enrichment during the Silurian-Devonian subduction.

The presence of phlogopite identified in the lamprophyres and also the higher Rb/Sr and lower Ba/Rb ratios strongly indicate that phlogopite was the dominant hydrous phase in the source (Figure II 11b) (Butvina et al. 2021; Condamine and Médard 2014; Safonov et al. 2019). Moreover, it is widely accepted that high-K₂O magmas with shoshonitic affinity are typical of partial melting of phlogopite-bearing lithospheric mantle metasomatized by fluid or melt derived from the continental crust during subduction (Conceição and Green 2004; Förster et al. 2019; Peccerillo 1999; Prelevič et al. 2012). (Figure II 11c).

Quartz $\delta^{18}\text{O}$ values can be used as a proxy for the original magma $\delta^{18}\text{O}$ values being an important parameter of source and/or crustal contamination (e.g. Harris et al. 2005; Ódri et al. 2020). The parental magma would be about 1‰ lower than quartz $\delta^{18}\text{O}$ values (Fourie and Harris 2011). The calc-alkaline lamprophyres display high $\delta^{18}\text{O}$ values in quartz ($\delta^{18}\text{O} = 10.76$ to 10.80). The average quartz $\delta^{18}\text{O}$ values of lamprophyres is 10.78‰ suggesting an average $\delta^{18}\text{O}$ value of ~10‰ for the original magma. This is close to the boundary between I- and S-type granites suggested by Harris et al. (1997) (Figure II 12). The $\delta^{18}\text{O}$ values expected for an uncontaminated mantle-derived magma is about 5.7‰ (Eiler 2001) and fractional crystallization from a primitive magma can at most change $\delta^{18}\text{O}$ values by 1 to 1.5‰ for a 20% increase in SiO₂ content (Bindeman 2008; Bucholz et al. 2017). Either a very high $\delta^{18}\text{O}$ contaminant or a very high proportion of crust assimilation was required to raise the $\delta^{18}\text{O}$ value from 5.7 to 10‰. Simple mixing calculations between mantle and average of upper continental crust ($\delta^{18}\text{O} = 15\text{\textperthousand}$) display that ~50% of crustal assimilation is necessary to raise $\delta^{18}\text{O}$ values above 10‰ (Figure II

13). This amount of crustal assimilation is inconsistent with the high compatible element content and the low $^{87}\text{Sr}/^{86}\text{Sr}$ values observed in the lamprophyres that point to little or no crustal assimilation. Therefore, oxygen isotopes are sensitive to melt source and the high $\delta^{18}\text{O}$ values in lamprophyres indicate a contaminant with high $\delta^{18}\text{O}$ value in the mantle source.

High $\delta^{18}\text{O}$ values are common in sedimentary rocks. Oceanic carbonate-bearing sediments have $\delta^{18}\text{O}$ values of 25 to 32‰ and pelagic clays from 15 to 25‰ (Eiler 2001). Values from the silicate upper continental crust are around 10 and 20‰ (Taylor and Shepard 1986). Extremely high $\delta^{18}\text{O}$ values have been reported in peraluminous granite in ophiolite as a product of mud melting in the mantle leading to magma $\delta^{18}\text{O}$ values above 20‰ (Spencer et al. 2017) (Figure II 12). In this work, the high $\delta^{18}\text{O}$ values from lamprophyres (over 10‰) indicate the contaminant has been in contact with surface conditions.

To quantify the nature of the mantle source we apply mixing calculations using Sr, Nd and O isotopic systems. Simple mixing calculations between mantle and a potential contaminants indicate that ~20% of oceanic carbonate-bearing sediments ($\delta^{18}\text{O} = 28\text{\textperthousand}$) or ~35% of pelagic clays ($\delta^{18}\text{O} = 20\text{\textperthousand}$) are necessary to increase $\delta^{18}\text{O}$ values to higher than 10‰ (Figure II 13). Following the same approach, we apply simple magma mixing calculations using $^{87}\text{Sr}/^{86}\text{Sr}$ and εNd from the Variscan mantle and a sedimentary material. A proxy for the Variscan mantle can be derived from Devonian arc-related magmatism and ophiolites of the Variscan Belt: arc magmatism, resulting from fluid-fluxed melting of the mantle, has εNd close to the depleted mantle values but $^{87}\text{Sr}/^{86}\text{Sr}$ values offset to higher values (e.g. Bouilhol et al. 2013; Dhuime et al. 2011). The Devonian rocks of Massif Central have εNd up to +7 (Pin and Paquette 1997, 2002; Shaw et al. 1993). They also have $^{87}\text{Sr}/^{86}\text{Sr}$ values that are invariably higher than the expected value of 0.703 on the “mantle array” for rocks with $\varepsilon\text{Nd} = +7$, as expected from arc magmatism. Consequently, we estimate the Variscan mantle composition at that time to be $\varepsilon\text{Nd} = +7$, $^{87}\text{Sr}/^{86}\text{Sr} = 0.703$. In the case of FMC, the pre-Variscan metasediments are compositionally close to former sediments from the northern Gondwana margin (Chelle-Michou et al. 2017; Couzinié et al. 2017). We modelled mixing with several end-members, covering the range of Variscan metasediments (Solgadi et al. 2007; Williamson et al. 1992) and GLOSS

(Plank and Langmuir 1998). Mixing calculations indicate that the amount of sedimentary material mixed with mantle required to display the crustal isotopic signatures in Sr-Nd isotopic systems is between 25% and 40% (Figure II 14a), depending on the actual composition of the sediment contribution.

Lu-Hf and Sm-Nd isotopic systems have similar behavior during most magmatic processes and the composition of mantle and crust are correlated, evolving in a “mantle array” trend (Chauvel et al. 2008; Vervoort et al. 1999). Subchondritic whole-rock ε Nd and ε Hf display mantle enrichment with crustal materials. However, the lamprophyres plot above the “mantle array” with slightly negative to positive $\Delta\varepsilon$ Hf(t) values (-0.48 to 2.82) indicating more radiogenic Hf than Nd (Figure II 14b). The decoupling between Lu-Hf and Sm-Nd isotopic systems has been attributed to sediment-derived melts or fluids as the metasomatic agent in the mantle wedge (Guo et al. 2014; Orejana et al. 2020; Polat and Münker 2004). In the case of Hf-Nd plotting above the mantle array, the metasomatic agent might be pelagic sediments, which lack of zircon and display more radiogenic Hf (Vervoort et al. 2011).

Likewise, the presence of carbonates in lamprophyre might indicate that the composition of the crustal component was likely carbonate-bearing sediment. This composition corroborates with the high oxygen fugacity identified in the mantle beneath FMC, which is attributed to the addition of volatiles including CO₂ in the mantle during Variscan subduction, triggering CO₂, H₂O and K-rich metasomatism (Martin et al. 2017).

After establishing the nature of the contaminant, we now investigate the partial melting conditions that generated the lamprophyres. Non-modal partial melting models of a calculated source with 65-80% of DM and 20-35% of a contaminant (GLOSS composition, Plank and Langmuir 1998) show that 10 to 20% of partial melting matches the trace element composition of lamprophyres and associated granites (Figure II 15a, b). The high HREE contents are consistent with melting at shallow depth in spinel-Iherzolite facies source in the absence of garnet. Lamprophyres and granites display higher contents of LREE than the modelling, which suggests heterogeneities in the sediments, considering a pelagic clay richer in Rb and Ba than the average global sediments used in the calculation (Plank and Langmuir 1998), or melts derived from sediments, more enriched in LREE than GLOSS.

In summary, evidence points to the origin of lamprophyres from lamprophyric-granitic composite dykes from the northern margin of Aigoual pluton are products of 10 – 20% melting in the spinel-Iherzolite field. This CO₂, H₂O, K-enriched metasomatized mantle mixed previously with sediment-derived melts or fluids introduced into the mantle during Silurian-Devonian subduction.

5.2.2 Origin of granites

The studied dykes are composite and include co-magmatic lamprophyric and granite components, which belong to the same magmatic system. In addition, both rock types show a mixture of “crust-like” and “mantle-like” geochemical features, as seen in the lamprophyres, pointing to the role of both sources in their formation. Three main hypotheses or combinations thereof are plausible:

1. The lamprophyres and the granites are related by differentiation processes such as fractional crystallization, although remelting of underplated lamprophyres would result in broadly the same patterns; the lamprophyres differentiated during intrusion into the crust;
2. The lamprophyres and the granites represent distinct magmas, an enriched-mantle derived magma for the lamprophyres and a crust-derived magma for the granites, that mingle and mix at the emplacement site;
3. The granite and the lamprophyres are both direct products of melting of the enriched mantle source but in different proportions.

We briefly discuss each hypothesis here.

Several lines point out that the granites are not a product of simple fractional crystallization from a lamprophyric magma. The granites in the dykes share many geochemical characteristics with the lamprophyres, including nearly identical isotopic and trace element concentrations. However, the granites and the lamprophyres are not connected by differentiation trends and, furthermore, the lamprophyres are richer in most incompatible elements than the granites. This enrichment is inconsistent with a simple model of fractional crystallization of mafic into felsic magmas.

Major elements such as K₂O, Na₂O and Al₂O₃ are relatively constant with increasing SiO₂ content, showing no significant fractionation of K-feldspar, plagioclase and biotite in

the magma (e.g. Wang et al. 2021) (Figure II 4a, b, c). The increase in volume and size of megacrysts of K-feldspar in the granitic component demonstrate that a considerable decrease in K_2O is expected in fractional crystallization. Furthermore, a fractionation process involving plagioclase would display similar behavior for CaO and Sr. Harker diagrams in Figure II 4 display distinct behavior from CaO and Sr against SiO_2 contents, demonstrating that pure fractional crystallization from lamprophyres is unlike to generate the granites. Moreover, no cumulate textures are observed in lamprophyres and no pyroxenites are described in the area.

In general, fractional crystallization involving pyroxene will remove compatible elements such as Cr and Ni. The high Cr (30 – 140 ppm; 80.9 on average and in some cases over 100 ppm in a granite with SiO_2 = 70 wt.%) and Ni (14 – 40 ppm; 24.4 on average) content in the granites are inconsistent with fractional crystallization playing an important role in the formation of granites. Therefore, we do not regard this model as very likely.

Co-genetic granite may result from mixing between lamprophyres and crustal-derived magmas at crustal conditions. Petrological evidence favoring this model consists in the presence of ca. 10% of zircon xenocrysts in granites from composite dykes and the existence of corroded of quartz xenocrysts mantled by carbonate and amphibole in lamprophyre. Quartz xenocrysts rimmed by amphibole and carbonate are interpreted as a typical magma-mixing texture (e.g. Janoušek et al. 2004). In this way, we consider that assimilation (at least physically) with a crustal component is involved in the petrogenesis of granites from composite dykes.

Linear trends observed in many (but not all) binary plots between lamprophyre and granite might indicate magma mixing between these two end members, however, similar trends are observed in fractional crystallization or partial melting processes (Janoušek et al. 2016). Radiogenic isotopes are generally not fractionated during melting or crystallization and therefore are the best tools to decipher open-system processes such as magma mixing (e.g. Sun et al. 2010; Janoušek et al. 2020). In-situ Lu-Hf isotopic analysis in zircon is a powerful tool to identify the source of the melt and changes in the magma system over time (e.g. Chen et al. 2008; Finch et al. 2021; Tang et al. 2014). Large variations in zircon ϵ_{Hf} in granitic rocks has been attributed to magma mixing

between crustal and mantle-derived magmas (Griffin et al. 2002; Regmi et al. 2016; Storck et al. 2021; Sun et al. 2010; Yang et al. 2007) or inheritance from heterogeneities in detrital zircon ε Hf from the sedimentary source in the case of S-type granites (Farina et al. 2014; Villaros et al. 2012). In this study, zircon ε Hf values from lamprophyres and granites vary from -7.8 and +0.4 with more than 90% of the data plotting between -5 and -1.6, less than 4 ε Hf units, which is a limited variation with respect the analytical uncertainty (about \pm 1.5 ε Hf units on average). In the case of mixing of magmas with contrasting compositions, a wider range in ε Hf values is expected (up to 10 ε Hf units). Also, crust and mantle signatures will be more prominent, i.e. mantellic component migrating towards positive values and crustal component towards negative ε Hf values (e.g. Storck et al. 2021; Yu et al. 2020). Likewise, magmatic rims mantling in an old inherited core display different Hf isotopic signatures than cores, which indicates that the pre-existing grain does not control the isotopic composition of the magmatic rim (e.g. Finch et al. 2021). The ε Hf values from lamprophyres and granites are similar and overlap, pointing that mixing within different and contrasting magmas did not play an important role.

In terms of oxygen isotopes, the lack of correlation between $\delta^{18}\text{O}$ values and $^{87}\text{Sr}/^{86}\text{Sr}$, εNd and εHf makes the slightly correlation with SiO_2 and Cr and Ni meaningless. Therefore, the extremely narrow range in $\delta^{18}\text{O}$ values between lamprophyres and granites (less than 0.5‰) is more consistent with a source related variation or homogenization of the magma than mixing between two different and contrasting magmas.

Although crustal-derived melts are regionally widespread in FMC, the ASGL pluton lacks purely crustal granites, e.g. in the form of peraluminous cordierite- and muscovite-bearing rocks that are ubiquitous in the FMC. In addition, the lack of well-defined mixing trends for major elements, trace elements and isotopes alike suggests that magma mixing was not a dominant process. On the other hand, a minimal degree of assimilation is likely. In light of its apparent limited role, we favor local and limited assimilation, perhaps mechanical processes at the emplacement level.

Due to the comagmatic relation between lamprophyres and granites and very similar isotopic signatures, a third hypothesis needs to be evaluated. The genesis of granites and lamprophyres was from partial melting of different portions of metasomatized mantle or partial melting of the same metasomatized mantle at different temperatures. Experimental

studies involving mixing of peridotite and sediments (Förster et al. 2019, 2020, 2021) or mixing between granitic melt and peridotite/Iherzolite (Gao et al. 2019; Mallik et al. 2015) under mantle conditions are widely accepted for the origin of post-collisional K-rich magmatism. More specifically, recent studies report that mixing between peridotite and sediment can reach high SiO₂ contents (> 67%) (Förster et al. 2020, 2021) with compositions of major and trace elements matching those in this work. However, this hypothesis is an unusual explanation for the genesis of granites, considering that, at upper crustal level, exposed granite is considerably dominant over lamprophyre.

The available data do not provide firm constraint between the three hypotheses. However, they are not mutually exclusive. Both lamprophyres and granites display evidence of crustal recycling in different ways and addition of new mantle-derived material as seen in the high contents of compatible elements such Cr, Ni, MgO and FeO.

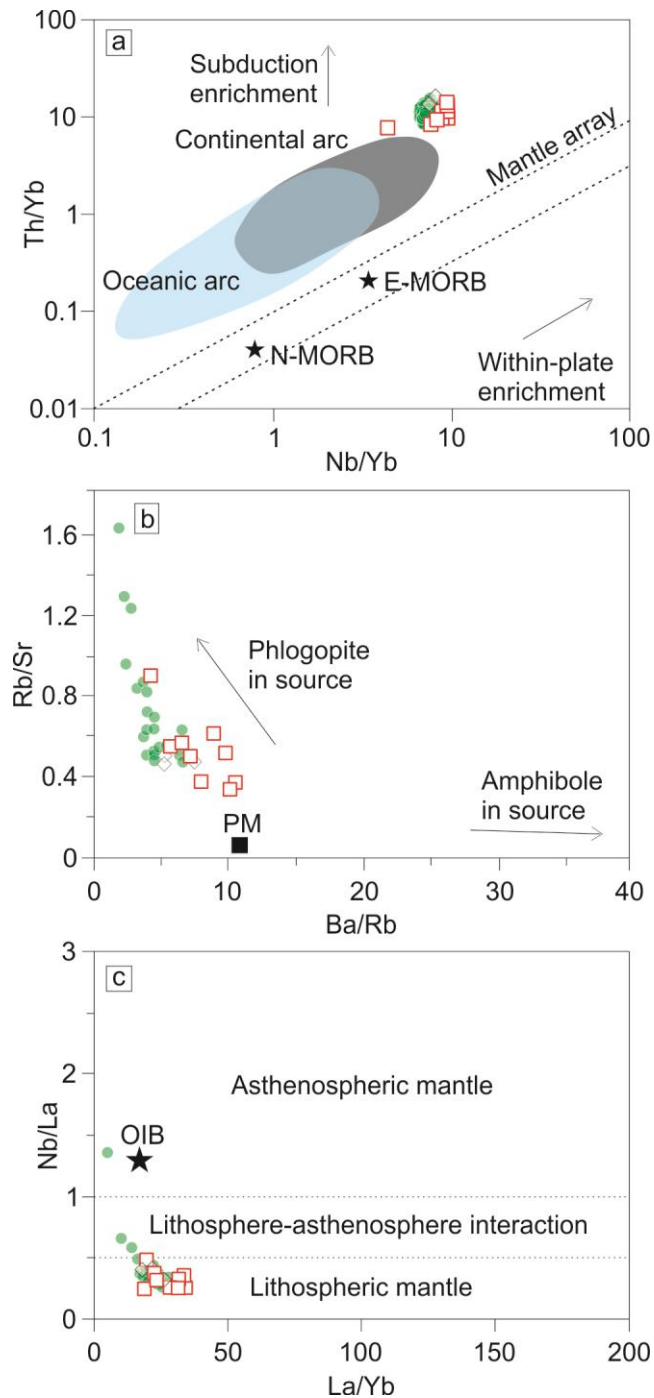


Figure II 11 (a) Ba/Rb vs. Rb/Sr diagram (after Furman and Graham, 1999) suggesting presence of phlogopite in the mantle source region; (b) La/Yb vs. Nb/La after Smith et al. (1999); (c) Nb/Yb vs. Th/Yb after Pearce (2008) suggesting subduction enrichment. Granite plotting together in pale colors, as they are co-magmatic. Symbols as in Figure II 3.

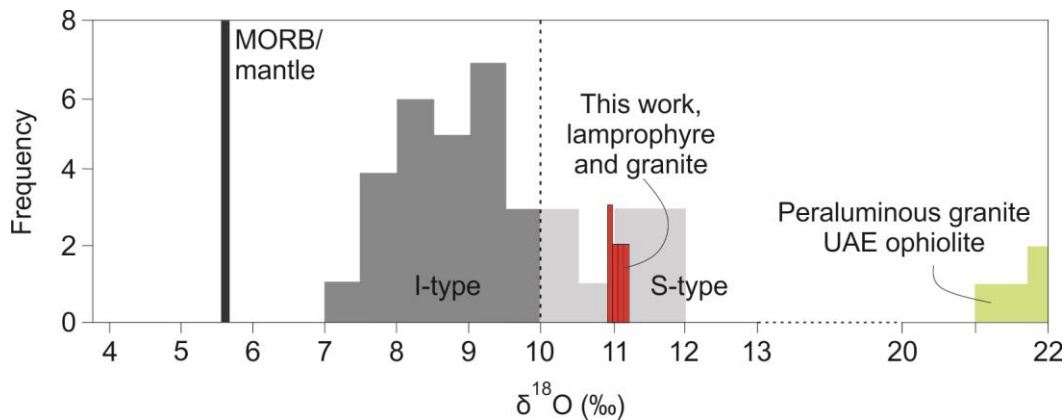


Figure II 12 Histogram of $\delta^{18}\text{O}$ quartz analysis. Mantle O isotopic value ($\sim 5.7\text{\textperthousand}$) from Eiler (2001); I- and S-type granites from Harris et al. (1997) and peraluminous granite from Oman-United Arab Emirates (UAE) ophiolite from Spencer et al. (2017).

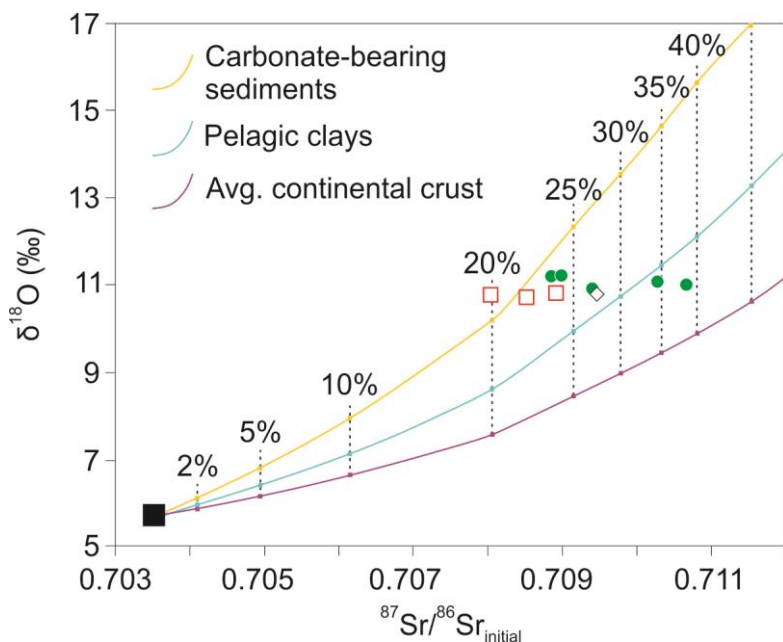


Figure II 13 (a) Results of mixing models between mantle ($\delta^{18}\text{O} = 5.7\text{\textperthousand}$ and $^{87}\text{Sr}/^{86}\text{Sr}_{\text{initial}} = 0.703$) and three different contaminants all characterized by $^{87}\text{Sr}/^{86}\text{Sr}_{\text{initial}} = 0.715$ (GLOSS, Plank and Langmuir 1998) but different $\delta^{18}\text{O}$ values characterizing different contaminants. Carbonate bearing sediments $\delta^{18}\text{O} = 28\text{\textperthousand}$; Pelagic clays $\delta^{18}\text{O} = 20\text{\textperthousand}$ and average continental crust $\delta^{18}\text{O} = 15\text{\textperthousand}$. $\delta^{18}\text{O}$ from Eiler (2001). Symbols as in Figure II 3.

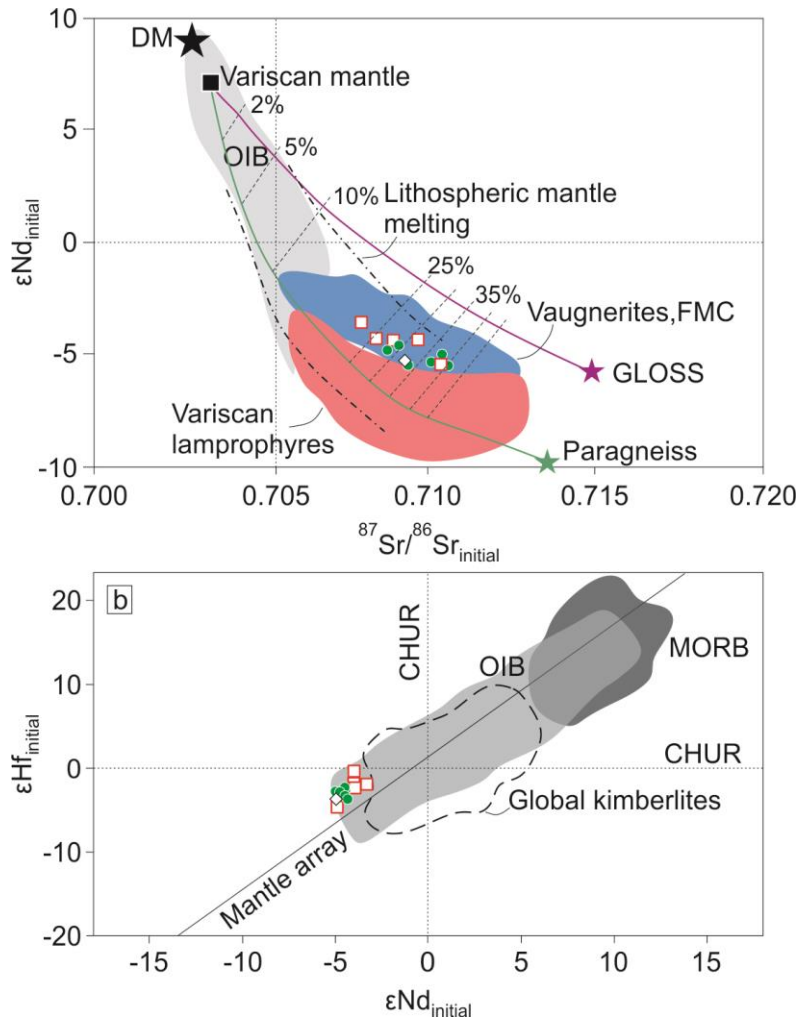


Figure II 14 (a) $\varepsilon\text{Nd}_{\text{initial}}$ vs. $^{87}\text{Sr}/^{86}\text{Sr}_{\text{initial}}$ for composite dykes and Aigoual pluton. Initial ratios calculated for 311 Ma. Lithospheric mantle melting field from Davis and Blanckenburg (1995); Vaugnerites French Massif Central (FMC) from Moyen et al. (2017); Variscan lamprophyres from Soder and Romer (2018). For mixing calculation we used Variscan mantle composition from Pin and Paquette (1997), GLOSS from Plank and Langmuir (1998) and paragneiss composition from FMC from Moyen et al. (2017); (b) $\varepsilon\text{Nd}_{\text{initial}}$ vs. $\varepsilon\text{Hf}_{\text{initial}}$ values for composite dykes and Aigoual pluton. Data from MORB and OIB is taken from Stracke (2012) and mantle array regression line from Chauvel et al. (2008). Global kimberlites field from Tappe et al. (2018). DM = depleted mantle; OIB = ocean island basalt; Symbols as in Figure II 3.

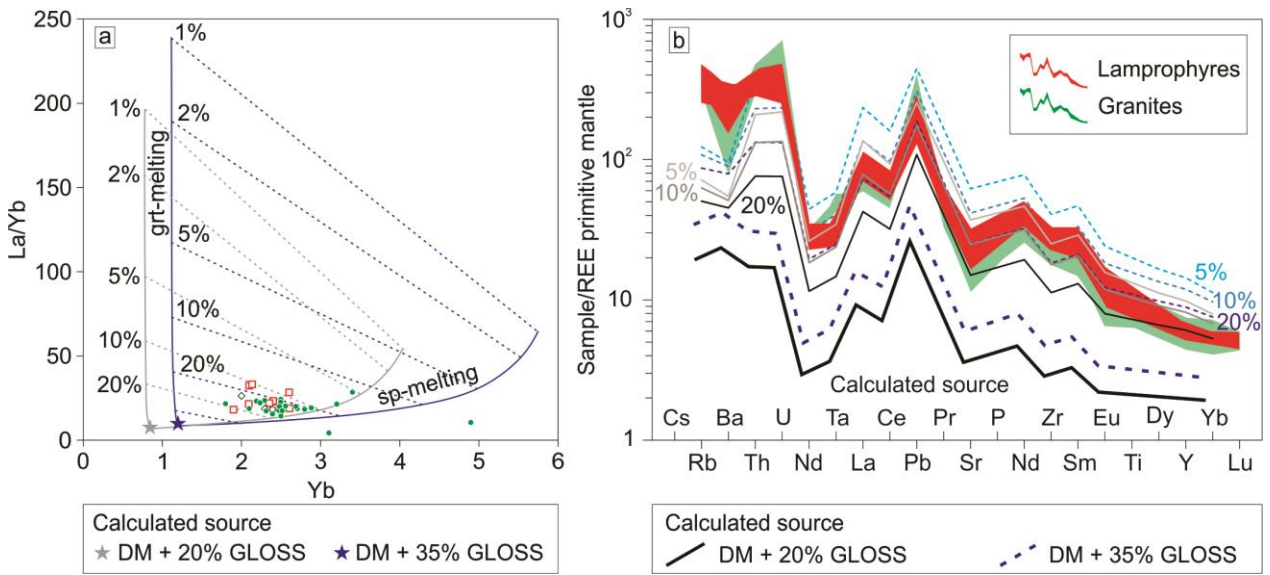


Figure II 15 (a) Yb vs. La/Yb plot with batch models of spinel and garnet phlogopite peridotite. The calculated sources correspond to Depleted Mantle (Workam and Hart 2005) mixed with 20% to 30% GLOSS (Plank and Langmuir 1998). Modal proportions in the residue are recalculated from Condamine and Médard (2014) for spinel peridotite (olivine 0.69, orthopyroxene 0.15, clinopyroxene 0.08, phlogopite 0.07, spinel 0.01) and Thibault et al. (1992) for garnet peridotite (olivine 0.25, orthopyroxene 0.5, clinopyroxene 0.15, phlogopite 0.03, garnet 0.07). Partition coefficients from mafic and intermediate rocks from Laurent (2012). (b) Multi-element pattern of lamprophyres and granites and calculated compositions generated by 5, 10 and 20% of partial melting of a spinel phlogopite-peridotite source. Black and gray continuous line represent partial melting of a calculated source with DM + 20% GLOSS and blue dashed lines represent partial melting of a calculated source with DM + 35% GLOSS. Partition coefficients from mafic and intermediate rocks from Laurent (2012). The melt composition from calculated source replicates the multi-element pattern exhibit by lamprophyres and granites as well, except for the LREEs. Symbols as in Figure II 3

5.2.3 Texture of the microgranites

The preservation of these unusual dykes with limited interaction between lamprophyres and granites and the fine grained, quenched textures in granites may be a direct consequence of the presence of carbonate in the system. The absence of pyroxene in the lamprophyres and its presence in the granites is explained by the association biotite/phlogopite with carbonate pseudomorphing the prior mafic phase. This reaction can be explained in response to increasing $a\text{CO}_2$ and $a\text{H}_2\text{O}$ in the cooling and crystallization of the lamprophyric magma possibly replacing pyroxene by biotite/phlogopite and carbonate (Blank and Brooker 1994; Solomatova et al. 2020; Tsuno and Dasgupta 2012). As the presence of carbonate fluxes the partial melting of mantle rocks (Dasgupta et al. 2013; Spandler and Pirard 2013), carbonated portions of the metasomatized mantle source melted preferentially to produce the lamprophyres.

CO_2 plays a fundamentally different role in the melting of mantle and crustal lithologies and its solubility is strongly dependent of pressure, melt composition and H_2O content (Blank and Brooker 1994; Lowenstern 2000; Ni and Keppler 2013; Tsuno and Dasgupta 2012). During melting of mafic and ultramafic rocks at mantle pressures, the solubility of CO_2 increases with increasing pressure and decreasing SiO_2 contents (Brooker et al. 2001). In silicate systems, at crustal pressures, the water-saturated solidus defines the lowest temperature of partial melting and CO_2 has very low solubility in such melts (Blank 1993; Brooker et al. 2001). The consequence of CO_2 being present in these systems is to raise the solidus temperature drastically (Scaillet et al. 1997). Therefore, CO_2 -fluids derived from cooling mafic melts that intruded the crust may limit the possibilities for interaction between the mafic magma and granites. This study records an example of this behavior where the mantle-derived lamprophyre interacted with granites. CO_2 saturation of the system provides a straightforward explanation for the quenching of the silicate magmas and therefore the lack of complete mixing of the lamprophyric component into the granites.

5.3 Implications for crustal growth

The ratio between addition of new mantle-derived magma and recycling of old crustal material sets the degree of crustal growth relative to recycling during a magmatic episode. In the case of the FMC, a large proportion of the magmatic rocks (MPG, CPG and Velay) was derived from melting of local crust and therefore, these rocks did not contribute to crustal growth and correspond to pure crustal recycling (e.g. Moyen et al. 2017). On the other hand, vaugnerite and its differentiated portions, i.e. KCG granites, had contribution of mantle-derived material and represent new crust formation (Couzinié et al. 2016; Moyen et al. 2017). Couzinié et al. (2016) has been demonstrated that Hf-O isotopes in zircon do not identify addition of new mantle-derived material to the crust and therefore the process of crustal growth may be underestimated throughout geological time, since many studies were carried out looking at the zircon record (e.g. Belousova et al. 2010; Campbell et al. 2020; Hawkesworth and Kemp 2006; Kemp et al. 2007).

Due to the strong contrasting compositions between the mantle and crust, a relatively small proportion of crustal material (<30%) recycled into the mantle is sufficient to control

all incompatible elements contents and form the “crust-like” isotopic signature observed in mafic post-collisional magmatism (Couzinié et al. 2016; Jacob et al. 2021). This study demonstrates that addition of new mantle-derived material is not identified by usual isotopic systems such as Rb-Sr, Sm-Nd and Lu-Hf, pointing out that crustal growth is hidden from the radiogenic record. Moreover, O isotopes in lamprophyres also display crustal signatures and hide the mantle signature. Our results demonstrate that between 20-35% of the budget of Sr, Nd, Hf and other incompatible elements comes from the crust and therefore do not contribute additions of new material. However, at the same time, the budget of compatible elements such as Mg, Fe, Ni, Cr is strongly controlled by the mantle component and represents addition of new material to the crust. This process is described in the lamprophyres where the mafic character and the dual geochemical signature display mantle and crustal contribution and, even though the mantle contribution is hidden from isotopic point of view, between 65 – 80% of material comes from the mantle.

Although less evident, the same process occurs in the granites of composite dykes. Assimilation with crustal material might be involved in their petrogenesis not representing input of a new crust, but the relative high Cr, Ni, also FeO, and MgO contents in relation to the others crustal-derived granites in FMC represent a mantle component must be involved in their genesis. The intimate relation (physically and geochemically) between lamprophyre and granite described in this work in the composite dykes of northern border of Aigoual pluton provides constrains about the mantle contribution in post-collisional granitoids from FMC.

High K-Mg mafic rocks in FMC are small volume in terms of outcrops (~10%) and therefore the contribution for crustal growth may less significant. However, assuming the petrogenesis of granites (i.e., direct influence of the mantle) from composite dykes similar to Aigoual pluton and others KCG granites in FMC (ca. 25% of outcrop area), we consider the addition of new mantle-derived material as significant. Considering that between 65% and 80% of the material from lamprophyres and KGC granites came from the mantle and both represent not more than 35% of granitoids outcrops in FMC, approximately 22 to 28% of the magmatic material came from the mantle and represent addition of crust.

6 Conclusions

In summary, lamprophyric-granitic composite dykes from the northern border of post-Variscan Aigoual pluton record mantle and crust interactions and represent significant long-term addition of new crust in post-collisional setting. Their emplacement is coeval with the emplacement of Aigoual pluton between 311 and 313 Ma. Lamprophyres display crustal-like signatures with Sr, Nd, Hf, O isotopes and other incompatible elements and were product of 10 – 20% of partial melting from metasomatized mantle. This mantle formed by mixing between 20 – 35% of sediments from northern Gondwana margin and 65 – 80% of mantle. The melting process occurred at shallow depth in the spinel stability field. Granites display a mantle-derived component in their genesis in the high Cr, Ni, FeO and MgO contents compared with other crustal-derived granites in FMC. In terms of crustal-growth, our results demonstrate that between 22 to 28% of magmatic material in FMC came from the mantle. This study demonstrates that, although hidden by crustal signatures in terms of isotopes and incompatible elements, the mantle contribution in post-collisional magmatism is significant. Considering the higher preservation potential throughout geological time, the post-collisional sites represent a meaningful contributor for the long-term crustal growth.

Acknowledgements

This research was supported by RSA NRF grant to Gary Stevens via the SARChI program and by IRP BuCoMo, a collaborative research project funded by the CNRS and the NRF. This is BuCoMo contribution A15. We thank Llelani Coetzer for sample preparation, Riana Russow from CAF Unit (Stellenbosch University) for LA-SF-ICP-MS analyses, Madelaine Frazenburg and Alicia Botes from CAF Unit for the help with remote analyses in 2020 and Sherissa Roopnarain for help with the O-isotope analyses.

7 References

- Barbarin B (1999). A review of the relationships between granitoid types, their origins and their geodynamic environments. *Lithos* 46(3):605-626.
- Belousova EA, Griffin WL, O'Reilly SY, Fisher NI (2015). Igneous zircon: trace element composition as an indicator of source rock type. *Contributions to Mineralogy and Petrology* 143:602-622.
- Belousova EA, Kostitsyn YA, Griffin WL, Begg GC, O'Reilly SY, Pearson NJ, (2010). The growth of the continental crust: Constraints from zircon Hf-isotope data. *Lithos* 119(3-4):457-466.
- Bindeman I (2008). Oxygen Isotopes in Mantle and Crustal Magmas as revealed by Single Crystal analysis. *Reviews in Mineralogy and Geochemistry* 69:445-478.
- Blank JG and Brooker RA (1994). Experimental studies of carbon dioxide in silicate melts: Solubility, speciation, and stable carbon isotope behavior. In: Carroll, M.R., Holloway, J.R. (Eds.), *Reviews in Mineralogy and Geochemistry*, American Mineralogical Society 30:157-186.
- Blichert-Toft J, Chauvel C, Albarède F (1997). Separation of Hf and Lu for high-precision isotope analysis of rock samples by magnetic sector-multiple collector ICP-MS. *Contributions to Mineralogy and Petrology* 127:248-260.
- Blichert-Toft J, Puchtel IS (2010). Depleted mantle sources through time: evidence from Lu-Hf and Sm-Nd isotope systematics of Archean komatiites. *Earth and Planetary Science Letters* 297:598-606.
- Bonin B (2004). Do coeval mafic and felsic magmas in post-collisional to within-plate regimes necessarily imply two contrasting, mantle and crustal, sources? A review. *Lithos* 78:1-24.
- Bouilhol P, Jagoutz O, Hanchar JM, Dudas FO (2013). Dating the India–Eurasia collision through arc magmatic records. *Earth and Planetary Science Letters* 366 :163-175.
- Bouvier A, Vervoort JD, Patchett PJ (2008). The Lu-Hf and Sm-Nd isotopic composition of CHUR: constraints from unequilibrated chondrites and implications for the bulk composition of terrestrial planets. *Earth and Planetary Science Letters* 273:48-57.
- Brichau S, Respaut JP, Monié P (2008) New age constraints on emplacement of the Cévenol granitoids, South French Massif Central. *Int J Earth Sci* 97:725–738.
- Brooker RA, Kohn SC, Holloway JR, McMillan PF (2001). Structural controls on the solubility of CO₂ in silicate melts: Part I: bulk solubility data. *Chemical Geology* 174:225-239.

Bucholz CE, Jagoutz O, VanTongeren JA, Setera J, Wang Z (2017). Oxygen isotope trajectories of crystallizing melts: Insight from modelling and the plutonic record. *Geochimica et Cosmochimica Acta* 207:154-184.

Butvina VG, Safonov OG, Vorobey SS, Limanov EV, Kosova SA, Van KV, Bondarenko GV, Garanin VK (2021). Experimental Study of Reactions Forming Phlogopite and Potassic Titanates as Mineral Indicators of Metasomatism in the Upper Mantle. *Geochemistry International* 59:757-777.

Campbell MJ, Rosenbaum G, Allen CM, Spandler C (2020). Continental Crustal Growth Processes Revealed by Detrital Zircon Petrochronology: Insights from Zealandia. *JGR Solid Earth* <https://doi.org/10.1029/2019JB019075>.

Cawood PA, Hawkesworth CJ, Dhuime B (2013). The continental record and the generation of continental crust. *GSA Bulletin* 125:14-32.

Cerva-Alves T, Hartmann LA, Lana C, Queiroga GN, Maciel LAC, Leandro CG, Savian JF (2021). Rutil and zircon age and geochemistry in the evolution of the juvenile São Gabriel terrane early in the Brasiliano Orogeny. *Journal of South American Earth Sciences* 112:103505.

Chantraine J, Autran A. and Cavelier C (1996). Carte géologique de la France à l'échelle du millionième (6e édition), BRGM, Orléans.

Chauvel C, Lewin E, Carpentier M, et al. (2008). Role of recycled oceanic basalt and sediment in generating the Hf–Nd mantle array. *Nature Geoscience* 1:64–67 <https://doi.org/10.1038/ngeo.2007.51>.

Chelle-Michou C, Laurent O, Moyen JF, Block S, Paquette JL, Couzinié S, Gardien V, Vanderhaeghe O, Villaros A, Zeh A (2017). Pre-Cadomian to late-Variscan odyssey of the eastern Massif Central, France: formation of the West European crust in a nutshell. *Gondwana Research* 46:170-190.

Chen B, Tian W, Jahn BM, Chen ZC (2008). Zircon SHRIMP U–Pb ages and in situ Hf isotopic analysis for the Mesozoic intrusions in South Taihang, North China craton: evidence for hybridization between mantle derived magmas and crustal components. *Lithos* 102:118–137.

Chiba H, Chacko T, Clayton RN, Goldsmith JR (1989). Oxygen isotope fractionations involving diopside, fayalite, magnetite, and calcite: applications to geothermometry. *Geochim Cosmochim Acta* 53:2985–2995.

Chu NC, Taylor RN, Chavagnac V et al (2002). Hf isotope ratio analysis using multi-collector inductively coupled plasma mass spectrometry: An evaluation of isobaric interference corrections. *Journal of Analytical Atomic Spectrometry* 17:1567-1574.

Clemens JD, Darbyshire DPF, Flinders J (2009). Sources of post-orogenic calc-alkaline magmas: the Arrochar and Garabal Hill–Glen Fyne complexes, Scotland. *Lithos* 112:524–542.

Conceição R, Green DH (2004). Derivation of potassic (shoshonitic) magmas by decompression melting of phlogopite+pargasite lherzolite. *Lithos* 72:209–229.

Condamine P, Médard E (2014). Experimental melting of phlogopite-bearing mantle at 1 GPa: Implications for potassic magmatism. *Earth and Planetary Science Letters* 397:80–92.

Condie KC (2014). Growth of continental crust: a balance between preservation and recycling. *Mineralogical Magazine* 78(3):623–637.

Condie KC, Bickford ME, Richard CA, Belousova E, Scholl DW (2011). Episodic zircon ages, Hf isotopic composition, and the preservation rate of continental crust. *GSA Bulletin*, 123(5-6):951–957.

Caron C (1994). Les minéralisations Pb-Zn associées au Paléozoïque inférieur d'Europe méridionale. Traçage isotropique Pb-Pb des gîtes de l'Iglesiente (SW Sardaigne) et des Cévennes et évolution du socle encaissant par la géochronologie U-Pb, ^{40}Ar - ^{39}Ar et K-Ar. PhD thesis, University of Montpellier 288 pp.

Couzinié S, Laurent O, Chelle-Michou C, Bouilhol P, Paquette JL, Gannoun AM, Moyen JF (2019). Detrital zircon U-Pb-Hf systematics of Ediacaran metasediments from the French Massif Central: Consequences for the crustal evolution of the north Gondwana margin. *Precambrian Research* 324:269–284.

Couzinié S, Laurent O, Moyen JF, Zeh A, Bouilhol P, Villaros A (2016). Post-collisional magmatism: Crustal growth not identified by zircon Hf-O isotopes. *Earth and Planetary Science Letters* 456:182–195.

Couzinié S. et al. (2014). Temporal relationships between Mg-K mafic magmatism and catastrophic melting of the Variscan crust in the southern part of the Velay Complex (Massif Central, France). *Journal of Geosciences* 59(1-4):1–18.

Couzinié S, Bouilhol P, Laurent O, Grocolas T, Montel JM (accepted for publication). Age and origin of the Cézarenque–Joyeuse gneisses (Cévennes paraautochton, French Massif Central): sediment-derived ferrosilicic magmas erupted along the Furongian Tremadocian volcanic belt of western Europe. *Bulletin de la Société Géologique de France-Earth Science*.

Dasgupta R (2013). Ingassing, Storage, and Outgassing of Terrestrial Carbon through Geologic Time. *Reviews in Mineralogy and Petrology* 75:183–229.

Davis JH and Von Blanckenburg F (1995). Slab breakoff: a model of lithosphere detachment and its test in the magmatism and deformation of collisional orogens. *Earth and Planetary Science Letters* 129:85–102.

Dhuime B, Hawkesworth C, Cawood P (2011). When continents formed. *Science* 331:154-155 DOI: 10.1126/science.1201245.

Dijkstra AH and Hatch C (2018). Mapping a hidden terrane boundary in the mantle lithosphere with lamprophyres. *Nature Communications* 9:3770 <https://doi.org/10.1038/s41467-018-06253-7>.

Do Couto D, Faure M, Augier R, Cocherie A, Rossi P, Li XH, Lin W (2015). Monazite U-Th-Pb EPMA and zircon U-Pb SIMS chronological constraints on the tectonic, metamorphic and thermal events in the inner part of the Variscan orogen, example from the Sioule series. *International Journal of Earth Sciences* 105:557-559.

Downes H, Shaw A, Williamson BJ, Thirlwall MF (1997). Sr, Nd and Pb isotope geochemistry of the Hercynian granodiorites and monzogranites, Massif Central, France. *Chemical Geology* 136:99–122.

Duthou JL, Cantagrel JM, Didier J, Vialette Y (1984). Paleozoic Granitoids from the French Massif Central - Age and Origin Studied by Rb-87-Sr-87 System. *Physics of the Earth and Planetary Interiors* 35(1-3):131-144.

Eiler JM (2001). Oxygen isotope variations of basaltic lavas and upper mantle rocks. *Reviews in Mineralogy and Geochemistry* 43:319–364.

Errandonea-Martin J, Sarrionandia F, Carracedo-Sánchez M., Gil Ibarguchi JI, Eguíluz L (2018). Petrography and geochemistry of late- to post-Variscanvaugnerite series rocks and calc-alkaline lamprophyres within a cordierite-bearing monzogranite (the Sierra Bermaja Pluton, southern Iberian Massif). *Geol. Acta* 16:237–255.

Ewing RC, Meldrum A, Wang LM, Weber WJ, Corrales RJ (2003). Radiation Effects in zircon. *Reviews in Mineralogy and Geochemistry* 53(1):387-485.

Farina F, Stevens G, Gerdes A, Frei D (2014). Small-scale Hf isotopic variability in the Peninsula pluton (South Africa): the processes that control inheritance of source $^{176}\text{Hf}/^{177}\text{Hf}$ diversity in S-type granites. *Contributions to Mineralogy and Petrology* 168:1065.

Faure F, Charonnat X, Chauvet A (1999). Schéma structural et évolution tectonique du domaine para-autochtone cévenol de la chaîne hercynienne (Massif central français). *Comptes Rendus de l'Académie de Sciences* 328:401-407.

Faure M, Bé Mézème E, Duguet M, Cartier C, Talbot J (2005). Paleozoic tectonic evolution of medio-Europa from the example of the French Massif Central and Massif Armorican. In: Carosi R, Dias R, Iacopini D, Rosenbaum G (eds) The southern Variscan belt, *Journal of the Virtual Explorer*, Electronic Edition, ISSN 1441-8142, volume 19, paper 5, doi:10.3809/jvirtex.2005.00120.

Faure M, Charonnat X, Chauvet A, Chen Y, Talbot JY, Martelet G, Courrioux G, Monié, P, Milesi JP (2001). Tectonic evolution of the Cévennes para-autochthonous domain of

the Hercynian French Massif Central and its bearing on ore deposits formation. *Bulletin de la Societe Geologique de France* 172(6):687-696.

Faure M, Lardeaux JM, Ledru P (2009). A review of the pre-Permian geology of the Variscan French Massif Central. *Comptes Rendus Geoscience* 341:202-213.

Finch MA, Weinberg RF, Barrote VR, Cawood PA (2021). Hf isotopic ratios in zircon reveal processes of anatexis and pluton construction. *Earth and Planetary Science Letters* 576:117215.

Förster MW, Buhre S, Xu B, Prelević D, Mertz-Kraus R, Foley SF (2020). Two-stage origin of K-enrichment in ultrapotassic magmatism simulated by melting of experimentally metasomatized mantle. *Minerals* 10(1):41. <https://doi.org/10.3390/min10010041>.

Förster MW, Bussweiler Y, Prelević D, Dackzo NR, Buhre S, Mertz-Kraus R, Foley SF (2021). Sediment-peridotite reaction controls fore-arc metasomatism and arc magma geochemical signature. *Geosciences*, 11(9):372 <https://doi.org/10.3390/geosciences11090372>.

Förster MW, Prelević D, Buhre S, Mertz-Kraus R, Foley SF (2019). An experimental study of the role of partial melts of sediments versus mantle melts in the sources of potassic magmatism. *Journal of Asian Earth Sciences* 177:76–88.

Fowler MB, Henney PJ (1996). Mixed Caledonian appinite magmas: implications for lamprophyre fractionation and high Ba-Sr granite genesis. *Contributions to Mineralogy and Petrology* 126:199-215.

Frei D, Gerdes A (2009). Precise and accurate in situ U-Pb dating of zircon with high sample throughput by automated LA-SF-ICP-MS. *Chemical Geology* 261(3-4):261-270.

Furman T, Graham D (1999). Erosion of lithospheric mantle beneath the East African Rift system: geochemical evidence from the Kivu volcanic province. *Lithos* 48:237–262.

Gao P, Santosh M, Cheng-Xue Y, Yunpeng D, Nakagawa M (2021). Arc volcanic suite from a Miocene subduction system in SW Japan: A geochemical and zircon U-Pb-Lu-Hf study. *Lithos* 398-399:106251.

Gao M, Xu H, Zhang J, Foley SF (2019). Experimental interactions of granitic melt and peridotite at 1.5 GPa: implications for the origin of post-collisional K-rich magmatism in continental subduction zones. *Lithos*, 350-351:105241.

Griffin WL, Wang X, Jackson SE, Pearson NJ, O'Reilly SY, Xu X., Zhou X (2002). Zircon chemistry and magma mixing, SE China: In-situ analysis of Hf isotopes, Tonglu and Pingtan igneous complexes. *Lithos* 61:237–269.

Griffin WL, Belousova EA, Shee SR, Pearson NJ, O'Reilly SY (2004). Archean crustal evolution in the northern Yilgarn Craton: U-Pb and Hf-isotope evidence from detrital zircons. *Precambrian Research* 131:231-282.

Guo F, Weiming F, Li C, Wang CY, Li H, Zhao L, Li J (2014). Hf-Nd-O isotopic evidence for melting of recycled sediments beneath the Sulu Orogen, North China. *Chemical Geology* 381:243-258.

Harris C and Ashwal LD (2002). The origin of low $\delta^{18}\text{O}$ granites and related rocks from the Seychelles. *Contributions to Mineralogy and Petrology* 143:366-376.

Harris C, Faure K, Diamond RE, Scheepers R (1997). Oxygen and hydrogen isotope geochemistry of S- and I-type granitoids: the Cape Granite suite, South Africa. *Chemical Geology* 143:95–114.

Harris C and Vogeli J (2010). Oxygen isotope compositions of garnet in the peninsula granite, Cape Granite Suite, South Africa: constraints on melting and emplacement mechanisms. *South African Journal of Geology* 113(4):385-396.

Hawkesworth CJ and Kemp AIS (2006). Using hafnium and oxygen isotopes in zircons to unravel the record of crustal evolution. *Chemical Geology* 226:144-162.

Hawkesworth C, Dhuime B, Pietranik AB, Cawood PA, Kemp AIS, Storey CD (2010). The generation and evolution of the continental crust. *Journal of the Geological Society*, 167(2):229-248.

Hawkesworth C, Cawood P, Kemp T, Storey C, Dhuime, B (2009). Geochemistry: A matter of preservation. *Science*, 323:49-50.

Horstwood MSA, Košler J, Gehrels G, Jackson SE et al (2016). Community-Derived Standards for LA-ICP-MS U-(Th-)Pb Geochronology – Uncertainty Propagation, Age Interpretation and Data Reporting. *Geostandards and Geoanalytical Research* 40(3):311-332.

Howarth GH, Moore AE, Harris C, van der Meer QHA, le Roux P (2019). Crustal versus mantle origin of carbonate xenoliths from Kimberley region kimberlites using C-O-Sr-Nd-Pb isotopes and trace element abundances. *Geochimica et Cosmochimica Acta* 266:258-273.

Huang Z, Liu C, Xiao H, Han R, Xu C, Li W, Zhong W (2002). Study on the carbonate ocelli-bearing lamprophyre dykes in the Ailaoshan gold deposit zone, Yunnan Province. *Science in China Series D: Earth Sciences* 45:494 <https://doi.org/10.1360/02yd9051>.

Jackson SE, Pearson NJ, Griffin WL, Belousova EA (2004). The application of laser ablation inductively coupled plasma mass spectrometry to in situ U-Pb zircon geochronology. *Chemical Geology* 211:47-69.

Jacob JB, Moyen JF, Fiannacca P, Laurent O, Bachmann O, Janoušek V, Farina F, Villaros A (2021). Crustal melting vs. fractionation of basaltic magmas: Part 2, attempting to quantify mantle and crustal contributions in granitoids. *Lithos* 402-403:106292.

Jagoutz OE et al (2009). Construction of the granitoid crust of an island arc part I: geochronological and geochemical constraints from the plutonic Kohistan (NW Pakistan). Contributions to Mineralogy and Petrology 158(6):739-755.

Janney PE, Le Roex P, Carlson RW (2005). Hafnium isotope and trace element contrains on the nature of mantle heterogeneity beneath the Central Southwest Indian Ridge (13°E to 47°E). Journal of Petrology 46(12): 2427-2464.

Janoušek V, Hanžl P, Svojtka M, et al. (2020). Ultrapotassic magmatism in the heyday of the Variscan Orogeny: the story of the Třebíč Pluton, the largest durbachitic bofy in the Bohemian Massif. International Journal of Earth Sciences 109:1767–1810.

Janoušek V and Holub FV (2007). The causal link between HP–HT metamorphism and ultrapotassic magmatism in collisional orogens: case study from the Moldanubian Zone of the Bohemian Massif. Proceedings of the Geologists' Association 118(1):75–86.

Janoušek V, Moyen JF, Martin H, Erban V, Farrow C (2016) Geochemical modelling of igneous processes—principles and recipes in R Language. Bringing the Power of R to a Geochemical Community. Springer-Verlag, Berlin, Heidelberg.

Jochum KP, Nohl U, Herwig K, Lammel E, Stoll B, Hofmann AW (2005a). GeoReM: A New Geochemical Database for Reference Materials and Isotopic Standards. Geostandards and Geoanalytical Research 29:333-338.

Jochum KP, Pfänder J, Woodhead, JD et al (2005b). MPI-DING glasses: New geological reference materials for in situ Pb isotope analysis. Geochemistry, Geophysics, Geosystems 6(10): doi:10.1029/2005GC000995.

Kemp AIS, Hawkesworth GL, Foster BA, Paterson JD, Woodhead JD, Hergt JM, Gray CM, Withehouse MJ (2007). Magmatic and Crustal Differentiation History of Granitic Rocks from H-O Isotopes in Zircon. Science 10.1126/science.1136154.

Korenaga J (2018). Crustal evolution and mantle dynamics through Earth history. Philosophical Transactions Royal Society A 376:20170408. <http://dx.doi.org/10.1098/rsta.2017.0408>.

Kröner U and Romer RL (2013). Two plates – many subduction zones: The Variscan orogeny reconsidered. Gondwana Research 24:298-329.

Lana C, Buick I, Stevens G, Rossouw R, De Wet William (2011). 3230-3200 Ma post-orogenic extension and mid-crustal magmatism along the southeastern margin of the Barberton Greenstone Belt, South Africa. Journal of Structural Geology 33(5):844-858.

Lardeaux JM, Ledru P, Daniel I, Duchene S (2001). The Variscan French Massif Central – a new addition to the ultra-high pressure metamorphic ‘club’: exhumation processes and geodynamic consequences. Tectonophysics 332:143-167.

Lardeaux JM et al. (2014). The Moldanubian Zone in the French Massif Central, Vosges/Schwarzwald and Bohemian Massif revisited: differences and similarities. In: K. Schulmann, J.R. Martinez Catalan, J.M. Lardeaux, V. Janousek and G. Oggiano (Editors), The Variscan Orogeny: Extent, Timescale and the Formation of the European Crust. Special publications. Geological Society, London.

Laurent O (2012). Les changements géodynamiques à la transition Archéen-Protérozoïque: étude des granitoïdes de la marge Nord du craton du Kaapvaal (Afrique du Sud). PhD thesis, Université Blaise Pascal, Clermont-Ferrand.

Laurent O, Rapopo M, Stevens G, Moyen JF, Martin H, Doucelance R, Bosq C (2014). Contrasting petrogenesis of Mg-K and Fe-K granitoids and implications for postcollisional magmatism: case study from the late-Archaean Matok pluton (Pietersburg block, South Africa). *Lithos* 196-197:131-149.

Laurent O, Couzinié S, Zeh A, Vanderhaeghe O, Moyen JF, Villaros A, Gardien V, Chelle-Michou C (2017). Protracted, coeval crust and mantle melting during Variscan late-orogenic evolution: U-Pb dating in the eastern French Massif Central. *Int J Earth Sci (Geol Rundsch)* 106:421–451.

Ledru P, Courrioux G, Dallain C, Lardeaux JM, Montel JM, Vanderhaeghe O, Vitel G (2001). The Velay dome (French Massif Central): melt generation and granite emplacement during orogenic evolution. *Tectonophysics*, 342(3-4): 207-237.

Lowenstern JB (2000). A review of the contrasting behavior of two magmatic volatiles: chlorine and carbon dioxide. *Journal of Geochemical Exploration* 69-70:287-290.

Mallik A, Nelson J, Dasgupta R (2015). Partial melting of fertile peridotite fluxed by hydrous rhyolitic melt at 2–3 GPa: implications for mantle wedge hybridization by sediment melt and generation of ultrapotassic magmas in convergent margins. *Contributions to Mineralogy and Petrology* 168:48.

Martin AM, Médard E, Righter K, Lanzotti A (2017). Intraplate mantle oxidation by volatile rich silicic magmas. *Lithos* 292-293:320-333.

Matte P (1991). Accretionary history and crustal evolution of the Variscan belt in Western Europe. *Tectonophysics* 196:309-337.

Matte P (2001). The Variscan collage and orogeny (480 - 290 Ma) and the tectonic definition of the Armorica microplate: a review. *Terra Nova*, 13(2) :122-128.

Mattinson JM (2010). Analysis of the relative decay constants of ^{235}U and ^{238}U by multi-step CA-TIMS measurements of closed-system natural zircon samples. *Chemical Geology* 275(3-4):186-198.

McDonough WF and Sun SS (1995). The composition of Earth. *Chemical Geology* 120:223-253.

Melleton J, Cocherie A, Faure M, Rossi P (2010). Precambrian protoliths and Early Paleozoic magmatism in the French Massif Central: U-Pb data and the North Gondwana connection in the west European Variscan belt. *Gondwana Research* 17(1):13-25.

Michon G (1987). Les vaugnérites de l'Est du Massif central français: apport de l'analyse statistique multivariée à l'étude géochimique des éléments majeurs. *Bulletin de la Société Géologique de France* 8:591-600.

Mitchell RH, Bergman SC (1991). Petrology of Lamproites. Plenum, New York, 447 pp.
Morel, M.L.A., Nebel, O., Nebel-Jacobsen, Y.J., Miller, J.S., Vroon, P.Z. 2008. Hafnium isotope characterization of the Gj-1 zircon reference material by solution and laserablation MC-ICPMS. *Chemical Geology* 255, 231-235.

Moyen J.F, Janoušek V, Laurent O, Bachmann O, Jacob FB, Farina F, Fiannacca P, Villaros A (2021). Crustal melting vs. fractionation of basaltic magmas: Part 1, granites and paradigms. *Lithos* 402-403:106291.

Moyen JF, Laurent O, Chelle-Michou C, Couzinie S, Vanderhaeghe O, Zeh. A, Villaros S, Gardien V (2017). Collision vs. subduction-related magmatism: Two contrasting ways of granite formation and implications for crustal growth. *Lithos* 277:154-177.

Mühlber M, Stevens G, Moyen JF, Kisters AFM, Lana C (2021). Thermal evolution of the Stolzburg Block, Barbeton granitid-greenstone terrain, South Africa: Implications for Paleoarchean tectonic processes. *Precambrian Research* 359:106082.

Naeraa T, Schersten A, Rosing MT, Kemp AIS, Hoffmann JE, Kokfelt TF et al. (2012). Hafnium isotope evidence for a transition in the dynamics of continental growth 3.2 Gyr ago. *Nature* 485:627–630. doi: 10.1038/nature11140.

Najoui K, Leyreloup AF, Monié P (2000). Conditions et âges 40Ar/39Ar de mise en place des granitoïdes de la zone externe sud du Massif central français: Exemple des granodiorites de St-Guiral et du Liron (Cévennes, France). *Bulletin de la Société Géologique de France* 171:495– 510.

Nasdala L, Hofmeister W, Norberg N et al (2008). Zircon M257 – a homogeneous natural reference material of the ion microprobe U-Pb analysis of zircon. *Geostandards and Geoanalytical Research* 32(3):247-265.

Ni H and Keppler H (2013). Carbon in silicate melts. *Reviews in Mineralogy and Geochemistry* 75:251-287.

Nosova AA, Sazonova LV, Kargin AV, Dubinina EO, Minervina EA (2021). Mineralogy and Geochemistry of Ocelli in the Damtjernite Dykes and Sills, Chadobets Uplift, Siberian Craton: Evidence of the Fluid Lamprophyric Magma Interaction. *Minerals* 11(7):724 <https://doi.org/10.3390/min11070724>.

Ódri A, Harris C, Le Roux P (2020). The role of crustal contamination in the petrogenesis of nepheline syenite to granite magmas in the Ditrău Complex, Romania: evidence from

O-, Nd-, Sr- and Pb-isotopes. Contributions to Mineralogy and Petrology 175:100
<https://doi.org/10.1007/s00410-020-01738-5>.

Orejana D, Villaseca C, Kristoffersen M (2020). Geochemistry and geochronology of mafic rocks from the Spanish Central System: Constrains on the mantle evolution beneath central Spain. Geoscience Frontiers 11:1651-1667.

Pandey A, Chalapathi Rao NV, Chakrabarti R, Pandit D, Pankaj P, Kumar A, Sahoo S (2017). Petrogenesis of a Mesoproterozoic shoshonitic lamprophyre dyke from the Wajrakarur kimberlite field, southern India: Geochemical and Sr-Nd isotopic evidence for a modified sub-continental lithospheric mantle source. Lithos 292–293:218–233.

Patchett PJ, Tatsumoto M (1981). A routine high-precision method for Lu-Hf isotope geochemistry and chronology. Contributions to Mineralogy and Petrology 75:263-267.

Paton C, Hellstrom J, Paul B, Woodhead J, Hergt J (2011). Iolite: Freeware for the visualisation and processing of mass spectrometric data. Journal of Analytical Atomic Spectrometry <https://doi.org/10.1039/C1JA10172B>.

Pearce JA (2008). Geochemical fingerprinting of oceanic basalts with applications to ophiolite classification and the search for Archean oceanic crust. Lithos 100:14–48.

Peccerillo A (1999). Multiple mantle metasomatism in central-southern Italy: Geochemical effects, timing and geodynamic implications. Geology 27(4):315-318.

Pin C and Duthou J (1990). Sources of Hercynian granitoids from the French Massif Central: inferences from Nd isotopes and consequences for crustal evolution. Chemical Geology 83:281–296.

Pin C and Paquette JL (1997). A mantle-derived bimodal suite in the Hercynian Belt: Nd isotope and trace element evidence for a subduction-related rift origin of the Late Devonian Brévenne metavolcanics, Massif Central (France). Contributions to Mineralogy and Petrology 129:222–238.

Pin C and Paquette JL (2002). Sr-Nd isotope and trace element evidence for a Late Devonian active margin in northern Massif-Central (France). Geodin. Acta 15: 63–77.

Plank T and Langmuir CH (1998). The chemical composition of subducting sediment and its consequences for the crust and mantle. Chemical Geology 145:325-394.

Polat A and Münker C (2004). Hf-Nd isotope evidence for contemporaneous subduction processes in the source of late Archean arc lavas from the Superior Province, Canada. Chemical Geology 213:403-429.

Prelević D, Akal C, Foley SF, Romer RL, Stracke A, van Den Bogaard P (2012). Ultrapotassic mafic rocks as geochemical proxies for post-collisional dynamics of Orogenic Lithospheric Mantle: The case of Southwestern Anatolia, Turkey. Journal of Petrology 53 (5):1019-1055.

Regmi KR, Weinberg RF, Nicholls IA, Maas R, Raveggi M, (2016). Evidence for hybridisation in the Tynong Province granitoids, Lachlan Fold Belt, eastern Australia. Australian Journal of Earth Sciences 63(3):235-255.

Rock NMS (1991). Lamprophyres. Blackie and Son, Glasgow (255 pp).

Sabatier H (1991). Vaugnerites: special lamprophyre derived mafic enclaves in some Hercynian granites from Western and Central Europe. In: Didier J, Barbarin B (eds) Enclaves and Granite Petrology. Elsevier: Amsterdam, pp. 63-81.

Sabourdy G (1975). Apport de la géochimie à la connaissance de la pétrogenèse des granitoïdes des Cévennes méridionales, Massif central Français, PhD thesis, Univ. de Clermont-Ferrand, Clermont- Ferrand, France, 278 pp.

Safonov O, Butvina V, Limanov E (2019). Phlogopite-Forming Reactions as Indicators of Metasomatism in the Lithospheric Mantle. Minerals 9(11):685 <https://doi.org/10.3390/min9110685>.

Santos MM, Lana C, Scholz R, et al (2017). A new appraisal of Sri Lankan BB zircon as a reference material for LA-ICP-MS U-Pb geochronology and Lu-Hf isotope tracing. Geostandards and Geoanalytical Research, 41 (3), 335-358.

Scaillet B, Holtz F, Pichavant M (1997). Rheological properties of granitic magmas in their crystallization range. In: Bouchez JL, Hutton DHW, Stephens WE (eds) Granite: From Segregation of Melt to Emplacement Fabrics. Petrology and Structural Geology, 8, pp. 19, Springer, Dordrecht.

Scarow JH, Bea F, Montero P, Molina JF (2008). Shoshonites, vaugnerites and potassic lamprophyres: similarities and differences between 'ultra'-high-K rocks. Earth and Env. Science Trans. of the Royal Society of Edinburgh 99:159-175.

Scarow JH, Molina JF, Bea F, Montero P, Vaughan APM (2011). Lamprophyre dikes as tectonic markers of late orogenic transtension timing and kinematics: A case study from the Central Iberian Zone. Tectonics 30:TC4007.

Schannor M, Lana C, Fonseca MA (2019). São Francisco-Congo Craton break up delimited by U-Pb-Hf isotopes and trace-elements of zircon from metasediments of the Araçuaí Belt. Geoscience Frontiers 10:611-628.

Scholl DW and von Huene R (2009). Implications of estimated magmatic additions and recycling losses at the subduction zones of accretionary (non-collisional) and collisional (suturing) orogens. Geological Society, London, Special Publications 318(1):105-125.

Sabatier H (1991). Vaugnerites: special lamprophyre-derived mafic enclaves in some Hercynian granites from Western and Central Europe. In: Didier, J.P., Barbarin, B. (eds) Enclaves and Granite Petrology. Elsevier 13:63-81.

Serra-Varela S, Heredia N, Otamendi J, Giacosa R (2021). Petrology and geochronology of the San Martín de los Andes batholith: Insights into Devonian magmatism of the North Patagonia Andes. *Journal of South America Earth Sciences* 109:103283.

Shand SJ (1943). Eruptive Rocks. Their Genesis, Composition, Classification, and Their Relation to Ore-Deposits with a Chapter on Meteorite. John Wiley & Sons, New-York.

Shaw A, Downes H, Thirlwall M (1993). The quartz-diorites of Limousin: elemental and isotopic evidence for Devono-Carboniferous subduction in the Hercynian belt of the French Massif Central. *Chemical Geology* 107:1-18.

Sláma J, Kosler J, Condon DJ et al (2008). Plesovice zircon - a new natural reference material for U-Pb and Hf isotopic microanalysis. *Chemical Geology* 249:1-35.

Smith EI, Sánchez A, Walker JD, Wang K (1999). Geochemistry of mafic magmas in the Hurricane volcanic field, Utah: implications for small- and large- scale chemical variability of the lithospheric mantle. *The Journal of Geology* 107:433–448.

Soder CG and Romer RL (2018). Post-collisional Potassic–Ultrapotassic Magmatism of the Variscan Orogen: Implications for Mantle Metasomatism during Continental Subduction. *Journal of Petrology* 59(6):1007-1034.

Söderlund U, Patchett PJ, Vervoort JD, Isachsen CE (2004). The ^{176}Lu decay constant determined by Lu-Hf and U-Pb isotope systematics of Precambrian mafic intrusions. *Earth and Planetary Science Letters* 219:311-324.

Solgadi F, Moyen JF, Vanderhaeghe O, Sawyer EW, Reisberg L (2007). The relative roles of crustal anatexis and mantle-derived magmas: Generation of Synorogenic, Hercynian granites in the Livradois area, French Massif Central. *Canadian Mineralogist* 45:581-606.

Solomatova N, Manning CE, Lin JF, Mao WL (2020). Carbon Speciation and Solubility in Silicate Melts. In: Manning, C.E., Lin, J.F., Mao, W.L. (eds) Carbon in Earth's Interior. *Journal of Geophysical Research: Solid Earth*, 126(2). <https://doi.org/10.1002/9781119508229.ch16>.

Spandler C and Pirard C (2013). Element recycling from subducting slabs to arc crust: a review. *Lithos*, 170-171:208-223.

Spencer CJ, Cavosie AJ, Raub TD et al (2017). Evidence for melting mud in Earth's mantle from extreme oxygen isotope signatures in zircon. *Geology* 45 (11):975–978. doi: <https://doi.org/10.1130/G39402.1>.

Spencer CJ, Cawood PA, Hawkesworth CJ, Prave AR, Roberts NMW, Horstwood MSA, Whitehouse MJ, EIMF (2015). Generation and preservation of continental crust in the Grenville Orogeny. *Geoscience Frontiers* 6 (3):357-372.

Stern CR (2011). Subduction erosion: rates, mechanisms, and its role in arc magmatism and the evolution of the continental crust and mantle. *Gondwana Research* 20(2):284-308.

Storck JC, Laurent O, Karakas O, Wotzlaw JF, Galli A, Sinigoi S, Bachmann O, Chelle-Michou C (2021). Mantle versus crustal contributions in crustal-scale magmatic systems (Sesia Magmatic System, northern Italy) from coupling Hf isotopes and numerical modelling. *Contributions to Mineralogy and Petrology* 176:95.

Stracke A (2012). Earth's heterogeneous mantle: A product of convection-driven interaction between crust and mantle. *Chemical Geology* 330-331:274-299.

Su HM, Jiang SY, Zhang DY, Wu XK (2017). Partial Melting of Subducted Sediments Produced Early Mesozoic Calc-alkaline Lamprophyres from Northern Guangxi Province, South China. *Scientific Reports* 7:4864 DOI:10.1038/s41598-017-05228-w.

Sun JF, Yang JH, Wu FY, Li XH, Yang YH, Xie LW, Wilde SA (2010). Magma mixing controlling the origin of the Early Cretaceous Fangshan granitic pluton, North China Craton: in situ U-Pb age and Sr-,Nd-,Hf-and O-isotope evidence. *Gondwana Research* 120:421–438.

Tabaud AS, Janoušek V, Skrzypek E, Schulmann K, Rossi P, Whitechurch W, Guerrot C, Paquette JL (2014). Chronology, petrogenesis and heat sources for successive Carboniferous magmatic events in the Southern-Central Variscan Vosges Mts (NE France). *Journal of the Geological Society* 172:87-102.

Talbot JY, Chen Y, Faure M (2005). A magnetic fabric study of the Aigoual–Saint Guiral–Liron granite pluton (French Massif Central) and relationships with its associated dikes. *Journal of Geophysical Research* 110:B121106.

Tanaka T, Togashi S, Kamioka H et al. (2000) JNdI-1: a neodymium isotopic reference in consistency with LaJolla neodymium. *Chemical Geology* 168:279–281.

Tang M, Wang XL, Shu XJ, Wang D, Yang T, Gopon P (2014). Hafnium isotopic heterogeneity in zircons from granitic rocks: Geochemical evaluation and modeling of “zircon effect” in crustal anatexis. *Earth and Planetary Science Letters* 389:188-199.

Tappe S, Smart K, Torsvik T, Massuyseau M, Wit M (2018). Geodynamics of kimberlites on a cooling Earth: Clues to plate tectonic evolution and deep volatile cycles. *Earth and Planetary Science Letters* 484:1-14.

Taylor HP and Sheppard SMF (1986). Igneous rocks: I. Processes of isotopic fractionation and isotope systematics, in *Stable Isotopes in High Temperature Geological Processes*, edited by J. W. Valley, H. P. Taylor and J. R. O'Neil, p. 227-271, Mineral. Soc. Am., Washington.

Thibault Y, Edgar AD, Lloyd FE (1992). Experimental investigation of melts from a carbonated phlogopite Iherzolite: implications for metasomatism in the continental lithospheric mantle. *Am. Mineral.* 77:784–794.

Tsuno K and Dasgupta R (2012). The effect of carbonates on near-solidus melting of pelite at 3 GPa: Relative efficiency of H₂O and CO₂ subduction. *Earth and Planetary Science Letters* 319-320:185–196.

Turpin L, Velde D, Pinte G (1988). Geochemical comparison between minettes and kersantites from the Western European Hercynian orogen: Trace element and Pb-Sr-Nd isotope constraints on their origin. *Earth and Planetary Science Letters* 87(1/2):73-86.

Van Achterbergh E, Ryan CG, Jackson SE, Griffin WL (2001). Data reduction software for LA-ICP-MS. In: Sylvester, P.J. (ed.), *Laser Ablation-ICP Mass Spectrometry in the Earth Sciences: Principles and Applications*. Mineralogical Association of Canada, Short Course, Ottawa, Ontario 29:239-243.

Vanderhaeghe O, Laurent O, Gardien V, Moyen JF, Gébelin A, Chelle-Michou C, Couzinié S, Villaros A, Bellanger M (2020). Flow of partially molten crust controlling construction, growth and collapse of the Variscan orogenic belt: the geologic record of the French Massif Central. *BSGF Earth Sciences Bulletin*, Société géologique de France 191, pp.25.

Vermeesch P (2018). IsoplotR: a free and open toolbox for geochronology. *Geoscience Frontiers* 9:1479-1493.

Vervoort J. D., Blichert-Toft J., Patchett P. J. and Albarède F. (1999) Relationships between Lu-Hf and Sm-Nd isotopic systems in the global sedimentary system. *Earth and Planetary Science Letters* 168:79–99.

Vervoort JD, Plank T, Prytulak J (2011). The Hf–Nd isotopic composition of marine sediments. *Geochimica et Cosmochimica Acta* 75:5903-5926.

Vichi G, Stoppa F, Wall F (2005). The carbonate fraction in carbonatitic Italian lamprophyres. *Lithos* 85:154-170.

Villaros A, Buick IS, Stevens G (2012). Isotopic variations in S-type granites: an inheritance from a heterogeneous source? *Contributions to Mineralogy and Petrology* 163:243-257.

Villaros A, Laurent O, Couzinié S, Moyen JF, Mintrone M (2018). Plutons and domes: the consequences of anatexic magma extraction – example from the south-eastern French Massif Central. *Int. J. Earth Sci.* 107:2819–2842.

von Raumer JF, Finger F, Vesela P, Stampfli GM (2014). Durbanchites-Vaugnerites – a geodynamic marker in the central European Variscan orogen. *Terra Nova* 26:85-95.

Wang D, Guo J, Romer RL, Liu F, Ouyang D (2021). Coeval shoshonitic and calc-alkaline mantle-derived magmatism in an ancient continental arc root. Contributions to Mineralogy and Petrology <https://doi.org/10.1007/s00410-021-01812-6>.

Warr LN (2021). IMA-CNMNC approved mineral symbols. Mineralogical Magazine 85:291-320.

Whitney DL, Hamelin C, Teyssier C, Raia NH, Korchinski MS, Seaton NCA, Bagley BC, von der Handt A, Roger F, Rey PF (2020). Deep crustal source of gneiss dome revealed by eclogite in migmatite (Montagne Noire, French Massif Central). Journal of Metamorphic Geology 38:297-327.

Wiedenbeck M, Allé P, Corfu F, Griffin WL, Meier M, Oberli F, von Quadt A, Roddick JC, Spiegel W (1995). Three natural zircon standards for U-Th-Pb, Lu-Hf, trace element and REE analyses. Geostandards Newsletter 19(1):1-23.

Williamson BJ, Downes H, Thirlwall MF (1992). The Relationship between Crustal Magmatic Underplating and Granite Genesis - an Example from the Velay Granite. Transactions of the Royal Society of Edinburgh-Earth Sciences 83:235-245.

Williamson B, Downes H, Thirlwall M, Beard A (1997). Geochemical constraints on restite composition and unmixing in the Velay anatetic granite, French Massif Central. Lithos 40(2–4):295–319.

Woodhead JD, Herdt JM (2005). A preliminary appraisal of seven natural zircon reference materials for in situ Hf isotope determination. Geostandards and Geoanalytical Research 29(2):183-195.

Workman RK and Hart SR (2005). Major and trace element composition of the depleted MORB mantle (DMM). Earth and Planetary Science Letters 231:53-72.

Yang JH, Wu FY, Wilde SA, Xie LW, Yang YH, Liu XM (2007). Tracing magma mixing in granite genesis: in situ U-Pb dating and Hf-isotope analysis of zircons. Contribution to Mineralogy and Petrology 153:177-190.

Yang WB, Niu HC, Shan Q, Chen HY, Hollings P, Li NB, Yan S, Zartman RE (2014). Geochemistry of primary-carbonate bearing K-rich igneous rocks in the Awulale Mountains, western Tianshan: Implications for carbon-recycling in subduction zone. Geochimica et Cosmochimica Acta 143:143–164.

Yu ZF, Peng QM, Zhao Z, Wang PA, Xia Y, Wang YQ, Wang H (2020). Geochronology, Geochemistry, and Geodynamic Relationship of the Mafic Dykes and Granites in the Quianlishan Complex, South China. Minerals 10:1069.

Chapter III

1. Summary of findings and general discussion

Composite lamprophyre to granite dykes in the northern extremity of the post-Variscan Aigoual pluton records an example of mantle and crust interaction in the post-collisional site. In the field, lamprophyres and granites display gradational contact with decametric variation between the two end members. Occasionally, lamprophyres and granites form independent dykes mutually intrusive. Lamprophyres display typical panidiomorphic texture with euhedral phenocrysts of mica and also display phenocrysts of plagioclase, K-feldspar and quartz. According to mineral chemistry analysis, mica composition varies from biotite to phlogopite and the positive correlation between FeO^t vs. Al_2O_3 and TiO_2 vs. Al_2O_3 shows that lamprophyres can be classified as a minette, i.e. calc-alkaline lamprophyres. Granites have variable porphyritic textures with extreme average crystal size variations between the phenocrysts and the matrix in most examples. In general, the porphyritic textures display phenocrysts and megacrysts (up to 5 cm) of plagioclase and K-feldspar and phenocrysts of quartz, biotite and \pm clinopyroxene in a fine to medium grained matrix composed by quartz, K-feldspar and plagioclase.

Geochronology data display $^{206}\text{Pb}/^{238}\text{U}$ ages between 313 ± 3.0 Ma and 311 ± 2.9 for dyke 5 and 10, respectively and 312 ± 3.1 Ma and 313 ± 3.18 Ma for localization 12 on the eastern border of Aigoual pluton and central Aigoual pluton, respectively. The dykes and Aigoual pluton have the same age within uncertainties.

Lamprophyres are metaluminous to slightly peraluminous and have high content of mantle-derived compatible elements such Cr, Ni, Fe and Mg and also high content in incompatible elements like K_2O , Ba, Pb, Sr. Furthermore, lamprophyres display crustal-like signatures in both radiogenic (Sr, Nd, Hf whole-rock and zircon) and stable (O in quartz) isotopic systems. This dual geochemical signature is typical of melting of an enriched mantle metasomatized by melts or fluids derived from sediments. Simple mixing calculation using isotopes displays that mixing between 20 – 35% of sediments with mantle explains the isotopic signatures of lamprophyres. Moreover, 10 – 20% of partial melting in the spinel-Iherzolite field from this enriched mantle source explains trace

elements signatures from lamprophyres. Oxygen isotopes indicate that the contaminant might have pelitic composition.

Granites from composite dykes are high K₂O with shoshonitic affinity, peraluminous and show similar isotopic compositions than lamprophyres. The lack of clear correlation between isotopes and absence of single trends in Harker plots rather than parallel evolution in most of the major and trace elements suggest the two rock types did not evolve from the same parental magma by fractional crystallization. Petrological evidence such as zircon xenocrysts in granites, quartz xenocrysts rimmed by amphibole and carbonate favour for a mixing between lamprophyres and crustal-derived magmas at crustal conditions. However, the lack in typical crustal-derived magmas (i.e. muscovite-cordierite – bearing peraluminous granite) and the similar isotopic compositions between granites and lamprophyres point that mixing within different and contrasting magmas do not play an important role in the granite petrogenesis. Rather, a minimal (at least physically) crustal assimilation might have occurred at the emplacement level.

Due to the co-magmatic relation and very similar isotopic signatures, lamprophyres and granites might be generated by similar processes from partial melting of different portions of metasomatized mantle or partial melting of the same metasomatized mantle at different temperatures. Moreover, recent experimental studies mixing peridotite and sediment reach high SiO₂ contents (> 67%) (Förster et al. 2020, 2021) with compositions of major and trace elements matching with those in this work from granites and lamprophyres, this is an unusual explanation for the genesis of granites.

The available data does not allow to establish a single model to the petrogenesis of granites. Despite the hypotheses presented above seems not mutually exclusive, both lamprophyres and granites display evidences of influence of new mantle-derived material and crustal recycling in different ways in their petrogenesis.

Subduction process is an important mechanism for exchanging elements between mantle and crust. Part of the elements introduced to the mantle during subduction are carried to great depths and are part of a deep-Earth recycling process (e.g. Smith et al. 2021; Tappe et al. 2020). Nonetheless, part of the crustal elements introduced to the mantle are re-incorporated to the crust in post-collisional magmatism. This process occurs shortly after (between 50 and 100 Ma) of the subduction period and controls the budget

of incompatible elements and isotopic signatures in post-collisional mafic rocks (Couzinié et al. 2016; Zhao et al. 2013).

In the case of FMC reported in this study, ca. 20 – 35% of crust incorporated into the mantle was responsible for the crustal isotopic signatures and the budget of LILE, Hf, Nd, Sr, K₂O. A simple sketch illustrates the geochemical cycle between crustal elements introduced to the mantle via subduction and subsequently re-incorporation to the crust in mafic (and its derivatives) post-collisional magmatism (Figure III 1). The addition of new magma representing new crust addition is marked by the compatible elements contents such Cr, Ni, Fe and Mg (Figure III 1). Couzinié (2018) demonstrated the new crust formed in this process is more basic, mafic and K-rich than the initial continental material introduced to the mantle during prior subduction.

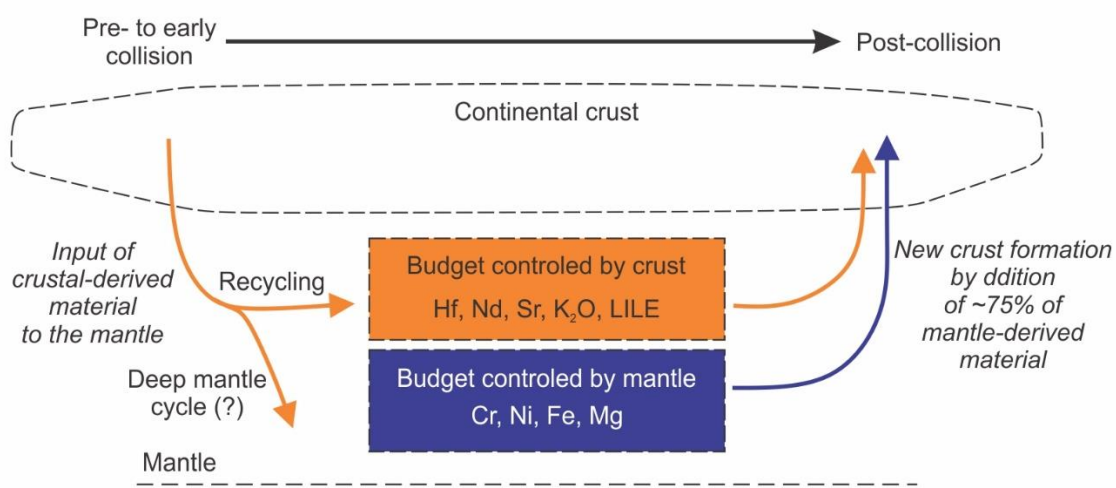


Figure III 1 Simple sketch showing the mantle and crust influence in the composition of post-collisional magmatism. Modified from Couzinié (2018).

Although buried by radiogenic and stable isotopic point of view, the post-collisional K-Mg rich mafic rocks represent a new addition of the crust. The mantle-derived material is evidenced by the mafic character and the high contents of compatible elements that ultimately came from the mantle.

The role of the granitic magmas in the crustal growth ratios is more ambiguous and problematic (e.g. Jacob et al. 2021; Moyen et al. 2021 and references therein). Some

authors argue that most of the continental crust was extracted from the mantle before ~3 Ga (Dhuime et al. 2012; Hawkesworth et al. 2019) with the formation of TTG rocks and represent the major period of crustal growth on Earth. Therefore, since Archean times, granites mostly correspond of reworking of previous continental crust either by melting of pre-existing igneous rocks in the crust or melting of metasediments (e.g. Armstrong 1991; Belousova et al. 2010). These processes correspond to crustal reworking and do not represent addition of new crust.

On the other hand, crustal growth might be a continuous process during Phanerozoic mostly identified in granitoids from arc sites (e.g. Western North America – Lee et al. 2007, Andes – Mišković and Shaltegger 2009; Gangdese belt, south Tibet – Ji et al. 2009). In these sites, granites can mostly be generated by melting from mafic and intermediate rocks shortly after added to the crust via magmatism or tectonic accretionary processes and represent new addition of crust. Granites directly derived from the mantle are rare. As examples we can cite plagiogranites in mid-oceanic ridges and ophiolites (e.g. Arena et al. 2016; El-Dien et al. 2021; Grimes et al. 2011) as products of a late-stage fractional crystallization of a basaltic magma or partial melting of a pre-existing mafic crust and granites derived through fractional crystallization from mafic and intermediate rocks in arcs (e.g. Castro et al. 2013, 2014; Müntener and Ulmer 2018). All examples cited above display mantle-like isotopic signatures (e.g. Chen and Arakawa 2005; Jagoutz et al. 2009; Wang et al. 2016).

This study records a further possibility of addition of crust through granitic magmatism, where a highly metasomatized mantle generates lamprophyres and also play an important role in the petrogenesis of granites from composite dykes. Since the isotopic signatures are undistinguishable from purely crust-derived rocks, the markers to identify this type of crustal growth in post-collisional sites are the intrinsic relation with lamprophyres and/or high K-Mg mafic rocks and more specifically, the high content of Cr and Ni related to granites derived from crust.

In the case of FMC reported in this study, lamprophyres and other high K-Mg mantle-derived rocks represent a minor part in terms of outcrop and thus do not represent a considerable addition of new mantle-derived material. However, taking as example granites from composite dykes and Aigoual pluton with similar petrogenesis, i.e. direct

mantle influence, the addition of new mantle-derived material becomes more significant. High K-Mg mantle-derived rocks (vaugnerites) and KCG granites represent about 35% of the outcrop surface of granites in FMC. Geochemical modelling display between 65 – 80% of the material came from the mantle. Combining these results with the outcrop pattern, between 22 – 28% of the magmatic material in FMC came from the mantle and thus represented crustal growth.

The findings impact in the long-term crustal growth throughout the geological time, where the mantle-derived rocks in post-collisional setting might be misinterpreted if just looking at the isotopic signatures instead the whole petrogenesis. This is further intensified when zircon, a mineral widely used in the study of crustal evolution, also can be misinterpreted with its isotopic signatures masked by the crustal budget into the mantle.

This thesis contribute for the petrogenesis of lamprophyres and granites in composite dykes from northern termination of post-Variscan Aigoual pluton and helps in the understanding of the mechanisms that control crustal growth through mantle and crust interactions in post-collisional sites.

2. Conclusions

The conclusions of this study can be summarized as follows:

- 1) Lamprophyres and granites are co-magmatic and coeval with the emplacement of Aigoual pluton (between 311 and 313 Ma);
- 2) Lamprophyres display high content of compatible (Cr, Ni, Fe, Mg) and incompatible elements (LILE, K₂O, Ba, Pb, Sr) and crustal-like signatures in both radiogenic and stable isotopic systems. Partial melting and mixing modelling suggest this dual geochemical signature results from 10 – 20% of partial melting in the spinel-Iherzolite stability field of a source composed by mixing between 20 – 35% of sediments and 65 – 80% peridotite;
- 3) Granites display trace elements and isotopic signatures alike lamprophyres and have a mantle-derived component involved in their petrogenesis. The intimate relation (physically and geochemically) between lamprophyre and granite in a system of composite dykes of northern Aigoual pluton provide constraints about the mantle contribution in the granites from FMC;

- 4) Although the isotopic signatures being broadly controlled by the crustal component in the mantle, approximately 70% of the material comes from the mantle and thus corresponds new crust formation;
- 5) Lamprophyres and granites from composite dykes represent significant addition of new crust in a post-collisional setting.

3. References

- Arena KR, Hartmann LA, Lana C (2016). Evolution of Neoproterozoic ophiolites from the southern Brasiliiano Orogen revealed by zircon U-Pb-Hf isotopes and geochemistry. *Precambrian Research* 285:299-314.
- Armstrong RL (1991). The persistent myth of crustal growth. *Australian Journal of Earth Sciences* 38:613-630.
- Belousova EA, Kostitsyn YA, Griffin WL, Begg GC, O'Reilly SYO, Pearson NJ (2010). The growth of the continental crust: constraints from zircon Hf-isotope data. *Lithos*, 119(3-4):457-466.
- Castro A (2014). The off-crust origin of granite batholiths. *Geoscience Frontiers* 5(1):63-75.
- Castro A, Vogt K, Geya T (2013). Generation of new continental crust by sublithospheric silicic-magma relamination in arcs: A test of Taylor's andesite model. *Gondwana Research* 23(4):1554-1566.
- Chen B and Arakawa Y (2005). Elemental and Nd-Sr isotopic geochemistry of granitoids from the West Junggar foldbelt (NW China), with implications for Phanerozoic continental growth. *Geochimica et Cosmochimica Acta* 69(5), 1307-1320.
- Couzinié S, Laurent O, Moyen JF, Zeh A, Bouilhol P, Villaros A (2016). Post-collisional magmatism: Crustal growth not identified by zircon Hf-O isotopes. *Earth and Planetary Science Letters* 456:182-195.
- Couzinié S (2018). Evolution of the continental crust and significance of the zircon record, a case study from the French Massif Central. PhD thesis, Stellenbosch University and Saint-Etienne University. 436 pp.
- Dhuime B, Hawkesworth CJ, Caroow PA, Storey CD (2012). A change in the geodynamics of continental growth 3 billion years ago. *Science* 335:60-74.
- El Dien HM, Li ZX, Anbar MA, Doucet LS, Murphy, JB, Evans NJ, Xia, XP, Li, J (2021). The largest plagiogranite on Earth formed by re-melting of juvenile proto-continental crust. *Communications Earth and Environment* 2(138) <https://doi.org/10.1038/s43247-021-00205-8>.
- Förster MW, Buhre S, Xu B, Prelević D, Mertz-Kraus R, Foley SF (2020). Two-stage origin of K-enrichment in ultrapotassic magmatism simulated by melting of experimentally metasomatized mantle. *Minerals* 10(1):41. <https://doi.org/10.3390/min10010041>.
- Förster MW, Bussweiler Y, Prelević D, Dackzo NR, Buhre S, Mertz-Kraus R, Foley SF (2021). Sediment-peridotite reaction controls fore-arc metasomatism and arc magma

geochemical signature. Geosciences, 11(9):372
<https://doi.org/10.3390/geosciences11090372>.

Grimes CB, Ushikubo T, John BE, Valley JW (2011). Uniformly mantle-like $\delta^{18}\text{O}$ in zircons from oceanic plagiogranites and gabbros. Contributions to Mineralogy and Petrology 161:13-33.

Hawkesworth C, Cawood PA, Dhuime B (2019). Rates of generation and growth of the continental crust. Geoscience Frontiers 10(1), 165-173.

Jacob JB, Moyen JF, Fiannacca P, Laurent O, Bachmann O, Janoušek V, Farina F, Villaros A (2021). Crustal melting vs. fractionation of basaltic magmas: Part 2, attempting to quantify mantle and crustal contributions in granitoids. Lithos 402-403:106292.

Jagoutz OE et al (2009). Construction of the granitoid crust of an island arc part I: geochronological and geochemical constraints from the plutonic Kohistan (NW Pakistan). Contributions to Mineralogy and Petrology 158(6):739-755.

Ji WQ, Wu FY, Chung SL, Li JX, Liu CZ (2009). Zircon U-Pb geochronology and Hf isotopic constrains on petrogenesis of the Gangdese batholith, southern Tibet. Chemical Geology 262:229-245.

Lee CTA, Morton DM, Kistler W, Baird AK (2007). Petrology and tectonics of Phanerozoic continent formation: from island arcs to accretion and continental arc magmatism. Earth and Planetary Science Letters, 263 (3-4):370-387.

Mišković A and Schaltegger U (2009). Crustal growth along a non-collisional cratonic margin: A Lu-Hf isotopic survey of the Eastern Cordilleran granitoids of Peru. Earth and Planetary Science Letters 279(3-4):303-315.

Moyen J.F, Janoušek V, Laurent O, Bachmann O, Jacob FB, Farina F, Fiannacca P, Villaros A (2021). Crustal melting vs. fractionation of basaltic magmas: Part 1, granites and paradigms. Lithos 402-403:106291.

Müntener O and Ulmer P (2018). Arc crust formation and differentiation constrained by experimental petrology. American Journal of Science 318:64-89.

Smith, E.M., Ni, P., Shirey, S.B., Richardson, S.H., Wang, W., Shahar, A. (2021). Heavy iron in large gem diamonds traces deep subduction of serpentinized ocean floor. Science Advances [DOI: 10.1126/sciadv.abe9773](https://doi.org/10.1126/sciadv.abe9773).

Tappe S, Stracke A, van Acken D, Strauss H, Luguet A (2020) Origins of kimberlites and carbonatites during continental collision – Insights beyond decoupled Nd-Hf isotopes. Earth-Science Review 208:103287.

Wang H, Wu YB, Gao S, Qin ZW, Hu ZC, Zheng JP, Yang SH (2016). Continental growth through accreted oceanic arc: zircon Hf-O isotope evidence for granitoids from the Qinling orogeny. Geochimica et Cosmochimica Acta 182:109-130.

Zhao ZF, Dai LQ, Zheng YF (2013). Postcollisional mafic igneous rocks record crust-mantle interaction during continental deep subduction. *Scientific Reports* 3:3413.

Supplementary Material

1. Introduction

Primary-magmatic carbonate in igneous rocks is an important component in the study of the carbon cycle between subduction slab, mantle and crust in orogenic systems (e.g. Vichi et al. 2005; Galvez and Pubellier 2019). Carbonates are commonly associated with lamprophyric rocks as a component of the groundmass, late veins, and pseudomorphs after a mafic phase (olivine, pyroxenes) and is also reported as ocelli or globules within the groundmass, possibly indicating two-phase liquid immiscibility (Rock 1991; Vichi et al. 2005).

In the Variscan belt of Western Europe, carbonates have been described in lamprophyres in the Iberian zone and Bohemian Massif, where they have been interpreted to represent alteration products of olivine and pyroxenes and also as ocellar structures possibly indicating immiscibility of liquids (Hrouda et al. 2016; Scarrow et al. 2011). The complex textural relations between carbonate and silicate phases as well as the significance of possible liquid immiscibility need to be further investigated, aiming at understanding whether the carbonate represents an integral part of the magmatic system or is related to later alteration.

Here we report textural forms of carbonate and the relation with co-genetic silicates in lamprophyric-granitic composite dykes in the northern border of post-Variscan Aigoual pluton, southern FMC. Calcite and dolomite were identified in three different textures: globular carbonate, interstitial carbonate in contact with euhedral quartz, feldspar and biotite and carbonate in association with biotite/phlogopite. Details about the textures and discussion about its significant are described below.

2. Textural evidence of magmatic carbonate

Petrography, BSE images and X-ray compositional maps indicate three main different textural forms of carbonate. 1) Globular, ocellar; 2) Interstitial in lamprophyre and 3) Carbonate associated with biotite/phlogopite in lamprophyre and granite.

The globules of carbonate vary from 1.6 mm to 200 µm in diameter and besides carbonate, they also contain very fine-grained K-feldspar (Figure S 1a). The matrix is

aphanitic, composed of quartz, plagioclase, biotite and chlorite. Plagioclase from the matrix displays an orientation tangential to the margins of the carbonate globules (Figure S 2e). Moreover, carbonate was observed involving corroded quartz xenocrysts which vary from 400 to 600 μm in size (Figure S 1b). BSE images and X-ray maps show high Ca and Mg contents for the carbonates indicating a dolomitic composition (Figure S 2b, c). The different textures of the plagioclase in the matrix and the K-feldspar within globules is clearly shown in the Na X-ray map (Figure S 2e). Inclusions of plagioclase inside the globular carbonate are identical in size and shape to the plagioclase in matrix (Figure S 2e).

Interstitial carbonate was observed in sample AG06A as an interstitial phase among euhedral quartz, plagioclase and biotite (Figure S 1c, d). The interstitial character of the carbonate relative to euhedral quartz, biotite and plagioclase crystals is well illustrated by the Si X-ray map (Figure S 3d). In the Na X-ray map, the plagioclase displays a normal magmatic zoning with increasing of Na content towards the rim (An_{44} to An_{15}) (Figure S 3e). The plagioclase zonation is also clear in the Si and Al X-ray maps (Figure S 3d and f, respectively), showing the coupled $\text{Na} + \text{Si} = \text{Ca} + \text{Al}$ substitution. The same plagioclase zonation is observed in portions of the sample devoid of interstitial carbonate. Biotite in contact with the carbonate is also of the same composition as biotite from portions where interstitial carbonate is absent.

The carbonate associated with biotite/phlogopite interpreted as pseudomorphing a high-temperature ferromagnesian phase was observed in both granitic and lamprophyric samples (Figure S 1e, f). Calcite-dolomite cores are rimmed by a mantle of blocky phlogopite and both replace a former phenocryst with rectangular habit (Figure S 4a), possibly pyroxene.

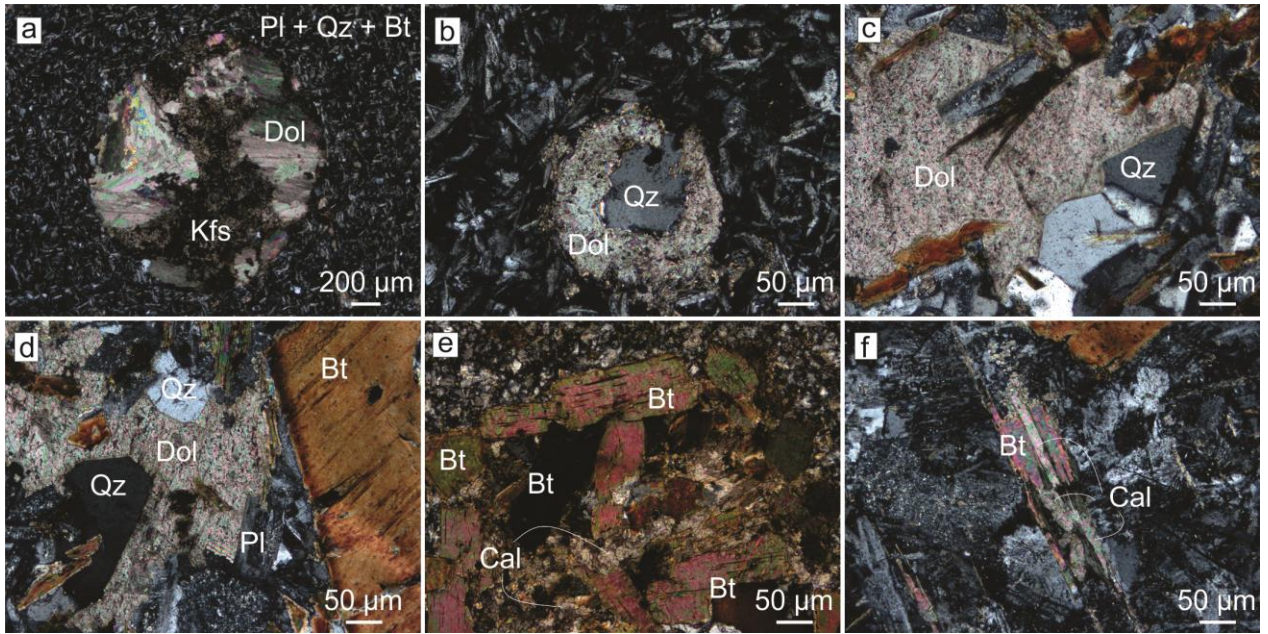


Figure S 1 Photomicrographs of different textures (cross-polarized light) (a) Ocellar – globules of dolomite and K-feldspar in a matrix with plagioclase, quartz and biotite. (b) Xenocrysts of quartz mantled by dolomite. (c) (d) Interstitial dolomite associated with euhedral quartz, biotite and plagioclase. (e) (f) Carbonate associated with biotite in granites.

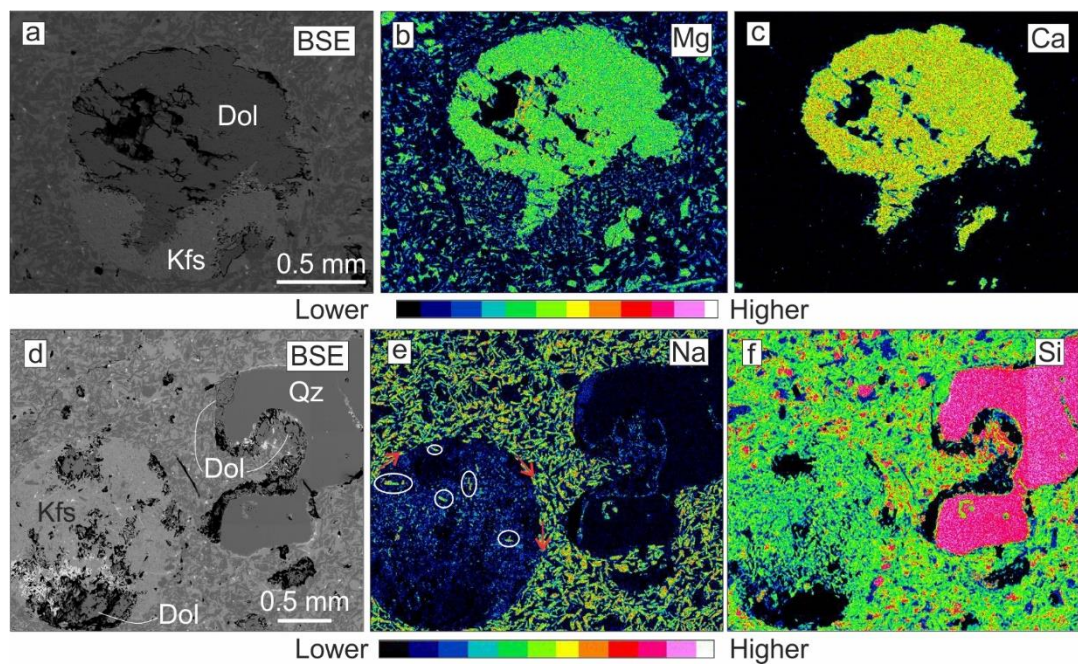


Figure S 2 BSE image and X-ray maps of ocellar dolomite.

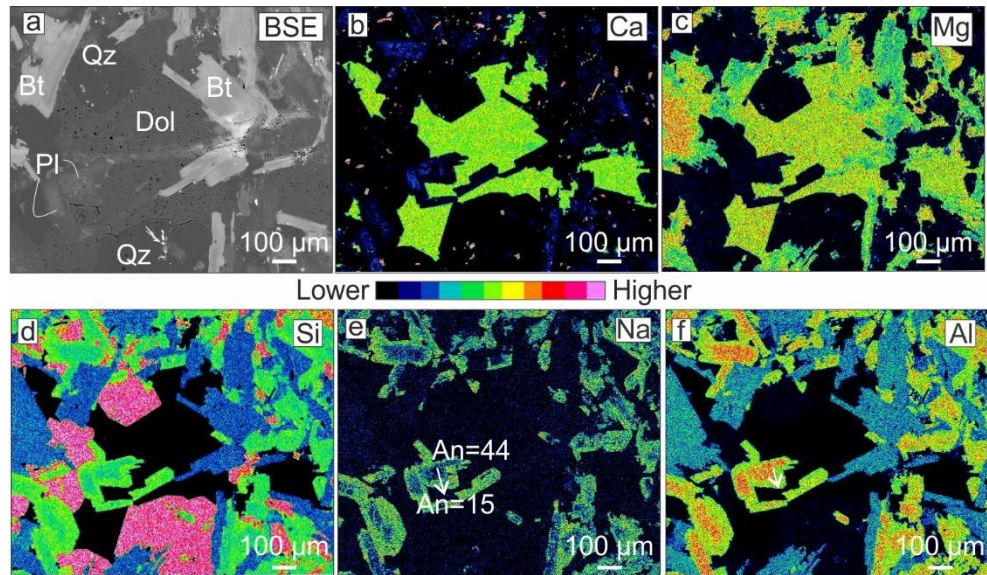


Figure S 3 BSE image and X-ray maps of interstitial carbonate.

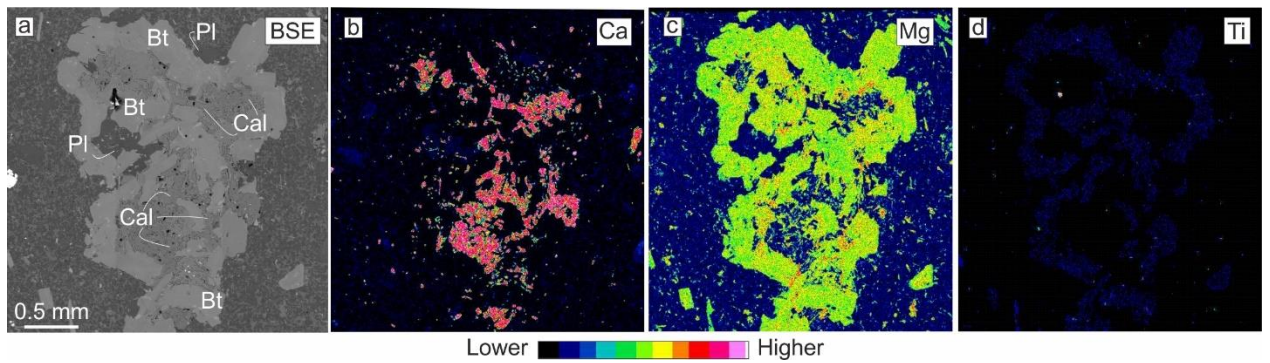


Figure S 4 BSE image and X-ray maps of the carbonate associated with biotite/phlogopite.

Carbonate in igneous rocks can be primary or secondary in origin. Here, primary carbonate is considered to be part of the magmatic system as an immiscible carbonate liquid or carbonate dissolved in the silicate liquid (e.g. Demény et al. 1994; Huang et al. 2002; Nosova et al. 2021; Yang et al. 2014). Secondary carbonate precipitated from a fluid that has interacted with the igneous rock after crystallization and was derived from some source other than the igneous rock result of subsolidus processes (Azbej et al. 2006). The information collected in this study indicates that ocellar, interstitial and carbonate associated with biotite/phlogopite reflect a magmatic origin. First, ocellar carbonate are commonly described in lamprophyres as the product of immiscibility between silicate and carbonate liquids (Huang et al. 2002; Nosova et al. 2021; Scarrow et al. 2011; Vichi et al. 2005). Alternatively, the ocellar texture has been interpreted as vugs filled by late stage fluids (Andronikov and Foley 2001; Azbej et al. 2006; Rock 1991).

The alignment of the plagioclase microphenocrysts with the external margin of the ocelli indicates clearly that the ocelli formed in the magma state. In addition, the existence of plagioclase within the carbonate ocelli, that are compositionally identical to the plagioclase microphenocrysts in the matrix, indicate that the ocelli represent a magmatic structure that captured plagioclase crystals from coexisting silicate magma (e.g. Yang et al. 2014). Furthermore, the association with microcrysts of K-feldspar present in all globules may indicate a K_2CO_3 component in the immiscible carbonate melt and its reaction with the silicate magma to form K-feldspar (e.g. Arefiev et al. 2019).

In the case of the interstitial carbonate, the euhedral quartz and plagioclase crystals in contact with the carbonate could represent crystals grown into fluid-filled vugs, with the carbonate representing a secondary, post magmatic infilling. This is unlikely due to the fact that the plagioclase crystals are unaltered and retain normal igneous zonation (Figure S 3e). The presence of euhedral biotite/phlogopite with high TiO_2 and low to moderate Cr_2O_3 contents together with interstitial carbonate is also taken as an evidence of crystallization at high temperature. Biotite/phlogopite crystals that appear almost completely suspended within carbonate are identical to biotite/phlogopite crystals unrelated to carbonate and these crystals show no sign of chlorite replacement, which may be unlikely if the carbonate bearing portions of the rock represented areas that interacted with a low temperature hydrothermal fluid.

The coarse-grained character of the blocky biotite/phlogopite crystals associated with carbonate and the existence of euhedral examples of phlogopite in the igneous matrix adjacent to the pseudomorphs is interpreted to reflect a magmatic origin of these crystals and the calcite in the cores of the pseudomorphs. These structures are interpreted to reflect carbonate and biotite/phlogopite replacement of pyroxene in response to increasing aCO_2 and aH_2O in the cooling and crystallizing magma (Blank and Brooker 1994; Solomatova et al. 2020; Tsuno and Dasgupta 2012).

3. C-O isotopes from carbonates

To try to constrain the source of carbon from carbonates we obtained C-O isotopic analysis in micro-drilled ocelli and powdered interstitial carbonate and in carbonate associated with biotite/phlogopite.

The $\delta^{13}\text{C}_{\text{PDB}}$ and $\delta^{18}\text{O}_{\text{SMOW}}$ values of all carbonates vary from -10.35 to -13.79‰ and +17.38 to +26.06‰ (n = 15), with average -11 and +23.23‰, respectively (Table S1, Figure S 5). A total of 12 individual ocelli was analysed, in some cases in triplicate. These were from a single sample (AG10B) taken from two cut slabs. The $\delta^{13}\text{C}$ and $\delta^{18}\text{O}$ values of ocelli carbonates have a narrow range from -10.6 ($\pm 0.25\text{\textperthousand}$, 1 σ) and -24.7 ($\pm 0.40\text{\textperthousand}$, 1 σ), respectively, including duplicates. There is no correlation between $\delta^{13}\text{C}$ and $\delta^{18}\text{O}$ in either the ocelli, or the carbonates as a whole (Figure S 5).

Carbon-oxygen isotopes of calcite and dolomite from composite dykes related to Aigoual pluton show low $\delta^{13}\text{C}$ values (-11‰; n = 15) and high $\delta^{18}\text{O}$ values, (+23.23‰, n = 15) on average, respectively. These values are substantially different from typical mantle carbonate values, where $\delta^{13}\text{C} \sim -5 \pm 2\text{\textperthousand}$ and $\delta^{18}\text{O} \sim +6$ to 9‰ (Deines 2002; Taylor 1986) (Figure S 5). The $\delta^{13}\text{C}$ values are consistent with an organic carbon component (~25‰; Sano and Marty 1995) mixed with mantle, and the high $\delta^{18}\text{O}$ values are typical of O-isotope exchange with external fluid at low temperature (Sharp 2017; Howarth et al. 2019). Assuming a magmatic origin for the ocelli, the organic component required to the lower the $\delta^{13}\text{C}$ values from -5 to -11‰ could have been derived from three distinct sources: 1) from subducted sedimentary organic material, as reported in eclogitic diamonds (Frezzotti et al. 2011; Li et al. 2019; Tumiati and Malaspina 2018) and carbonate veins form peridotite xenoliths (Ducea et al. 2005); 2) from assimilation of organic C-bearing rocks during emplacement of the dykes (e.g. black micaschists with graphite metapelites in Cévennes area; Faure et al. 2001); or 3) from low-T fluid carrying organic carbon from soil, calcrete (e.g. Pandit et al. 2002; Potts et al. 2009) and speleothems (e.g. Chauvet-Pont-d'Arc cave ~90km NE of Mt Aigoual, France; Genti 2012).

Despite the three different textures being consistent with a magmatic origin for carbonates, the C-O isotope data do not provide firm constraints and is inconclusive. The high $\delta^{18}\text{O}$ values for the ocelli are consistent with low-temperature equilibration with surface fluids; $\delta^{13}\text{C}$ values of ~-11‰ probably reflect a mantle source of C with a

component of reduced C derived from subducted sediments, graphite-bearing country rock or low-T fluid infiltration.

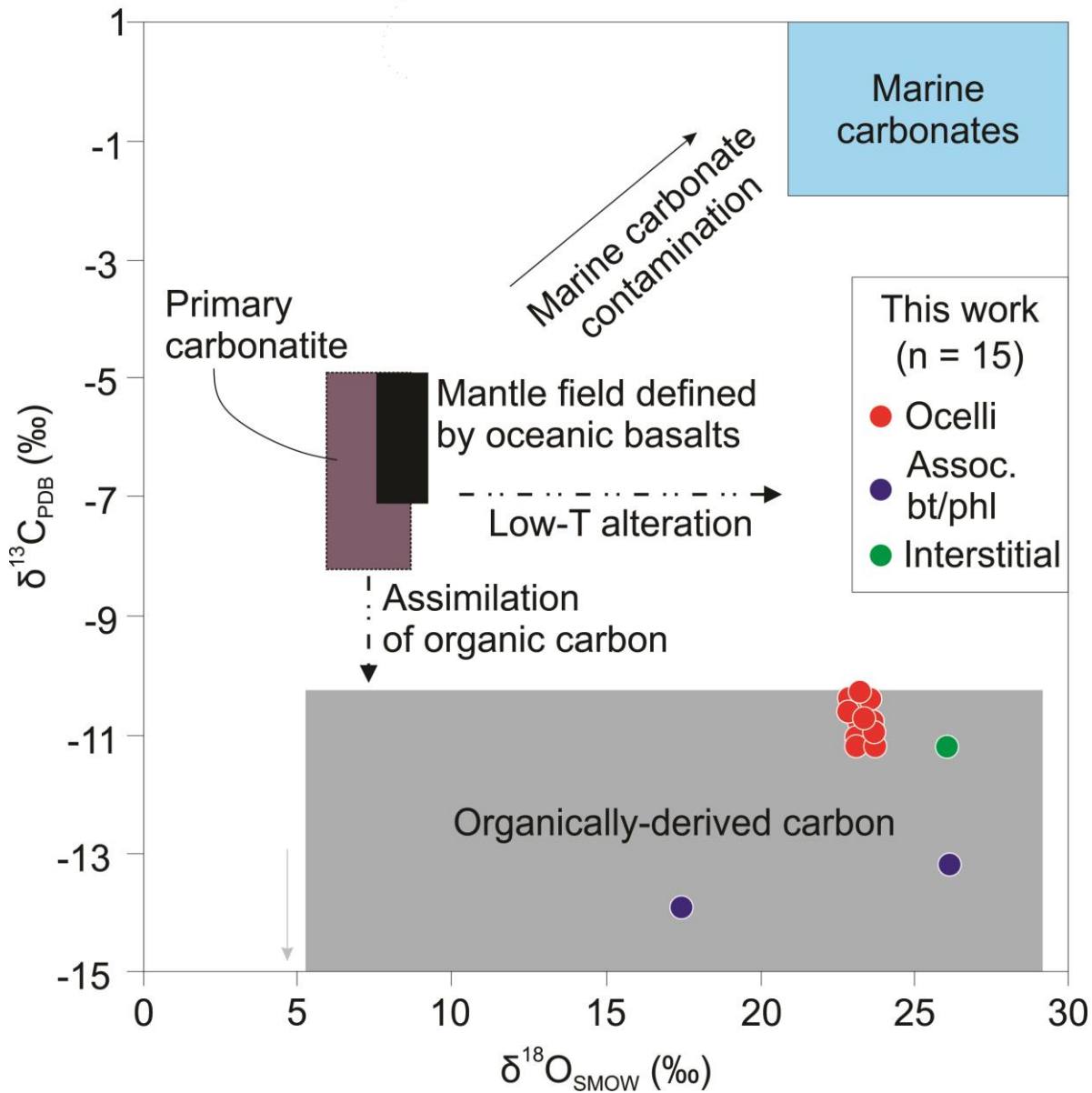


Figure S 5 Oxygen and carbon isotopic compositions of different carbonates from lamprophyric-granite composite dykes, northern Aigoual pluton, FMC. C-O isotope ratios from ocelli dolomite were measured in pure carbonate whereas carbonate associated with biotite/phlogopite and interstitial were analyzed in powdered samples and include different textural forms.

Primary carbonatites field from Taylor et al. (1967) and mantle field defined by oceanic basalts from Bell and Simonetti (2010). Field of marine carbonate is from Valley (1986) and organically-derived carbon from Longstaffe (1989) and Hu et al. (2017). Low-T alteration and assimilation of organic carbon vectors are from Howarth et al. (2019).

Table S1 1 C-O isotope data from carbonates.

Sample	Texture	Mineral	$\delta^{13}\text{C-PDB}$ (‰)	$\delta^{18}\text{O-SMOW}$ (‰)			
AG06D	assoc. bt/phl*	calcite	-13.79	17.38			
AG07	assoc. biot/phl*	dolomite	-13.15	26.06			
AG06A	interstitial	dolomite	-11.17	25.98	Duplicate analysis		
					$\delta^{13}\text{C}$	$\delta^{18}\text{O}$	% carb.
AG10B	Ocelli 01**	dolomite	-11.07	23.44	-11.14	23.34	97
					-11.05	23.50	97
					-11.03	23.48	97
AG10B	Ocelli 02**	dolomite	-10.35	23.02	-10.35	23.02	51
AG10B	Ocelli 03**	dolomite	-10.60	23.09	-10.65	23.10	73
					-10.55	23.08	73
AG10B	Ocelli 04**	dolomite	-10.64	23.66	-10.64	23.66	95
AG10B	Ocelli 05**	dolomite	-10.46	23.04	-10.46	23.04	73
AG10B	Ocelli 06**	dolomite	-10.40	23.13	-10.48	23.04	62
					-10.32	23.22	62
AG10B	Ocelli 07**	dolomite	-10.43	23.22	-10.43	23.22	87
AG10B	Ocelli 08**	dolomite	-10.88	23.20	-10.88	23.20	87
AG10B	Ocelli 09**	dolomite	-10.45	23.54	-10.45	23.62	48
					-10.45	23.46	48
AG10B	Ocelli 10**	dolomite	-10.39	23.26	-10.35	23.34	65
					-10.42	23.18	65
AG10B	Ocelli 11**	dolomite	-10.44	23.01	-10.47	22.98	39
					-10.41	23.03	39
AG10B	Ocelli 12**	dolomite	-10.72	23.58	-10.77	23.70	92
					-10.65	23.58	92
					-10.73	23.47	92

*associated with biotite/phlogopite

**micro-drilled from slabs; $\delta^{13}\text{C-PDB}$ and $\delta^{18}\text{O-SMOW}$ values are average from duplicated in some cases triplicated analysis.

4. References

- Andronikov AV, Foley SF (2001). Trace element and Nd–Sr isotopic composition of ultramafic lamprophyres from the East Antarctic Beaver Lake area. *Chemical Geology* 175:291-305.
- Arefiev AV, Shatskiy A, Podborodnikov IV, Bekhtenova A, Litasov KD (2019). The System K_2CO_3 - $CaCO_3$ - $MgCO_3$ at 3 GPa: Implications for Carbonatite Melt Compositions in the Shallow Continental Lithosphere. *Minerals* 9(5):296.
- Azbej T, Szabó C, Bodar RJ, Dobosi G (2006). Genesis of carbonate aggregates in lamprophyres from the northeastern Transdanubian Central Range, Hungary: Magmatic or hydrothermal origin? *Mineralogy and Petrology* 88:479-497.
- Bell K and Simonetti A (2010). Source of parental melts to carbonatites-critical isotopic constraints. *Mineralogy and Petrology* 98:77–89.
- Blank JG and Brooker RA (1994). Experimental studies of carbon dioxide in silicate melts: Solubility, speciation, and stable carbon isotope behavior. In: Carroll, M.R., Holloway, J.R. (Eds.), Rev. in Mineral. 30, American Mineralogical Society, pp. 157-186.
- Deines P (2002). The carbon isotope geochemistry of mantle xenoliths. *Earth Sciences Review* 58:247-278.
- Demény A, Fóriz I, Molnár F (1994). Stable isotope and chemical compositions of carbonate ocelli and veins in Mesozoic lamprophyres of Hungary. *European Journal of Mineralogy* 6:679-690.
- Ducea MN, Saleeby J, Morrison J, Valencia VA (2005). Subducted carbonates, metasomatism of mantle wedges, and possible connections to diamond formation: an example from California. *American Mineralogist* 90:864-870.
- Faure M, Charonnat X, Chauvet A, Chen Y, Talbot JY, Martelet G, Courrioux G, Monié P, Milesi JP (2001). Tectonic evolution of the Cévennes para autochthonous domain of the Hercynian French Massif Central and its bearing on ore deposits formation. *Bulletin de la Societe Geologique de France* 172(6) :687-696.
- Frezzotti ML, Silverstone J, Sharp ZD, Compagnoni R (2011). Carbonate dissolution during subduction revealed by diamond-bearing rocks from the Alps. *Nature Geoscience*, 4:703–706.
- Galvez M, Pubellier M (2019). How do subduction zones regulate the carbon cycle? In: Orcutt, B., Daniel, I., Dasgupta, R., (eds) Deep Carbon: Past to Present. Cambridge: Cambridge University Press, pp. 276-312.

Genty D (2012). Les spéléothèmes de la grotte Chauvet-Pont-d'Arc: apports chronologiques et paléoclimatiques. Synthèse des travaux publiés. In: Collection EDYTEM. Cahiers de géographie, 13. Karsts, Paysages et Préhistoire. pp. 79-88.

Howarth GH, Moore AE, Harris C, van der Meer QHA, le Roux P (2019). Crustal versus mantle origin of carbonate xenoliths from Kimberley region kimberlites using C-O-Sr-Nd-Pb isotopes and trace element abundances. *Geochimica et Cosmochimica Acta* 266(1): 258-273.

Hrouda F, Verner K, Kubínová S, Buriánek D, Faryad SW, Chlupáčová M, Holub FV (2016). Magnetic fabric and emplacement of dykes of lamprophyres and related rocks of the Central Bohemian Dyke Swarm (Central European Variscides). *Journal of Geosciences* 61:335-354.

Huang Z, Liu C, Xiao H, Han R, Xu C, Li W, Zhong W (2002). Study on the carbonate ocelli-bearing lamprophyre dykes in the Ailaoshan gold deposit zone, Yunnan Province. *Science in China Series D: Earth Sciences* 45:494.

Hu R, Fu S, Huang Y, Zhou MF, Fu S, Zhao C, Wang Y, Bi X, Xiao J (2017). The giant South China Mesozoic low-temperature metallogenetic domain: Reviews and a new geodynamic model. *Journal of Asian Earth Sciences* 137:9-34.

Li K, Li L, Pearson DG, Stachel T (2019). Diamond isotope compositions indicate altered igneous oceanic crust dominates deep carbon recycling. *Earth and Planetary Sciences Letters* 516:190-201.

Longstaffe FJ (1989). Stable isotopes as tracers in clastic diagenesis. Short course in burial diagenesis. In: Hutcheon IE (eds) Mineral Association of Canada Short Course, pp 201–284.

Nosova AA, Sazonova LV, Kargin AV, Dubinina EO, Minervina EA (2021). Mineralogy and Geochemistry of Ocelli in the Damtjernite Dykes and Sills, Chadobets Uplift, Siberian Craton: Evidence of the Fluid Lamprophyric Magma Interaction. *Minerals* 11(7):724 <https://doi.org/10.3390/min11070724>

Pandit MK, Sial AN, Sukumaran GB, Pimentel MM, Ramasamy AK, Ferreira VP (2002). Depleted and enriched mantle sources for Paleo-and Neoproterozoic carbonatites of southern India: Sr, Nd, C–O isotopic and geochemical constraints. *Chemical Geology* 189:69–89.

Potts AJ, Midgley JJ, Harris C (2009). Stable isotope and ^{14}C study of biogenic calcrete in a termite mound, Western Cape, South Africa, and its palaeoenvironmental significance. *Quaternary Research* 72:258-264.

Rock NMS (1991). *Lamprophyres*. Blackie and Son, Glasgow.

Sano Y, Marty B (1995). Origin of carbon in fumarolic gas from island arcs. *Chemical Geology* 119:265– 274.

Scarrow JH, Molina JF, Bea F, Montero P, Vaughan APM (2011). Lamprophyre dikes as tectonic markers of late orogenic transtension timing and kinematics: A case study from the Central Iberian Zone. *Tectonics* 30:TC4007.

Sharp Z. (2017). Principles of Stable Isotope Geochemistry, 2nd Edition. doi: <https://doi.org/10.25844/h9q1-0p82>

Solomatova N, Manning CE, Lin JF, Mao WL (2020). Carbon Speciation and Solubility in Silicate Melts. In: Manning, C.E., Lin, J.F., Mao, W.L. (eds) Carbon in Earth's Interior. *Journal of Geophysical Research: Solid Earth*, 126(2). <https://doi.org/10.1002/9781119508229.ch16>

Spandler C and Pirard C (2013). Element recycling from subducting slabs to arc crust: a review. *Lithos* 170-171:208-223.

Taylor HP, Frechen J. and Degens ET (1967). Oxygen and carbon isotope studies of carbonatites from the Laacher See District, West Germany and the Alnö District, Sweden. *Geochimica et Cosmochimica Acta* 31:407–430.

Taylor BE, Bucher-Nurminen K. (1986). Oxygen and carbon isotope and cation geochemistry of metasomatic carbonates and fluids — Bergell aureole, Northern Italy. *Geochimica et Cosmochimica Acta* 50:1267–1279.

Tsunoo K, Dasgupta R (2012). The effect of carbonates on near-solidus melting of pelite at 3 GPa: Relative efficiency of H₂O and CO₂ subduction. *Earth and Planetary Science Letters* 319-320:185–196.

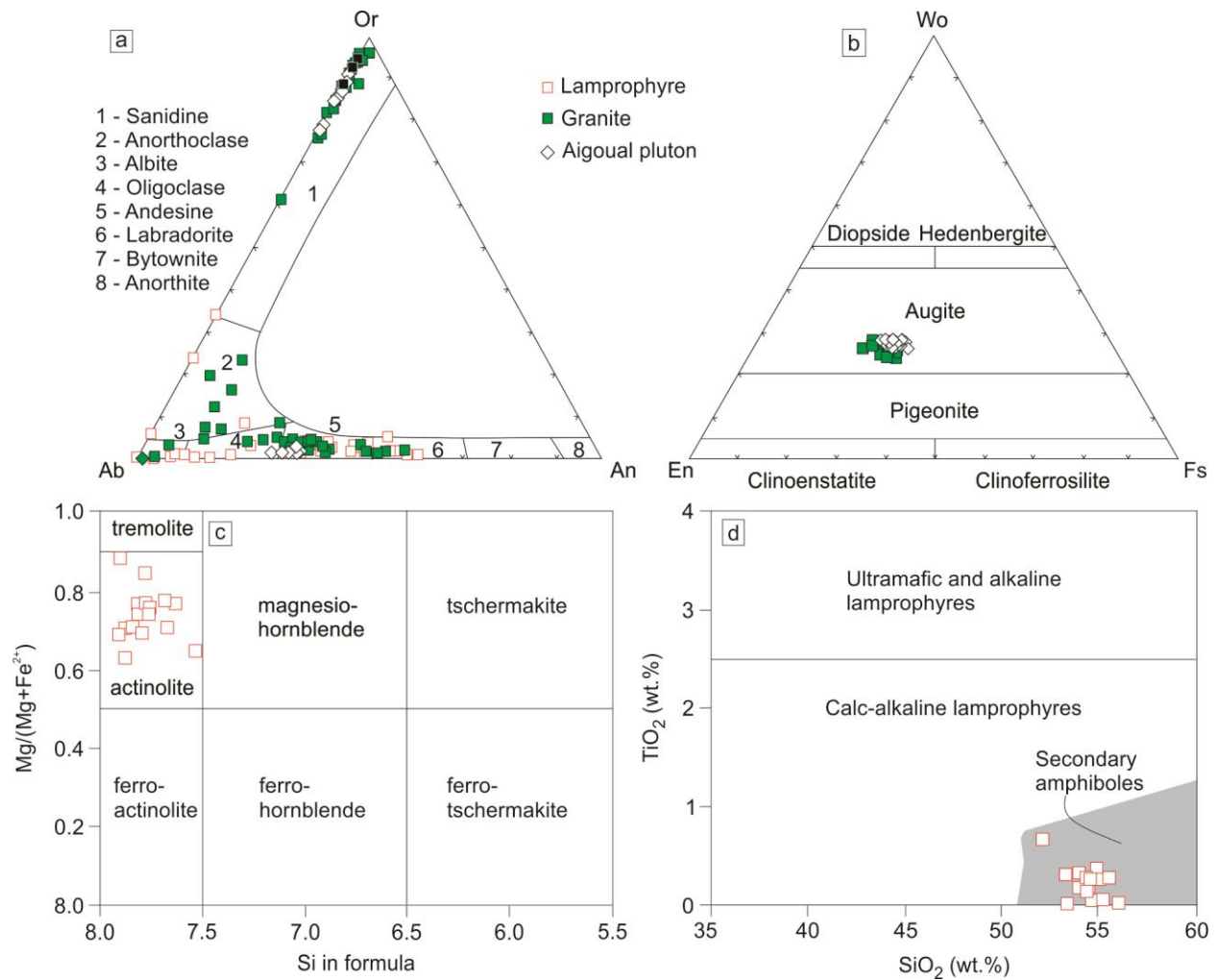
Tumiati S, Malaspina N (2018). Redox processes and the role of carbon-bearing volatiles from the slab–mantle interface to the mantle wedge. *Journal of Geological Society* 176(2):388 <http://dx.doi.org/10.1144/jgs2018-046>.

Valley JW (1986). Stable isotope geochemistry of metamorphic rocks. In: Valley, J.W., Taylor, H.P., O’Neil, J.R. (eds). *Stable isotopes in high temperature geological processes. Reviews in Mineralogy and Geochemistry* 16:445–489.

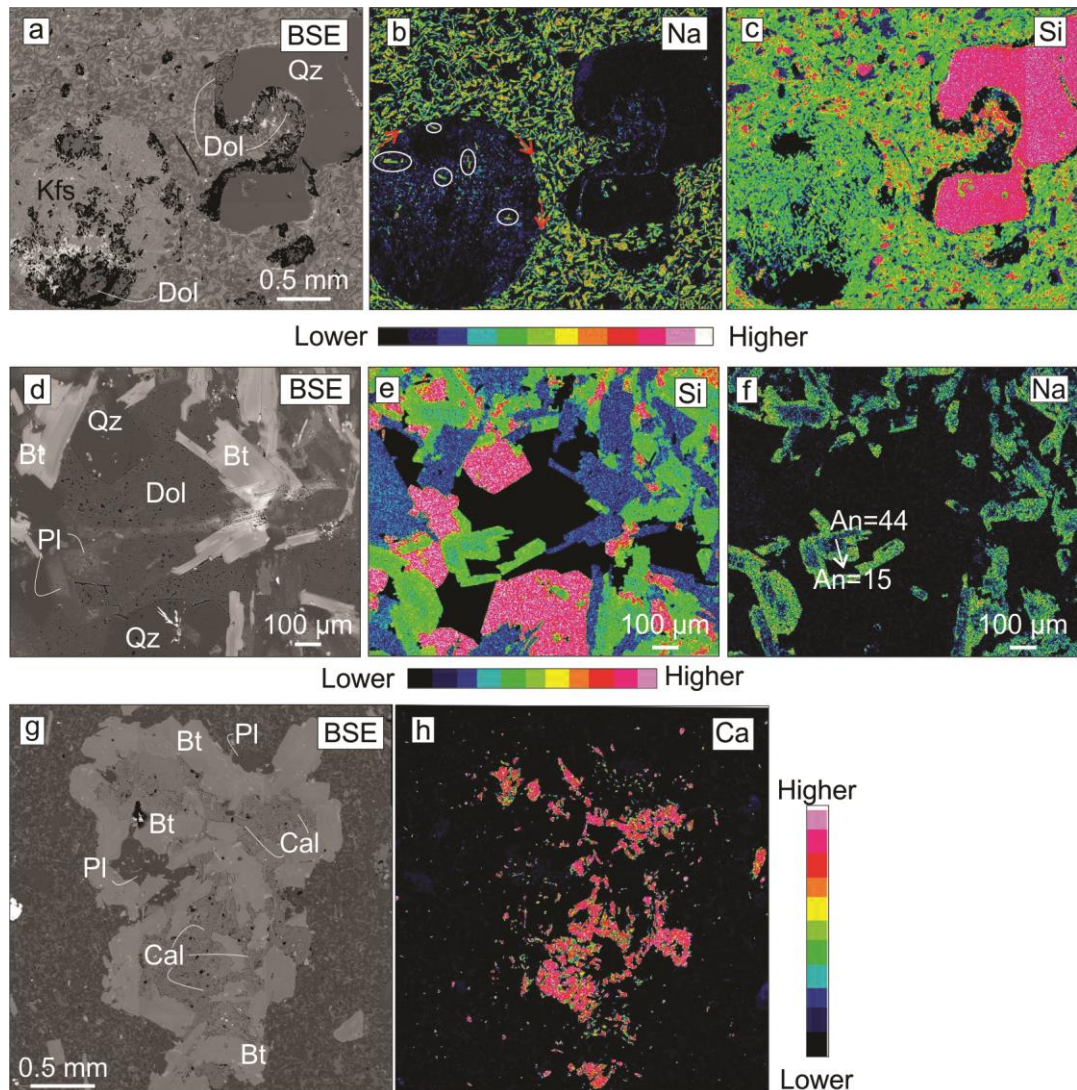
Vichi G, Stoppa F, Wall F (2005). The carbonate fraction in carbonatitic Italian lamprophyres. *Lithos* 85:154-170.

Yang WB, Niu HC, Shan Q, Chen HY, Hollings P, Li NB, Yan S, Zartman RE (2014). Geochemistry of primary-carbonate bearing K-rich igneous rocks in the Awulale Mountains, western Tianshan: Implications for carbon-recycling in subduction zone. *Geochimica et Cosmochimica Acta* 143:143–164.

Appendices



Appendice Figure 1 (a) Ternary diagram of classification of feldspars; (b) Ternary diagram of classification of pyroxene; (c) (d) Amphibole classification.



Appendice Figure 2 BSE images and X-ray maps of three different magmatic textures of carbonate.



Appendice Figure 3 Selected CL images of zircon from composite dykes and Aigoual pluton with U-Pb age and ϵ_{Hf} values.

Table 1 Sample name, coordinates and lithology

Sample	Coordinate		Lithology
	Latitude	Longitude	
AG01	44.0719	3.6743	Granite
AG01B	44.0719	3.6743	Granite
AG02A	44.1438	3.5638	Granite
AG02B	44.1438	3.5638	Granite
AG03	44.1725	3.5638	Granite
AG04A	44.1879	3.5801	Granite
AG04B	44.1879	3.5801	Granite
AG04C	44.1879	3.5801	Lamprophyre/monzonite
AG05A	44.1964	3.5889	Granite/quartz monzonite
AG05B	44.1964	3.5889	Granite/quartz monzonite
AG05C	44.1964	3.5889	Granite/quartz monzonite
AG05D	44.1964	3.5889	Granite/quartz monzonite
AG06A	44.2014	3.5900	Lamprophyre/monzonite
AG06B	44.2014	3.5900	Lamprophyre/monzonite
AG06C	44.2014	3.5900	Granite
AG06D	44.2014	3.5900	Quartz monzonite
AG06E	44.2014	3.5900	Quartz monzonite
AG06F	44.2014	3.5900	Quartz monzonite
AG07	44.2757	3.5880	Lamprophyre/monzonite
AG08A	44.1887	3.5943	Granite
AG08B	44.1887	3.5943	Granite
AG09	44.1828	3.6126	Lamprophyre/monzonite
AG10A	44.1752	3.6149	Lamprophyre/monzonite
AG10B	44.1752	3.6149	Lamprophyre/monzonite
AG10C	44.1752	3.6149	Granite
AG10D	44.1752	3.6149	Granite
AG10E	44.1752	3.6149	Quartz monzonite
AG12A	44.1666	3.6069	Quartz monzonite
AG12B	44.1666	3.6069	Lamprophyre/monzonite
AG14	44.1118	3.8616	Aigoual pluton – quartz monzonite

Table 2 Whole-rock major (wt.%) and trace (ppm) element compositions of composite dykes from Aigoual pluton, French Massif Central.

Sample	AG01	AG01(AG1)	AG01B	AG02A	AG02B	AG-03	AG04A	AG04C	AG05A	AG05B	AG05C	AG05D	AG06A	AG06B
SiO ₂	72.02	66.97	71.90	72.57	69.83	67.16	68.00	58.01	68.13	68.90	67.61	70.90	56.67	57.20
Al ₂ O ₃	13.63	15.69	13.98	14.38	14.45	15.37	14.72	14.31	14.90	14.13	15.24	14.76	14.92	15.56
CaO	0.65	0.88	1.43	0.71	1.54	2.18	2.32	4.15	1.82	1.63	1.82	0.97	3.25	3.69
Cr ₂ O ₃	b.d.	0.01	b.d.	b.d.	0.01	0.01	0.01	0.05	0.01	0.01	0.01	b.d.	0.06	0.04
Fe ₂ O ₃ (t)	3.46	5.06	2.67	2.31	3.21	3.80	3.48	7.20	3.76	3.46	3.51	2.98	6.98	6.52
K ₂ O	5.51	5.48	5.13	5.89	5.41	5.50	5.18	5.45	5.35	5.64	5.63	5.93	5.55	5.66
MgO	1.79	2.69	1.52	0.80	1.89	2.29	2.44	6.71	2.32	2.53	2.43	1.16	8.56	7.00
MnO	0.04	0.04	0.04	0.04	0.06	0.06	0.06	0.15	0.06	0.05	0.06	0.06	0.09	0.09
Na ₂ O	1.99	1.81	2.69	2.88	2.89	2.69	2.90	2.13	2.72	2.81	2.87	2.73	1.98	2.18
P ₂ O ₅	0.34	0.45	0.22	0.14	0.26	0.33	0.32	0.71	0.33	0.31	0.30	0.17	0.76	0.84
TiO ₂	0.58	0.91	0.40	0.28	0.45	0.62	0.58	1.12	0.60	0.53	0.52	0.33	1.16	1.22
Total	100	100	100	100	100	100	100	100	100	100	100	100	100	100
LOI	1.92	2.75	0.91	1.17	1.02	1.02	0.90	1.41	1.25	1.02	1.22	1.26	2.51	1.87
Mg#	50.55	51.23	53.02	40.59	53.80	54.41	58.11	64.87	54.98	59.22	57.83	43.57	70.84	68.04
Sc	9.6	14.5	11.1	9.0	8.5	12.1	24.1	9.8	11.5	10.6	11.2	11.6	19.8	20.1
V	56.0	84.4	51.2	23.4	41.8	61.4	160.7	52.0	64.6	27.9	58.2	56.9	128.7	130.4
Cr	67.3	108.5	80.9	30.4	54.3	98.0	433.3	87.6	82.6	53.9	97.3	118.6	398.0	313.2
Co	99.5	84.9	71.2	67.3	113.6	51.1	66.4	55.1	102.1	59.7	41.3	56.8	56.6	55.4
Ni	23.8	33.8	23.3	15.3	19.7	26.6	112.0	25.6	24.8	21.5	26.8	40.6	118.8	79.2
Cu	4.5	8.4	9.2	19.9	7.1	15.4	12.4	6.9	9.1	11.4	17.2	53.7	25.5	13.8
Zn	26.1	36.1	73.9	87.5	41.2	73.9	127.2	44.7	57.5	54.0	55.6	60.8	82.5	79.4
Rb	187.9	219.8	242.0	213.3	220.0	246.8	374.1	186.9	235.1	208.6	227.3	240.0	288.7	288.8
Sr	150.8	133.6	332.7	164.0	228.3	395.8	585.7	336.5	421.0	241.5	431.5	352.0	510.7	576.3
Y	30.8	48.9	28.4	21.8	21.7	24.4	41.0	22.0	24.8	32.0	25.0	28.4	27.5	29.3
Zr	274.0	393.2	235.9	198.0	186.3	279.8	510.5	235.8	284.8	272.0	234.7	269.0	321.0	342.7
Nb	20.8	33.3	18.5	20.3	15.2	18.7	26.6	15.2	18.9	20.8	16.5	19.9	21.4	22.8

AG06C	AG06D(1)	AG06D(2)	AG06E	AG06F	AG06X	AG07	AG08A	AG08b	AG09	AG10A	AG10B	AG10C	AG10D	AG10E
67.06	67.16	67.45	67.81	67.81	53.16	61.91	71.30	67.35	59.61	61.58	60.46	70.74	69.78	68.26
15.00	15.14	15.12	15.02	14.68	15.10	16.64	14.45	15.67	14.58	16.39	17.18	14.85	15.20	14.77
1.91	2.09	2.04	1.93	1.89	4.39	2.16	1.28	1.93	3.16	3.34	1.08	1.12	1.20	2.21
0.02	0.01	0.01	0.01	0.01	0.08	b.d.	b.d.	0.01	0.07	0.01	0.03	b.d.	b.d.	b.d.
3.69	3.67	3.57	3.72	3.68	8.54	5.79	2.65	3.17	6.81	5.27	5.89	2.37	2.96	3.60
5.58	5.42	5.43	5.25	5.65	5.11	5.14	5.68	6.32	4.76	5.55	4.08	5.84	5.03	5.17
2.95	2.49	2.48	2.40	2.54	9.84	4.03	1.16	1.83	7.40	3.58	6.21	1.54	1.93	2.05
0.07	0.06	0.06	0.06	0.06	0.19	0.08	0.04	0.05	0.12	0.10	0.10	0.03	0.04	0.06
2.72	3.06	2.93	2.91	2.78	1.63	2.78	2.91	2.86	1.90	2.74	4.19	2.92	3.14	2.97
0.39	0.34	0.33	0.32	0.34	0.75	0.49	0.18	0.28	0.59	0.56	0.16	0.21	0.26	0.32
0.61	0.57	0.57	0.56	0.56	1.21	0.97	0.36	0.52	1.00	0.88	0.62	0.38	0.47	0.58
100	100	100	100	100	100	100	100	100	100	100	100	100	100	100
2.10	2.68	1.04	1.29	1.44	5.87	4.09	1.41	0.89	4.06	1.42	4.32	1.48	1.66	2.46
61.26	57.34	57.89	56.05	57.80	69.53	57.98	46.31	53.36	68.28	57.37	67.62	56.26	56.31	53.00
12.0	11.4	11.3	11.8	11.5	23.1	16.2	9.0	9.9	18.5	14.2	15.9	7.5	8.7	10.6
66.6	59.7	60.5	60.7	61.1	164.1	106.1	31.2	54.4	123.7	97.1	98.6	35.9	47.4	59.2
140.7	98.3	99.4	94.5	110.9	572.9	74.8	43.7	71.3	479.1	98.7	203.3	43.3	51.4	74.2
51.8	83.1	68.3	70.5	44.2	48.6	37.7	78.9	65.6	53.2	44.2	39.0	114.3	92.4	128.4
35.7	27.6	27.1	25.6	28.3	148.9	23.8	14.7	20.9	131.2	36.6	108.5	17.8	18.5	23.1
10.6	11.1	10.9	6.5	11.4	34.9	17.0	7.4	13.1	13.5	6.1	24.9	3.1	5.3	14.4
60.4	47.5	49.3	51.5	47.6	98.1	75.2	50.4	46.6	109.4	86.4	236.7	22.8	39.2	45.5
214.1	229.5	232.0	226.0	257.5	234.7	152.3	214.4	235.3	237.4	239.7	205.5	213.5	196.6	231.3
419.0	440.2	491.2	438.0	475.6	375.9	421.5	262.5	480.0	460.3	631.1	227.7	262.5	314.3	376.8
24.5	25.1	25.3	26.2	24.9	28.1	28.1	25.9	22.6	26.5	25.8	28.4	19.0	21.2	25.5
271.8	263.9	265.2	259.4	266.9	288.5	346.6	239.6	243.6	325.6	329.6	141.4	186.5	224.1	258.2
17.4	17.6	17.3	17.7	17.2	17.6	19.5	18.8	16.3	19.3	18.7	8.0	15.4	16.6	18.4

AG12A	AG12B	AG14(1)	AG14(2)	AG14(3)
69.03	57.64	66.27	66.08	66.57
15.36	15.72	15.29	16.02	15.32
1.53	4.62	2.45	1.85	2.45
b.d.	0.04	0.01	0.01	0.01
2.89	6.50	4.17	3.49	4.02
5.63	5.08	5.25	6.55	5.11
1.69	6.23	2.70	2.32	2.63
0.04	0.10	0.07	0.06	0.06
3.11	2.45	2.80	2.77	2.84
0.25	0.61	0.37	0.31	0.37
0.47	1.00	0.63	0.53	0.63
100	100	100	100	100
1.13	1.65	0.94	1.08	1.00
53.63	65.52	56.24	56.83	56.47
8.8	18.2	12.0	10.4	11.8
45.7	125.7	67.6	57.3	66.1
49.8	263.3	100.1	80.2	91.8
61.7	55.7	86.8	89.7	88.4
17.0	111.9	27.7	23.5	25.0
10.3	22.1	12.3	7.9	7.2
69.9	82.6	60.2	50.9	59.2
225.2	187.7	234.0	247.4	226.8
355.5	566.7	458.6	510.1	465.3
23.3	24.2	26.3	21.8	24.8
230.8	341.2	292.1	247.4	287.1
16.6	19.0	19.4	16.0	18.7

b.d = below detection limit

Table 3 Mineral chemistry of biotite/phlogopite

Sample	12B lamp.	12B lamp.	12B lamp.	12B lamp.	12B lamp.	12B lamp.	12B lamp.	12B lamp.	12B lamp.	12B lamp.	12B lamp.	12B lamp.	12B lamp.	12B lamp.	12B lamp.	12B lamp.	
Spectrum	rim1	rim 2	10	11	12	13	14	15	16	17	18	19	20	21	22	23	24
Na ₂ O	0.23	0.37	0.23	0.37	0.32	0.27	0.25	0.29	0.30	0.38	0.00	0.29	0.21	0.21	0.24	0.00	0.45
MgO	10.06	9.88	11.30	10.74	12.46	12.42	9.80	9.54	10.06	11.16	12.28	11.79	12.46	9.89	9.72	9.57	11.04
Al ₂ O ₃	13.95	14.20	14.26	14.77	13.75	13.41	13.75	13.72	13.90	13.98	13.15	13.44	13.14	13.99	13.87	13.76	14.56
SiO ₂	35.53	35.42	36.53	35.55	37.85	37.73	34.40	34.16	34.76	34.42	36.45	36.62	37.43	34.73	34.50	34.91	35.90
K ₂ O	9.11	8.89	9.07	8.88	9.22	9.36	9.16	8.89	8.73	8.61	9.03	9.03	9.23	8.85	8.87	8.89	8.73
CaO	0.00	0.00	0.00	0.00	0.00	0.00	0.00	0.00	0.00	0.00	0.00	0.00	0.14	0.00	0.00	0.00	0.00
TiO ₂	8.10	8.22	4.96	5.09	4.08	4.18	7.52	7.94	8.21	8.31	4.08	4.20	4.00	7.74	7.86	7.82	7.85
Cr ₂ O ₃	0.00	0.00	0.00	0.00	0.00	0.00	0.00	0.00	0.00	0.14	0.00	0.17	0.00	0.00	0.00	0.00	0.00
MnO	0.39	0.18	0.19	0.27	0.26	0.22	0.31	0.31	0.27	0.16	0.23	0.30	0.23	0.30	0.29	0.24	0.22
FeO	19.56	19.61	19.86	19.97	18.35	18.27	19.28	19.08	18.44	16.12	17.22	18.58	18.04	18.89	18.77	18.83	17.69
Total	96.93	96.76	96.41	95.64	96.29	95.85	94.47	93.93	94.67	93.15	92.60	94.27	95.04	94.61	94.11	94.02	96.45
*	Structural formula based on 22O																
Na	0.07	0.11	0.07	0.11	0.09	0.08	0.07	0.09	0.09	0.11	0.00	0.09	0.06	0.06	0.07	0.00	0.13
K	1.76	1.71	1.75	1.73	1.77	1.80	1.82	1.77	1.71	1.70	1.80	1.78	1.79	1.74	1.76	1.76	1.67
Sum I	1.82	1.82	1.82	1.84	1.86	1.88	1.89	1.86	1.80	1.81	1.80	1.86	1.85	1.81	1.83	1.76	1.80
Mg	2.27	2.23	2.55	2.45	2.79	2.80	2.27	2.22	2.31	2.57	2.85	2.71	2.83	2.28	2.25	2.21	2.47
Fe	2.47	2.48	2.51	2.55	2.31	2.31	2.51	2.49	2.37	2.09	2.24	2.40	2.30	2.44	2.44	2.44	2.22
Cr	0.00	0.00	0.00	0.00	0.00	0.00	0.00	0.00	0.00	0.02	0.00	0.02	0.00	0.00	0.00	0.00	0.00
Ti	0.92	0.93	0.57	0.59	0.46	0.48	0.88	0.93	0.95	0.97	0.48	0.49	0.46	0.90	0.92	0.91	0.89
Al (vi)	-0.15	-0.12	0.07	0.10	0.12	0.08	-0.13	-0.14	-0.13	-0.12	0.10	0.09	0.06	-0.09	-0.10	-0.07	-0.05
Sum M	5.51	5.52	5.70	5.69	5.68	5.66	5.53	5.50	5.50	5.50	5.69	5.68	5.67	5.52	5.50	5.50	5.52
Al (iv)	2.63	2.65	2.47	2.56	2.31	2.30	2.65	2.67	2.65	2.67	2.32	2.36	2.30	2.64	2.64	2.58	2.62
Si	5.37	5.35	5.53	5.44	5.69	5.70	5.35	5.33	5.35	5.33	5.68	5.64	5.70	5.36	5.36	5.42	5.38
Sum T	8.00	8.00	8.00	8.00	8.00	8.00	8.00	8.00	8.00	8.00	8.00	8.00	8.00	8.00	8.00	8.00	8.00
Sum cations	15.33	15.34	15.52	15.53	15.53	15.55	15.42	15.36	15.31	15.32	15.49	15.54	15.52	15.33	15.33	15.26	15.32
Mg#	0.48	0.47	0.50	0.49	0.55	0.55	0.48	0.47	0.49	0.55	0.56	0.53	0.55	0.48	0.48	0.53	

12B lamp.																						
25	26	27	28	29	30	31	32	33	34	35	36	37	38	39	40	41	42	43				
0.46	0.25	0.29	0.25	0.24	0.43	0.31	0.34	0.30	0.20	0.22	0.22	0.24	0.23	0.22	0.22	0.23	0.16	0.22				
12.61	12.38	11.43	11.38	12.38	11.69	11.83	10.71	11.47	10.82	9.62	9.90	12.92	13.15	12.96	13.27	12.85	10.09	10.65				
14.66	13.57	13.96	13.26	13.46	14.32	14.20	14.12	14.06	14.13	14.07	13.66	13.63	13.63	13.49	13.68	13.48	13.81	14.33				
36.19	37.84	36.60	35.88	37.43	35.15	35.67	35.32	35.27	36.25	34.90	34.90	38.31	37.88	37.67	38.53	37.76	34.67	35.98				
8.68	9.27	8.94	9.02	9.36	8.71	8.75	8.76	8.77	9.43	8.94	8.52	9.26	9.27	9.17	9.34	9.35	8.90	9.20				
0.00	0.00	0.00	0.00	0.00	0.00	0.00	0.00	0.00	0.00	0.00	0.55	0.00	0.00	0.00	0.00	0.00	0.26	0.00				
8.33	3.91	4.43	4.30	3.85	8.14	7.36	8.20	7.64	6.01	7.58	7.83	4.06	3.71	3.80	3.72	3.93	7.70	6.88				
0.00	0.00	0.00	0.16	0.00	0.00	0.00	0.23	0.00	0.00	0.00	0.15	0.00	0.00	0.00	0.00	0.00	0.00	0.00				
0.00	0.24	0.16	0.30	0.16	0.20	0.14	0.00	0.25	0.24	0.27	0.26	0.15	0.00	0.27	0.19	0.19	0.20	0.15				
14.81	18.04	19.02	18.56	18.45	15.89	16.06	17.26	16.57	19.05	19.37	18.01	17.81	16.68	17.53	16.91	17.21	18.21	18.45				
95.74	95.51	94.83	93.10	95.32	94.51	94.32	94.96	94.33	96.14	94.97	94.00	96.38	94.54	95.11	95.86	95.00	93.99	95.87				
0.13	0.07	0.09	0.07	0.07	0.13	0.09	0.10	0.09	0.06	0.07	0.06	0.07	0.07	0.06	0.06	0.07	0.05	0.07				
1.65	1.79	1.75	1.80	1.82	1.69	1.70	1.70	1.71	1.83	1.76	1.68	1.76	1.79	1.77	1.78	1.81	1.76	1.78				
1.78	1.86	1.83	1.87	1.89	1.81	1.79	1.80	1.80	1.88	1.82	1.75	1.83	1.86	1.84	1.85	1.88	1.81	1.84				
2.79	2.79	2.61	2.66	2.81	2.65	2.68	2.43	2.61	2.45	2.21	2.28	2.88	2.97	2.93	2.96	2.90	2.33	2.41				
1.84	2.28	2.44	2.43	2.35	2.02	2.04	2.20	2.12	2.42	2.50	2.33	2.23	2.11	2.22	2.12	2.18	2.36	2.34				
0.00	0.00	0.00	0.02	0.00	0.00	0.00	0.03	0.00	0.00	0.00	0.02	0.00	0.00	0.00	0.00	0.00	0.00	0.00				
0.93	0.44	0.51	0.51	0.44	0.93	0.84	0.94	0.88	0.69	0.88	0.91	0.46	0.42	0.43	0.42	0.45	0.90	0.78				
-0.05	0.14	0.13	0.06	0.10	-0.09	-0.03	-0.09	-0.08	0.03	-0.07	-0.11	0.12	0.18	0.12	0.17	0.13	-0.10	0.01				
5.52	5.66	5.69	5.67	5.70	5.51	5.54	5.50	5.53	5.58	5.52	5.44	5.68	5.69	5.70	5.67	5.66	5.49	5.54				
2.62	2.28	2.39	2.38	2.31	2.66	2.57	2.62	2.61	2.50	2.62	2.60	2.28	2.26	2.29	2.24	2.28	2.62	2.55				
5.38	5.72	5.61	5.62	5.69	5.34	5.43	5.38	5.39	5.50	5.38	5.40	5.72	5.74	5.71	5.76	5.72	5.38	5.45				
8.00	8.00	8.00	8.00	8.00	8.00	8.00	8.00	8.00	8.00	8.00	8.00	8.00	8.00	8.00	8.00	8.00	8.00	8.00				
15.29	15.52	15.52	15.54	15.58	15.32	15.33	15.31	15.33	15.46	15.34	15.18	15.52	15.55	15.54	15.51	15.54	15.30	15.39				
0.60	0.55	0.52	0.52	0.54	0.57	0.57	0.53	0.55	0.50	0.47	0.49	0.56	0.58	0.57	0.58	0.57	0.50	0.51				

06X lamp.	5C granite	5C granite	5C granite	5C granite	5C granite											
12	13	14	15	16	17	18	19	20	21	22	10	14	20	36	39	48
0.40	0.47	0.22	0.25	0.23	0.00	0.00	0.00	0.00	0.21	0.27	0.27	0.18	0.21	0.39	0.24	0.00
18.50	18.94	17.36	14.97	13.66	12.52	11.91	10.07	14.66	13.53	16.97	11.45	11.73	11.56	12.06	11.81	11.65
14.91	14.87	14.83	14.12	14.12	14.30	14.53	14.59	14.48	13.92	14.49	12.90	12.93	12.72	13.04	13.31	13.17
38.41	38.95	38.16	37.13	37.21	37.22	35.92	35.28	37.87	37.49	38.61	37.17	37.66	36.72	37.60	38.08	37.40
9.51	9.40	9.34	9.29	9.34	9.40	9.55	9.21	9.61	9.27	9.10	9.39	9.50	9.44	9.32	9.44	9.55
0.00	0.00	0.00	0.00	0.00	0.45	0.00	0.00	0.00	0.00	0.00	0.00	0.00	0.00	0.00	0.00	0.00
5.78	5.74	5.72	5.39	5.36	5.35	6.01	6.45	5.42	5.63	5.10	3.44	3.50	3.39	3.44	3.35	3.40
0.33	0.26	0.31	0.00	0.26	0.00	0.00	0.00	0.00	0.17	0.00	0.00	0.00	0.15	0.00	0.14	0.00
0.00	0.00	0.15	0.14	0.00	0.22	0.31	0.25	0.22	0.25	0.00	0.26	0.21	0.19	0.27	0.32	0.35
8.51	8.53	9.49	13.56	15.95	17.56	17.63	20.25	14.31	16.46	12.03	18.81	18.41	18.57	18.34	19.12	19.44
96.35	97.16	95.58	94.84	96.32	97.42	95.87	96.10	96.57	96.94	96.58	93.69	94.12	92.94	94.45	95.82	95.37
0.11	0.13	0.06	0.07	0.07	0.00	0.00	0.00	0.00	0.06	0.08	0.08	0.05	0.06	0.12	0.07	0.00
1.74	1.70	1.73	1.77	1.78	1.79	1.84	1.79	1.80	1.75	1.68	1.86	1.87	1.89	1.82	1.83	1.87
1.85	1.83	1.79	1.84	1.84	1.79	1.84	1.79	1.80	1.81	1.76	1.94	1.92	1.95	1.94	1.90	1.87
3.96	4.01	3.76	3.33	3.04	2.78	2.69	2.29	3.21	2.99	3.66	2.65	2.69	2.70	2.76	2.67	2.67
1.02	1.01	1.15	1.69	1.99	2.19	2.23	2.59	1.76	2.04	1.46	2.44	2.37	2.44	2.35	2.43	2.50
0.04	0.03	0.04	0.00	0.03	0.00	0.00	0.00	0.00	0.02	0.00	0.00	0.00	0.02	0.00	0.02	0.00
0.62	0.61	0.62	0.61	0.60	0.60	0.68	0.74	0.60	0.63	0.56	0.40	0.41	0.40	0.40	0.38	0.39
0.03	0.02	0.07	0.03	0.02	0.05	0.02	0.01	0.08	-0.02	0.06	0.14	0.15	0.11	0.13	0.16	0.13
5.66	5.68	5.64	5.67	5.68	5.61	5.63	5.63	5.65	5.66	5.74	5.64	5.63	5.66	5.65	5.65	5.69
2.49	2.47	2.46	2.45	2.46	2.46	2.57	2.61	2.43	2.45	2.41	2.22	2.19	2.24	2.23	2.22	2.25
5.51	5.53	5.54	5.55	5.54	5.54	5.43	5.39	5.57	5.55	5.59	5.78	5.81	5.76	5.77	5.78	5.75
8.00	8.00	8.00	8.00	8.00	8.00	8.00	8.00	8.00	8.00	8.00	8.00	8.00	8.00	8.00	8.00	8.00
15.52	15.51	15.43	15.51	15.52	15.40	15.47	15.42	15.45	15.47	15.50	15.58	15.55	15.61	15.59	15.55	15.56
0.79	0.80	0.77	0.66	0.60	0.56	0.55	0.47	0.65	0.59	0.72	0.52	0.53	0.53	0.54	0.52	0.52

14(3) Aigou al pluton																	
1	2	3	4	5	6	7	8	9	10	11	12	13	14	15	16	17	18
0.22	0.21	0.23	0.22	0.20	0.20	0.00	0.22	0.28	0.21	0.21	0.30	0.18	0.23	0.33	0.20	0.22	0.20
11.91	11.62	11.99	12.24	12.37	11.72	12.25	11.50	11.79	12.32	11.92	11.98	12.22	12.33	11.77	11.78	12.17	12.46
13.41	13.72	13.57	13.36	13.56	13.72	13.48	13.42	13.63	13.51	13.55	13.77	13.61	13.44	13.39	13.68	13.54	13.39
37.07	36.53	37.46	37.68	37.87	37.07	38.02	36.62	37.51	37.80	36.97	37.58	37.91	37.58	37.10	36.69	37.68	37.64
9.45	9.01	9.43	9.34	9.40	9.40	9.47	9.43	9.29	9.47	9.42	9.48	9.47	9.41	9.36	9.29	9.41	9.45
0.00	0.00	0.00	0.00	0.00	0.00	0.00	0.00	0.00	0.00	0.00	0.00	0.00	0.00	0.00	0.00	0.00	0.00
3.95	4.25	3.84	4.04	3.61	4.11	3.90	4.49	3.70	3.53	3.71	3.72	3.82	4.12	3.95	4.14	3.81	3.70
0.00	0.00	0.16	0.15	0.00	0.00	0.00	0.00	0.15	0.00	0.00	0.00	0.00	0.14	0.19	0.00	0.00	0.00
0.34	0.35	0.33	0.29	0.32	0.35	0.29	0.39	0.34	0.34	0.27	0.34	0.38	0.31	0.32	0.40	0.32	0.32
19.27	19.64	19.53	19.29	18.84	19.54	19.32	19.55	19.44	18.91	19.78	19.29	19.31	18.76	19.61	19.58	19.65	19.22
95.62	95.34	96.54	96.63	96.17	96.10	96.71	95.63	96.13	96.09	95.83	96.46	96.91	96.32	96.02	95.70	96.88	96.38
0.06	0.06	0.07	0.07	0.06	0.06	0.00	0.07	0.08	0.06	0.06	0.09	0.05	0.07	0.10	0.06	0.06	0.06
1.84	1.76	1.82	1.80	1.81	1.82	1.82	1.84	1.80	1.83	1.83	1.83	1.81	1.81	1.82	1.81	1.81	1.82
1.90	1.82	1.89	1.86	1.87	1.88	1.82	1.91	1.88	1.89	1.90	1.91	1.87	1.88	1.91	1.87	1.87	1.88
2.71	2.65	2.70	2.75	2.78	2.65	2.74	2.62	2.66	2.78	2.71	2.70	2.74	2.77	2.67	2.68	2.73	2.81
2.46	2.52	2.47	2.43	2.38	2.48	2.43	2.50	2.46	2.39	2.52	2.43	2.42	2.37	2.50	2.50	2.47	2.43
0.00	0.00	0.02	0.02	0.00	0.00	0.00	0.00	0.02	0.00	0.00	0.00	0.00	0.02	0.02	0.00	0.00	0.00
0.45	0.49	0.44	0.46	0.41	0.47	0.44	0.52	0.42	0.40	0.43	0.42	0.43	0.47	0.45	0.48	0.43	0.42
0.07	0.07	0.08	0.05	0.13	0.08	0.10	0.02	0.12	0.12	0.08	0.12	0.10	0.06	0.05	0.06	0.07	0.07
5.69	5.72	5.70	5.70	5.70	5.69	5.71	5.67	5.68	5.69	5.73	5.68	5.69	5.68	5.69	5.72	5.71	5.72
2.34	2.41	2.34	2.32	2.29	2.37	2.29	2.40	2.32	2.29	2.36	2.33	2.31	2.33	2.35	2.40	2.33	2.32
5.66	5.59	5.66	5.68	5.71	5.63	5.71	5.60	5.68	5.71	5.64	5.67	5.69	5.67	5.65	5.60	5.67	5.68
8.00	8.00	8.00	8.00	8.00	8.00	8.00	8.00	8.00	8.00	8.00	8.00	8.00	8.00	8.00	8.00	8.00	8.00
15.59	15.54	15.59	15.56	15.56	15.57	15.53	15.57	15.56	15.58	15.63	15.59	15.56	15.56	15.60	15.59	15.58	15.60

0.52	0.51	0.52	0.53	0.54	0.52	0.53	0.51	0.52	0.54	0.52	0.53	0.53	0.54	0.52	0.52	0.54
------	------	------	------	------	------	------	------	------	------	------	------	------	------	------	------	------

AG06A lamp.																									
1	2	3	4	5	6	7	8	9	10	11	12	13	14	15	16	17	18								
0.28	0.00	0.27	0.31	0.23	0.28	0.30	0.28	0.24	0.20	0.38	0.00	0.19	0.20	0.40	0.25	0.38	0.23								
17.09	13.56	17.05	16.08	11.84	18.85	14.35	18.13	17.70	11.20	17.88	17.09	13.13	12.20	18.50	16.74	17.96	14.37								
15.19	14.95	14.73	15.76	14.59	14.93	15.00	14.93	14.95	14.10	15.31	15.43	15.03	14.09	14.88	14.25	14.75	14.18								
38.16	37.41	38.49	39.24	36.23	39.01	38.33	38.63	37.39	35.70	38.60	38.34	37.44	36.63	38.30	37.17	38.21	38.11								
9.52	9.31	9.33	9.43	9.26	9.22	9.24	9.25	9.17	9.45	9.10	9.42	9.65	9.54	9.33	9.68	9.17	9.34								
0.00	0.00	0.00	0.00	0.00	0.00	0.00	0.00	0.00	0.00	0.00	0.00	0.00	0.00	0.00	0.00	0.00	0.00								
3.47	4.14	4.36	4.49	4.94	4.97	4.99	5.01	5.01	5.05	5.08	5.09	5.12	5.17	5.23	5.24	5.29	5.36								
0.24	0.00	0.00	0.27	0.00	0.29	0.21	0.19	0.72	0.00	0.27	0.24	0.00	0.00	0.35	0.31	0.43	0.25								
0.00	0.00	0.00	0.00	0.00	0.00	0.00	0.00	0.00	0.41	0.00	0.00	0.16	0.00	0.00	0.00	0.00	0.00								
10.60	16.46	11.35	12.71	18.00	7.85	14.67	8.59	8.45	19.40	8.53	10.31	16.60	17.77	7.87	10.34	8.54	14.58								
94.55	95.83	95.56	98.30	95.08	95.40	97.09	95.01	93.63	95.52	95.15	95.92	97.32	95.61	94.86	93.98	94.73	96.42								
0.08	0.00	0.08	0.09	0.07	0.08	0.08	0.08	0.07	0.06	0.11	0.00	0.05	0.06	0.11	0.07	0.11	0.07								
1.79	1.77	1.74	1.72	1.80	1.69	1.72	1.71	1.73	1.85	1.68	1.74	1.82	1.84	1.73	1.84	1.70	1.75								
1.87	1.77	1.81	1.80	1.86	1.77	1.80	1.79	1.79	1.91	1.79	1.74	1.87	1.90	1.84	1.91	1.81	1.82								
3.75	3.02	3.71	3.42	2.69	4.04	3.12	3.92	3.89	2.56	3.85	3.69	2.89	2.76	4.00	3.71	3.90	3.15								
1.31	2.05	1.39	1.52	2.29	0.94	1.79	1.04	1.04	2.49	1.03	1.25	2.05	2.25	0.95	1.29	1.04	1.80								
0.01	0.00	0.00	0.02	0.00	0.02	0.01	0.01	0.04	0.00	0.02	0.01	0.00	0.00	0.02	0.04	0.02	0.01								
0.38	0.47	0.48	0.48	0.57	0.54	0.55	0.55	0.56	0.58	0.55	0.55	0.57	0.59	0.57	0.59	0.58	0.59								
0.26	0.21	0.15	0.24	0.13	0.14	0.17	0.15	0.11	0.03	0.19	0.18	0.14	0.06	0.10	0.03	0.09	0.07								
5.71	5.75	5.73	5.67	5.68	5.67	5.64	5.66	5.65	5.66	5.64	5.68	5.64	5.66	5.64	5.66	5.64	5.63								
2.38	2.42	2.38	2.41	2.49	2.39	2.41	2.40	2.48	2.52	2.42	2.45	2.48	2.45	2.45	2.47	2.44	2.39								
5.62	5.58	5.62	5.59	5.51	5.61	5.59	5.60	5.52	5.48	5.58	5.55	5.52	5.55	5.53	5.56	5.61									
8.00	8.00	8.00	8.00	8.00	8.00	8.00	8.00	8.00	8.00	8.00	8.00	8.00	8.00	8.00	8.00	8.00	8.00								
15.58	15.52	15.54	15.47	15.54	15.44	15.45	15.45	15.44	15.57	15.43	15.42	15.52	15.56	15.48	15.57	15.45	15.45								

0.74	0.59	0.73	0.69	0.54	0.81	0.64	0.79	0.79	0.51	0.79	0.75	0.58	0.55	0.81	0.74	0.79	0.64
AG06A lamp.																	
19	20	21	22	23	24	25	26	27	28	29	30	31	32	33	34	35	36
0.22	0.23	0.43	0.00	0.00	0.30	0.17	0.35	0.21	0.29	0.32	0.24	0.00	0.26	0.18	0.34	0.31	0.40
14.57	18.05	16.13	14.24	12.32	17.57	13.93	15.87	13.40	16.50	17.74	12.32	11.48	13.98	13.32	13.81	14.44	15.80
14.58	15.72	14.64	15.07	13.63	15.82	14.98	15.23	14.72	14.81	14.81	14.84	13.73	14.91	14.79	14.73	14.89	15.27
36.42	38.36	37.04	37.98	36.47	38.87	37.14	36.78	37.39	38.22	38.31	36.09	35.52	37.25	36.98	37.25	36.70	37.82
9.23	9.35	9.13	9.62	9.46	9.34	9.58	9.12	9.52	9.23	9.39	9.12	9.05	9.36	9.34	9.28	9.21	9.12
0.00	0.00	0.00	0.00	0.21	0.00	0.00	0.00	0.00	0.00	0.00	0.00	0.00	0.00	0.00	0.00	0.00	0.00
5.46	5.46	5.72	5.74	5.76	5.76	5.82	5.83	5.84	5.85	5.90	5.98	6.07	6.11	6.12	6.12	6.20	6.23
0.75	0.60	0.00	0.36	0.35	0.29	0.15	0.27	0.00	0.23	0.22	0.00	0.00	0.24	0.00	0.00	0.00	0.25
0.14	0.00	0.00	0.17	0.23	0.00	0.23	0.00	0.16	0.00	0.00	0.00	0.17	0.00	0.00	0.00	0.14	0.00
12.68	7.80	11.17	15.01	16.33	9.21	13.91	10.44	14.94	11.29	9.21	16.27	17.36	14.75	15.25	14.17	12.80	11.16
94.04	95.58	94.25	98.20	94.75	97.17	95.92	93.89	96.19	96.42	95.92	94.85	93.39	96.84	95.97	95.70	94.68	96.04
0.06	0.07	0.12	0.00	0.00	0.08	0.05	0.10	0.06	0.08	0.09	0.07	0.00	0.07	0.05	0.10	0.09	0.11
1.77	1.72	1.73	1.78	1.84	1.69	1.81	1.73	1.80	1.70	1.73	1.76	1.79	1.75	1.77	1.75	1.75	1.69
1.84	1.78	1.85	1.78	1.84	1.78	1.86	1.83	1.86	1.79	1.82	1.83	1.79	1.83	1.82	1.85	1.84	1.80
3.27	3.87	3.57	3.08	2.79	3.72	3.08	3.51	2.96	3.56	3.82	2.78	2.65	3.06	2.95	3.05	3.21	3.42
1.59	0.94	1.39	1.82	2.08	1.09	1.72	1.30	1.85	1.37	1.11	2.06	2.25	1.81	1.90	1.76	1.60	1.36
0.04	0.03	0.00	0.02	0.04	0.02	0.01	0.02	0.00	0.01	0.01	0.00	0.00	0.01	0.00	0.00	0.00	0.01
0.62	0.59	0.64	0.63	0.66	0.62	0.65	0.65	0.64	0.64	0.68	0.71	0.68	0.68	0.68	0.70	0.68	0.68
0.06	0.18	0.06	0.08	0.00	0.17	0.11	0.13	0.11	0.06	0.05	0.10	0.01	0.06	0.09	0.09	0.09	0.11
5.59	5.61	5.66	5.63	5.57	5.62	5.57	5.61	5.57	5.64	5.63	5.62	5.62	5.62	5.58	5.59	5.59	5.59
2.52	2.49	2.50	2.49	2.45	2.48	2.50	2.54	2.46	2.46	2.47	2.54	2.50	2.53	2.50	2.48	2.53	2.50
5.48	5.51	5.50	5.51	5.55	5.52	5.50	5.46	5.54	5.54	5.53	5.46	5.50	5.47	5.50	5.52	5.47	5.50
8.00	8.00	8.00	8.00	8.00	8.00	8.00	8.00	8.00	8.00	8.00	8.00	8.00	8.00	8.00	8.00	8.00	8.00
15.42	15.39	15.51	15.41	15.41	15.39	15.43	15.44	15.43	15.43	15.45	15.45	15.41	15.45	15.44	15.44	15.43	15.39

0.67	0.80	0.72	0.63	0.57	0.77	0.64	0.73	0.62	0.72	0.77	0.57	0.54	0.63	0.61	0.63	0.67	0.72
AG06A lamp.																	
37	38	39	40	41	42	43	44	45	46	47	48	49	50	51	52	53	54
0.23	0.00	0.24	0.38	0.30	0.26	0.34	0.41	0.21	0.34	0.19	0.00	0.35	0.35	0.42	0.33	0.25	0.31
15.28	12.84	11.91	16.08	15.86	13.74	15.31	16.96	13.51	14.44	14.03	11.53	15.72	16.26	15.68	12.32	15.82	12.93
15.09	14.07	14.42	14.87	15.59	15.59	15.21	15.01	14.77	14.90	14.94	14.72	14.76	15.14	14.77	14.47	14.85	15.34
37.13	36.19	36.33	37.29	39.07	36.58	37.50	37.90	36.69	37.55	37.13	36.53	37.54	38.09	37.28	36.27	37.40	36.64
9.54	9.58	9.36	9.22	9.06	9.13	9.34	9.28	8.95	9.27	9.42	9.19	9.16	9.01	9.15	8.76	9.18	9.07
0.00	0.23	0.00	0.00	0.11	0.00	0.11	0.00	0.00	0.00	0.00	0.00	0.00	0.00	0.00	0.00	0.00	0.00
6.25	6.27	6.29	6.33	6.37	6.39	6.39	6.46	6.46	6.48	6.53	6.55	6.62	6.71	6.71	6.72	6.77	6.83
0.51	0.00	0.00	0.00	0.00	0.00	0.24	0.22	0.00	0.00	0.00	0.00	0.00	0.45	0.32	0.24	0.00	0.00
0.00	0.25	0.17	0.00	0.00	0.00	0.23	0.00	0.22	0.00	0.00	0.16	0.00	0.00	0.25	0.00	0.16	
11.76	15.73	17.43	10.70	11.54	13.82	12.38	10.00	15.07	13.87	14.23	18.03	10.84	9.70	10.86	15.94	10.54	15.43
95.78	95.16	96.14	94.87	97.90	95.50	97.06	96.24	95.88	96.83	96.47	96.70	95.00	95.70	95.20	95.29	94.80	96.72
0.06	0.00	0.07	0.11	0.08	0.08	0.10	0.12	0.06	0.10	0.05	0.00	0.10	0.10	0.12	0.09	0.07	0.09
1.79	1.85	1.80	1.73	1.64	1.73	1.73	1.71	1.70	1.73	1.77	1.75	1.72	1.66	1.71	1.68	1.72	1.71
1.85	1.85	1.87	1.84	1.72	1.80	1.83	1.83	1.76	1.82	1.82	1.75	1.82	1.76	1.83	1.77	1.79	1.80
3.34	2.89	2.67	3.53	3.36	3.04	3.31	3.65	2.99	3.15	3.08	2.57	3.44	3.51	3.43	2.76	3.47	2.85
1.44	1.99	2.19	1.32	1.37	1.71	1.50	1.21	1.87	1.69	1.75	2.25	1.33	1.17	1.33	2.00	1.29	1.90
0.03	0.00	0.00	0.00	0.00	0.00	0.01	0.01	0.00	0.00	0.00	0.00	0.00	0.03	0.02	0.01	0.00	0.00
0.69	0.71	0.71	0.70	0.68	0.71	0.70	0.70	0.72	0.71	0.72	0.74	0.73	0.73	0.74	0.76	0.75	0.76
0.06	0.00	0.02	0.06	0.17	0.14	0.04	0.03	0.04	0.05	0.05	0.05	0.07	0.10	0.03	0.02	0.07	0.07
5.57	5.59	5.59	5.61	5.58	5.60	5.57	5.61	5.63	5.61	5.61	5.61	5.57	5.53	5.55	5.56	5.57	5.58
2.55	2.53	2.54	2.51	2.45	2.58	2.56	2.52	2.55	2.51	2.54	2.54	2.49	2.49	2.53	2.55	2.50	2.59
5.45	5.47	5.46	5.49	5.55	5.42	5.44	5.48	5.45	5.49	5.46	5.46	5.51	5.51	5.47	5.45	5.50	5.41
8.00	8.00	8.00	8.00	8.00	8.00	8.00	8.00	8.00	8.00	8.00	8.00	8.00	8.00	8.00	8.00	8.00	8.00
15.42	15.44	15.46	15.44	15.30	15.41	15.40	15.43	15.38	15.43	15.43	15.36	15.39	15.29	15.39	15.33	15.37	15.38

0.70	0.59	0.55	0.73	0.71	0.64	0.69	0.75	0.62	0.65	0.64	0.53	0.72	0.75	0.72	0.58	0.73	0.60
AG06C granite	AG06D granite	AG06D granite	AG06D granite	AG06D granite	AG06D granite	AG06D granite											
1	2	3	4	5	6	7	8	9	10	11	12	1	2	3	4	5	6
0.29	0.21	0.35	0.34	0.38	0.41	0.39	0.25	0.33	0.31	0.24	0.19	0.18	0.34	0.24	0.20	0.24	0.00
15.19	13.65	15.64	17.20	15.98	15.45	15.26	12.96	13.45	13.27	12.88	10.49	12.51	14.59	12.37	15.04	11.43	11.87
14.02	13.61	14.66	14.02	14.55	14.14	13.75	13.53	13.80	13.72	14.04	14.89	13.35	13.70	13.36	13.92	13.27	13.18
38.09	38.55	39.26	40.52	39.40	39.53	39.11	37.22	38.47	38.10	38.97	37.74	38.66	39.48	38.41	39.47	38.14	37.99
8.71	9.36	9.11	9.05	9.13	9.24	8.98	8.90	9.66	9.04	9.46	9.50	9.44	9.54	9.18	9.62	9.44	9.34
0.00	0.00	0.00	0.00	0.00	0.00	0.00	0.00	0.00	0.00	0.00	0.00	0.00	0.00	0.00	0.00	0.00	0.00
3.70	3.73	3.94	3.96	3.97	5.20	5.74	5.78	5.79	5.90	6.19	6.19	3.60	3.64	3.68	3.94	5.43	5.69
0.17	0.00	0.15	0.00	0.00	0.25	0.35	0.00	0.25	0.00	0.23	0.00	0.00	0.00	0.00	0.23	0.23	0.23
0.00	0.14	0.00	0.00	0.00	0.00	0.00	0.00	0.16	0.00	0.30	0.23	0.19	0.19	0.24	0.20	0.26	0.21
13.13	16.03	13.52	11.73	13.06	11.83	11.85	14.89	14.25	14.68	15.71	18.91	16.48	13.52	17.09	12.72	16.53	16.68
94.00	95.29	97.55	96.82	97.22	96.82	95.91	94.47	96.86	95.78	98.79	99.22	94.40	95.00	94.57	95.12	94.97	95.19
0.08	0.06	0.10	0.10	0.11	0.12	0.11	0.07	0.09	0.09	0.07	0.05	0.05	0.10	0.07	0.06	0.07	0.00
1.67	1.79	1.68	1.66	1.69	1.71	1.67	1.72	1.82	1.72	1.75	1.78	1.83	1.80	1.78	1.81	1.82	1.80
1.75	1.85	1.78	1.75	1.80	1.82	1.79	1.79	1.91	1.81	1.82	1.84	1.88	1.90	1.85	1.87	1.89	1.80
3.40	3.05	3.38	3.68	3.45	3.34	3.32	2.93	2.96	2.94	2.79	2.30	2.83	3.23	2.80	3.31	2.58	2.67
1.65	2.01	1.64	1.41	1.58	1.43	1.45	1.89	1.76	1.83	1.91	2.33	2.09	1.68	2.17	1.57	2.09	2.10
0.02	0.00	0.02	0.00	0.00	0.03	0.04	0.00	0.03	0.00	0.03	0.00	0.00	0.00	0.00	0.03	0.03	0.00
0.42	0.42	0.43	0.43	0.43	0.57	0.63	0.66	0.64	0.66	0.68	0.69	0.41	0.41	0.42	0.44	0.62	0.65
0.20	0.18	0.20	0.18	0.20	0.15	0.08	0.06	0.07	0.08	0.06	0.14	0.25	0.25	0.22	0.25	0.13	0.07
5.69	5.66	5.67	5.70	5.67	5.52	5.53	5.53	5.45	5.51	5.46	5.45	5.57	5.56	5.60	5.57	5.44	5.52
2.28	2.22	2.31	2.19	2.29	2.27	2.28	2.36	2.33	2.33	2.34	2.45	2.14	2.14	2.17	2.17	2.23	2.27
5.72	5.78	5.69	5.81	5.71	5.73	5.72	5.64	5.67	5.67	5.66	5.55	5.86	5.86	5.83	5.83	5.77	5.73
8.00	8.00	8.00	8.00	8.00	8.00	8.00	8.00	8.00	8.00	8.00	8.00	8.00	8.00	8.00	8.00	8.00	8.00
15.44	15.51	15.45	15.45	15.46	15.34	15.31	15.33	15.36	15.32	15.28	15.29	15.45	15.47	15.45	15.44	15.33	15.31

0.67	0.60	0.67	0.72	0.69	0.70	0.70	0.61	0.63	0.62	0.59	0.50	0.57	0.66	0.56	0.68	0.55	0.56
------	------	------	------	------	------	------	------	------	------	------	------	------	------	------	------	------	------

AG6D granite	AG6D granite	AG6D granite	AG6D granite	AG6D granite	AG6D granite	AG06E granite										
7	8	9	10	11	12	100	101	102	103	104	105	106	107	108	109	
0.23	0.26	0.00	0.00	0.00	0.24	0.00	0.18	0.00	0.17	0.28	0.20	0.18	0.18	0.00	0.23	
12.22	12.35	9.49	9.56	9.53	10.74	11.03	11.48	11.70	11.14	12.44	11.44	11.70	11.70	11.35	10.40	
13.02	13.24	13.46	13.69	13.53	13.72	12.95	13.48	13.49	12.95	13.70	13.34	13.22	13.22	13.79	13.93	
38.09	38.10	36.67	37.14	36.96	37.46	37.00	38.68	38.14	37.77	38.99	38.16	38.23	38.23	38.53	36.50	
9.06	9.10	9.33	9.38	9.28	9.24	8.98	9.63	9.23	9.58	9.38	9.73	9.13	9.13	9.43	8.74	
0.00	0.00	0.00	0.16	0.15	0.00	0.20	0.00	0.16	0.00	0.00	0.00	0.00	0.00	0.00	0.00	
5.71	5.72	5.83	5.88	5.90	6.19	3.10	3.41	3.54	3.57	3.65	3.71	3.83	3.83	3.87	5.64	
0.24	0.00	0.44	0.00	0.24	0.19	0.38	0.00	0.00	0.00	0.16	0.17	0.00	0.00	0.00	0.00	
0.21	0.19	0.27	0.42	0.31	0.31	0.20	0.29	0.30	0.25	0.19	0.25	0.26	0.26	0.33	0.29	
15.27	15.33	19.55	19.28	19.18	17.55	18.56	18.42	18.33	18.78	17.02	18.59	18.29	18.29	18.33	19.14	
94.05	94.28	95.05	95.50	95.09	95.63	92.41	95.56	94.89	94.22	95.83	95.58	94.83	94.83	95.62	94.88	
0.07	0.08	0.00	0.00	0.00	0.07	0.00	0.05	0.00	0.05	0.08	0.06	0.05	0.05	0.00	0.07	
1.75	1.75	1.83	1.83	1.81	1.78	1.80	1.86	1.79	1.89	1.79	1.89	1.77	1.77	1.82	1.71	
1.82	1.83	1.83	1.83	1.81	1.85	1.80	1.91	1.79	1.94	1.87	1.94	1.83	1.83	1.82	1.78	
2.76	2.78	2.18	2.17	2.18	2.42	2.58	2.59	2.66	2.56	2.77	2.59	2.65	2.65	2.55	2.37	
1.93	1.94	2.51	2.46	2.46	2.21	2.44	2.33	2.33	2.42	2.13	2.36	2.33	2.33	2.31	2.45	
0.03	0.00	0.05	0.00	0.03	0.02	0.05	0.00	0.00	0.00	0.02	0.02	0.00	0.00	0.00	0.00	
0.65	0.65	0.67	0.67	0.68	0.70	0.37	0.39	0.40	0.41	0.41	0.42	0.44	0.44	0.44	0.65	
0.09	0.11	0.08	0.13	0.11	0.09	0.21	0.26	0.23	0.18	0.25	0.18	0.19	0.19	0.27	0.10	
5.47	5.48	5.49	5.44	5.45	5.45	5.64	5.57	5.62	5.58	5.58	5.58	5.61	5.61	5.57	5.58	
2.23	2.25	2.36	2.33	2.34	2.35	2.19	2.15	2.19	2.17	2.17	2.21	2.18	2.18	2.19	2.41	
5.77	5.75	5.64	5.67	5.66	5.65	5.81	5.85	5.81	5.83	5.83	5.79	5.82	5.82	5.81	5.59	
8.00	8.00	8.00	8.00	8.00	8.00	8.00	8.00	8.00	8.00	8.00	8.00	8.00	8.00	8.00	8.00	
15.28	15.31	15.32	15.26	15.26	15.30	15.44	15.48	15.41	15.52	15.45	15.52	15.44	15.44	15.39	15.35	

0.59	0.59	0.46	0.47	0.47	0.52	0.51	0.53	0.53	0.51	0.57	0.52	0.53	0.53	0.52	0.49
------	------	------	------	------	------	------	------	------	------	------	------	------	------	------	------

Table 4 Mineral chemistry of feldspars

Sample	9 lamp.	9 lamp.	9 lamp.	9 lamp.	9 lamp.	9 lamp.	9 lamp.	9 lamp.	9 lamp.	6D granite						
Spectrum	1	2	3	4	5	6	7	8	9	68	69	70	71	72	73	74
Na ₂ O	5.85	6.27	7.96	8.83	6.63	6.12	0.77	0.57	1.16	4.99	5.76	5.44	0.35	0.42	7.26	6.92
MgO	0.00	0.29	0.35	0.00	0.00	0.32	0.00	0.00	0.00	0.20	0.00	0.00	0.00	0.00	0.00	0.28
Al ₂ O ₃	26.82	25.81	22.71	22.25	26.07	25.40	18.05	18.19	18.10	27.37	27.53	28.18	18.02	17.68	25.06	25.05
SiO ₂	58.46	58.41	62.95	64.52	58.77	58.11	66.25	67.57	66.50	56.77	56.72	55.76	65.98	67.31	59.81	60.91
K ₂ O	0.58	0.41	0.53	1.48	0.71	0.40	15.42	15.69	14.12	1.58	0.26	0.20	15.96	15.34	0.54	3.76
CaO	9.01	8.79	4.41	4.23	8.18	8.02	0.00	0.00	0.00	9.12	10.09	10.66	0.00	0.00	7.58	2.06
TiO ₂	0.00	0.00	0.00	0.00	0.00	0.00	0.00	0.00	0.00	0.00	0.00	0.00	0.00	0.17	0.00	0.00
MnO	0.00	0.00	0.00	0.00	0.00	0.00	0.00	0.00	0.00	0.00	0.00	0.00	0.00	0.00	0.00	0.00
FeO	0.69	0.47	0.64	0.00	0.74	0.80	0.00	0.00	0.00	0.00	0.00	0.00	0.00	0.00	0.00	0.63
Total	101.41	100.44	99.54	101.31	101.10	99.16	100.48	102.02	100.51	100.04	100.36	100.24	100.31	100.91	100.23	99.61
*	Structural formula based on 8O															
Na	0.50	0.54	0.69	0.75	0.57	0.54	0.07	0.05	0.10	0.44	0.50	0.47	0.03	0.04	0.63	0.60
Ca	0.43	0.42	0.21	0.20	0.39	0.39	0.00	0.00	0.00	0.44	0.48	0.51	0.00	0.00	0.36	0.10
Mg	0.00	0.02	0.02	0.00	0.00	0.02	0.00	0.00	0.00	0.01	0.00	0.00	0.00	0.00	0.00	0.02
Fe	0.03	0.02	0.02	0.00	0.03	0.03	0.00	0.00	0.00	0.00	0.00	0.00	0.00	0.00	0.00	0.02
K	0.03	0.02	0.03	0.08	0.04	0.02	0.90	0.90	0.82	0.09	0.01	0.01	0.93	0.89	0.03	0.22
Sum	0.99	1.02	0.97	1.03	1.03	1.00	0.97	0.95	0.93	0.98	1.00	1.00	0.97	0.92	1.02	0.96
Al	1.40	1.36	1.19	1.15	1.37	1.35	0.97	0.96	0.97	1.45	1.45	1.49	0.97	0.94	1.32	1.32
Si	2.59	2.61	2.80	2.83	2.61	2.63	3.03	3.04	3.04	2.55	2.54	2.50	3.03	3.05	2.67	2.73
Sum	3.99	3.97	3.99	3.98	3.98	3.98	4.00	4.00	4.01	4.00	3.99	3.99	4.00	4.00	3.98	4.06
An	44.44	42.67	22.70	19.27	38.95	41.03	0.00	0.00	0.00	45.56	48.47	51.42	0.00	0.00	35.51	10.81
Ab	52.17	54.98	74.07	72.70	57.03	56.55	7.01	5.22	11.08	45.08	50.07	47.45	3.23	4.01	61.50	65.71
Or	3.39	2.35	3.23	8.03	4.02	2.43	92.99	94.78	88.92	9.36	1.47	1.13	96.77	95.99	2.99	23.48

6D granite	6D granite	6D granite	6D granite	6D granite	6D granite	6E granite													
75	76	77	78	79	80	81	178	182	183	184	185	186	187	188	189	190	191		
7.95	0.75	7.69	0.37	0.93	8.68	0.75	1.92	6.91	6.85	2.46	1.01	0.93	11.69	11.67	7.90	5.18	8.29		
0.16	0.24	0.21	9.75	0.00	0.00	0.00	0.00	0.00	0.00	0.00	0.00	0.00	0.00	0.00	0.00	0.12	0.00		
23.87	19.29	20.95	12.23	18.25	20.19	17.70	18.22	25.84	25.58	18.44	17.99	17.99	19.63	19.49	23.44	28.23	23.04		
63.76	65.74	66.78	50.06	65.94	68.02	66.26	65.81	59.53	59.27	65.94	65.61	65.65	68.34	68.63	62.56	55.59	63.04		
1.88	13.98	3.03	6.21	14.53	0.75	15.61	13.52	0.41	0.54	12.63	15.15	15.14	0.13	0.13	0.87	0.30	0.76		
1.95	0.16	1.12	0.00	0.23	2.28	0.00	0.00	7.85	8.10	0.15	0.00	0.00	0.78	0.79	5.87	10.88	5.24		
0.00	0.00	0.00	2.33	0.00	0.00	0.00	0.40	0.00	0.00	0.42	0.16	0.19	0.00	0.00	0.00	0.00	0.00		
0.00	0.00	0.00	0.32	0.00	0.00	0.00	0.00	0.00	0.00	0.00	0.00	0.00	0.00	0.00	0.00	0.00	0.00		
0.00	0.00	0.00	14.31	0.00	0.00	0.00	0.00	0.00	0.00	0.00	0.00	0.00	0.00	0.00	0.00	0.00	0.14		
99.57	100.17	99.79	95.58	99.89	99.92	100.31	99.87	100.67	100.35	100.04	99.94	99.89	100.57	100.71	100.64	100.31	100.52		
0.68	0.07	0.66	0.04	0.08	0.74	0.07	0.17	0.60	0.59	0.22	0.09	0.08	0.99	0.98	0.68	0.45	0.71		
0.09	0.01	0.05	0.00	0.01	0.11	0.00	0.00	0.37	0.39	0.01	0.00	0.00	0.04	0.04	0.28	0.52	0.25		
0.01	0.02	0.01	0.74	0.00	0.00	0.00	0.00	0.00	0.00	0.00	0.00	0.00	0.00	0.00	0.00	0.01	0.00		
0.00	0.00	0.00	0.61	0.00	0.00	0.00	0.00	0.00	0.00	0.00	0.00	0.00	0.00	0.00	0.00	0.00	0.01		
0.11	0.81	0.17	0.40	0.85	0.04	0.91	0.79	0.02	0.03	0.73	0.89	0.89	0.01	0.01	0.05	0.02	0.04		
0.89	0.90	0.89	1.78	0.94	0.88	0.98	0.96	0.99	1.01	0.96	0.98	0.97	1.03	1.03	1.00	1.00	1.01		
1.24	1.03	1.09	0.73	0.99	1.04	0.96	0.98	1.35	1.34	0.99	0.97	0.97	1.01	1.00	1.22	1.49	1.20		
2.82	2.99	2.94	2.54	3.02	2.97	3.04	3.01	2.64	2.64	3.00	3.02	3.02	2.98	2.98	2.76	2.50	2.79		
4.06	4.03	4.03	3.27	4.01	4.01	3.99	3.99	4.00	3.99	3.99	3.99	3.99	3.98	3.98	3.98	3.99	3.98		
10.49	0.91	6.00	0.00	1.20	12.10	0.00	0.00	37.66	38.33	0.77	0.00	0.00	3.55	3.60	27.68	52.80	24.81		
77.43	7.44	74.64	8.38	8.79	83.20	6.79	17.75	59.99	58.63	22.67	9.23	8.51	95.76	95.70	67.44	45.46	70.90		
12.08	91.66	19.36	91.62	90.01	4.71	93.21	82.25	2.35	3.03	76.56	90.77	91.49	0.69	0.70	4.88	1.74	4.29		

6E	6C																
granite																	
192	193	194	195	196	197	198	199	200	201	202	203	204	205	206	207	208	15

8.76	1.25	1.61	1.72	10.83	4.46	0.51	4.16	0.14	8.72	3.46	0.62	0.62	9.03	5.78	0.43	0.69	0.71
0.00	0.00	0.00	0.00	0.14	0.00	0.15	0.23	3.26	1.11	0.30	0.00	0.00	0.33	0.00	0.00	0.00	0.00
22.43	17.88	18.06	18.22	20.53	18.20	17.97	28.11	24.12	23.04	26.99	17.77	18.04	22.39	27.02	17.87	17.98	18.22
64.02	65.90	66.47	66.67	67.36	66.94	66.37	56.18	58.91	63.43	57.27	66.34	66.25	64.37	56.93	65.72	65.87	66.79
0.70	14.56	13.91	14.15	0.54	10.93	15.61	4.52	9.79	1.22	5.55	15.45	15.58	1.25	0.60	15.65	15.34	15.73
4.65	0.00	0.00	0.14	1.18	0.00	0.00	5.60	0.18	2.13	5.84	0.00	0.00	3.04	9.79	0.00	0.00	0.00
0.00	0.23	0.00	0.00	0.00	0.00	0.00	0.00	0.00	0.00	0.00	0.15	0.17	0.00	0.00	0.00	0.20	0.00
0.00	0.00	0.00	0.00	0.00	0.00	0.00	0.00	0.00	0.00	0.00	0.00	0.00	0.00	0.00	0.00	0.00	0.00
0.00	0.00	0.00	0.00	0.24	0.00	0.22	0.35	1.38	0.84	0.38	0.26	0.25	0.21	0.00	0.00	0.00	0.19
100.57	99.82	100.05	100.91	100.82	100.53	100.83	99.13	97.79	100.50	99.79	100.58	100.92	100.62	100.12	99.68	100.09	101.64
0.75	0.11	0.14	0.15	0.92	0.39	0.05	0.37	0.01	0.75	0.30	0.05	0.05	0.77	0.50	0.04	0.06	0.06
0.22	0.00	0.00	0.01	0.06	0.00	0.00	0.27	0.01	0.10	0.28	0.00	0.00	0.14	0.47	0.00	0.00	0.00
0.00	0.00	0.00	0.00	0.01	0.00	0.01	0.02	0.22	0.07	0.02	0.00	0.00	0.02	0.00	0.00	0.00	0.01
0.00	0.00	0.00	0.00	0.01	0.00	0.01	0.01	0.05	0.03	0.01	0.01	0.01	0.01	0.00	0.00	0.00	0.00
0.04	0.85	0.81	0.82	0.03	0.63	0.91	0.26	0.58	0.07	0.32	0.90	0.91	0.07	0.03	0.92	0.90	0.91
1.01	0.96	0.95	0.98	1.02	1.02	0.97	0.93	0.88	1.02	0.95	0.96	0.97	1.01	1.01	0.96	0.96	0.98
1.16	0.97	0.97	0.97	1.05	0.97	0.97	1.51	1.31	1.20	1.44	0.96	0.97	1.16	1.43	0.97	0.97	0.97
2.82	3.02	3.03	3.02	2.94	3.02	3.03	2.56	2.72	2.80	2.60	3.03	3.02	2.83	2.56	3.03	3.02	3.02
3.98	3.99	4.00	4.00	3.99	3.99	3.99	4.07	4.04	3.99	4.04	3.99	3.99	3.99	3.99	4.00	3.99	4.00
21.81	0.00	0.00	0.68	5.54	0.00	0.00	30.28	1.50	11.02	31.23	0.00	0.00	14.58	46.71	0.00	0.00	0.00
74.27	11.50	14.93	15.48	91.46	38.28	4.74	40.65	2.16	81.46	33.47	5.74	5.69	78.30	49.89	4.04	6.40	6.41
3.92	88.50	85.07	83.84	3.01	61.72	95.26	29.07	96.33	7.52	35.31	94.26	94.31	7.12	3.40	95.96	93.60	93.59

6C granite	6A lamp.	6A lamp.	6A lamp.	6A lamp.	6A lamp.	6A lamp.											
16	17	18	19	20	21	22	23	24	25	26	27	64	65	66	67	68	69
0.68	0.58	0.66	0.81	0.77	4.64	4.69	7.32	6.34	7.16	7.07	7.16	4.39	4.73	0.12	4.35	0.94	4.30
0.00	0.00	0.00	0.00	0.00	0.15	0.00	0.00	0.00	0.00	0.00	0.00	0.00	0.00	0.00	0.00	0.00	0.95
18.03	18.01	18.26	18.18	18.06	28.92	28.43	24.05	24.65	25.18	25.16	24.56	29.36	29.75	19.06	29.24	19.06	28.63

66.27	66.35	65.86	67.63	65.87	54.64	54.82	60.63	59.98	60.61	60.86	60.67	54.79	55.32	64.88	53.91	65.81	54.73
15.34	15.25	15.30	13.96	15.01	0.37	0.89	0.63	1.89	0.53	0.59	0.53	0.67	0.63	16.60	0.52	15.16	2.36
0.00	0.00	0.00	0.62	0.23	11.54	10.16	6.44	6.32	7.17	7.08	6.98	10.24	10.36	0.00	10.81	0.00	7.63
0.00	0.00	0.00	0.00	0.00	0.00	0.00	0.00	0.00	0.00	0.00	0.00	0.00	0.00	0.00	0.00	0.00	0.00
0.00	0.00	0.00	0.00	0.00	0.00	0.00	0.00	0.00	0.00	0.00	0.00	0.00	0.00	0.00	0.00	0.00	0.00
0.00	0.00	0.00	0.00	0.00	0.39	0.31	0.00	0.14	0.17	0.17	0.00	0.38	0.36	0.00	0.23	0.00	0.75
100.33	100.19	100.08	101.20	99.96	100.48	99.46	99.07	99.33	100.82	100.92	99.88	99.84	101.16	100.66	99.05	100.98	99.34
0.06	0.05	0.06	0.07	0.07	0.40	0.41	0.64	0.55	0.61	0.60	0.62	0.38	0.41	0.01	0.38	0.08	0.38
0.00	0.00	0.00	0.03	0.01	0.56	0.49	0.31	0.31	0.34	0.33	0.33	0.50	0.49	0.00	0.53	0.00	0.37
0.00	0.00	0.00	0.00	0.00	0.01	0.01	0.00	0.01	0.01	0.01	0.00	0.04	0.04	0.97	0.03	0.88	0.14
0.00	0.00	0.00	0.00	0.00	0.00	0.01	0.00	0.00	0.00	0.00	0.00	0.00	0.00	0.00	0.00	0.00	0.06
0.90	0.89	0.89	0.80	0.88	0.02	0.05	0.04	0.11	0.03	0.03	0.03	0.01	0.01	0.00	0.01	0.00	0.03
0.96	0.94	0.95	0.90	0.96	1.00	0.98	0.98	0.97	0.99	0.98	0.98	0.93	0.95	0.98	0.95	0.96	0.98
0.97	0.97	0.99	0.96	0.98	1.53	1.52	1.27	1.31	1.31	1.31	1.29	1.56	1.56	1.03	1.57	1.02	1.53
3.03	3.03	3.02	3.04	3.02	2.46	2.49	2.72	2.70	2.68	2.68	2.70	2.47	2.46	2.98	2.45	2.99	2.49
4.00	4.00	4.00	4.01	4.00	3.99	4.01	3.99	4.01	3.99	3.99	3.99	4.03	4.03	4.01	4.02	4.01	4.02
0.00	0.00	0.00	3.31	1.19	56.69	51.56	31.54	31.57	34.58	34.43	33.96	55.45	53.99	0.00	57.35	0.00	47.75
6.35	5.48	6.13	7.88	7.19	41.17	43.08	64.79	57.20	62.40	62.18	62.98	42.94	44.55	100.00	41.70	100.00	48.60
93.65	94.52	93.87	88.81	91.63	2.14	5.36	3.67	11.24	3.02	3.39	3.06	1.61	1.46	0.00	0.95	0.00	3.66

6A lamp.																	
70	71	72	73	74	75	76	77	78	79	80	81	82	83	84	85	86	87
10.17	1.20	0.55	0.68	1.09	0.42	5.29	0.55	4.79	5.45	8.73	9.07	0.74	10.10	4.35	9.12	11.76	0.15
0.00	0.00	0.00	0.00	0.00	0.00	0.00	0.00	0.14	0.49	0.00	0.00	0.00	0.00	0.00	0.00	0.00	0.00
21.51	19.13	18.87	18.80	18.81	19.13	28.24	19.11	27.88	27.71	22.66	22.21	18.39	21.24	29.75	22.40	20.36	18.32
67.09	65.60	66.08	65.54	65.46	64.67	57.01	64.83	57.24	55.82	63.91	64.42	65.15	66.23	53.01	64.82	67.46	65.09
0.00	14.45	15.29	14.99	14.82	15.79	0.78	15.46	1.93	1.09	1.11	0.53	15.86	0.34	0.53	0.75	0.24	16.67
1.47	0.17	0.00	0.00	0.00	0.00	8.95	0.00	7.89	8.94	3.92	3.00	0.00	1.98	12.11	2.38	0.82	0.00

0.00	0.00	0.00	0.00	0.00	0.00	0.00	0.00	0.00	0.00	0.00	0.00	0.00	0.00	0.00	0.00	0.00	0.00
0.00	0.00	0.00	0.00	0.00	0.00	0.00	0.00	0.00	0.00	0.00	0.00	0.00	0.00	0.00	0.00	0.00	0.00
0.17	0.00	0.00	0.00	0.16	0.31	0.49	0.00	0.23	0.59	0.19	0.00	0.00	0.18	0.29	0.00	0.00	0.18
100.41	100.53	100.79	100.01	100.35	100.73	100.91	100.56	100.28	100.09	100.52	99.24	100.15	100.28	100.05	99.47	100.63	100.41
0.86	0.11	0.05	0.06	0.10	0.04	0.46	0.05	0.42	0.48	0.75	0.78	0.07	0.86	0.38	0.78	1.00	0.01
0.07	0.01	0.00	0.00	0.00	0.00	0.43	0.00	0.38	0.43	0.19	0.14	0.00	0.09	0.59	0.11	0.04	0.00
0.00	0.84	0.89	0.88	0.86	0.93	0.04	0.91	0.11	0.06	0.06	0.03	0.93	0.02	0.03	0.04	0.01	0.98
0.00	0.00	0.00	0.00	0.00	0.00	0.00	0.00	0.01	0.03	0.00	0.00	0.00	0.00	0.00	0.00	0.00	0.00
0.01	0.00	0.00	0.00	0.01	0.01	0.02	0.00	0.01	0.02	0.01	0.00	0.00	0.01	0.01	0.00	0.00	0.01
0.93	0.95	0.94	0.94	0.97	0.98	0.95	0.96	0.92	1.03	1.00	0.95	1.00	0.98	1.01	0.94	1.05	1.00
1.10	1.03	1.01	1.02	1.01	1.04	1.48	1.03	1.47	1.47	1.18	1.16	1.00	1.10	1.59	1.17	1.05	1.00
2.92	2.99	3.01	3.00	3.00	2.97	2.54	2.98	2.56	2.52	2.82	2.86	3.00	2.91	2.40	2.86	2.94	3.00
4.02	4.02	4.02	4.02	4.01	4.01	4.02	4.01	4.03	3.99	4.00	4.02	4.00	4.00	3.99	4.03	3.99	4.00
7.38	7.20	0.00	0.00	0.00	0.00	47.35	0.00	47.16	46.44	19.74	15.48	0.00	9.72	59.94	12.63	3.71	0.00
91.96	92.80	100.00	100.00	93.91	75.86	50.63	100.00	51.78	51.15	79.52	84.52	100.00	89.59	38.92	87.37	96.29	65.82
0.67	0.00	0.00	0.00	6.09	24.14	2.02	0.00	1.07	2.41	0.74	0.00	0.00	0.69	1.13	0.00	0.00	34.18

| 14(3)
Aigoual
pluton |
|----------------------------|----------------------------|----------------------------|----------------------------|----------------------------|----------------------------|----------------------------|----------------------------|----------------------------|----------------------------|----------------------------|----------------------------|----------------------------|----------------------------|----------------------------|----------------------------|----------------------------|----------------------------|
| 8 | 9 | 10 | 11 | 12 | 13 | 14 | 15 | 16 | 17 | 18 | 19 | 20 | 21 | | | | |
| 7.75 | 7.97 | 8.02 | 8.40 | 12.06 | 1.55 | 2.41 | 2.29 | 1.39 | 1.57 | 1.61 | 1.20 | 1.00 | 1.68 | | | | |
| 0.00 | 0.00 | 0.00 | 0.00 | 0.00 | 0.00 | 0.00 | 0.00 | 0.00 | 0.00 | 0.00 | 0.00 | 0.00 | 0.00 | | | | |
| 25.12 | 25.31 | 24.68 | 24.30 | 19.67 | 18.42 | 18.88 | 18.98 | 18.22 | 18.27 | 18.45 | 18.13 | 18.13 | 18.48 | | | | |
| 60.56 | 59.79 | 60.21 | 61.68 | 68.89 | 65.61 | 64.88 | 64.85 | 65.33 | 64.72 | 65.67 | 65.59 | 65.29 | 65.31 | | | | |
| 0.49 | 0.42 | 0.31 | 0.26 | 0.00 | 14.93 | 13.28 | 13.57 | 15.31 | 15.05 | 15.03 | 15.38 | 15.34 | 14.65 | | | | |
| 7.10 | 7.02 | 6.82 | 6.18 | 0.18 | 0.00 | 0.00 | 0.00 | 0.00 | 0.00 | 0.00 | 0.00 | 0.00 | 0.00 | | | | |

0.00	0.00	0.00	0.00	0.00	0.00	0.00	0.00	0.00	0.00	0.00	0.00	0.00	0.00	0.00	0.00	0.00
0.00	0.00	0.00	0.00	0.00	0.00	0.00	0.00	0.00	0.00	0.00	0.00	0.00	0.00	0.00	0.00	0.00
0.00	0.00	0.00	0.00	0.00	0.00	0.00	0.00	0.00	0.00	0.00	0.00	0.00	0.00	0.00	0.00	0.00
101.01	100.50	100.04	100.82	100.80	100.51	99.45	99.69	100.25	99.62	100.76	100.30	99.76	100.13			
0.66	0.69	0.69	0.72	1.01	0.14	0.21	0.20	0.12	0.14	0.14	0.11	0.09	0.15			
0.34	0.34	0.33	0.29	0.01	0.00	0.00	0.00	0.00	0.00	0.00	0.00	0.00	0.00	0.00	0.00	0.00
0.00	0.00	0.00	0.00	0.00	0.00	0.00	0.00	0.00	0.00	0.00	0.00	0.00	0.00	0.00	0.00	0.00
0.00	0.00	0.00	0.00	0.00	0.00	0.00	0.00	0.00	0.00	0.00	0.00	0.00	0.00	0.00	0.00	0.00
0.03	0.02	0.02	0.01	0.00	0.87	0.78	0.80	0.90	0.89	0.88	0.90	0.90	0.86			
1.03	1.05	1.04	1.03	1.02	1.01	0.99	1.00	1.02	1.03	1.02	1.01	0.99	1.01			
1.31	1.33	1.30	1.26	1.01	0.99	1.02	1.03	0.99	1.00	0.99	0.98	0.99	1.00			
2.68	2.66	2.69	2.72	2.99	3.00	2.98	2.98	3.00	3.00	3.00	3.01	3.01	3.00			
3.99	3.99	3.98	3.99	3.99	4.00	4.01	4.01	3.99	3.99	3.99	4.00	4.00				
32.72	32.03	31.44	28.50	0.82	0.00	0.00	0.00	0.00	0.00	0.00	0.00	0.00				
64.58	65.71	66.85	70.05	99.18	13.60	21.60	20.38	12.16	13.70	14.03	10.61	9.05	14.88			
2.69	2.26	1.71	1.45	0.00	86.40	78.40	79.62	87.84	86.30	85.97	89.39	90.95	85.12			

12B lamp.	12B granite	12A granite	12A granite	12A granite	12A granite	12A granite											
4	5	6	7	8	9	10	11	12	13	14	15	1	2	3	4	5	6
7.34	7.42	7.29	7.19	7.28	7.28	7.31	7.26	7.40	7.60	7.20	7.77	7.79	7.81	7.55	7.57	7.45	7.04
0.00	0.00	0.00	0.00	0.00	0.00	0.00	0.00	0.00	0.00	0.00	0.00	0.00	0.00	0.00	0.00	0.00	0.00
24.96	25.51	25.97	25.93	25.19	25.34	25.32	25.41	25.36	24.93	25.47	24.48	25.77	25.62	26.03	25.18	25.39	26.71
59.94	61.62	60.55	60.97	60.35	60.19	60.40	60.08	60.70	60.96	60.49	61.58	59.70	60.38	59.91	58.96	59.42	58.04
0.62	0.61	0.52	0.50	0.54	0.60	0.52	0.55	0.59	0.52	0.53	0.69	0.46	0.58	0.50	0.53	0.49	0.32
6.98	7.27	7.83	7.93	7.32	7.44	7.44	7.47	7.34	6.94	7.66	6.44	7.45	7.22	7.69	7.28	7.41	8.74

0.00	0.00	0.00	0.00	0.00	0.00	0.00	0.00	0.00	0.00	0.00	0.00	0.00	0.00	0.00	0.00	0.00	0.00
0.00	0.00	0.00	0.00	0.00	0.00	0.00	0.00	0.00	0.00	0.00	0.00	0.00	0.00	0.00	0.00	0.00	0.00
0.00	0.00	0.00	0.00	0.00	0.00	0.00	0.00	0.00	0.00	0.00	0.00	0.00	0.00	0.00	0.00	0.00	0.00
99.84	102.43	102.34	102.53	100.82	100.85	101.14	100.93	101.62	100.95	101.50	101.23	101.16	101.62	101.68	99.52	100.16	100.85
0.64	0.63	0.62	0.61	0.63	0.63	0.63	0.62	0.63	0.65	0.62	0.66	0.67	0.67	0.64	0.66	0.64	0.61
0.33	0.34	0.37	0.37	0.35	0.35	0.35	0.36	0.35	0.33	0.36	0.30	0.35	0.34	0.36	0.35	0.35	0.42
0.00	0.00	0.00	0.00	0.00	0.00	0.00	0.00	0.00	0.00	0.00	0.00	0.00	0.00	0.00	0.00	0.00	0.00
0.00	0.00	0.00	0.00	0.00	0.00	0.00	0.00	0.00	0.00	0.00	0.00	0.00	0.00	0.00	0.00	0.00	0.00
0.04	0.03	0.03	0.03	0.03	0.03	0.03	0.03	0.03	0.03	0.03	0.04	0.03	0.03	0.03	0.03	0.03	0.02
1.01	1.00	1.02	1.01	1.00	1.01	1.01	1.01	1.01	1.01	1.01	1.01	1.05	1.04	1.04	1.04	1.03	1.04
1.31	1.31	1.34	1.33	1.32	1.32	1.32	1.33	1.32	1.30	1.32	1.27	1.34	1.33	1.35	1.33	1.34	1.40
2.68	2.68	2.65	2.66	2.67	2.67	2.67	2.66	2.67	2.69	2.67	2.72	2.64	2.66	2.64	2.65	2.65	2.58
3.99	3.99	3.99	3.99	3.99	3.99	3.99	3.99	3.99	3.99	3.99	3.99	3.99	3.99	3.99	3.99	3.99	3.99
33.28	33.96	36.22	36.84	34.66	34.92	34.96	35.15	34.27	32.58	35.94	30.24	33.75	32.77	35.06	33.70	34.55	40.03
63.21	62.62	60.94	60.37	62.29	61.74	62.12	61.78	62.45	64.50	61.08	65.92	63.80	64.11	62.22	63.39	62.76	58.23
3.51	3.41	2.85	2.79	3.06	3.34	2.93	3.07	3.28	2.92	2.98	3.84	2.45	3.13	2.72	2.91	2.69	1.74

| 12A
granite |
|----------------|----------------|----------------|----------------|----------------|----------------|----------------|
| 7 | 8 | 9 | 10 | 11 | 12 | 13 |
| 7.47 | 7.20 | 7.95 | 7.52 | 8.16 | 7.70 | 7.81 |
| 0.00 | 0.00 | 0.00 | 0.00 | 0.00 | 0.00 | 0.00 |
| 25.73 | 25.50 | 25.06 | 25.98 | 25.01 | 25.09 | 25.00 |
| 59.69 | 58.61 | 60.18 | 59.89 | 61.17 | 59.21 | 59.17 |
| 0.41 | 0.80 | 0.52 | 0.52 | 0.68 | 0.54 | 0.57 |
| 7.68 | 7.72 | 6.91 | 7.48 | 6.52 | 7.10 | 6.97 |
| 0.00 | 0.00 | 0.00 | 0.00 | 0.00 | 0.00 | 0.00 |
| 0.00 | 0.00 | 0.00 | 0.00 | 0.00 | 0.00 | 0.00 |
| 0.00 | 0.00 | 0.00 | 0.00 | 0.00 | 0.00 | 0.00 |
| 100.98 | 99.82 | 100.62 | 101.40 | 101.54 | 99.63 | 99.53 |
| 0.64 | 0.63 | 0.68 | 0.64 | 0.70 | 0.67 | 0.68 |
| 0.37 | 0.37 | 0.33 | 0.35 | 0.31 | 0.34 | 0.34 |
| 0.00 | 0.00 | 0.00 | 0.00 | 0.00 | 0.00 | 0.00 |
| 0.00 | 0.00 | 0.00 | 0.00 | 0.00 | 0.00 | 0.00 |
| 0.02 | 0.05 | 0.03 | 0.03 | 0.04 | 0.03 | 0.03 |
| 1.03 | 1.05 | 1.04 | 1.03 | 1.04 | 1.04 | 1.05 |
| 1.34 | 1.35 | 1.31 | 1.35 | 1.30 | 1.33 | 1.32 |
| 2.64 | 2.63 | 2.67 | 2.64 | 2.69 | 2.66 | 2.66 |
| 3.99 | 3.98 | 3.98 | 3.99 | 3.99 | 3.99 | 3.98 |
| 35.45 | 35.58 | 31.57 | 34.48 | 29.55 | 32.80 | 32.01 |
| 62.31 | 60.02 | 65.62 | 62.64 | 66.78 | 64.26 | 64.85 |
| 2.23 | 4.40 | 2.82 | 2.88 | 3.67 | 2.94 | 3.14 |

Table 5 Mineral chemistry of pyroxene

Sample	4A granite	4A granite	4A granite	4A granite	4A granite	4A granite	4A granite	4A granite	4A granite	4A granite	4A granite	4A granite	4A granite	4A granite	4A granite	4A granite	4A granite	
Spectrum	4	5	6	7	8	9	10	11	12	13	14	15	16	17	18	19	20	
SiO ₂	51.94	52.09	52.29	51.73	51.13	53.52	55.60	52.70	55.21	52.56	51.61	51.91	51.39	51.68	52.27	51.05	51.59	
TiO ₂	0.61	0.63	0.65	0.73	0.75	0.56	0.18	0.70	0.29	0.62	0.76	0.72	0.62	0.60	0.59	0.78	0.66	
Al ₂ O ₃	4.56	4.20	4.00	5.00	5.03	3.43	1.83	4.68	2.15	4.08	4.59	4.70	4.48	4.27	4.10	4.85	4.30	
Cr ₂ O ₃	0.00	0.19	0.18	0.00	0.19	0.18	0.21	0.41	0.33	0.19	0.16	0.19	0.23	0.17	0.00	0.15	0.15	
Fe ₂ O ₃	0.00	0.00	0.00	0.07	0.00	0.00	0.00	0.00	0.00	0.00	0.00	0.00	0.00	0.00	0.00	0.87	0.00	
FeO	15.17	15.16	15.56	15.11	15.23	15.08	13.50	13.14	11.88	15.52	15.19	15.54	15.69	15.92	15.13	14.68	15.94	
MnO	0.62	0.49	0.45	0.51	0.50	0.47	0.56	0.47	0.43	0.59	0.51	0.49	0.52	0.54	0.48	0.56	0.51	
MgO	14.47	14.47	14.50	14.34	14.03	14.76	15.87	15.15	16.69	14.48	14.69	14.24	13.97	14.40	14.80	14.18	13.98	
CaO	11.60	11.24	11.40	11.65	11.33	11.68	12.26	12.08	12.33	11.40	11.32	11.39	11.28	11.09	11.28	11.36	11.32	
Na ₂ O	1.07	0.88	0.95	1.07	0.96	0.67	0.38	0.68	0.43	0.94	1.00	1.00	0.99	0.92	0.89	1.16	0.96	
K ₂ O	0.41	0.33	0.33	0.48	0.46	0.25	0.09	0.33	0.00	0.39	0.36	0.41	0.39	0.30	0.28	0.42	0.41	
TOTAL	100.44	99.68	100.31	100.69	99.60	100.59	100.48	100.34	99.75	100.76	100.18	100.59	99.56	99.90	99.83	100.08	99.82	
*	Structural formula based on 6O																	
Si	1.93	1.95	1.95	1.92	1.92	1.98	2.04	1.94	2.02	1.95	1.92	1.93	1.93	1.94	1.95	1.91	1.94	
Al (iv)	0.07	0.05	0.05	0.08	0.08	0.02	-0.04	0.06	-0.02	0.05	0.08	0.07	0.07	0.06	0.05	0.09	0.06	
Sum	2.00	2.00	2.00	2.00	2.00	2.00	2.00	2.00	2.00	2.00	2.00	2.00	2.00	2.00	2.00	2.00	2.00	
Al (vi)	0.13	0.13	0.12	0.14	0.14	0.13	0.11	0.14	0.11	0.13	0.12	0.13	0.13	0.12	0.13	0.13	0.13	
Fe(iii)	0.00	0.00	0.00	0.00	0.00	0.00	0.00	0.00	0.00	0.00	0.00	0.00	0.00	0.00	0.00	0.02	0.00	
Cr	0.00	0.01	0.01	0.00	0.01	0.01	0.01	0.01	0.01	0.01	0.00	0.01	0.01	0.01	0.00	0.00	0.00	
Ti	0.02	0.02	0.02	0.02	0.02	0.02	0.00	0.02	0.01	0.02	0.02	0.02	0.02	0.02	0.02	0.02	0.02	
Fe(ii)	0.47	0.48	0.49	0.47	0.48	0.47	0.42	0.41	0.37	0.48	0.47	0.48	0.49	0.50	0.47	0.46	0.50	
Mn	0.02	0.02	0.01	0.02	0.02	0.01	0.02	0.01	0.01	0.02	0.02	0.02	0.02	0.02	0.02	0.02	0.02	
Mg	0.80	0.81	0.80	0.79	0.78	0.81	0.87	0.83	0.91	0.80	0.82	0.79	0.78	0.80	0.82	0.79	0.78	
Ca	0.46	0.45	0.45	0.46	0.46	0.46	0.48	0.48	0.48	0.45	0.45	0.45	0.44	0.45	0.46	0.46	0.46	
Na	0.08	0.06	0.07	0.08	0.07	0.05	0.03	0.05	0.03	0.07	0.07	0.07	0.07	0.07	0.06	0.08	0.07	
K	0.02	0.02	0.02	0.02	0.02	0.01	0.00	0.02	0.00	0.02	0.02	0.02	0.01	0.01	0.02	0.02	0.02	

TOTAL	4.00	3.98	3.99	4.00	3.99	3.97	3.94	3.97	3.94	3.99	4.00	3.99	3.99	3.99	3.99	4.01	3.99
Wo	25.21	24.84	24.87	25.44	25.25	25.56	26.55	26.78	26.74	24.85	24.69	25.01	24.96	24.28	24.68	24.87	24.95
En	43.78	44.50	44.04	43.59	43.49	44.96	47.81	46.73	50.37	43.94	44.60	43.51	43.02	43.87	45.02	43.19	42.87
Fs	26.80	27.15	27.36	26.74	27.40	26.84	24.15	23.76	21.19	27.52	26.76	27.52	28.04	28.19	26.76	27.34	28.37
Ac	4.20	3.51	3.73	4.22	3.87	2.64	1.49	2.73	1.70	3.69	3.95	3.96	3.98	3.65	3.53	4.60	3.81
Wo	26.32	25.75	25.83	26.57	26.26	26.25	26.95	27.53	27.21	25.81	25.71	26.04	26.00	25.20	25.58	26.07	25.94
En	45.70	46.11	45.74	45.51	45.24	46.18	48.53	48.04	51.24	45.62	46.43	45.30	44.80	45.54	46.67	45.27	44.57
Fs	27.98	28.14	28.43	27.92	28.50	27.57	24.52	24.43	21.56	28.57	27.86	28.66	29.20	29.26	27.75	28.66	29.49

4A granite	4A granite	4A granite	4A granite	4A granite	14(3) Aigoual pluton						
21	22	23	24	25	1	2	3	4	5	6	
51.49	52.52	51.98	52.84	51.82	52.17	51.80	51.11	53.23	51.52	51.39	
0.54	0.44	0.67	0.60	0.68	0.46	0.50	0.59	0.27	0.56	0.48	
4.57	4.00	4.44	4.10	4.53	3.08	3.72	4.28	2.35	3.91	3.99	
0.21	0.18	0.00	0.00	0.16	0.19	0.92	1.02	0.58	0.66	0.68	
0.00	0.00	0.00	0.00	0.00	0.00	0.00	0.15	0.00	0.40	0.11	
15.39	15.60	15.70	15.23	15.29	15.74	16.08	16.18	15.37	16.14	16.17	
0.53	0.61	0.47	0.52	0.54	0.64	0.61	0.69	0.60	0.67	0.63	
14.15	14.52	14.31	14.65	14.45	14.21	13.98	13.30	14.76	13.90	13.90	
11.36	11.42	11.58	11.58	11.49	11.80	11.67	11.84	11.87	11.82	11.81	
1.00	0.94	0.96	0.96	0.91	0.86	0.90	1.06	0.60	0.96	0.86	
0.38	0.33	0.40	0.34	0.40	0.20	0.32	0.31	0.13	0.29	0.39	
99.63	100.57	100.50	100.82	100.26	99.36	100.50	100.55	99.76	100.84	100.42	
1.93	1.95	1.93	1.95	1.93	1.97	1.94	1.92	1.99	1.93	1.93	
0.07	0.05	0.07	0.05	0.07	0.03	0.06	0.08	0.01	0.07	0.07	
2.00	2.00	2.00	2.00	2.00	2.00	2.00	2.00	2.00	2.00	2.00	
0.13	0.13	0.13	0.13	0.13	0.10	0.10	0.11	0.09	0.10	0.10	

0.00	0.00	0.00	0.00	0.00	0.00	0.00	0.00	0.00	0.00	0.01	0.00
0.01	0.01	0.00	0.00	0.00	0.01	0.03	0.03	0.02	0.02	0.02	0.02
0.02	0.01	0.02	0.02	0.02	0.01	0.01	0.02	0.01	0.02	0.02	0.01
0.48	0.49	0.49	0.47	0.48	0.50	0.50	0.51	0.48	0.50	0.51	0.51
0.02	0.02	0.01	0.02	0.02	0.02	0.02	0.02	0.02	0.02	0.02	0.02
0.79	0.80	0.79	0.81	0.80	0.80	0.78	0.74	0.82	0.78	0.78	0.78
0.46	0.45	0.46	0.46	0.46	0.48	0.47	0.48	0.48	0.47	0.47	0.47
0.07	0.07	0.07	0.07	0.07	0.06	0.07	0.08	0.04	0.07	0.07	0.06
0.02	0.02	0.02	0.02	0.02	0.01	0.02	0.02	0.01	0.01	0.01	0.02
3.99	3.99	3.99	3.99	3.99	3.99	3.99	4.00	3.97	4.00	4.00	4.00
25.08	24.82	25.24	25.15	25.18	25.67	25.48	26.00	25.77	25.54	25.73	
43.45	43.90	43.41	44.27	44.07	43.02	42.48	40.62	44.59	41.78	42.14	
27.49	27.58	27.58	26.82	27.15	27.92	28.50	29.14	27.29	28.92	28.76	
3.99	3.70	3.77	3.77	3.60	3.39	3.54	4.23	2.34	3.76	3.37	
26.12	25.77	26.23	26.14	26.12	26.57	26.41	27.15	26.39	26.53	26.63	
45.25	45.59	45.11	46.00	45.71	44.53	44.04	42.42	45.66	43.41	43.61	
28.63	28.64	28.66	27.87	28.17	28.90	29.55	30.43	27.95	30.05	29.76	

| 14(3)
Aigoual
pluton |
|----------------------------|----------------------------|----------------------------|----------------------------|----------------------------|----------------------------|----------------------------|----------------------------|----------------------------|----------------------------|----------------------------|----------------------------|----------------------------|----------------------------|----------------------------|----------------------------|
| 7 | 8 | 9 | 10 | 11 | 12 | 13 | 14 | 15 | 16 | 17 | 18 | 19 | 20 | 21 | |
| 50.95 | 53.77 | 51.05 | 51.16 | 52.89 | 53.78 | 52.87 | 50.85 | 51.88 | 50.62 | 50.51 | 50.90 | 51.06 | 53.95 | 53.46 | |
| 0.62 | 0.20 | 0.71 | 0.59 | 0.21 | 0.29 | 0.40 | 0.56 | 0.47 | 0.73 | 0.63 | 0.69 | 0.62 | 0.22 | 0.42 | |
| 4.57 | 2.01 | 4.73 | 4.64 | 2.65 | 2.30 | 2.74 | 4.77 | 3.54 | 4.77 | 4.83 | 4.87 | 4.65 | 2.55 | 2.75 | |
| 0.23 | 0.23 | 0.16 | 0.30 | 0.33 | 0.19 | 0.49 | 0.41 | 0.25 | 0.18 | 0.20 | 0.00 | 0.00 | 0.22 | 0.17 | |
| 0.05 | 0.00 | 1.50 | 1.50 | 0.00 | 0.00 | 0.00 | 1.46 | 0.00 | 1.65 | 2.38 | 2.28 | 1.47 | 0.00 | 0.00 | |
| 16.30 | 14.78 | 15.38 | 15.32 | 15.72 | 15.58 | 15.86 | 15.53 | 16.09 | 15.46 | 14.41 | 14.51 | 15.46 | 15.25 | 15.96 | |

0.58	0.46	0.50	0.49	0.67	0.66	0.63	0.68	0.59	0.66	0.52	0.63	0.51	0.48	0.70
13.61	15.25	13.54	13.79	14.79	15.17	14.53	13.61	14.21	13.62	13.64	13.74	13.79	15.21	14.84
11.71	12.42	11.77	11.51	11.72	11.83	11.65	11.76	11.76	11.39	11.79	11.67	11.81	12.43	12.13
0.90	0.46	1.13	1.11	0.53	0.63	0.65	1.00	0.83	1.08	1.14	1.18	1.01	0.52	0.70
0.37	0.00	0.45	0.47	0.25	0.10	0.17	0.37	0.22	0.39	0.43	0.47	0.41	0.14	0.13
99.89	99.58	100.92	100.88	99.76	100.53	99.99	101.00	99.84	100.54	100.49	100.93	100.79	100.96	101.24
1.92	2.01	1.91	1.91	1.98	1.99	1.98	1.90	1.95	1.90	1.90	1.91	1.91	1.99	1.98
0.08	-0.01	0.09	0.09	0.02	0.01	0.02	0.10	0.05	0.10	0.10	0.09	0.09	0.01	0.02
2.00	2.00	2.00	2.00	2.00	2.00	2.00	2.00	2.00	2.00	2.00	2.00	2.00	2.00	2.00
0.12	0.09	0.12	0.12	0.10	0.09	0.10	0.11	0.11	0.12	0.12	0.12	0.12	0.10	0.09
0.00	0.00	0.04	0.04	0.00	0.00	0.00	0.04	0.00	0.05	0.07	0.06	0.04	0.00	0.00
0.01	0.01	0.00	0.01	0.01	0.01	0.01	0.01	0.01	0.01	0.01	0.00	0.00	0.01	0.00
0.02	0.01	0.02	0.02	0.01	0.01	0.01	0.02	0.01	0.02	0.02	0.02	0.02	0.01	0.01
0.51	0.47	0.48	0.48	0.50	0.49	0.50	0.48	0.51	0.48	0.45	0.45	0.48	0.47	0.50
0.02	0.01	0.02	0.02	0.02	0.02	0.02	0.02	0.02	0.02	0.02	0.02	0.02	0.02	0.02
0.76	0.85	0.76	0.77	0.83	0.84	0.81	0.76	0.80	0.76	0.77	0.77	0.77	0.84	0.82
0.47	0.50	0.47	0.46	0.47	0.47	0.47	0.47	0.47	0.46	0.48	0.47	0.47	0.49	0.48
0.07	0.03	0.08	0.08	0.04	0.04	0.05	0.07	0.06	0.08	0.08	0.09	0.07	0.04	0.05
0.02	0.00	0.02	0.02	0.01	0.00	0.01	0.02	0.01	0.02	0.02	0.02	0.02	0.01	0.01
4.00	3.96	4.01	4.01	3.98	3.97	3.98	4.01	3.99	4.01	4.02	4.02	4.01	3.97	3.98
25.74	26.71	25.56	24.99	25.40	25.26	25.33	25.49	25.52	24.77	25.58	25.22	25.51	26.49	25.74
41.64	45.63	40.91	41.66	44.61	45.05	43.95	41.03	42.90	41.21	41.18	41.32	41.48	45.12	43.84
29.04	25.86	29.10	28.99	27.91	27.27	28.17	29.55	28.33	29.78	28.77	28.85	29.08	26.38	27.74
3.58	1.81	4.44	4.36	2.08	2.42	2.55	3.93	3.25	4.24	4.47	4.61	3.93	2.00	2.67
26.70	27.20	26.75	26.13	25.94	25.88	25.99	26.53	26.38	25.86	26.77	26.44	26.56	27.03	26.45
43.19	46.47	42.80	43.56	45.56	46.17	45.10	42.70	44.34	43.03	43.11	43.31	43.18	46.04	45.05
30.12	26.34	30.45	30.31	28.50	27.95	28.91	30.76	29.28	31.10	30.12	30.25	30.27	26.92	28.50

Table 6 Mineral chemistry of amphibole

Sample	4C lamp.	4C lamp.	4C lamp.	4C lamp.	4C lamp.	4C lamp.	4C lamp.	4C lamp.	4C lamp.	4C lamp.	4C lamp.
Spectrum	1	2	3	4	5	6	7	8	9	10	11
SiO ₂	54.34	54.65	54.51	56.09	55.16	54.14	54.22	53.40	55.13	54.26	54.54
TiO ₂	0.21	0.20	0.16	0.00	0.00	0.17	0.16	0.30	0.00	0.23	0.23
Al ₂ O ₃	2.30	2.29	1.84	0.72	2.31	1.93	2.57	2.96	1.92	2.14	2.13
Cr ₂ O ₃	0.00	0.00	0.00	0.00	0.00	0.00	0.00	0.00	0.00	0.00	0.00
Fe ₂ O ₃	2.24	2.87	1.26	3.07	2.68	2.49	3.27	3.46	2.27	0.00	0.00
FeO	9.73	9.38	10.09	4.66	9.54	9.94	9.05	8.83	9.40	11.75	11.97
MnO	0.41	0.48	0.47	0.48	0.41	0.56	0.53	0.50	0.51	0.32	0.33
MgO	15.87	15.99	16.20	19.29	16.16	15.85	16.00	15.75	16.38	14.98	15.09
CaO	12.04	12.11	12.31	12.27	12.14	12.25	12.08	11.89	12.27	12.04	12.11
Na ₂ O	0.38	0.31	0.44	0.20	0.49	0.42	0.52	0.54	0.39	0.38	0.31
K ₂ O	0.09	0.12	0.00	0.00	0.00	0.00	0.00	0.11	0.00	0.09	0.12
TOTAL	97.61	98.38	97.29	96.79	98.88	97.74	98.40	97.75	98.27	96.20	96.82
*	Structural formula based on 23O										
Si	7.76	7.74	7.81	7.90	7.77	7.75	7.69	7.63	7.81	7.88	7.87
Al (iv)	0.24	0.26	0.19	0.10	0.23	0.25	0.31	0.37	0.19	0.12	0.13
T	8.00	8.00	8.00	8.00	8.00	8.00	8.00	8.00	8.00	8.00	8.00
Al (vi)	0.15	0.13	0.12	0.02	0.15	0.07	0.12	0.13	0.13	0.24	0.24
Ti	0.02	0.02	0.02	0.00	0.00	0.02	0.02	0.03	0.00	0.02	0.03
Cr	0.00	0.00	0.00	0.00	0.00	0.00	0.00	0.00	0.00	0.00	0.00
Fe(iii)	0.24	0.31	0.14	0.33	0.28	0.27	0.35	0.37	0.24	0.00	0.00
Fe(ii)	1.16	1.11	1.21	0.55	1.12	1.19	1.07	1.05	1.11	1.43	1.44
Mn	0.05	0.06	0.06	0.06	0.05	0.07	0.06	0.06	0.06	0.04	0.04
Mg	3.38	3.38	3.46	4.05	3.39	3.38	3.38	3.35	3.46	3.24	3.25
Sum	5.00	5.00	5.00	5.00	5.00	5.00	5.00	5.00	5.00	4.98	4.99
Ca	1.84	1.84	1.89	1.85	1.83	1.88	1.84	1.82	1.86	1.87	1.87

Na	0.10	0.08	0.11	0.06	0.13	0.12	0.14	0.15	0.11	0.11	0.09
Sum	1.95	1.92	2.00	1.91	1.96	1.99	1.98	1.97	1.97	1.98	1.96
Na	0.00	0.00	0.01	0.00	0.00	0.00	0.00	0.00	0.00	0.00	0.00
K	0.02	0.02	0.00	0.00	0.00	0.00	0.00	0.02	0.00	0.02	0.02
Sum	0.02	0.02	0.01	0.00	0.00	0.00	0.00	0.02	0.00	0.02	0.02
Mg#	0.74	0.75	0.74	0.88	0.75	0.74	0.76	0.76	0.76	0.69	0.69
Classification	actinolite										

4C lamp.	4C lamp.	4C lamp.	4C lamp.	6E granite	6E granite	6C granite	6C granite
12	13	14	1	2	3	4	5
55.21	55.61	54.13	54.83	54.76	52.14	53.46	54.97
0.25	0.26	0.28	0.36	0.00	0.68	0.00	0.14
2.03	1.80	2.43	1.99	2.34	4.01	3.63	2.04
0.00	0.00	0.00	0.00	0.00	0.00	0.00	0.34
0.00	0.00	0.26	0.58	0.00	1.87	4.00	3.92
12.26	12.31	11.88	11.73	14.59	13.35	10.55	5.83
0.30	0.24	0.69	0.31	0.00	0.00	0.42	0.39
15.05	15.32	15.14	15.48	13.52	13.44	13.92	17.44
12.31	12.58	12.26	12.29	12.68	11.55	11.55	11.73
0.49	0.33	0.55	0.38	0.34	0.91	0.28	0.25
0.00	0.09	0.11	0.00	0.00	0.39	0.00	0.00
97.90	98.56	97.74	97.95	98.23	98.33	97.81	97.05
7.89	7.89	7.78	7.83	7.88	7.53	7.66	7.78
0.11	0.11	0.22	0.17	0.12	0.47	0.34	0.22
8.00	8.00	8.00	8.00	8.00	8.00	8.00	8.00

0.23	0.20	0.19	0.16	0.27	0.22	0.28	0.12
0.03	0.03	0.03	0.04	0.00	0.07	0.00	0.01
0.00	0.00	0.00	0.00	0.00	0.00	0.00	0.04
0.00	0.00	0.03	0.06	0.00	0.20	0.43	0.42
1.46	1.46	1.43	1.40	1.75	1.61	1.26	0.69
0.04	0.03	0.08	0.04	0.00	0.00	0.05	0.05
3.21	3.24	3.24	3.30	2.90	2.89	2.97	3.68
4.96	4.96	5.00	5.00	4.93	5.00	5.00	5.00
1.88	1.91	1.89	1.88	1.95	1.79	1.77	1.78
0.12	0.09	0.11	0.11	0.05	0.21	0.08	0.07
2.00	2.00	2.00	1.99	2.00	2.00	1.85	1.85
0.02	0.00	0.04	0.00	0.05	0.04	0.00	0.00
0.00	0.02	0.02	0.00	0.00	0.07	0.00	0.00
0.02	0.02	0.06	0.00	0.05	0.11	0.00	0.00
0.69	0.69	0.69	0.70	0.62	0.64	0.70	0.84
actinolite							

Table 7 Whole-rock Sr, Nd, Hf isotopes

Sample	Sm (ppm)	Nd (ppm)	$^{147}\text{Sm}/^{144}\text{Nd}$	$^{143}\text{Nd}/^{144}\text{Nd}_{\text{m}}$	$\pm 2 \text{ SE}$	$(^{143}\text{Nd}/^{144}\text{Nd})\text{t}$	$\pm 2 \text{ SE}$	$\epsilon\text{Nd}_{(\text{t})}$	$T_{\text{DM}}(\text{Ga})$
AG04C	8.12	42.10	0.1167	0.512199	0.000010	0.511961	1.0278E-05	-5.39	1.32
AG05C	8.88	45.80	0.1173	0.512197	0.000010	0.511958	1.0281E-05	-5.45	1.33
AG06C	8.68	45.60	0.1151	0.512210	0.000012	0.511976	1.2227E-05	-5.11	1.29
AG06E	8.72	44.70	0.1180	0.512204	0.000012	0.511964	1.2238E-05	-5.34	1.33
AG06F	8.96	46.05	0.1176	0.512200	0.000016	0.511961	1.6178E-05	-5.41	1.33
AG09	10.45	58.40	0.1082	0.512238	0.000010	0.512018	1.0240E-05	-4.29	1.16
AG10A	11.07	62.17	0.1077	0.512235	0.000014	0.512016	1.4171E-05	-4.33	1.16
AG10B	5.70	29.19	0.1180	0.512253	0.000009	0.512013	9.3153E-06	-4.39	1.26
AG10D	6.90	37.10	0.1125	0.512230	0.000014	0.512001	1.4186E-05	-4.62	1.22
AG12A	7.66	41.20	0.1124	0.512219	0.000013	0.511990	1.3200E-05	-4.83	1.24
AG12B	10.04	58.54	0.1037	0.512264	0.000010	0.512053	1.0220E-05	-3.60	1.08
AG14(3)	8.78	43.10	0.1232	0.512211	0.000012	0.511960	1.2259E-05	-5.42	1.40

Sample	Rb (ppm)	Sr (ppm)	$^{87}\text{Rb}/^{86}\text{Sr}$	$^{87}\text{Sr}/^{86}\text{Sr}_{\text{m}}$	$\pm 2 \text{ SE}$	$(^{87}\text{Sr}/^{86}\text{Sr})\text{t}$	$\pm 2 \text{ SE}$
AG04C	186.85	336.45	1.6084	0.717702	0.000011	0.710583	7.203E-05
AG05C	227.25	431.50	1.5250	0.716184	0.000009	0.709434	6.809E-05
AG06C	214.05	418.95	1.4796	0.717086	0.000011	0.710537	6.64E-05
AG06E	226.00	438.00	1.4942	0.716861	0.000012	0.710248	6.721E-05
AG06F	257.45	475.55	1.5678	0.717573	0.000011	0.710634	7.026E-05
AG09	237.40	460.25	1.4934	0.715107	0.000011	0.708497	6.701E-05
AG10A	239.70	631.05	1.0996	0.713787	0.000009	0.708920	4.949E-05
AG10B	205.45	227.65	2.6146	0.721300	0.000009	0.709728	0.0001161
AG10D	196.60	314.30	1.8114	0.716984	0.000009	0.708967	8.068E-05
AG12A	225.20	355.50	1.8345	0.716957	0.000010	0.708838	8.181E-05
AG12B	187.70	566.70	0.9587	0.712273	0.000012	0.708030	4.41E-05

AG14(3)	226.8	465.25	1.4115	0.715656	0.000008	0.709409	6.298E-05
---------	-------	--------	--------	----------	----------	----------	-----------

Sample	Lu (ppm)	Hf (ppm)	$^{175}\text{Lu}/^{177}\text{Hf}$	$^{176}\text{Hf}/^{177}\text{Hf}_{\text{m}}$	$\pm 2 \text{ SE}$	Age	$(^{176}\text{Hf}/^{177}\text{Hf})t$	$\pm 2 \text{ SE}$	eHf(t)	error (t)
AG04C	0.31	7.18	0.006015	0.282453	0.000005	311	0.282452	0.000018	-4.92	0.19
AG05C	0.35	7.09	0.006896	0.282512	0.000006	311	0.282511	0.000013	-2.83	0.10
AG06C	0.33	8.29	0.005652	0.282513	0.000004	311	0.282512	0.000016	-2.79	0.15
AG06E	0.35	7.74	0.006403	0.282520	0.000004	311	0.282519	0.000016	-2.55	0.15
AG06F	0.34	7.92	0.006093	0.282510	0.000005	311	0.282509	0.000016	-2.90	0.15
AG09	0.34	9.17	0.005117	0.282552	0.000008	311	0.282551	0.000016	-1.41	0.15
AG10A	0.34	8.95	0.005274	0.282521	0.000009	311	0.282520	0.000016	-2.51	0.15
AG10B	0.27	4.13	0.009220	0.282585	0.000007	311	0.282584	0.000016	-0.26	0.15
AG10D	0.37	6.68	0.007718	0.282527	0.000007	311	0.282526	0.000016	-2.31	0.15
AG12A	0.35	7.07	0.006896	0.282494	0.000006	311	0.282493	0.000016	-3.47	0.15
AG12B	0.29	9.00	0.004553	0.282538	0.000007	311	0.282537	0.000016	-1.90	0.15
AG14(3)	0.33	8.48	0.005456	0.282487	0.000005	311	0.282486	0.000016	-3.71	0.15

Table 8 Zircon LA-SF-ICP-MS U-Pb geochronology data

Dyke 5 Sample, spot number	Isotopic ratios										Ages					
	U (ppm)	Th U	$\frac{^{207}\text{Pb}}{^{206}\text{Pb}}$	$\pm 2\sigma$ (%)	$\frac{^{207}\text{Pb}}{^{235}\text{U}}$	$\pm 2\sigma$ (%)	$\frac{^{206}\text{Pb}}{^{238}\text{U}}$	$\pm 2\sigma$ (%)	rho	$\frac{^{207}\text{Pb}}{^{206}\text{Pb}}$	$\pm 2\sigma$ (Ma)	$\frac{^{207}\text{Pb}}{^{235}\text{U}}$	$\pm 2\sigma$ (Ma)	$\frac{^{206}\text{Pb}}{^{238}\text{U}}$	$\pm 2\sigma$ (Ma)	conc. ^a (%)
AG05B - 1	983	0.10	0.053	1.498	0.378	1.614	0.051	1.263	0.78	333	33	323.9	4.1	325.2	4.5	100.40
AG05B - 19	733	1.17	0.059	1.489	0.699	2.289	0.087	1.954	0.85	564	33	537.7	9.9	537.6	9.6	99.98
AG05B - 46	407	0.25	0.053	1.229	0.374	1.552	0.051	1.187	0.76	304	44	323.1	3.7	310	5.4	95.95
AG05B - 42	334	0.41	0.054	0.987	0.382	1.099	0.052	1.001	0.91	295	53	312.7	2.8	312.1	6.9	99.81
AG05A - 2	529	0.71	0.053	1.758	0.359	1.837	0.049	1.007	0.55	334	39	311.3	4.9	306.1	3	98.33
AG05A - 6	495	0.35	0.054	1.866	0.368	2.009	0.050	1.080	0.54	341	42	318	5.5	314.4	3.3	98.87
AG05A - 16	416	0.77	0.062	1.417	0.938	1.386	0.110	1.181	0.85	675	29	671.3	6.7	673.2	7.4	100.28
AG05A - 39	272.8	0.47	0.053	2.820	0.347	2.882	0.047	1.317	0.46	322	61	302	7.8	296.6	3.8	98.21
AG05A - 43	393	0.62	0.053	2.268	0.369	2.276	0.050	1.176	0.52	320	51	318.3	6.2	315.5	3.6	99.12
AG05A - 58	617	0.46	0.053	1.894	0.367	1.907	0.050	1.052	0.55	310	42	317	5.2	316.8	3.2	99.94
AG05A - 59	809	1.20	0.054	1.655	0.380	1.686	0.051	1.277	0.76	348	36	326.3	4.7	320	4	98.07
AG05A - 67	457	0.53	0.052	1.923	0.366	2.131	0.051	0.968	0.45	277	42	316.3	5.8	318.3	3	100.63
AG05A - 78	210.4	0.46	0.054	2.612	0.358	2.567	0.049	1.145	0.45	328	58	310.2	6.9	307.8	3.4	99.23
AG05A - 79	277	0.36	0.052	2.682	0.351	2.706	0.049	1.206	0.45	277	59	304.8	7	308	3.6	101.05
AG05A - 80	511	0.35	0.053	1.724	0.359	1.756	0.049	1.121	0.64	328	39	310.9	4.7	308.8	3.4	99.32
AG05A - 84	656	0.86	0.053	1.622	0.364	1.813	0.050	1.004	0.55	317	36	314.8	4.9	313.2	3.1	99.49
AG05A - 87	185.5	0.07	0.060	2.852	0.729	3.155	0.088	1.586	0.50	563	62	554	13	545.4	8.5	98.45
AG05C - 2	685	0.12	0.054	2.048	0.359	2.173	0.049	1.366	0.63	338	45	312.3	5.8	308.6	4.1	98.82
AG05C - 29	997	0.29	0.053	2.087	0.376	2.206	0.050	1.810	0.82	297	46	323.8	6.1	316.1	5.6	97.62
AG05C - 36	726	0.40	0.053	2.647	0.376	3.457	0.051	1.826	0.53	318	58	324.9	8.9	320.1	5.7	98.52
AG05C - 38	323	0.39	0.053	2.260	0.363	2.317	0.049	1.221	0.53	310	50	313.5	6.2	309.3	3.7	98.66
AG05C - 40	387	0.41	0.053	2.087	0.363	2.041	0.050	1.312	0.64	298	45	313.6	5.5	311.7	4	99.39
AG05C - 4	118.3	0.23	0.059	4.068	0.712	4.213	0.088	2.743	0.65	517	88	543	18	541	14	99.63
AG05C - 6	219	0.36	0.062	2.258	0.910	2.527	0.106	1.700	0.67	647	51	654	12	649	10	99.24
AG05C - 12	172	0.80	0.055	3.853	0.370	4.054	0.050	2.020	0.50	348	85	318	11	311.2	6.1	97.86
AG05C - 13	291	0.84	0.054	3.525	0.368	3.533	0.050	1.603	0.45	334	76	317	9.6	313.9	4.9	99.02

AG05C - 14	553	0.32	0.053	2.448	0.402	2.414	0.055	1.631	0.68	318	53	343.1	7.2	346.1	5.5	100.87	
AG05C - 19	589	0.68	0.054	2.230	0.381	2.625	0.052	1.658	0.63	342	50	327.3	7.3	325.9	5.3	99.57	
AG05D - 41	492	0.42	0.053	2.642	0.370	3.514	0.051	2.335	0.66	302	59	318.4	9.5	322.7	7.5	101.35	
AG05D - 43	445	0.47	0.053	2.247	0.359	2.370	0.050	1.728	0.73	330	49	310.6	6.3	313.1	5.3	100.80	
AG05D - 54	577	0.53	0.053	2.079	0.349	2.206	0.049	1.410	0.64	305	45	303.5	5.8	307.8	4.3	101.42	
AG05D - 55	330	0.46	0.054	2.607	0.362	2.541	0.049	1.605	0.63	328	59	313.9	7.1	305.8	4.8	97.42	
AG05D - 25	596	0.26	0.052	2.500	0.341	2.496	0.046	1.729	0.69	281	53	297	6.4	291.5	4.9	98.15	
Dyke 10																	
AG10A - 4	525	0.50	0.053	1.810	0.362	1.879	0.050	1.322	0.70	291	40	313.1	5	314	4.1	100.29	
AG10A - 16	529	0.09	0.060	1.554	0.826	1.695	0.100	1.404	0.83	607	34	610.3	7.9	612.3	8.2	100.33	
AG10A - 31	466	0.65	0.053	2.825	0.361	3.324	0.050	1.835	0.55	310	64	313.7	9.4	311.9	5.6	99.43	
AG10A - 42	502.6	0.39	0.053	1.757	0.376	1.864	0.052	1.385	0.74	310	40	324.2	5.4	326.6	4.4	100.74	
AG10C - 1	219.1	0.32	0.064	1.890	1.041	2.305	0.119	1.591	0.69	712	41	722	12	727	11	100.69	
AG10C - 2	336.2	0.57	0.052	2.115	0.359	2.228	0.050	1.348	0.60	265	46	310.9	5.9	317.3	4.2	102.06	
AG10C - 3	338	0.52	0.054	2.226	0.368	2.389	0.050	1.592	0.67	346	49	317.8	6.5	316	4.9	99.43	
AG10C - 6	236.8	0.48	0.053	2.657	0.361	2.601	0.050	1.321	0.51	293	58	312.4	7	314.3	4	100.61	
AG10C - 9	761	0.41	0.053	1.749	0.358	1.983	0.050	1.358	0.68	296	40	310.2	5.3	314.9	4.1	101.52	
AG10C - 10	145.4	0.54	0.053	3.409	0.354	3.107	0.050	1.490	0.48	282	74	307.8	8.2	312.3	4.5	101.46	
AG10C - 11	866	0.36	0.055	1.669	0.421	2.613	0.057	2.124	0.81	381	38	355.8	8	353.9	7.1	99.47	
AG10C - 14	338.4	0.45	0.052	2.107	0.357	2.495	0.050	1.430	0.57	284	49	309	6.6	312.2	4.4	101.04	
AG10C - 19	352	0.41	0.053	2.095	0.353	2.010	0.049	1.425	0.71	291	45	306.7	5.3	309.1	4.3	100.78	
AG10C - 20	330.2	0.13	0.056	1.779	0.564	1.773	0.073	1.501	0.85	442	40	453.4	6.8	455.8	6.3	100.53	
AG10C - 24	252.1	0.44	0.052	2.490	0.353	2.496	0.049	1.284	0.51	270	53	306	6.6	308.6	3.9	100.85	
AG10C - 25	529	0.08	0.055	2.015	0.493	2.840	0.065	2.141	0.75	379	44	405.6	9.2	408.4	8.6	100.69	
AG10C - 26	439	0.43	0.053	1.735	0.346	1.851	0.047	1.370	0.74	316	39	301.9	4.6	298.7	4	98.94	
AG10C - 27	475	0.70	0.053	2.830	0.355	2.675	0.049	1.760	0.66	306	61	308.1	7.1	307.5	5.3	99.81	
AG10C - 45	550	0.37	0.052	1.700	0.351	1.850	0.048	1.299	0.70	287	39	306	5.1	305.2	3.9	99.74	
AG10D - 1	597	1.06	0.053	1.898	0.364	1.949	0.050	1.207	0.62	304	45	314.9	5.3	312.7	3.7	99.30	
AG10D - 7	290	0.50	0.053	2.087	0.369	2.086	0.051	1.651	0.79	303	44	319.3	6	319.9	5.1	100.19	
AG10D - 8	115.4	0.37	0.051	3.333	0.339	3.540	0.048	1.545	0.44	216	74	294.6	9.3	301.5	4.5	102.34	

AG10D - 9	246	0.21	0.059	2.034	0.784	2.168	0.097	1.347	0.62	546	44	586.3	9.5	593.7	7.7	101.26
AG10D - 10	506.2	0.53	0.052	1.919	0.350	1.971	0.049	1.270	0.64	274	43	304.4	5.2	307.2	3.8	100.92
AG10D - 13	152.4	0.52	0.051	3.333	0.348	3.448	0.049	1.718	0.50	236	72	302.9	9.2	307.6	5.2	101.55
AG10D - 15	190.1	0.49	0.053	3.013	0.354	3.107	0.049	1.402	0.45	310	62	307.8	8.2	305.3	4.2	99.19
AG10D - 22	267	0.35	0.053	3.396	0.357	3.361	0.049	1.989	0.59	304	74	309.4	9.3	306.8	5.9	99.16
AG10D - 23	199.1	0.46	0.054	2.788	0.375	2.933	0.050	1.984	0.68	341	59	322.5	8.1	317	6.2	98.29
AG10D - 27	198.7	0.53	0.054	2.788	0.365	2.492	0.049	1.485	0.60	341	58	315.3	6.8	309.3	4.5	98.10
AG10D - 28	280.6	0.59	0.053	2.457	0.357	2.637	0.049	1.970	0.75	300	56	308.8	7	306.6	5.9	99.29
AG10D - 29	305.5	0.45	0.053	2.091	0.352	2.759	0.048	1.382	0.50	296	47	305	7.2	300.7	4.1	98.59
AG10D - 31	683	0.78	0.162	0.989	10.480	1.527	0.468	1.518	0.99	2471	16	2477	15	2471	31	99.76
AG10D - 35	456	0.47	0.052	2.115	0.352	2.275	0.049	2.049	0.90	270	47	305.3	5.9	307.3	6.4	100.66
AG10D - 38	212.7	0.46	0.053	3.002	0.361	3.047	0.049	1.526	0.50	302	67	312.9	8.1	309.2	4.6	98.82
AG10D - 40	241.6	0.48	0.054	4.664	0.367	4.632	0.050	2.213	0.48	312	99	316	13	312.3	7	98.83
AG10D - 43	381.2	0.39	0.054	2.239	0.399	2.757	0.054	2.048	0.74	332	49	340	8.1	337.3	6.5	99.21
AG10D - 44	147.1	0.46	0.053	3.396	0.366	3.279	0.050	1.435	0.44	317	69	320	9.1	315.5	4.4	98.59
AG10D - 52	579.7	0.55	0.052	1.912	0.356	2.192	0.050	1.374	0.63	287	45	308.6	5.8	311.4	4.2	100.91
AG10D - 53	382	0.49	0.054	2.033	0.385	2.312	0.052	1.375	0.59	355	46	330	6.5	324.6	4.4	98.36
AG10D - 54	259.7	0.48	0.054	2.588	0.369	2.710	0.050	1.571	0.58	351	56	317.8	7.5	312.3	4.8	98.27
AG10D - 58	650	0.33	0.054	1.577	0.377	1.828	0.051	1.370	0.75	353	36	325.6	5.4	321.1	4.3	98.62
AG10D - 60	154	0.49	0.053	3.232	0.360	3.333	0.050	1.664	0.50	286	71	311	8.8	313.7	5.1	100.87
AG10D - 61	259.3	0.76	0.053	2.471	0.355	2.589	0.049	1.504	0.58	292	55	307.9	6.9	309.6	4.6	100.55
AG10D - 62	308	0.60	0.054	2.597	0.382	2.880	0.051	1.878	0.65	338	56	327.2	8	321.3	5.8	98.20
AG10D - 63	644	0.48	0.052	1.454	0.379	1.796	0.052	1.318	0.73	286	33	325.6	5	328.9	4.2	101.01
AG10D - 64	378.1	0.39	0.053	3.008	0.364	2.747	0.050	1.746	0.64	312	66	314.8	7.4	313.5	5.3	99.59
AG10D - 72	196.6	0.57	0.071	2.270	1.511	2.647	0.154	1.946	0.73	943	43	932	16	924	17	99.14
AG10E - 2	291.9	0.42	0.053	2.457	0.366	3.005	0.050	1.680	0.56	302	56	315.7	7.8	314.4	5.2	99.59
AG10E - 4	321	0.65	0.053	2.273	0.349	2.119	0.048	1.258	0.59	299	50	303.6	5.6	300.4	3.7	98.95
AG10E - 5	335	0.47	0.053	2.444	0.365	2.247	0.050	1.244	0.55	318	57	316.3	6.3	313.4	3.8	99.08
AG10E - 6	243.9	0.41	0.052	2.290	0.352	2.613	0.048	1.451	0.56	289	51	305.5	6.9	303.7	4.3	99.41
AG10E - 7	455	0.65	0.053	1.873	0.365	1.975	0.050	1.370	0.69	305	42	315.8	5.5	312.2	4.2	98.86

AG10E - 8	150.3	0.52	0.053	3.396	0.357	3.361	0.048	1.365	0.41	290	72	308.4	9.1	304.3	4.1	98.67			
AG10E - 10	201.5	0.58	0.072	1.524	1.668	1.679	0.166	1.446	0.86	983	33	994	10	990	13	99.60			
AG10E - 11	2026	0.18	0.052	1.263	0.380	1.397	0.052	1.186	0.85	288	29	326.4	3.9	328.4	3.8	100.61			
AG10E - 12	309.7	0.58	0.053	2.662	0.355	2.733	0.049	1.765	0.65	288	58	307.7	7.2	306.6	5.3	99.64			
AG10E - 16	179.2	0.71	0.053	2.852	0.356	2.809	0.049	1.417	0.50	289	62	308.4	7.7	306.5	4.2	99.38			
AG10E - 17	262.3	0.48	0.054	3.352	0.354	3.390	0.048	1.696	0.50	333	74	307.1	8.8	300.7	5	97.92			
AG10E - 23	600	0.40	0.053	1.732	0.384	1.876	0.052	1.449	0.77	325	38	329.4	5.3	329.6	4.7	100.06			
AG10E - 25	161.7	0.44	0.053	2.667	0.361	3.047	0.050	1.479	0.49	286	61	312.3	7.8	314.6	4.5	100.74			
AG10E - 26	308.4	0.67	0.053	2.264	0.367	2.510	0.050	1.476	0.59	312	50	316.3	6.8	315.4	4.5	99.72			
AG10E - 34	214	0.51	0.059	2.034	0.745	2.013	0.092	1.515	0.75	552	45	564.4	8.8	569.8	8.4	100.96			
AG10E - 35	764	1.02	0.054	2.412	0.372	2.688	0.051	1.681	0.63	352	56	320.4	7.5	318.1	5.2	99.28			
AG10E - 39	420	0.37	0.054	2.416	0.356	2.500	0.048	1.568	0.63	342	53	308.7	6.6	305.1	4.7	98.83			
Dyke 12																			
AG12A - 16	540	0.86	0.053	2.448	0.370	2.539	0.052	1.622	0.64	314	53	319.2	7	325.5	5.1	101.97			
AG12A - 22	423	0.41	0.053	2.846	0.357	2.801	0.049	1.976	0.71	298	65	309.2	7.6	309	6	99.94			
AG12A - 31	812	0.38	0.053	2.996	0.382	2.385	0.052	2.119	0.89	330	66	327.9	6.7	326.1	6.7	99.45			
AG12A - 35	725	0.84	0.054	2.052	0.362	2.679	0.049	1.657	0.62	342	45	313.1	7.2	311.3	5	99.43			
AG12A - 37	212	0.49	0.054	4.074	0.363	3.581	0.050	1.703	0.48	338	91	314	9.9	314	5.2	100.00			
AG12A - 38	229	0.36	0.053	2.996	0.357	2.774	0.049	1.398	0.50	323	62	309.1	7.4	310.6	4.2	100.49			
AG12A - 44	821	0.37	0.053	1.817	0.372	1.857	0.051	1.289	0.69	311	40	320.3	5.1	321.8	4.1	100.47			
AG12A - 45	410	0.54	0.053	2.268	0.356	2.194	0.049	1.264	0.58	310	50	308.4	5.9	308.7	3.8	100.10			
AG12A - 46	203	0.57	0.053	3.422	0.366	3.825	0.050	1.254	0.33	277	75	316	11	315.8	3.9	99.94			
AG12A - 50	432	0.54	0.052	2.505	0.337	2.433	0.046	1.178	0.48	256	54	294.3	6.2	288.9	3.3	98.17			
AG12A - 51	250	0.50	0.053	3.232	0.367	3.270	0.049	1.724	0.53	281	71	316.6	8.6	310.2	5.2	97.98			
AG12A - 57	216	0.78	0.052	3.824	0.346	3.757	0.047	2.006	0.53	263	83	300.3	9.6	295.2	5.8	98.30			
AG12A - 58	292	0.71	0.054	3.178	0.381	2.887	0.050	1.684	0.58	322	68	327.4	8.5	317.5	5.2	96.98			
AG12A - 59	435	0.55	0.053	2.448	0.360	2.251	0.048	1.432	0.64	308	53	311.5	6	303.4	4.2	97.40			
AG12A - 62	224.9	0.38	0.053	3.592	0.364	3.846	0.050	2.012	0.52	310	83	315	10	312.5	6.2	99.21			
AG12A - 63	196	0.48	0.052	3.065	0.349	3.152	0.048	1.363	0.43	262	65	302.5	8	304.8	4.1	100.76			
AG12A - 64	233	0.55	0.053	3.403	0.366	3.552	0.050	1.600	0.45	291	74	315.5	9.5	314.4	4.9	99.65			

AG12A - 68	236	0.77	0.053	2.467	0.363	2.725	0.051	1.469	0.54	297	52	313.7	7.4	320.9	4.6	102.30
AG12B - 23	760	0.11	0.056	4.804	0.420	5.952	0.056	5.197	0.87	440	110	355	18	350	18	98.59
Aigoual pluton																
AG14(1) - 10	573	1.69	0.053	1.872	0.378	2.036	0.052	1.424	0.70	306	42	325.9	5.8	326.6	4.5	100.21
AG14(1) - 27	648	0.19	0.053	1.723	0.368	1.876	0.050	0.973	0.52	331	39	317.6	5.1	316.6	3	99.69
AG14(1) - 102	423	0.43	0.053	2.068	0.365	2.084	0.050	1.151	0.55	323	46	315.2	5.7	311.6	3.5	98.86
AG14(1) - 119	229.7	0.49	0.053	2.836	0.359	2.760	0.049	1.199	0.43	293	64	310.4	7.4	309.7	3.6	99.77
AG14(1) - 121	345	0.59	0.052	2.481	0.361	2.383	0.050	1.282	0.54	286	55	313.1	6.6	314.1	3.9	100.32
AG14(1) - 124	317	0.39	0.053	3.612	0.359	4.735	0.049	2.444	0.52	296	82	311	13	308.8	7.6	99.29
AG14(1) - 154	928	0.42	0.053	1.710	0.382	1.753	0.052	1.216	0.69	325	39	328.4	4.9	325.6	3.9	99.15
AG14(3) - 2	364	0.31	0.053	2.841	0.364	3.022	0.050	1.550	0.51	296	62	314	8.2	316.5	4.8	100.80
AG14(3) - 10	611	0.94	0.052	1.611	0.374	2.165	0.052	1.309	0.60	277	36	322.1	6	326.3	4.1	101.30
AG14(3) - 16	771	0.36	0.054	1.690	0.379	1.795	0.051	1.154	0.64	350	38	325.7	5	321.5	3.6	98.71
AG14(3) - 20	793	0.64	0.052	1.830	0.360	1.916	0.050	1.458	0.76	293	42	312	5.1	314.8	4.5	100.90

^a (²⁰⁶Pb/²³⁸U age / ²⁰⁷Pb/²³⁵U age) * 100

Table 9 Analytical results zircon Lu-Hf isotopes

Sample/spot	$^{176}\text{Yb}/^{177}\text{Hf}$ ^a	$\pm 2\sigma$	$^{176}\text{Lu}/^{177}\text{Hf}$ ^a	$\pm 2\sigma$	$^{178}\text{Hf}/^{177}\text{Hf}$	$^{180}\text{Hf}/^{177}\text{Hf}$	Sig_{Hf} ^b	$^{176}\text{Hf}/^{177}\text{Hf}$	$\pm 2\sigma$ ^c	$^{176}\text{Hf}/^{177}\text{Hf}_{(t)}$ ^d	$e\text{Hf}(t)$ ^d	$\pm 2\sigma$ ^c	T_{DM2} ^e	age ^f
	(V)												(Ga)	(Ma)
AG5D														
65	0.0178	15.35	0.00066	4.39	1.467232	1.886955	14.27	0.282470	20.30	0.282466	-4.02	1.01	1.47	326
66	0.0088	20.15	0.00034	6.95	1.467222	1.886783	9.76	0.282472	24.76	0.282470	-4.14	1.24	1.47	315.6
67	0.0168	18.27	0.00064	5.37	1.467230	1.886810	14.72	0.282472	17.13	0.282468	-4.05	0.86	1.47	322.1
68	0.0188	15.72	0.00072	4.63	1.467254	1.886855	10.93	0.282466	22.54	0.282462	-4.66	1.13	1.49	304.6
69	0.0284	24.09	0.00109	7.21	1.467280	1.886704	8.08	0.282496	27.53	0.282490	-3.67	1.38	1.44	304.9
70	0.0171	16.65	0.00066	4.82	1.467171	1.886762	12.46	0.282454	21.79	0.282450	-5.36	1.09	1.52	291.5
71	0.0353	28.47	0.00126	7.72	1.467189	1.886708	8.10	0.282470	23.01	0.282463	-4.64	1.15	1.49	304.2
72	0.0175	15.73	0.00067	4.59	1.467225	1.886766	7.82	0.282455	29.79	0.282451	-4.64	1.49	1.51	322.7
73	0.0179	15.14	0.00071	4.67	1.467224	1.886833	9.13	0.282496	18.28	0.282492	-3.41	0.91	1.43	312.4
74	0.0340	47.85	0.00124	16.13	1.467416	1.886696	6.02	0.282467	76.28	0.282460	-4.54	3.81	1.49	313.1
75	0.0362	54.76	0.00133	17.15	1.467282	1.886695	7.38	0.282530	52.50	0.282522	-2.34	2.62	1.37	313.4
76	0.0477	81.04	0.00171	26.13	1.467146	1.886611	5.78	0.282511	75.94	0.282501	-3.25	3.80	1.42	305.8
77	0.0261	34.54	0.00098	11.17	1.467268	1.886664	7.65	0.282537	40.41	0.282532	-2.11	2.02	1.36	307.8
AG5C														
78	0.0172	17.41	0.00070	5.68	1.467211	1.886864	16.79	0.282453	17.73	0.282449	-4.64	0.89	1.51	325.4
79	0.0139	11.32	0.00055	3.41	1.467209	1.886728	14.60	0.282441	16.02	0.282438	-5.41	0.80	1.54	308.6
80	0.0137	11.04	0.00054	3.26	1.467227	1.886854	14.79	0.282456	13.76	0.282453	-4.81	0.69	1.51	311.6
81	0.0107	10.78	0.00041	3.30	1.467224	1.886828	12.79	0.282450	22.29	0.282448	-4.89	1.11	1.51	316.4
82	0.0284	23.41	0.00107	6.73	1.467247	1.886798	11.38	0.282465	19.54	0.282459	-4.68	0.98	1.50	308.2
83	0.0194	19.70	0.00071	6.07	1.467216	1.886922	11.53	0.282466	24.69	0.282461	-4.27	1.23	1.49	322.5
84	0.0163	16.37	0.00063	5.21	1.467259	1.886787	8.68	0.282516	34.05	0.282512	-2.30	1.70	1.38	330.1
85	0.0236	19.48	0.00089	5.61	1.467239	1.886748	10.41	0.282512	23.72	0.282507	-3.14	1.19	1.41	301.1
86	0.0148	14.73	0.00057	4.60	1.467188	1.886763	12.61	0.282467	20.29	0.282463	-4.43	1.01	1.49	312.2
87	0.0139	11.30	0.00054	3.34	1.467220	1.886762	13.99	0.282443	19.16	0.282440	-5.39	0.96	1.53	305.9
88	0.0295	26.25	0.00114	8.08	1.467252	1.886818	9.77	0.282513	24.30	0.282501	2.03	1.22	1.31	541
89	0.0204	17.88	0.00080	5.42	1.467203	1.886901	11.10	0.282578	21.67	0.282568	6.84	1.08	1.13	649

90	0.0402	40.25	0.00146	12.12	1.467211	1.886773	11.41	0.282485	22.48	0.282475	-3.25	1.12	1.45	346.1
91	0.0279	22.37	0.00106	6.38	1.467184	1.886707	9.62	0.282512	24.73	0.282506	-2.89	1.24	1.40	313.9
92	0.0097	8.06	0.00038	2.42	1.467165	1.886743	10.66	0.282452	19.50	0.282449	-4.95	0.97	1.51	311.2
93	0.0160	12.81	0.00062	3.75	1.467188	1.886858	11.57	0.282460	20.19	0.282457	-4.68	1.01	1.50	311.7
94	0.0205	16.48	0.00079	4.73	1.467192	1.886805	11.54	0.282466	25.82	0.282462	-4.55	1.29	1.49	309.3
95	0.0240	20.69	0.00093	6.26	1.467191	1.886725	10.17	0.282486	22.88	0.282480	-3.07	1.14	1.44	346.9
96	0.0199	15.96	0.00081	4.85	1.467273	1.886801	10.31	0.282528	22.75	0.282523	-2.15	1.14	1.37	320.1
AG5B														
97	0.0154	12.36	0.00058	3.51	1.467268	1.886711	11.42	0.282473	16.94	0.282470	-4.04	0.85	1.47	319.2
99	0.0224	18.38	0.00084	5.10	1.467276	1.886818	14.76	0.282452	17.82	0.282447	-4.35	0.89	1.51	342
100	0.0096	7.86	0.00038	2.30	1.467236	1.886763	14.44	0.282451	15.56	0.282449	-4.65	0.78	1.51	325.2
126	0.0275	22.52	0.00108	6.74	1.467211	1.886787	14.34	0.282470	22.35	0.282464	-3.84	1.12	1.47	338.1
127	0.0261	29.44	0.00100	9.77	1.467188	1.886890	12.93	0.282460	17.19	0.282454	-4.20	0.86	1.49	337.5
128	0.0204	17.76	0.00078	5.53	1.467199	1.886671	12.49	0.282491	22.74	0.282486	-3.37	1.14	1.44	323.4
129	0.0264	21.47	0.00100	6.15	1.467198	1.886880	14.05	0.282482	18.61	0.282476	-3.79	0.93	1.46	320.6
130	0.0235	19.31	0.00092	5.73	1.467211	1.886663	11.21	0.282481	19.50	0.282471	0.90	0.97	1.37	537.6
131	0.0197	15.76	0.00075	4.52	1.467230	1.886813	11.99	0.282472	21.46	0.282467	-4.25	1.07	1.48	313.7
132	0.0268	21.49	0.00102	6.16	1.467187	1.886779	10.21	0.282502	24.09	0.282496	-3.10	1.20	1.42	319.8
133	0.0867	76.76	0.00297	20.41	1.467196	1.886772	9.64	0.282545	27.12	0.282526	-1.65	1.36	1.35	337.2
134	0.0187	20.67	0.00071	6.80	1.467241	1.886748	13.55	0.282481	20.50	0.282477	-4.70	1.02	1.47	278
135	0.0204	25.64	0.00073	8.08	1.467191	1.886927	12.89	0.282470	22.47	0.282466	-4.16	1.12	1.48	320.8
136	0.0235	18.78	0.00090	5.41	1.467194	1.886708	9.83	0.282488	28.02	0.282483	-3.52	1.40	1.44	322.1
137	0.0252	20.15	0.00100	6.03	1.467225	1.886868	11.11	0.282487	19.79	0.282481	-3.83	0.99	1.45	310.5
138	0.0134	10.90	0.00051	3.17	1.467190	1.886793	12.49	0.282453	21.20	0.282450	-4.62	1.06	1.51	325.9
139	0.0139	12.22	0.00055	3.79	1.467177	1.886780	12.31	0.282354	27.77	0.282351	-8.15	1.39	1.70	324.6
140	0.0358	29.49	0.00120	7.77	1.467202	1.886885	12.29	0.282437	20.02	0.282430	-5.40	1.00	1.55	322.6
141	0.0401	32.13	0.00143	8.57	1.467191	1.886764	15.48	0.282457	19.26	0.282449	-4.80	0.96	1.51	318.7
142	0.0172	13.75	0.00066	3.96	1.467260	1.887002	10.70	0.282496	20.18	0.282492	-3.23	1.01	1.43	321.1
143	0.0120	9.58	0.00047	2.80	1.467186	1.886761	11.09	0.282478	18.26	0.282475	-3.79	0.91	1.46	322.3
144	0.0341	27.39	0.00126	7.58	1.467206	1.886669	15.41	0.282497	15.94	0.282490	-3.15	0.80	1.43	327.6

145	0.0203	16.26	0.00079	4.72	1.467169	1.886712	10.04	0.282493	24.05	0.282488	-3.55	1.20	1.44	312.1
AG5A														
146	0.0296	23.71	0.00111	6.66	1.467228	1.886728	9.58	0.282482	25.87	0.282476	-4.12	1.29	1.46	306.1
147	0.0340	27.23	0.00126	7.59	1.467247	1.886781	7.81	0.282545	36.56	0.282538	-1.76	1.83	1.34	314.1
148	0.0212	16.97	0.00079	4.72	1.467211	1.886771	12.67	0.282460	18.28	0.282455	-4.15	0.91	1.49	338.3
149	0.0513	41.08	0.00184	11.05	1.467181	1.886839	11.37	0.282495	24.37	0.282483	-3.15	1.22	1.44	337.9
150	0.0195	15.61	0.00084	5.06	1.467205	1.886821	11.80	0.282530	21.88	0.282519	5.64	1.09	1.22	673.2
151	0.0161	13.11	0.00063	3.81	1.467208	1.886673	10.24	0.282443	25.57	0.282439	-4.96	1.28	1.53	326.2
152	0.0181	14.87	0.00069	4.21	1.467193	1.886688	10.50	0.282482	23.05	0.282478	-4.25	1.15	1.46	296.6
153	0.0224	18.18	0.00082	4.99	1.467200	1.886748	9.54	0.282521	24.10	0.282516	-2.41	1.20	1.38	319.5
154	0.0280	22.72	0.00105	6.33	1.467247	1.886490	6.12	0.282526	47.83	0.282520	-2.34	2.39	1.38	315.5
155	0.0239	19.46	0.00089	5.40	1.467217	1.886674	10.12	0.282479	17.99	0.282473	-3.88	0.90	1.46	321.3
156	0.0295	23.66	0.00109	6.57	1.467214	1.886602	7.57	0.282542	34.69	0.282535	-1.70	1.73	1.34	320
157	0.0221	17.73	0.00082	4.94	1.467208	1.886739	10.00	0.282501	24.38	0.282496	-3.16	1.22	1.42	316.8
158	0.0208	16.62	0.00080	4.83	1.467186	1.886748	9.82	0.282468	23.99	0.282463	-4.29	1.20	1.48	318.3
AG10E														
159	0.0187	14.96	0.00073	4.39	1.467269	1.886749	12.22	0.282462	26.43	0.282458	-4.58	1.32	1.50	314.4
160	0.0138	11.03	0.00054	3.25	1.467195	1.886739	8.57	0.282440	24.44	0.282437	-5.51	1.22	1.54	305.2
161	0.0127	10.19	0.00049	2.92	1.467185	1.886688	8.45	0.282426	32.63	0.282424	-5.99	1.63	1.57	305.2
162	0.0120	10.05	0.00047	2.96	1.467240	1.886642	10.45	0.282458	21.77	0.282456	-4.67	1.09	1.50	313.4
163	0.0163	13.55	0.00062	3.95	1.467227	1.886710	10.18	0.282493	22.17	0.282489	-3.78	1.11	1.44	300.4
164	0.0103	8.72	0.00041	2.62	1.467210	1.886891	9.20	0.282484	24.07	0.282481	-3.79	1.20	1.45	312.2
165	0.0176	14.69	0.00068	4.41	1.467167	1.886770	10.41	0.282424	13.80	0.28242	-6.16	0.69	1.57	303.7
166	0.0138	14.63	0.00054	4.64	1.467194	1.886758	10.68	0.282448	20.05	0.282444	-5.28	1.00	1.53	304.3
167	0.0152	12.15	0.00059	3.56	1.467198	1.886734	9.92	0.282462	25.68	0.282458	-4.73	1.28	1.50	306.6
168	0.0184	14.73	0.00072	4.35	1.467292	1.886625	11.63	0.282461	23.00	0.282457	-4.30	1.15	1.49	328.4
169	0.0111	8.92	0.00045	2.69	1.467200	1.886870	10.94	0.282087	38.33	0.282079	-2.81	1.92	1.93	990
171	0.0198	15.88	0.00074	4.43	1.467276	1.886706	11.39	0.282463	20.04	0.282458	-4.47	1.00	1.49	318.4
172	0.0129	10.32	0.00051	3.06	1.467198	1.886848	8.69	0.282456	25.19	0.282453	-4.93	1.26	1.51	306.5
174	0.0295	23.68	0.00106	6.38	1.467221	1.886737	11.61	0.282478	24.75	0.282471	-3.50	1.24	1.46	340.9

175	0.0130	10.44	0.00051	3.04	1.467252	1.886757	7.38	0.282484	31.84	0.282481	-3.90	1.59	1.45	307.9
176	0.0154	12.33	0.00061	3.67	1.467218	1.886763	9.13	0.282460	28.25	0.282457	-4.61	1.41	1.50	314.6
177	0.0233	19.22	0.00091	5.49	1.467242	1.886589	8.85	0.282528	74.18	0.282523	-2.24	3.71	1.37	315.4
178	0.0234	19.13	0.00093	5.62	1.467285	1.886644	6.60	0.282454	46.11	0.282448	-4.59	2.30	1.51	329.6
179	0.0399	32.88	0.00148	9.00	1.467160	1.886768	12.34	0.282460	22.33	0.282452	-4.72	1.12	1.51	318.1
AG10D														
181	0.0224	18.43	0.00091	5.48	1.467244	1.886431	4.84	0.282572	49.20	0.282567	-0.75	2.46	1.29	312.7
182	0.0240	19.27	0.00094	5.64	1.467212	1.886779	12.67	0.282462	19.91	0.282456	-4.43	1.00	1.50	324.2
183	0.0308	24.69	0.00106	6.34	1.467196	1.886717	12.36	0.282492	22.20	0.282480	2.47	1.11	1.33	593.7
184	0.0118	9.48	0.00046	2.74	1.467239	1.886746	9.65	0.282493	34.56	0.282490	-3.58	1.73	1.44	307.2
185	0.0131	10.47	0.00051	3.09	1.467246	1.886728	10.67	0.282509	24.88	0.282506	-3.06	1.24	1.41	305.3
186	0.0144	11.57	0.00056	3.37	1.467157	1.886723	9.88	0.282463	19.18	0.282460	-4.67	0.96	1.50	307.6
187	0.0115	17.19	0.00045	6.19	1.467241	1.886802	11.07	0.282480	26.72	0.282478	-4.16	1.34	1.46	301.5
188	0.0155	13.68	0.00059	4.16	1.467235	1.886768	9.63	0.282524	21.63	0.282520	-2.24	1.08	1.37	319.9
189	0.0092	7.45	0.00041	2.51	1.467224	1.886770	10.73	0.281359	33.47	0.281340	2.94	1.67	2.71	2381
190	0.0128	10.79	0.00050	3.24	1.467215	1.886791	10.83	0.282450	24.15	0.282447	-5.08	1.21	1.52	309.3
191	0.0199	16.22	0.00077	4.72	1.467270	1.886798	9.88	0.282478	24.04	0.282474	-4.31	1.20	1.47	300.7
192	0.0147	11.91	0.00058	3.52	1.467379	1.886142	4.10	0.282697	120.78	0.282694	3.62	6.04	1.04	306.8
193	0.0273	70.84	0.00102	24.72	1.467278	1.886664	6.72	0.282528	46.78	0.282522	-2.25	2.34	1.37	317.6
194	0.0227	19.19	0.00089	5.89	1.467256	1.886680	8.78	0.282534	38.77	0.282529	-2.58	1.94	1.37	290.7
195	0.0320	32.92	0.00121	10.14	1.467262	1.886658	9.42	0.282458	34.71	0.282451	-5.01	1.73	1.51	306.6
196	0.0132	10.74	0.00051	3.16	1.467290	1.886818	9.53	0.282467	24.82	0.282464	-4.34	1.24	1.48	315.5
197	0.0236	20.37	0.00088	5.97	1.467250	1.886622	9.73	0.282483	38.17	0.282477	-3.38	1.91	1.45	337.3
198	0.0130	10.66	0.00051	3.22	1.467217	1.886923	10.14	0.281458	21.86	0.281438	-1.29	1.09	2.68	2049
199	0.0139	11.26	0.00053	3.25	1.467340	1.886722	7.06	0.282436	43.69	0.282433	-5.51	2.18	1.55	312.3
200	0.0150	16.92	0.00058	5.59	1.467242	1.886612	9.83	0.282495	30.20	0.282492	-3.52	1.51	1.43	307.3
226	0.0197	18.19	0.00073	5.08	1.467208	1.886801	9.84	0.282515	27.21	0.282511	-2.82	1.36	1.40	309.6
227	0.0195	17.17	0.00073	4.93	1.467262	1.886618	6.98	0.282546	34.61	0.282541	-1.46	1.73	1.33	321.3
228	0.0321	25.72	0.00122	7.33	1.467262	1.886672	8.40	0.282513	34.91	0.282505	-2.57	1.74	1.40	328.9
229	0.0134	10.83	0.00052	3.19	1.467288	1.886461	7.44	0.282517	47.28	0.282514	-2.62	2.36	1.39	312.3

230	0.0213	17.85	0.00081	5.16	1.467227	1.886762	11.44	0.282367	23.67	0.282362	-7.75	1.18	1.68	324.6
231	0.0216	17.30	0.00082	4.96	1.467200	1.886647	11.16	0.282454	23.59	0.282449	-4.95	1.18	1.51	311.4
AG10C														
232	0.0158	16.92	0.00061	5.26	1.467255	1.886843	9.69	0.282482	21.23	0.282478	-3.79	1.06	1.46	317.3
233	0.0143	11.62	0.00058	3.55	1.467219	1.886780	11.99	0.282085	29.83	0.282077	-8.81	1.49	2.05	727
234	0.0167	15.66	0.00066	5.08	1.467239	1.886753	9.67	0.282478	24.05	0.282474	-4.01	1.20	1.47	314.3
235	0.0131	10.83	0.00052	3.28	1.467265	1.886868	8.54	0.282489	22.93	0.282486	-3.39	1.15	1.44	323.3
236	0.0158	13.19	0.00062	3.97	1.467237	1.886785	11.10	0.282493	15.94	0.282490	-3.41	0.80	1.43	316
237	0.0230	20.79	0.00081	5.66	1.467277	1.886802	7.29	0.282460	33.96	0.282456	-4.70	1.70	1.50	312.3
238	0.0160	14.46	0.00062	4.41	1.467259	1.886622	8.59	0.282476	27.31	0.282472	-3.18	1.37	1.45	353.9
239	0.0170	14.38	0.00066	4.40	1.467256	1.886514	8.67	0.282469	27.13	0.282465	-4.31	1.36	1.48	314.9
240	0.0161	14.69	0.00063	4.44	1.467251	1.886693	9.85	0.282462	27.96	0.282458	-4.67	1.40	1.50	309.7
241	0.0401	32.81	0.00150	9.34	1.467250	1.886718	10.02	0.282510	37.84	0.282497	-0.01	1.89	1.36	455.8
242	0.0129	20.82	0.00051	7.31	1.467313	1.886787	10.46	0.282480	24.48	0.282477	-4.01	1.22	1.46	309.1
243	0.0207	25.51	0.00079	8.36	1.467255	1.886754	8.77	0.282503	23.18	0.282499	-2.95	1.16	1.41	322.9
245	0.0123	23.92	0.00049	8.52	1.467266	1.886603	7.50	0.282489	36.17	0.282486	-3.70	1.81	1.44	308.6
246	0.0368	47.01	0.00135	15.19	1.467377	1.886382	7.86	0.282562	72.68	0.282554	-1.33	3.63	1.31	307.5
247	0.0323	30.58	0.00125	9.60	1.467425	1.886613	9.68	0.282558	40.11	0.282548	0.72	2.01	1.28	408.4
248	0.0287	25.06	0.00109	7.45	1.467255	1.886636	9.56	0.282523	28.58	0.282517	-2.84	1.43	1.39	298.7
249	0.0162	13.10	0.00063	3.87	1.467261	1.886817	9.57	0.282425	33.27	0.282421	-6.23	1.66	1.57	298.5
250	0.0295	24.16	0.00109	6.78	1.467290	1.886658	7.76	0.282506	44.05	0.282500	-3.29	2.20	1.42	305.2
AG10A														
251	0.0212	18.30	0.00084	5.66	1.467214	1.886786	10.45	0.282470	21.90	0.282465	-4.32	1.09	1.48	314
252	0.0162	13.56	0.00063	4.05	1.467258	1.886795	12.58	0.282466	18.85	0.282462	-4.59	0.94	1.49	307.2
253	0.0178	15.38	0.00069	4.67	1.467311	1.886493	9.87	0.282473	34.73	0.282469	-4.21	1.74	1.47	312.5
254	0.0144	12.24	0.00058	3.83	1.467226	1.886907	10.87	0.282471	26.98	0.282467	-4.22	1.35	1.48	315.2
255	0.0401	33.13	0.00141	8.80	1.467184	1.886753	11.97	0.282473	24.44	0.282464	-4.01	1.22	1.48	330.1
256	0.0079	6.57	0.00033	2.07	1.467241	1.886740	12.88	0.282020	19.31	0.282016	-13.55	0.96	2.22	612.3
257	0.0616	49.91	0.00216	13.29	1.467200	1.886649	12.14	0.282501	30.29	0.282488	-3.25	1.51	1.43	325.8
258	0.0194	19.64	0.00073	6.27	1.467202	1.886802	10.45	0.282445	22.50	0.282441	-4.99	1.12	1.53	323.2

260	0.0348	71.25	0.00126	23.64	1.467273	1.886542	12.47	0.282442	33.45	0.282434	-5.16	1.67	1.54	325.6
261	0.0298	27.68	0.00111	8.10	1.467279	1.886612	12.99	0.282467	28.37	0.282460	-4.53	1.42	1.49	312.4
263	0.0202	17.12	0.00078	5.41	1.467309	1.886587	8.34	0.282488	40.95	0.282483	-3.27	2.05	1.44	333.3
265	0.0399	58.75	0.00145	19.24	1.467248	1.886532	10.02	0.282510	37.34	0.282501	-2.78	1.87	1.41	326.6
AG12B														
26	0.0311	26.27	0.00117	7.89	1.467284	1.886929	7.75	0.282607	25.66	0.282600	0.43	1.28	1.22	313.8
27	0.0271	22.53	0.00104	6.58	1.467287	1.886775	11.18	0.28248	19.50	0.282474	-3.44	0.97	1.45	340.2
28	0.0265	21.34	0.00105	6.35	1.467161	1.886669	11.85	0.28245	24.74	0.282444	-5.53	1.24	1.53	294.2
29	0.0381	30.51	0.00141	8.51	1.467224	1.886571	11.31	0.28247	27.95	0.282462	-4.54	1.40	1.49	309.7
30	0.0139	11.19	0.00053	3.21	1.46721	1.886698	10.64	0.28247	27.06	0.282467	-4.03	1.35	1.47	324.3
31	0.0167	17.50	0.00066	5.84	1.467212	1.88673	7.77	0.282495	25.45	0.282491	-3.22	1.27	1.43	322.5
32	0.0308	25.13	0.00110	6.76	1.467151	1.886656	10.09	0.282579	24.58	0.282572	-0.32	1.23	1.27	324.3
33	0.0244	20.60	0.00093	5.99	1.467226	1.886524	7.29	0.282536	44.16	0.282530	-1.62	2.21	1.35	332.1
34	0.0170	13.71	0.00065	4.00	1.467246	1.886624	10.51	0.282469	30.16	0.282466	-4.21	1.51	1.48	318.8
35	0.0284	24.97	0.00106	6.95	1.467345	1.886665	6.54	0.282538	34.55	0.282532	-1.92	1.73	1.35	316.1
36	0.0250	23.04	0.00093	6.65	1.467279	1.886684	9.15	0.282516	26.54	0.282510	-2.23	1.33	1.39	336.4
37	0.0257	27.65	0.00098	9.00	1.467209	1.886663	12.80	0.282486	21.07	0.282479	-2.89	1.05	1.44	356
38	0.0245	27.73	0.00091	8.80	1.467289	1.886541	9.48	0.282482	42.25	0.282477	-3.82	2.11	1.46	317.8
39	0.0290	32.91	0.00108	9.75	1.467224	1.886754	7.52	0.282486	37.55	0.282479	-3.98	1.88	1.46	307
40	0.0502	42.56	0.00179	12.17	1.467254	1.886648	9.11	0.282534	29.85	0.282523	-1.86	1.49	1.36	333
41	0.0427	39.84	0.00170	11.85	1.467314	1.886736	9.43	0.282538	58.64	0.282528	-1.65	2.93	1.35	335
42	0.0304	24.59	0.00114	6.96	1.467172	1.886636	6.28	0.282543	45.64	0.282536	-2.13	2.28	1.35	300.1
AG12A														
43	0.0221	19.77	0.00082	5.80	1.467200	1.886871	10.71	0.282483	22.54	0.282478	-3.80	1.13	1.46	317.5
44	0.0238	22.01	0.00090	6.72	1.467204	1.886848	12.05	0.282470	24.95	0.282464	-4.15	1.25	1.48	323
45	0.0155	14.83	0.00060	4.74	1.467161	1.886777	14.54	0.282440	20.00	0.282436	-5.24	1.00	1.54	319
46	0.0283	22.83	0.00108	6.57	1.467199	1.886918	9.99	0.282508	24.61	0.282502	-2.78	1.23	1.41	325.5
48	0.0149	12.59	0.00055	3.49	1.467221	1.886683	10.72	0.282433	22.50	0.282430	-5.55	1.12	1.55	315.3
49	0.0169	13.97	0.00065	4.11	1.467249	1.886733	12.36	0.282490	20.24	0.282485	-3.09	1.01	1.43	337.4
50	0.0298	28.40	0.00114	8.84	1.467175	1.886824	13.94	0.282416	18.92	0.282410	-6.15	0.95	1.59	320.5

51	0.0187	15.40	0.00071	4.48	1.467252	1.886783	11.34	0.282470	23.82	0.282466	-4.04	1.19	1.48	326.1
52	0.0197	16.93	0.00073	4.84	1.467187	1.886822	8.93	0.282497	23.63	0.282492	-3.43	1.18	1.43	311.3
53	0.0197	15.81	0.00077	4.66	1.467229	1.886794	11.21	0.282485	19.90	0.282481	-3.78	0.99	1.45	314
55	0.0151	13.75	0.00059	4.06	1.467203	1.886750	9.15	0.282482	23.86	0.282478	-3.98	1.19	1.46	308.7
56	0.0234	34.32	0.00089	11.73	1.467267	1.886830	9.57	0.282479	28.24	0.282474	-3.87	1.41	1.46	320.4
57	0.0147	12.25	0.00064	4.21	1.467213	1.886723	11.53	0.282431	25.94	0.282427	-5.64	1.30	1.56	315.8
58	0.0197	19.57	0.00076	5.92	1.467252	1.886874	12.56	0.282468	19.96	0.282464	-4.20	1.00	1.48	321.8
59	0.0178	17.33	0.00070	5.07	1.467170	1.886703	9.55	0.282505	21.53	0.282501	-3.62	1.08	1.42	288.9
60	0.0228	18.64	0.00085	5.28	1.467302	1.886690	7.17	0.282477	48.26	0.282472	-4.17	2.41	1.47	310.2
61	0.0191	17.53	0.00072	5.18	1.467210	1.886742	9.59	0.282486	31.50	0.282481	-3.80	1.57	1.45	312.1
62	0.0156	13.86	0.00058	3.81	1.467203	1.886779	9.81	0.282458	25.95	0.282455	-5.10	1.30	1.51	295.2
63	0.0262	22.71	0.00095	6.38	1.467284	1.886696	6.61	0.282564	40.40	0.282558	-0.89	2.02	1.30	320.9
64	0.0156	13.82	0.00061	4.01	1.467171	1.886752	10.44	0.282520	24.01	0.282516	-2.50	1.20	1.38	314.4
AG14(1)														
266	0.0365	33.84	0.00135	9.78	1.467213	1.886700	11.10	0.282475	31.82	0.282467	-4.39	1.59	1.48	308
267	0.0214	17.14	0.00081	4.84	1.467198	1.886621	12.65	0.282439	18.70	0.282434	-5.44	0.93	1.54	313
268	0.0394	31.53	0.00139	8.36	1.467255	1.886857	9.11	0.282492	22.70	0.282484	-3.39	1.13	1.44	326.6
269	0.0108	8.64	0.00042	2.53	1.467211	1.886745	13.36	0.282454	20.16	0.282452	-5.30	1.01	1.52	291.4
270	0.0222	17.75	0.00083	4.97	1.467245	1.886795	14.72	0.282438	19.93	0.282433	-5.39	1.00	1.54	317.8
271	0.0260	20.78	0.00100	5.99	1.467196	1.886684	16.17	0.282453	17.05	0.282447	-4.79	0.85	1.51	321.7
272	0.0059	4.73	0.00024	1.43	1.467258	1.886878	13.63	0.282462	20.52	0.282460	-4.44	1.03	1.49	316.6
273	0.0110	8.83	0.00042	2.54	1.467201	1.886752	12.04	0.282442	20.07	0.282440	-5.32	1.00	1.53	309.7
274	0.0198	15.89	0.00075	4.53	1.467205	1.886709	12.10	0.282473	23.38	0.282468	-4.26	1.17	1.48	312.4
277	0.0282	23.11	0.00103	6.25	1.467194	1.886757	13.68	0.281866	17.05	0.281843	-6.85	0.85	2.30	1180
278	0.0196	16.10	0.00075	4.56	1.467157	1.886759	8.89	0.282446	21.92	0.282442	-4.90	1.10	1.52	325.6
AG14(3)														
279	0.0097	7.96	0.00038	2.28	1.467164	1.886678	13.10	0.282464	24.03	0.282462	-4.39	1.20	1.49	316.5
280	0.0325	26.75	0.00118	7.16	1.467233	1.886883	10.90	0.282478	21.60	0.282471	-4.03	1.08	1.47	318.5
281	0.0442	36.21	0.00157	9.55	1.467197	1.886721	10.79	0.282479	24.40	0.282470	-3.90	1.22	1.47	326.3
282	0.0100	7.98	0.00040	2.41	1.467253	1.886707	11.83	0.282445	23.55	0.282443	-5.58	1.18	1.53	293.5

283	0.0182	14.61	0.00069	4.17	1.467226	1.886799	14.38	0.282453	22.16	0.282449	-4.63	1.11	1.51	326.3
284	0.0155	12.41	0.00059	3.56	1.467176	1.886821	12.96	0.282457	19.05	0.282454	-4.53	0.95	1.50	322.9
285	0.0207	16.59	0.00079	4.73	1.467158	1.886683	15.60	0.282451	18.28	0.282446	-5.52	0.91	1.53	290.7
286	0.0130	10.44	0.00051	3.04	1.467233	1.886847	13.01	0.282458	23.45	0.282454	-4.54	1.17	1.50	321.5
287	0.0328	30.33	0.00125	9.39	1.467232	1.886810	11.16	0.282481	25.52	0.282473	-3.94	1.28	1.46	318.7
289	0.0328	26.67	0.00120	7.33	1.467189	1.886786	11.47	0.282455	33.10	0.282448	-4.73	1.65	1.51	322.9

Quoted uncertainties (absolute) relate to the last quoted figure. The effect of the inter-element fractionation on the Lu/Hf was estimated to be about 6 % or less based on analyses of the GJ-1 zircon. Accuracy and reproducibility was checked by repeated analyses of reference zircon GJ-1 (data given as mean with 2 standard deviation uncertainties)

a $^{176}\text{Yb}/^{177}\text{Hf} = (^{176}\text{Yb}/^{173}\text{Yb})_{\text{true}} \times (^{173}\text{Yb}/^{177}\text{Hf})_{\text{meas}} \times (\text{M}^{173}(\text{Yb})/\text{M}^{177}(\text{Hf}))_{\text{b(Hf)}}, \text{b(Hf)} = \ln(^{179}\text{Hf}/^{177}\text{Hf} \text{ true} / ^{179}\text{Hf}/^{177}\text{Hf} \text{meas}) / \ln(\text{M}^{179}(\text{Hf})/\text{M}^{177}(\text{Hf}))$, M=mass of respective isotope. The $^{176}\text{Lu}/^{177}\text{Hf}$ were calculated in a similar way by using the $^{175}\text{Lu}/^{177}\text{Hf}$ and b(Yb);

b Mean Hf signal in volt;

c Uncertainties are quadratic additions of the within-run precision and the daily reproducibility of the zircon standards;

d Initial $^{176}\text{Hf}/^{177}\text{Hf}$ and ϵ_{Hf} calculated using the apparent U-Pb age determined by LA-ICP-MS dating, and the CHUR parameters: $^{176}\text{Lu}/^{177}\text{Hf} = 0.0336$, and $^{176}\text{Hf}/^{177}\text{Hf} = 0.282785$ (Bouvier et al. 2008);

e Two stage "maximum" model age in billion years using the measured $^{176}\text{Lu}/^{177}\text{Hf}$ of each spot (first stage = age of zircon), a value of $^{176}\text{Lu}/^{177}\text{Hf} = 0.0113$ for the average continental crust (second stage), and an average MORB (DM) $^{176}\text{Lu}/^{177}\text{Lu}$ and $^{176}\text{Hf}/^{177}\text{Hf}$ of 0.03933 and 0.283294, respectively (Blichert-Toft and Puchtel 2010);

f $^{206}\text{Pb}/^{238}\text{U}$ age